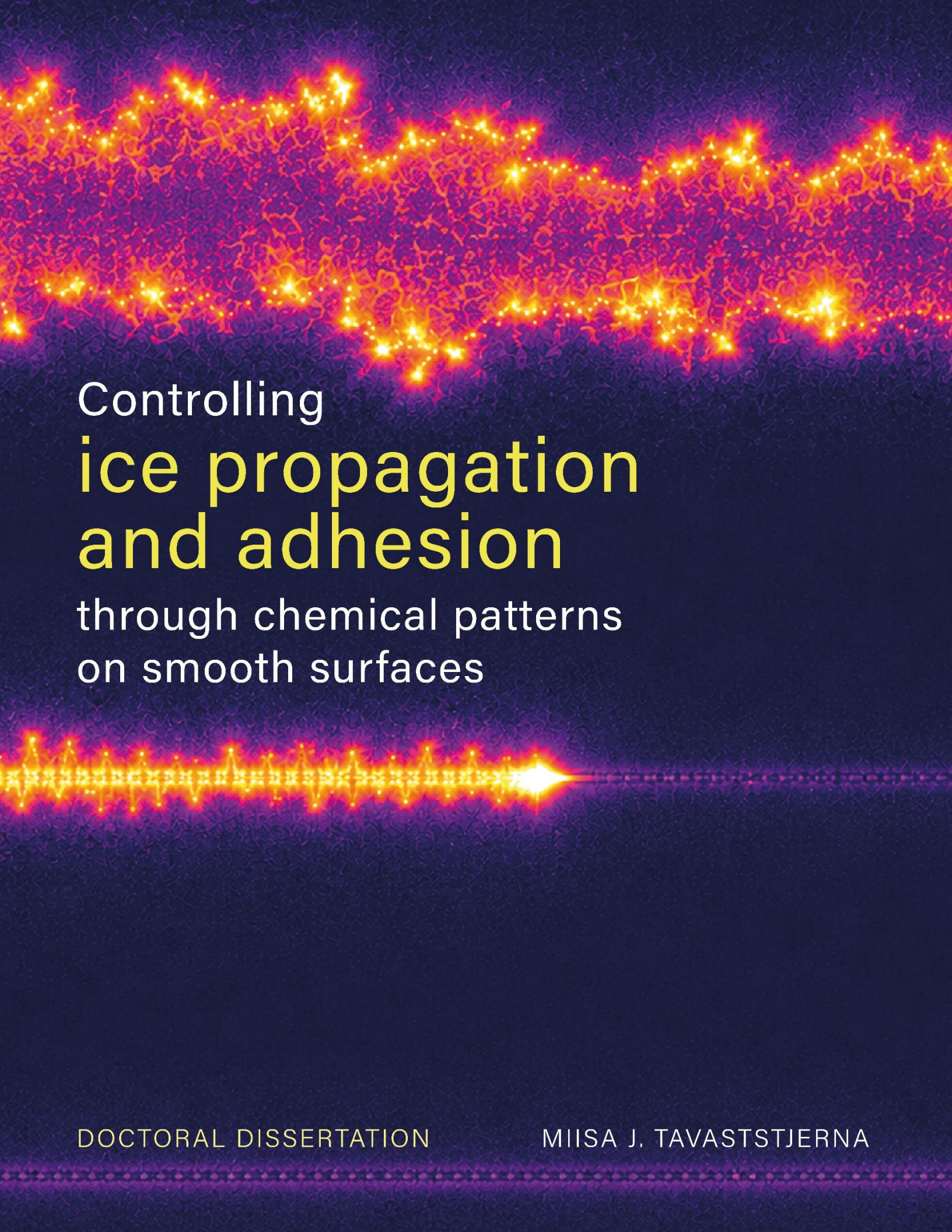

Controlling ice propagation and adhesion through chemical patterns on smooth surfaces

DOCTORAL DISSERTATION

MIISA J. TAVASTSTJERNA

Controlling ice propagation and adhesion through chemical patterns on smooth surfaces

Dissertation

for the purpose of obtaining the degree of doctor
at Delft University of Technology
by the authority of the Rector Magnificus, Prof.dr.ir. H. Bijl,
chair of the Board for Doctorates
to be defended publicly on
Wednesday 8th of July 2026 at 10:00h

by

Miisa Jasmin TAVASTSTJERNA

This dissertation has been approved by the promotors.

Composition of the doctoral committee:

Rector Magnificus	Chairperson
Dr. S. J. Garcia Espallargas	Delft University of Technology, promotor
Prof. dr. S. J. Picken	Delft University of Technology, promotor

Independent members:

Prof. C. A. Dransfeld	Delft University of Technology
Prof. dr. J. H. van Esch	Delft University of Technology
Prof. dr. I. K. Voets	Eindhoven University of Technology
Prof. dr. D. Bonn	University of Amsterdam
Dr. D. Seveno	KU Leuven

This project has received funding from the European Union's Horizon 2020 research and innovation programme under the Marie Skłodowska-Curie grant agreement No 956703.

Keywords: Anti-icing, ice adhesion, molecular water layer, ice-binding proteins
Printed by: Ipskamp Printing B.V.
Cover by: Miisa J. Tavaststjerna

ISBN: 978-94-6384-979-1

An electronic version of this dissertation is available at https://repository.tudelft.nl/

Summary

The objective of this dissertation is to learn more about the factors governing freezing nucleation, propagation, and adhesion on surfaces, and to utilize this information to bring forward new ideas for the design of effective passive anti-icing surfaces. The methodology focuses on two state-of-the-art characterization techniques that were developed and built in-house for quantitative and qualitative analysis of icing on surfaces: 1) A high-resolution thermal imaging device to monitor and quantify nucleation and propagation on surfaces, and 2) A horizontal shear test to measure ice adhesion to surfaces under controlled environmental conditions.

Chapter 1 provides an introduction to the hazards of surface icing, as well as the most relevant issues researchers face when developing materials that could provide a solution to this problem. To position the work of this dissertation in the field of aerospace engineering, an emphasis is placed on the dangers of aircraft icing and the urgent need for passive low-ice adhesion coatings in the aviation industry. The purpose of this chapter is to acquaint the reader with the main challenges in the development and characterization of new anti-icing surfaces.

Section 1 consists of **Chapters 2** and **3**, which focus on the factors governing the initiation and propagation of frost formation on surfaces at a molecular level. Both chapters utilize high-resolution thermal imaging to monitor and quantify freezing events under controlled environmental conditions.

Chapter 2 systematically investigates the effect of surface wettability and environmental humidity on initial freezing events on smooth surfaces. Additionally, this chapter introduces high-resolution thermal imaging as an effective and essential technique for in-situ monitoring and characterization of freezing onset and propagation on surfaces. Image analysis of thermal videos capturing freezing events on silane-modified glass surfaces reveals four characteristic freezing propagation modes. On a molecular level, these freezing modes are connected to the state and continuity of thin interfacial water layers, here referred to as molecular water layers (MWL). This work demonstrates how the MWL state changes through adjustments in humidity and surface chemistry, which in turn influence freezing onset times and propagation rates on surfaces.

Chapter 3 introduces hydrophilic chemical micropatterns as a method to control initial freezing events on surfaces. A patterning technique based on UV-lithography and surface-initiated polymerization was developed to functionalize hydrophobic polymers (PVC, PU, PMMA, PP, and PC) with hydrophilic stripes (PHEMA grafting). Thermal imaging videos show freezing events on the patterned surfaces to initiate on the hydrophilic stripes, propagate rapidly along the stripes, and finally spread over the hydrophobic substrate. This localized

freezing phenomenon is connected to a continuous MWL on the stripes, thus demonstrating the ability of the wettability patterns to control freezing events locally on surfaces.

Section 2 consists of **Chapters 4** and **5**, which advance from frost formation towards investigating ice accretion on the micropatterned surfaces from the perspective of supercooled droplet impact and ice adhesion mechanisms.

Chapter 4 centres around understanding supercooled impact, spreading, and freezing behaviour on the chemically micropatterned surfaces. The experimental tests were carried out in collaboration with the Institute of Fluid Mechanics and Aerodynamics at the Technical University of Darmstadt in Germany, where supercooled droplet impact on surfaces can be monitored using high-speed cameras inside a wind tunnel using controlled isothermal conditions (T = -10 °C). After droplet impact, small dry voids were seen to appear and spread within the receding droplet on some of the patterned samples. These events were connected to the simultaneous wetting of the hydrophilic patterns and de-wetting of the hydrophobic substrate – a process which was not completed before droplet freezing. An in-depth analysis of the high-speed video data shows that faster dry void formation and reduced droplet nucleation rates can be obtained by increasing patterning density, substrate hydrophobicity, and droplet impact velocity.

Chapter 5 compares various easy-to-apply surface treatments to reduce ice adhesion to polymeric substrates and commercial aircraft coatings. For this investigation, a new horizontal ice-adhesion test setup was designed and built in collaboration with MSc students Ronan Connolly and Sara Caliari. The investigated surface modifications include oil lubrication, extended UV-light exposure, hydrophilic micropatterning, and a UV-curable hydrophilic spray coating. Although oil lubrication has previously been the most popular approach to reduce ice adhesion in the literature, surprisingly, prolonged UV exposure was found to reduce ice adhesion more effectively on polypropylene surfaces. In addition, the lowest ice adhesion values were measured on all micropatterned and spray-coated surfaces, with the hydrophilic coating performing slightly better than the micropatterns. The explanation behind the success of the hydrophilic modifications was linked to the presence of non-freezable water layers that can act as lubricating layers at the ice-substrate interface.

Section 3 (**Chapter 6**) explores the potential application of ice-binding proteins in future anti-icing surfaces. Ice-binding proteins are proteins that can attach to ice crystals and either inhibit or promote the growth of that ice crystal, depending on the structure of the protein. These proteins can be found in nature in the cells of certain species of fish, insects, and plants that need protection from freezing in arctic climates. In this investigation, two such proteins (anti-freezing and ice-nucleating proteins) were attached to aluminium alloys via surface grafting and hydrogel coatings. The influence of these proteins on surface freezing was then monitored using the high-resolution thermal imaging technique introduced in Section 1. Surprisingly, the anti-freeze proteins attached to the surfaces using short linker chains promoted earlier freezing events instead of preventing them, which was

connected to the mobility of the anti-freeze proteins being the key factor in ensuring their ice-inhibiting function.

Overall, this dissertation advances the understanding of freezing nucleation, propagation, and ice adhesion on surfaces, offering new insights into the development of passive anti-icing materials. The following findings of this thesis should be considered in the development of new durable anti-icing coatings with potential applications in aviation, energy production, transportation, and cryopreservation industries:

I. Although hydrophobic and superhydrophobic surfaces delay freezing events under controlled laboratory conditions, humidity fluctuations and surface defects encountered in practical applications can induce the formation of liquid-like molecular water layers (MWLs). These MWLs accelerate ice nucleation and freezing propagation, ultimately reversing the intended anti-icing behaviour of hydrophobic surface treatments.

II. Because ice adhesion results are sensitive to various environmental and experimental parameters, publications reporting such results should provide full transparency regarding test conditions and the parameters chosen. Furthermore, evaluating new anti-icing surfaces in the presence of simulated real-world contaminations -- such as dust, scratches, or surface wear -- can yield valuable insight into their practical performance and durability.

III. This work demonstrates that anti-freeze proteins (AFPs) promote, rather than inhibit, freezing when short linker chains restrict their mobility. Future research on AFP-grafted surfaces should therefore ensure that the linker length allows sufficient protein mobility to maintain their ice-inhibiting function.

In addition, this dissertation provides several strategies that may offer an alternative scientific basis for developing more effective passive anti-icing materials:

I. **Hydrophilic micropatterning**: Although MWLs on hydrophilic surfaces can promote earlier ice nucleation and faster freezing propagation, hydrophobic polypropylene (PP) substrates micropatterned with hydrophilic poly(2-hydroxyethyl methacrylate) (PHEMA) grafts exhibited reduced ice nucleation rates during supercooled droplet impact compared to unpatterned PP. At higher impact velocities, the hydrophilic patterns also influenced the shape of the frozen droplets, suggesting a potential method for controlling ice accretion on aircraft wings. After impact, water recedes from hydrophobic regions and freezes preferentially on the hydrophilic patterns, which may help prevent clear-ice buildup and can protect vulnerable electronic components. The same concept could be useful in frost-sensitive electronics more generally by incorporating sacrificial hydrophilic regions into the device surfaces. To advance this concept toward practical applications, the patterning procedure should be improved by: a) developing a patterning method that modifies deeper layers in

aircraft coatings to improve durability, b) enhancing wetting contrast to accelerate the droplet receding rate from hydrophobic areas, c) investigating the effect of higher droplet impact velocities on freezing behaviour, and d) exploring different pattern geometries, densities, dimensions, and chemistries for optimal performance.

II. **Hydrophilic coatings with non-freezing water:** Hydrophilic polyelectrolyte gels are known to exhibit freezing delay due to water molecules being tightly bound to the charged polymer chains. Aiming to improve their durability, this dissertation introduces UV-curable coatings based on DMC monomers, which demonstrate exceptionally low ice adhesion and show encouraging durability. The reduction in adhesion is attributed to a liquid-like MWL that remains unfrozen at −10 °C and functions as a lubricating interfacial layer. Before such coatings can be considered for use in the aviation industry, further research is required to: a) explore different polyelectrolyte chemistries and their effects on the state and quantity of non-freezing water, b) examine water uptake and its implications for long-term durability and corrosion resistance, c) evaluate coating performance under various icing conditions, including frost formation and impact icing, and d) further investigate the structure, dynamics, and freezing behaviour of MWLs on these coatings using advanced surface-sensitive characterization techniques. Such studies could help establish a stronger mechanistic understanding of how MWLs influence ice nucleation and ice adhesion.

III. **Coatings utilizing ice-binding proteins:** Since anti-freeze proteins (AFPs) can inhibit freezing events in solutions and on surfaces, this dissertation also examines their incorporation into coating formulations. As a first step, AFPs were embedded into hydrogel matrices using sufficiently long linkers to maintain protein mobility. These AFP-hydrogels exhibited delayed freezing compared with hydrogels without AFPs, indicating potential for AFP-based passive anti-icing materials. Although such water-rich systems are unlikely to be applicable in the aviation sector, they may be promising for other fields, including cryopreservation and certain food-industry applications.

Samenvatting

Het doel van dit proefschrift is om meer inzicht te verkrijgen in de factoren die het ontstaan, de voortplanting en de hechting van ijs op oppervlakken bepalen, en om deze kennis te benutten voor de ontwikkeling van nieuwe concepten voor effectieve passieve anti-ijsoppervlakken. De toegepaste methodologie richt zich op twee geavanceerde karakterisatietechnieken die in eigen huis zijn ontwikkeld en gebouwd voor zowel kwantitatieve als kwalitatieve analyse van ijsvorming op oppervlakken: 1) een thermische beeldvormingstechniek met hoge resolutie om nucleatie en voortplanting van bevriezing op oppervlakken te volgen en te kwantificeren, en 2) een horizontale afschuiftest om de ijshechting aan oppervlakken te meten onder gecontroleerde omgevingscondities.

Hoofdstuk 1 geeft een introductie tot de gevaren van ijsvorming op oppervlakken en tot de belangrijkste uitdagingen waarmee onderzoekers worden geconfronteerd bij het ontwikkelen van materialen die een oplossing voor dit probleem kunnen bieden. Om het werk van dit proefschrift binnen het vakgebied van de luchtvaarttechniek te positioneren, wordt bijzondere aandacht besteed aan de risico's van ijsvorming op vliegtuigen en aan de dringende behoefte aan passieve coatings met lage ijshechting in de luchtvaartindustrie. Het doel van dit hoofdstuk is de lezer vertrouwd te maken met de belangrijkste uitdagingen bij de ontwikkeling en karakterisering van nieuwe anti-ijsoppervlakken.

Sectie 1 bestaat uit **Hoofdstukken 2** en **3** en richt zich op de factoren die op moleculair niveau het ontstaan en de voortplanting van rijpvorming op oppervlakken bepalen. In beide hoofdstukken wordt gebruikgemaakt van thermische beeldvorming met hoge resolutie om bevriezingsprocessen onder gecontroleerde omgevingscondities te monitoren en te kwantificeren.

Hoofdstuk 2 onderzoekt systematisch het effect van oppervlakte-bevochtigbaarheid en omgevingsvochtigheid op de initiële bevriezingsprocessen op gladde oppervlakken. Daarnaast introduceert dit hoofdstuk thermische beeldvorming met hoge resolutie als een effectieve en essentiële techniek voor het in-situ volgen en karakteriseren van het begin en de voortplanting van bevriezing op oppervlakken. Beeldanalyse van thermische video's die bevriezingsprocessen op met silaan gemodificeerd glas tonen, onthult vier karakteristieke voortplantingsmodi van bevriezing. Op moleculair niveau worden deze modi in verband gebracht met de toestand en continuïteit van dunne interfaciale waterlagen, hier aangeduid als moleculaire waterlagen (in het Engels "molecular water layers" of MWL). Dit werk laat zien hoe de toestand van deze MWL verandert door variaties in luchtvochtigheid en oppervlaktesamenstelling, wat op zijn beurt de tijd tot het begin van bevriezing en de voortplantingssnelheid van bevriezing op oppervlakken beïnvloedt.

Hoofdstuk 3 introduceert hydrofiele chemische micropatronen als methode om initiële bevriezingsprocessen op oppervlakken te sturen. Er werd een patroonvormingstechniek ontwikkeld op basis van UV-lithografie en door het oppervlak geïnitieerde polymerisatie om hydrofobe polymeren (PVC, PU, PMMA, PP en PC) te functionaliseren met hydrofiele strepen (PHEMA-grafting). Thermische beeldvormingsvideo's laten zien dat bevriezing op de gepatroneerde oppervlakken begint op de hydrofiele strepen, zich snel langs deze strepen voortplant en zich vervolgens over het hydrofobe substraat verspreidt. Dit gelokaliseerde bevriezingsverschijnsel wordt in verband gebracht met een continue moleculaire waterlaag op de strepen, waarmee wordt aangetoond dat bevochtigbaarheidspatronen lokale controle over bevriezingsprocessen op oppervlakken mogelijk maken.

Sectie 2 bestaat uit **Hoofdstukken 4** en **5** en verlegt de focus van rijpvorming naar ijsaanwas op de micropatronen, bekeken vanuit het perspectief van impact van onderkoelde druppels en mechanismen van ijshechting.

Hoofdstuk 4 richt zich op het begrijpen van het gedrag van onderkoelde druppels bij impact, uitspreiding en bevriezing op chemisch gemicropatroneerde oppervlakken. De experimentele testen werden uitgevoerd in samenwerking met het Institute of Fluid Mechanics and Aerodynamics van de Technische Universiteit Darmstadt in Duitsland, waar de impact van onderkoelde druppels op oppervlakken kan worden geobserveerd met hogesnelheidscamera's in een windtunnel onder gecontroleerde isotherme omstandigheden (T = −10 °C). Na de impact van de druppel werden op sommige gepatroneerde monsters kleine droge holtes waargenomen die zich binnen de terugtrekkende druppel vormden en uitbreidden. Deze verschijnselen werden gekoppeld aan de gelijktijdige bevochtiging van de hydrofiele patronen en ontvochtiging van het hydrofobe substraat – een proces dat niet volledig was voltooid voordat de druppel bevroor. Een gedetailleerde analyse van de hogesnelheidsvideodata toont aan dat snellere vorming van droge holtes en lagere nucleatiesnelheden van druppels kunnen worden bereikt door de patroondichtheid, de hydrofobiciteit van het substraat en de impactsnelheid van de druppel te verhogen.

Hoofdstuk 5 vergelijkt verschillende eenvoudig toepasbare oppervlaktebehandelingen om de ijshechting op polymeersubstraten en commerciële vliegtuigcoatings te verminderen. Voor dit onderzoek werd een nieuwe horizontale ijshechtingstestopstelling ontworpen en gebouwd in samenwerking met MSc-studenten Ronan Connolly en Sara Caliari. De onderzochte oppervlaktemodificaties omvatten oliesmering, langdurige UV-blootstelling, hydrofiele micropatronering en een UV-uithardbare hydrofiele spraycoating. Hoewel oliesmering in de literatuur vaak wordt beschouwd als de meest effectieve methode om ijshechting te verminderen, bleek verrassend genoeg dat langdurige UV-blootstelling de ijshechting op polypropyleenoppervlakken nog effectiever verminderde. Daarnaast werden de laagste ijshechtingswaarden gemeten op alle micropatroneerde en gespraycoate oppervlakken, waarbij de hydrofiele coating iets beter presteerde dan de micropatronen. De

verklaring voor het succes van de hydrofiele modificaties werd in verband gebracht met de aanwezigheid van niet-bevriesbare waterlagen die als smerende interfaciale lagen tussen ijs en substraat kunnen fungeren.

Sectie 3 (**Hoofdstuk 6**) onderzoekt de mogelijke toepassing van ijsbindende eiwitten in toekomstige anti-ijsoppervlakken. IJsbindende eiwitten zijn eiwitten die zich aan ijskristallen kunnen binden en afhankelijk van hun structuur de groei van deze kristallen kunnen remmen of juist bevorderen. Deze eiwitten komen in de natuur voor in de cellen van bepaalde soorten vissen, insecten en planten die bescherming nodig hebben tegen bevriezing in arctische klimaten. In dit onderzoek werden twee van dergelijke eiwitten (antivries- en ijsnucleërende eiwitten, in het Engels “anti-freeze proteins” of AFP en “ice-nucleating proteins” of INP) via oppervlakte-grafting en hydrogelcoatings aan aluminiumlegeringen bevestigd. De invloed van deze eiwitten op het bevriezen van oppervlakken werd vervolgens gemonitord met behulp van de thermische beeldvormingstechniek met hoge resolutie die in sectie 1 werd geïntroduceerd. Verrassend genoeg bleken AFP’s die via korte koppelketens aan het oppervlak waren bevestigd juist eerdere bevriezingsprocessen te bevorderen in plaats van te voorkomen. Dit werd in verband gebracht met het feit dat de mobiliteit van de AFP's een cruciale factor is voor hun ijsremmende functie.

In het algemeen draagt dit proefschrift bij aan een beter begrip van ijsnucleatie, voortplanting van bevriezing en ijshechting op oppervlakken en biedt het nieuwe inzichten voor de ontwikkeling van passieve anti-ijsmaterialen. De volgende bevindingen van dit proefschrift dienen in overweging te worden genomen bij de ontwikkeling van nieuwe duurzame anti-ijscoatings met potentiële toepassingen in de luchtvaart, energieproductie, transport en cryopreservatie:

I. Hoewel hydrofobe en superhydrofobe oppervlakken het begin van bevriezing onder gecontroleerde laboratoriumomstandigheden kunnen vertragen, kunnen vochtigheidsschommelingen en oppervlakteschade in praktische toepassingen leiden tot de vorming van vloeistofachtige moleculaire waterlagen (MWL). Deze MWL versnellen ijsnucleatie en de voortplanting van bevriezing en kunnen daardoor uiteindelijk het beoogde anti-ijseffect van hydrofobe oppervlaktebehandelingen tenietdoen.

II. Omdat metingen van ijshechting gevoelig zijn voor verschillende omgevings- en experimentele parameters, dienen publicaties waarin dergelijke resultaten worden gerapporteerd volledige transparantie te bieden over testomstandigheden en gekozen parameters. Daarnaast kan het evalueren van nieuwe anti-ijsoppervlakken in aanwezigheid van gesimuleerde realistische verontreinigingen — zoals stof, krassen of oppervlakteslijtage — waardevolle inzichten opleveren in hun praktische prestaties en duurzaamheid.

III. Dit werk toont aan dat antivrieseiwitten (AFP's) bevriezing juist bevorderen wanneer korte koppelketens hun mobiliteit beperken. Toekomstig onderzoek naar met AFP's gemodificeerde oppervlakken moet er daarom voor zorgen dat de lengte van de koppelketens voldoende mobiliteit van de eiwitten mogelijk maakt, zodat hun ijsremmende functie behouden blijft.

Daarnaast presenteert dit proefschrift verschillende strategieën die een alternatieve wetenschappelijke basis kunnen bieden voor de ontwikkeling van effectievere passieve anti-ijsmaterialen:

I. **Hydrofiele micropatronering:** Hoewel moleculaire waterlagen op hydrofiele oppervlakken eerdere ijsnucleatie en snellere voortplanting van bevriezing kunnen bevorderen, vertoonden hydrofobe polypropyleen-substraten (PP) met hydrofiele poly(2-hydroxyethyl methacrylaat) (PHEMA)-grafts een lagere nucleatiesnelheid tijdens de impact van onderkoelde druppels dan ongepatroneerd PP. Bij hogere impactsnelheden beïnvloedden de hydrofiele patronen bovendien de vorm van de bevroren druppels, wat een mogelijke methode suggereert om ijsaanwas op vliegtuigvleugels te sturen. Na impact trekt water zich terug uit hydrofobe gebieden en bevriest het bij voorkeur op de hydrofiele patronen, wat kan helpen om de vorming van helder ijs te voorkomen en kwetsbare elektronische componenten te beschermen. Hetzelfde concept zou breder toepasbaar kunnen zijn in rijpgevoelige elektronica door opofferende hydrofiele zones in apparaatoppervlakken te integreren. Om dit concept verder richting praktische toepassingen te ontwikkelen, moet de patroonvorming worden verbeterd door: a) een patroonmethode te ontwikkelen die diepere lagen in vliegtuigcoatings modificeert om de duurzaamheid te vergroten, b) het contrast in bevochtigbaarheid te vergroten om de terugtreksnelheid van druppels uit hydrofobe gebieden te versnellen, c) het effect van hogere druppelimpactsnelheden op het bevriezingsgedrag te onderzoeken, en d) verschillende patroongeometrieën, dichtheden, afmetingen en chemieën te verkennen voor optimale prestaties.

II. **Hydrofiele coatings met niet-bevriesbaar water:** Hydrofiele polyelektrolyt-gels staan erom bekend dat zij bevriezing kunnen vertragen doordat watermoleculen sterk gebonden zijn aan geladen polymeerketens. Met het doel de duurzaamheid te verbeteren introduceert dit proefschrift UV-uithardbare coatings op basis van DMC-monomeren, die uitzonderlijk lage ijshechting vertonen en een veelbelovende duurzaamheid laten zien. De vermindering van hechting wordt toegeschreven aan een vloeistofachtige moleculaire waterlaag die bij −10 °C niet bevriest en als

smerende interfaciale laag fungeert. Voordat dergelijke coatings in de luchtvaartindustrie kunnen worden toegepast, is verder onderzoek nodig om: a) verschillende polyelektrolytchemieën en hun effect op de toestand en hoeveelheid niet-bevriesbaar water te onderzoeken, b) wateropname en de implicaties daarvan voor duurzaamheid en corrosiebestendigheid op lange termijn te bestuderen, c) de prestaties van coatings onder verschillende ijscondities te evalueren, waaronder rijpvorming en impact-ijs, en d) de structuur, dynamiek en het vriesgedrag van MWLs op deze coatings met behulp van geavanceerde oppervlakgevoelige karakteriseringstechnieken. Dergelijke studies kunnen bijdragen aan een beter mechanistisch begrip van de invloed van MWLs op ijsnucleatie en ijshechting.

III. **Coatings met ijsbindende eiwitten:** Aangezien antivrieseiwitten (AFP) bevriezingsprocessen in oplossingen en op oppervlakken kunnen remmen, onderzoekt dit proefschrift ook hun integratie in coatingformuleringen. Als eerste stap werden AFP's ingebed in hydrogelmatrices met behulp van voldoende lange koppelketens om de mobiliteit van de eiwitten te behouden. Deze AFP-hydrogels vertoonden een vertraagd begin van bevriezing in vergelijking met hydrogels zonder AFP's, wat wijst op potentieel voor AFP-gebaseerde passieve anti-ijsmaterialen. Hoewel dergelijke water-rijke systemen waarschijnlijk niet geschikt zijn voor toepassingen in de luchtvaartsector, kunnen zij veelbelovend zijn voor andere gebieden, waaronder cryopreservatie en bepaalde toepassingen in de voedingsindustrie.

Yhteenveto

Tämän väitöskirjan tavoitteena on tuottaa uutta tietoa tekijöistä, jotka vaikuttavat jäätymisen alkupisteeseen, etenemiseen ja kiinnittymiseen pinnoilla. Lisäksi näitä havaintoja pyritään hyödyntämään uusien tehokkaiden jäätä hylkivien pinnoitteiden suunnittelussa. Tutkimuksissa käytetyt analyysimenetelmät keskittyvät kahteen eri korkealuokkaiseen koelaitteistoon, jotka kehitettiin ja rakennettiin tätä väitöskirjatutkimusta varten: 1) Tarkan erotuskyvyn omaava lämpökamera, jolla on mahdollista tarkkailla jäätymisen alkukohtia ja etenemistä sekä määrällisesti että laadullisesti. 2) Vaakasuora työntövoiman mittauslaitteisto, jolla voidaan määritellä jään tarttuvuus pintoihin säädellyissä ympäristöolosuhteissa.

Luku 1 johdattaa lukijan jään muodostumisen ja kasautumisen yhteiskunnallisiin vaaroihin sekä kaikkein olennaisimpiin ongelmiin, joita tutkijat kohtaavat jäätä hylkivien materiaalien suunnittelussa. Lento- ja avaruustekniikan näkökulmaa painottaen, erityistä huomiota kiinnitetään jään muodostumiseen lentokoneiden siivillä, mikä on johtanut merkittävään määrään lentotapaturmia viime vuosikymmenillä. Tämän luvun tarkoitus on tutustuttaa lukija jäätä hylkivien pinnoitteiden merkityksellisyyteen ja käydä läpi nykyajan suurimpia haasteita tuottaa tehokkaita materiaaleja jäätymisen aiheuttamien ongelmien ratkaisemiseksi.

Osa 1 sisältää **Luvut 2** ja **3**, jotka keskittyvät jäätymisen alkupisteeseen ja etenemiseen vaikuttaviin tekijöihin molekyylitasolla. Molemmat luvut hyödyntävät tarkan resoluution omaavaa lämpökameraa pintajäätymisprosessien kuvantamisessa säädellyissä ympäristöolosuhteissa.

Luku 2 tutkii järjestelmällisesti pintojen kostuvuuden ja ilman kosteuden vaikutusta jäätymistapahtumiin tasaisilla pinnoilla. Lisäksi tämä luku luo pohjaa lämpökameran käytölle pintajäätymisprosessien reaaliaikaisessa kuvantamisessa sekä niiden alkupisteen ja etenemisnopeuden määrittämisessä. Silaaneilla muunneltuilta lasipinnoilta kuvattu videomateriaali tuo ilmi neljä tunnusomaista jäärintamien etenemistapaa, jotka voidaan yhdistää vaihteleviin ohuisiin molekyylitason vesikalvoihin (englanniksi molecular water layer eli MWL). Tämä työ havainnollistaa, kuinka näiden MWL:n paksuus ja tiheys vaihtelevat ilman kosteuden ja kiinteiden aineiden pintakemian muuttuessa, mikä puolestaan vaikuttaa jäätymisen alkupisteeseen sekä jäätymisrintamien etenemisnopeuteen tasaisilla pinnoilla.

Luku 3 esittelee uuden keinon ohjata jäätymistapahtumia pinnoilla lisäämällä niihin vettä puoleensa vetäviä hydrofiilisiä mikrokuvioita. Tämän havainnollistamiseksi viisi erilaista vettä hylkivää hydrofobista muovialustaa (PVC, PU, PMMA, PP ja PC) kuvioitiin hydrofiilisillä polymeeriharjoilla (PHEMA, PDMAEMA ja PPEGMA). Kuvionti toteutettiin yhdistämällä kaksi eri kemiallista menetelmää: UV-litografia ja pintainitioitu atominsiirtoradikaalipolymerointi (englanniksi surface-initiated atom transfer radical polymerization eli SI-ATRP). Kuvioitujen muovialustojen lämpökameratutkimukset osoittavat, että jäätymistapahtumien alkupiste

sijaitsee aina hydrofiilisillä kuvioilla ja että ne etenevät salaman nopeasti kuvioita pitkin. Jäätymisrintamat etenevät myöhemmin kuvioilta hydrofobiselle muovialustalle, jolloin niiden etenemisnopeudet vähenevät huomattavasti. Tämä jäätymisilmiö voidaan liittää hydrofiiliset kuviot peittävään tiheään MWL:ään, joka tarjoaa optimaalisen pinnan kidealkioiden muodostumiselle ja kasvamiselle. Lisäksi paikallisten jäärintamien etenemisnopeutta voidaan säädellä kuvioiden ja muovialustan pintakemiaa muunnellen.

Osa 2 sisältää **Luvut 4** ja **5**, jotka siirtyvät yksittäisten jäätymistapahtumien erittelystä jääkertymien tutkimiseen samoilla mikrokuvioiduilla muovialustoilla. Kiinteiden jääkerrosten muodostumista tutkittiin keskittymällä alijäädytettyjen vesipisaroiden iskeytymiskäyttäytymiseen ja jään tarttuvuuteen pinnoilla.

Luku 4 keskittyy alijäädytettyjen vesipisaroiden iskeytymis-, leviämis- ja jäätymiskäyttäytymiseen mikrokuvioiduilla pinnoilla. Tämän luvun kokeelliset tutkimukset suoritettiin Saksassa yhteistyössä Darmstadtin teknillisen yliopiston virtausmekaniikan ja aerodynamiikan laitoksen kanssa. Koelaitteistossa alijäädytettyjen pisaroiden iskeytymistä pinnoille kuvattiin suurnopeuskameralla jäähdytetyn tuulitunnelin sisällä, jossa lämpötila oli säädetty −10 °C:een. Tutkimuksissa havaittiin, että vesipisaran iskeytymisen jälkeen vetäytyvän pisaran sisälle ilmestyy ajoittain kuivia aukkoja. Nämä poikkeavuudet johtuvat hydrofiilisten kuvioiden kostumisesta sekä samanaikaisesta hydrofobisten alueiden kuivumisesta, joka keskeytyi pisaran jo jäätyessä. Suurnopeuskameralla kuvatun videomateriaalin tarkka erittely selventi, että tiheämpi pintojen kuviointi, lisääntynyt alustan hydrofobisuus ja suurempi pisaran iskeytymisnopeus johtavat useampiin pisaroiden vetäytymispoikkeamiin ja alempiin jäätymisnopeuksiin.

Luku 5 vertaa useaa eri helppokäyttöistä pintakäsittelyä, jotka alentavat jään tarttuvuutta muovipinnoilla sekä kaupallisilla lentokoneiden pinnoitteilla. Jään tarttumisvoiman mittaamiseksi tässä työssä suunniteltiin ja rakennettiin ensin uusi vaakasuoraan työntövoimaan perustuva mittauslaitteisto yhteistyössä kahden maisteriopiskelijan kanssa (MSc Ronan Connolly ja MSc Sara Caliari). Kokeissa vertailtiin neljää eri pintakäsittelyä: öljypisaroita, pitkäaikasta UV-säteilyä, hydrofiilistä mikrokuviointia ja UV-kovettuvaa hydrofiilistä suihkutettavaa pinnoitetta. Vaikka öljyvoiteluun perustuvat pinnoitteet ovat saavuttaneet suurta suosiota viimeaikaisissa tutkimuksissa, UV-säteily osoittautui öljypisaroita tehokkaammaksi keinoksi vähentää jään tarttuvuutta PP-muovipinnoilla. Lisäksi pienimmät jään tarttuvuuden arvot mitattiin mikrokuvioiduilla ja hydrofiilisillä pinnoitteilla, joista suihkutettava hydrofiilinen pinnoite osoittautui kaikkein tehokkaimmaksi. Hydrofiilisten pintakäsittelyjen toimivuus perustuu niiden sisältämiin tiukasti sitoutuneisiin vesimolekyyleihin, jotka voivat muodostaa ohuen jäätymättömän nestemäisen kerroksen kiinteän muovipinnan ja jään väliin.

Osa 3 (**Luku 6**) tutkii mahdollisuutta hyödyntää jäähän sitoutuvia proteiineja jäätä hylkivissä pinnoitteissa. Rakenteestaan riippuen nämä proteiinit voivat joko hidastaa tai nopeuttaa jääkiteiden kasvua (englanninksi Anti-Freeze Proteins eli AFP ja Ice-Nucleating Proteins eli INP). Luonnossa jäähän sitoutuvat proteiinit (AFP) suojaavat tiettyjä arktisia kala-, hyönteis-

ja kasvilajeja jäätymisen aiheuttamalta solurikolta talvella. Tässä tutkimuksessa jäätä sitovia proteiineja lisättiin alumiinipinnoille käyttäen joko suoraa kovalenttista pintakemian muokkausta tai hydrogeeli-pinnoitusta. Proteiinien vaikutusta alumiinipintojen jäätymisprosesseihin seurattiin tämän väitöskirjan ensimmäisessä osassa mainitun lämpökameran avulla. Näissä tutkimuksissa havaittiin, että proteiinit, jotka luonnossa estävät jääkiteiden kasvua, yllättäen johtivatkin alumiinipintojen nopeampaan jäätymiseen. Tämä tapahtui vain, jos proteiinit kiinnitettiin alumiinipinnoille käyttäen lyhyitä polymeeriketjuja, mikä vähentää proteiinien liikkumiskykyä. Tämä oivallus tuo esiin proteiinien liikkumisvapauden tärkeyden niiden toiminnassa jäätymistä vastaan.

Kokonaisuudessaan tämä väitöskirja tuo esiin uutta tietoa jäätymistapahtumien alkupisteestä ja etenemisestä pinnoilla sekä jään tarttumisesta pintoihin. Seuraavia edellä mainittuja oivalluksia voidaan myös hyödyntää tulevaisuudessa uusien jäätä hylkivien pinnoitteiden kehittämisessä:

I. Vaikka hydrofobiset ja superhydrofobiset pinnoitteet voivat viivyttää jäätymistapahtumia laboratoriotutkimuksissa, reaalimaailman vaihteleva ilmankostus, pintanaarmut ja muut pintojen epäpuhtaudet luovat näillekin pinnoitteille paikallisia vesimolekyylien kerrostumia (MWL). Nämä MWL:t kiihdyttävät jäätymisprosesseja, mikä lopulta kumoaa hydrofobisten pintojen toimivuuden jäätä hylkivissä tarkoituksissa.

II. Koska jään tarttuvuutta mittaavat testit ovat erittäin herkkiä vaihteleville mittausparametreille ja ympäristötekijöille, julkaistujen artikkeleiden tulisi ilmoittaa selkeästi ja läpinäkyvästi kaikki testausolosuhteet ja kokeissa käytetyt parametrit. Lisäksi uusien jäätä hylkivien pinnoitteiden testaaminen niin sanotuissa “epäpuhtaissa” olosuhteissa, esimerkiksi pölyn tai naarmujen kanssa, voi tuottaa arvokasta uutta tietoa pinnoitteiden todellisesta suorituskyvystä vaativissa sovelluskohteissa.

III. Tämä väitöskirja osoittaa, että jääkiteiden kasvamista estävät proteiinit (AFP:t) nimestään huolimatta nopeuttavat jäätymistä, jos ne kiinnitetään pinnoille liian lyhyillä, proteiinien liikkumiskykyä rajoittavilla polymeeriketjuilla. Tulevien tutkimuksien tulisi siksi käyttää tarpeeksi pitkiä polymeeriketjuja AFP:tä hyödyntävien pinointien kehittämisessä.

Lisäksi tämä väitöskirja tarjoaa useita vaihtoehtoisia tieteellisiä perustoja uusien jäätä hylkivien kemiallisten stategioiden kehittämiseksi:

I. **Hydrofiilinen pintakuviointi**: Vaikka MWL:t tyypillisesti kiihdyttävät jäätapahtumien etenemistä hydrofiilisillä pinnoilla, hydrofiiliset kuviot hidastivat jäätymisnopeuksia alijäädytettyjen vesipisaroiden iskeytyessä hydrofobisen polypropyleenin (PP) pinnalle. Korkeimmilla iskeytymisnopeuksilla hydrofiiliset kuviot vaikuttivat myös pisaran vetäytymiskäyttäytymiseen, mikä voi mahdollisesti auttaa jääkertymien

säätelemisessä lentokoneen siipien pinnalla. Iskeytymisen jälkeen vesipisara vetäytyy hydrofobiselta alustalta hydrofiilisiä kuviota kohden, täten jäätyen vain kuvioiden yllä ja estäen koko siiven peittävän jääkerroksen muodostumisen. Sama prosessi voi olla hyödyllinen elektronisten komponenttien suojelemisessa kylmiltä ja kosteilta olosuhteilta. Tämän konseptin edistämiseksi nykyistä kuviontimenetelmää tulisi kehittää seuraavasti: a) Jos kuviointi ulottuisi pintakerrosta syvemmälle, kuvioitu pinnoite kestäisi kulumista paremmin. b) Kuvioiden ja alustan kostuvuuskontrastin maksimoiminen nopeuttaisi vesipisaroiden vetäytymisnopeutta ennen jäätymistä. c) Lisää tutkimustietoa tarvitaan suuremmilta iskeytymisnopeuksilta, jotka vastaavat jäätävän sateen iskeytymisnopeutta lennon aikana. d) Parhaan mahdollisen suorituskyvyn löytämiseksi tutkimuksia tulisi myös tehdä erilaisilla kuviointimuodoilla, -kooilla, -tiheyksillä ja kuvioiden kemiallisilla koostumuksilla.

II. **Hydrofiiliset pinnoitteet:** Hydrofiilisten polyelektrolyyttigeelien tiedetään jäätyvän viiveellä, sillä niiden sisältävät vesimolekyylit ovat sitoutuneet tiukasti polyelektrolyyttien varautuneisiin funktionaalisiin ryhmiin. Hydrogeelien mekaanisen kestävyyden parantamiseksi tämä väitöskirja esittelee DMC-monomeeriin perustuvan UV-kovettuvan pinnoitteen, joka hylkii jäätä tehokkaasti ja kestävästi. Jään alentunut tarttuvuus tähän pinnoitteeseen johtuu sen pinnalle kehittyvästä nestemäisestä MWL:stä, joka pysyy jäätymättömänä −10 °C:ssa sekä vähentää jään ja pinnoitteen välistä kitkaa. Ennen kuin tähän innovaatioon perustuvia pinnoitteita voidaan hyödyntää ilmailuteollisuudessa, lisätutkimusta tarvitaan seuraavilta näkökulmilta: a) Myös muiden polyelektrolyyttien vaikutusta MWL:n muodostumiseen tulisi tutkia. b) Tarkempaa tutkimusta tarvitaan pinnoitteen kostumisesta sekä sen mekaaniseen ja kemialliseen kestävyyteen vaikuttavista seikoista. c) Pinnoitteen toimivuutta vaihtelevissa ilmasto-olosuhteissa tulisi tutkia tarkemmin muuttamalla esimerkiksi ilman kosteutta, lämpötilaa ja jäätyyppiä jään tarttuvuuden testaamisen aikana. d) MWL:ien rakennetta, dynamiikkaa ja jäätymiskäyttäytymista tulisi tutkia lisää kehittyneillä pintaherkkillä karakterisointimenetelmillä. Tällaiset tutkimukset voivat auttaa muodostamaan vahvemman mekanistisen ymmärryksen MWL:ien vaikutuksesta jään nukleaatioon ja jään tarttuvuuteen.

III. **Jäätä sitovia proteiineja hyödyntävät pinnoitteet:** Koska jäätä sitovat proteiinit (AFP:t) voivat estää jäätymistä liuoksissa ja pinnoilla, tässä väitöskirjassa tunnustellaan myös niiden potentiaalia jäätä hylkivissä pinnoitteissa. Lähtökohtana tälle tutkimukselle AFP:itä kiinnitettiin hydrogeelipinnoitteiden sisälle käyttäen pitkiä polymeeriketjuja proteiinien liikkumiskyvyn turvaamiseksi. Nämä AFP-hydrogeelit jäätyivät testeissä myöhemmin kuin tavalliset proteiinittomat hydrogeelit, mikä osoittaa niiden mahdollisen toimivuuden tulevaisuuden pinnoitteissa. Vaikka hydrogeelit itsessään ovat sopimattomia ilmailuteollisuuden käyttöön, niitä voitaisiin hyödyntää jo muilla aloilla, kuten kryosäilytyksessä lääketieteellisissä tarkoituksissa sekä elintarviketeollisuudessa.

Contents

Chapter 1: Introduction 1

The Problem of Ice Accretion ***1***

Challenges in Ice Adhesion Testing ***6***

Developing Passive Anti-Icing Surfaces ***10***

Thesis Objective and Outline ***14***

Chapter 2: Role of Molecular Water Layer State on Freezing Front Propagation Rate and Mode 27

Introduction ***28***

Experimental ***31***

Materials *31*

Surface activation of the glass slides *31*

Surface silanization *31*

Sol-gel surface treatment *32*

Water contact angle measurements *32*

Measuring and quantifying freezing events with thermal imaging *33*

Results and Discussion ***34***

Water contact angles *34*

Frost propagation in the absence of water droplets *37*

Frost propagation in the presence of deposited water microdroplets *40*

Freezing of the microdroplets *41*

Freezing onset time at the surface with and without a droplet *42*

Relation between freezing front propagation, surface chemistry, and MWL *45*

Conclusions ***53***

Chapter 3: Controlling Frost Propagation on Polymeric Surfaces Using SI-ATRP Chemical Micropatterning 73

Introduction..... *74*

Experimental Section..... *76*

Reagents and Materials..... 76
Synthesis of PGMA backbone..... 76
Introduction of azide groups onto PGMA (PAzMA)..... 77
Introduction of bromide groups onto PAzMA (PAzBrMA)..... 77
Surface functionalization with PAzBrMA..... 78
Grafting of hydrophilic monomers on PAzBrMA-modified polymer substrates..... 78
Water contact angle measurements..... 79
Surface Imaging..... 79
Measuring and quantifying freezing events with thermal imaging..... 79

Results and Discussion..... *80*

Preparation of patterned and non-patterned surfaces..... 80
Surface wettability and roughness..... 85
Frost propagation on non-patterned polymer substrates..... 87
Frost propagation on patterned polymer substrates..... 92

Conclusions..... *99*

Chapter 4: The Influence of Chemical Surface Patterning on the Freezing Behaviour of Impacting Supercooled Water Droplets..... 117

Introduction..... *118*

Materials and methods..... *121*

Sample Preparation..... 121
Surface Imaging..... 122
Supercooled Water Droplet Impact Test..... 122

Results and Discussion..... *124*

Sample preparation..... 124
Influence of hydrophilic patterns on droplet impact..... 126

Influence of hydrophilic patterns on droplet freezing after impact *133*

Conclusions ***142***

Chapter 5: From Patterned to Continuous Hydrophilic Surface Lubrication as Strategies to Decrease Ice Adhesion ***157***

Introduction ***159***

Materials and methods ***163***

Materials *163*

Preparation of samples exposed to UV *163*

Preparation of samples with hydrophobic oil droplets *164*

Preparation of PHEMA-coated Surfaces *164*

Preparation of DMC-coated Surfaces *164*

Surface Characterization *165*

Ice Adhesion Tests *166*

Results and Discussion ***168***

Design, Construction, and Validation of the Ice Adhesion Test Setup *168*

Sample Preparation and Surface Characterization *171*

Influence of UV Exposure on Ice Adhesion *177*

Role of Oil and Water Lubrication in Reducing Ice Adhesion *180*

Comparison to Existing Anti-Icing Strategies and Literature Benchmarks *185*

Conclusions ***189***

Chapter 6: Mobility of Antifreeze Proteins is a Key Factor in Their Use to Control Ice Growth on Surfaces and Polymers ***201***

Introduction ***202***

Materials and methods ***204***

Materials *204*

Preparation of IBP-grafted aluminium alloy surfaces *204*

Water contact angle (WCA) measurements *206*

Raman spectroscopy *207*
Fourier transform infrared spectroscopy (FTIR) *207*
Differential scanning calorimetry (DSC) *207*
Frosting tests monitored by thermal imaging *208*
Results and Discussion ***209***
Aluminium surface functionalization with IBPs *209*
Influence of protein degrees of freedom on freezing onset and propagation in the presence of molecular water layer *213*
AFP-induced freezing delay in confined polymeric environments rich in water *220*
Conclusions ***227***
Acknowledgements ***237***
List of Publications ***241***
About the Author ***244***

1

Introduction

The Problem of Ice Accretion

Although a white winter wonderland would be a refreshing change to the never-ending rain in the Netherlands, unfortunately, ice in its various forms also causes many issues for critical transport and energy infrastructures: ice accretion on wind turbine blades reduces their power generation efficiency and can cause severe damage during stop-start operations[1,2], slippery roads cause traffic accidents on the highways[3,4], and frost-covered overhead power lines generate delays in the NS train schedules[5,6]. Specifically in the aviation industry, ice on the aircraft wings disturbs the airflow around the airfoil, decreases lift, increases drag, and adds weight to the aircraft.[7–9] Ice can also accumulate inside the aircraft engines on the nacelle inlet or around the fan blades, thus reducing air intake to the engine and reducing thrust. Altogether, these effects contribute to increased fuel consumption and safety risks, that can lead to significant financial losses and disastrous accidents.

Currently, the aviation industry is using active anti-icing and de-icing methods to combat ice accretion on aircraft.[10,11] **Figure 1.1**. provides an overview of the various ice accretion types on aircraft and the de-icing methods currently used to prevent their formation. On the

ground, the aircraft surfaces are sprayed with de-icing fluids (formulations based on ethylene glycol or propylene glycol) that lower the freezing temperature of water. This helps remove any present ice build-up, prevents frost growth on surfaces, and temporarily reduces the probability of freezing during supercooled droplet impact on the aircraft wings. However, de-icing fluids need to be continuously reapplied, the application process itself is time-consuming and expensive, and the sprayed chemicals are harmful to the ecosystems surrounding airports.[12–14] Regardless of these negative effects, de-icing fluids are still in standard worldwide use, demanding up to 3 800 L consumption per aircraft and costing airlines up to €75 000[15] per aircraft in mandatory de-icing services.

To prevent in-flight ice accretion, the surfaces of the aircraft wings are typically heated during take-off and landing as the aircraft flies through clouds consisting of supercooled water droplets.[16–18] As visualized in **Figure 1.2**, without the heating system, the impacting supercooled water droplets would freeze and quickly accumulate layers of ice, mainly on the leading edge of the aircraft wing. At temperatures below – 20 °C, the supercooled droplets would freeze immediately upon impact, creating brittle rime ice with air trapped within its structure. At temperatures closer to – 10 °C, the droplets would freeze after spreading over a wider area of the wing, resulting in clear glaze ice with a denser structure and higher adhesion to the surface. Even though the heating system, as an active anti-icing method, is effective and reliable, it consumes energy and adds weight to the aircraft. Consequently, mitigating ice accretion or adhesion without increasing weight or energy consumption would yield significant benefits for both the aviation industry and society by reducing operational costs, lowering CO_2 emissions, and minimizing environmental impact.

Given the limitations of active anti-icing systems considerable research efforts have focused on implementing passive anti-icing surfaces either as standalone solutions or in combination with active anti-icing methods.[10,18–22] In such strategies, the surfaces most vulnerable to ice accretion would be designed to delay freezing events or significantly lower the adhesion of ice forming onto these surfaces, thereby reducing the energy demand and operational burden of active de-icing systems. In practice, this could theoretically be achieved by applying permanent anti-/low-icing coatings on the surfaces of aircraft wings,

sensors, antennae, and turbine blades. Unfortunately, due to the challenging performance and durability requirements as well as the lack of standardization in ice adhesion testing, such coatings are not yet commercially available. Further research is needed to better understand the parameters that affect ice/frost propagation and adhesion and to develop coatings that are both effective in preventing ice accretion and sufficiently durable to avoid frequent maintenance and reapplication costs. These goals inevitably require robust methods to quantify ice propagation and adhesion in all their dimensions, thereby contextualizing the multifaceted focus of this work. The following sections detail the state-of-the-art techniques for characterizing ice adhesion to surfaces and the most promising strategies for developing successful passive anti-icing coatings.

a)

b)

	FROSTING	ICE CRYSTALS	GLAZE ICE	RIME ICE
Temperatures	*T < 0℃*	*T < -20 ℃*	*0 ℃ > T > -15 ℃*	*-10 ℃ < T < -20 ℃*
Flight phase	*Mainly on-ground*	*Cruising altitudes*	*During take-off and landing*	*During take-off and landing*
Risk areas	*All outside surfaces*	*Engine blades*	*Leading edge of the wings*	*Leading edge of the wings*
Cause	*Condensation and air humidity*	*Impacting ice crystals*	*Supercooled droplet impact*	*Supercooled droplet impact*
Appearance	*Thin layer of frost*	*Build-up of slushy ice*	*Smooth clear ice*	*Irregular white ice*
Prevention	*De-icing fluids*	*Flight planning*	*Heating systems*	*Heating systems*

Figure 1.1. a) Visualization of different aircraft icing types and b) a list of their main characteristics.

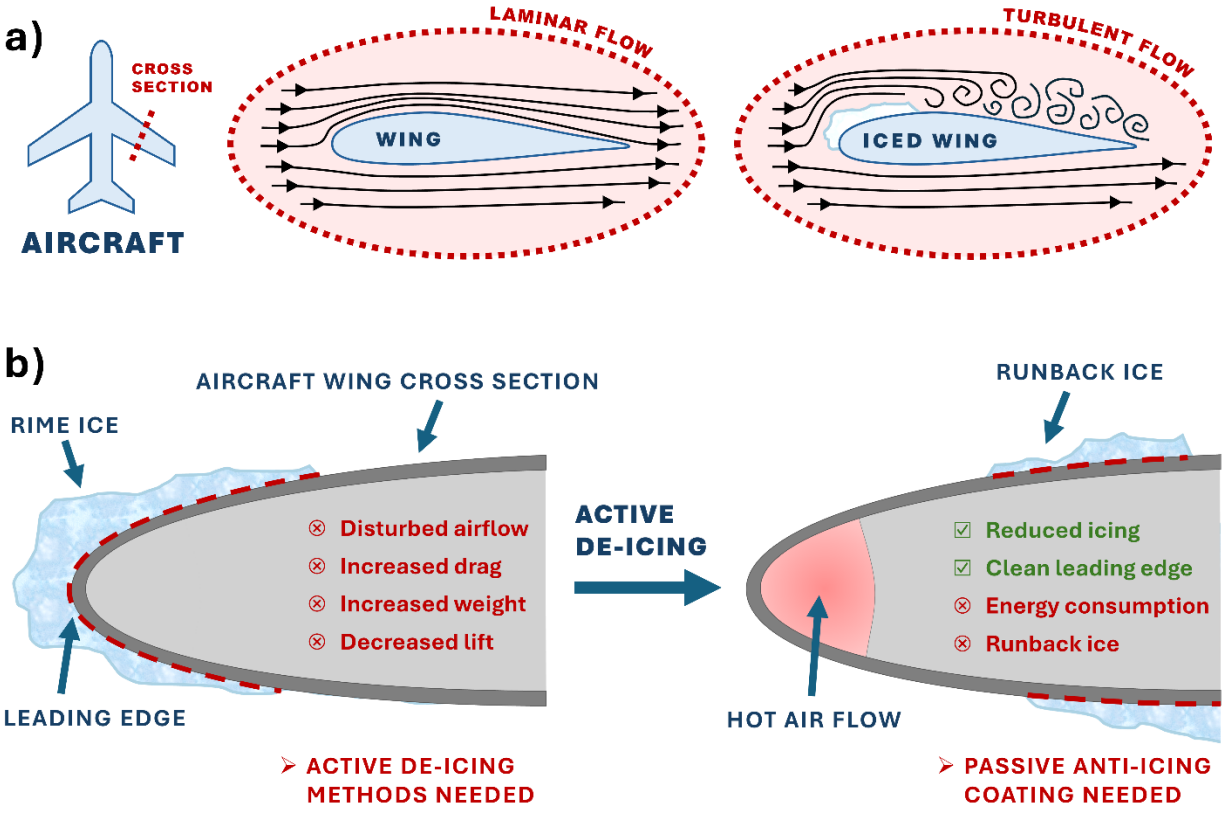

Figure 1.2. a) A schematic showing laminar air flow around an ice-free aircraft wing and turbulent airflow after ice accretion. b) A schematic of ice coverage on an aircraft wing with and without active ice protection. Even when the leading edge of the wing is heated during the flight, ice accretion is still possible elsewhere on the wing, and ice detached from the leading edge can still adhere to the back of the airfoil (runback ice). Even a small amount of ice accretion can disturb the air flow around the wing, leading to increased drag and reduced lift. Once commercially available, passive anti-icing coatings with low ice-adhesion strength could prevent the accretion of runback ice.[20]

CHALLENGES IN ICE ADHESION TESTING

Passive anti-icing surfaces are generally designed to delay freezing events and/or reduce the adhesion of ice to surfaces.[23,24] For the aviation industry, surfaces that only delay freezing events unfortunately do not provide sufficient ice protection without complementary de-icing technologies.[20] No matter how long freezing is delayed, once the first nucleation event occurs somewhere on the aircraft wing, build-up of impact ice is inevitable. Therefore, low ice adhesion is a key performance characteristic of future passive anti-icing surfaces in the aviation industry. Ideally, the ice adhesion strength should approach values below approximately 30 kPa, a commonly cited engineering benchmark theoretically associated with conditions under which aerodynamic forces may remove accreted ice during flight.[25] However, this threshold should not be interpreted as a universal criterion for icephobicity, since measured ice adhesion values strongly depend on the experimental setup, environmental conditions, and ice morphology used in the test.

Since commercial instrumentation specifically designed for testing ice adhesion to surfaces has not been available before 2019, almost all ice adhesion values reported in the literature have been obtained using lab-built testing equipment. **Figure 1.3a** illustrates several ice adhesion test configurations that are sufficiently simple to be constructed in-house. Such lab-built devices are still in continuous use today, as research groups do not have an incentive to replace them with costly new equipment. Consequently, testing devices used for this purpose vary from each other not only in design but also in the results they generate. As shown in **Figure 1.3b**, over the past 15 years, numerous independent studies have reported widely diverging values for ice adhesion strength to aluminium surfaces.[26–57] Unexpectedly, studies that used the same type of measurement technique under the same temperature conditions (horizontal shear test at -10 °C) also recorded contradicting values ranging between 100 and 1500 kPa.

Several reasons can explain why different ice adhesion setups can give considerably different values for the same material. Although the most common ice adhesion test setup is designed solely to push an ice cube off the sample surface, this simple experiment

involves a large number of parameters that can influence its outcome (**Figure 1.3c**). The experimental setup should be designed with consideration for various environmental and technical parameters, including the pushing speed and the height of the pushing rod, environmental temperature and humidity, surface temperature of the sample, the dimensions of the ice cube, and the type of ice used in the experiment. A more comprehensive list of parameters affecting ice adhesion results is provided in **Figure 1.2.1c**.

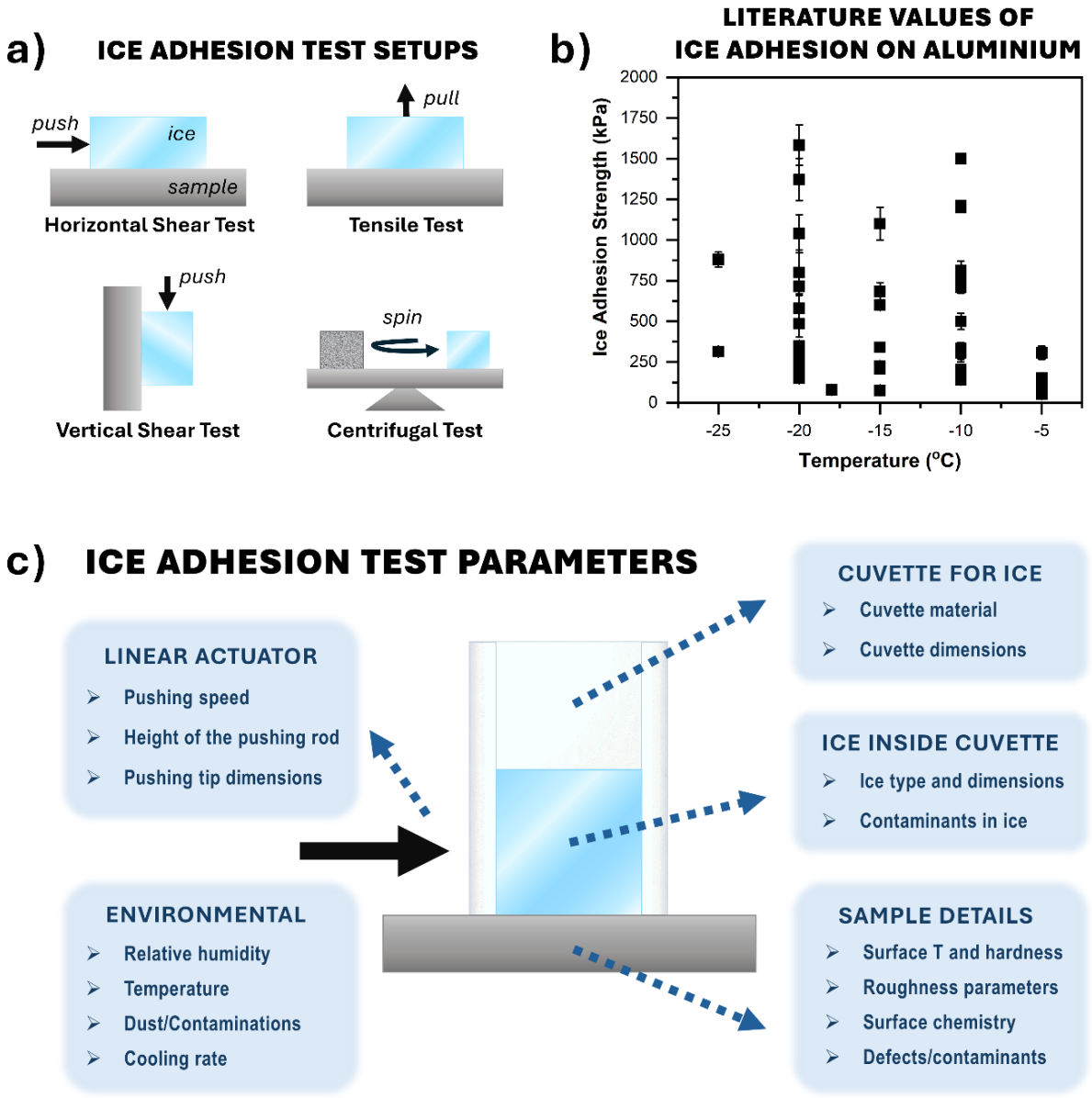

Figure 1.3. a) Schematic showing the differences between lab-built ice adhesion test configurations. The most commonly used ice adhesion setup is the horizontal shear test. b) Literature values for ice adhesion strength to aluminium, collected from all reports published in the last 12 years. c) List of parameters influencing ice adhesion strength values in a horizontal shear test. For reproducibility, all of these values should be specified when reporting ice adhesion results in the literature. Additional experimental and geometrical factors may also affect the measured adhesion strength.

In the literature, most studies commonly report the type of measurement technique and the temperature conditions used for obtaining the ice adhesion strength values. However, the rest of the experimental parameters and surface characteristics of the tested materials are often left undefined.[58] The most likely reason for this oversight is that the literature lacks systematic studies investigating the effect of these critical parameters on the ice adhesion strength. In addition to a couple of individual studies reporting variations in test results with different pushing heights, pushing speeds, and surface roughness, the field of ice adhesion testing is in urgent need of more in-depth investigations to understand how all operational experimental parameters influence the mechanisms of ice adhesion.

Today, several studies have reported new low-icing surfaces with adhesion strength values close to the target value of 30 kPa,[59–73] which has been proposed as the threshold below which aerodynamic forces during flight (wind speed ≥12 m/s) can continuously remove accreted ice from airfoil surfaces. However, these results lose their significance if the authors do not share a full list of the experimental parameters used during the tests or the original data files showing the evolution of the detected force curves over time. Without complete and transparent reporting, the reproducibility of the results is lost, and meaningful comparison between different low-ice-adhesion surfaces becomes difficult. To advance promising passive anti-icing coatings toward commercial application, good durability and low ice adhesion values are essential. Equally important are test methods that provide detailed and realistic information, together with a thorough understanding of the ice adhesion mechanisms underlying the reported favourable results.

DEVELOPING PASSIVE ANTI-ICING SURFACES

Currently, there are no commercially available passive anti-icing coatings that reach the targeted ice-adhesion strength below 30 kPa. Although various icephobic materials have been developed since the early 2000s, and several studies have reported adhesion values below 50 kPa, these coatings are either ineffective or too fragile in in-field applications. For example, superhydrophobic surfaces with water-repelling properties based on double topologies (e.g., lotus effect) have been proposed for anti-icing applications since 2008.[74] For aircraft coatings, superhydrophobicity could ideally prevent freezing events by repelling impacting water droplets and/or delaying their freezing onset time.[75,76] However, many studies[77–81] thereafter have shown that once ice inevitably accumulates on superhydrophobic structured surfaces via frosting or impact icing, its removal is even more challenging due to the mechanical interlocking of ice with the topologically complex surface (see **Figure 1.4**). This demonstrates that, despite their ability to delay freezing, superhydrophobicity alone does not inherently translate to icephobicity and cannot reliably ensure low ice adhesion in the design of anti-icing surfaces.

Another more recent yet thoroughly explored design for anti-icing coatings is the so-called SLIPS (slippery liquid-infused porous surface)[82–84]. The fundamental underlying idea of the concept consists of filling sponge-like porous or structured surfaces with a water-repelling oil. Although SLIPS were originally intended for anti-fouling and biomedical applications[85], they have also shown ice adhesion strength lower than 20 kPa. In this approach, the infused oil creates a smooth and thin oil layer at the ice-coating interface, which reduces the ice adhesion strength through lubrication. Unfortunately, the infused liquid depletes after approximately 10 icing cycles and would need periodic refilling in real-life applications before ice adhesion is increased through interlocking.[86–88] Since such maintenance would be even more expensive than applying de-icing fluids on aircraft, the SLIPS have also not yet been fully deployed in the aviation industry.

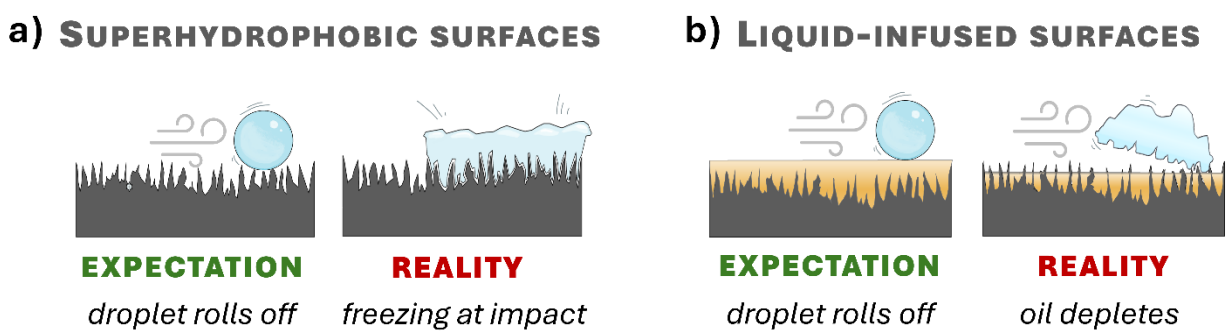

Figure 1.4. a) Superhydrophobic surfaces repel water droplets by minimizing contact area between the liquid and the solid surface. However, when supercooled water droplets impact these surfaces at high velocity, the droplets freeze upon impact and remain mechanically interlocked into the surface structures. Furthermore, frost formation under humid conditions can infiltrate the surface texture, eliminating the air pockets responsible for superhydrophobicity and increasing ice adhesion. b) Structured and/or porous surfaces can also be infused with water-repelling oils to lower the adhesion of impact ice (SLIPS concept). In long-term use, the infused oil slowly depletes into the environment and needs to be reapplied to maintain its low ice adhesion properties.

Although SLIPS are not durable enough to be applied to aircraft surfaces, the idea of using a lubricating layer to reduce ice adhesion is still being explored in the literature. However, instead of oil-based liquids, the focus has turned towards aqueous lubricating layers[89–94] that can be self-replenished after each icing cycle (see **Figure 1.5a**). Similar to aircraft sprayed with de-icing fluids and roads covered with salt, anti-icing surfaces with an aqueous lubricating layer utilize polar groups and/or charged ions to lower the freezing temperature of water. For example, hydrogels made with polyelectrolytes have repeating units that carry either positive or negative charges (i.e., cationic or anionic groups), which can form strong interactions with nearby water molecules. When the hydrogels are subjected to temperatures below the freezing point of water, these competing interactions with the polyelectrolyte chain thermodynamically hinder the phase transition of liquid water to solid ice, therefore leading to reduced freezing temperatures (can remain completely unfrozen down to -20 ℃).[95]

In passive anti-icing, the reduced freezing temperature of polyelectrolyte hydrogels can also help to reduce ice adhesion strength.[96] When ice accretes on top of polyelectrolyte chains,

the water molecules at the ice-hydrogel interface form hydrogen bonds with the charged chemical groups, thereby hydrating the polyelectrolyte chains. This hydration layer (also known as the aqueous lubrication layer) can remain unfrozen even at -20 ℃, and function as a lubrication layer between the accreted ice and the hydrogel. Since the lubricating layer consists of water, unlike in the case of oil-infused surfaces, there is no risk of the lubricant depleting over time due to self-replenishment with the surrounding atmosphere through the formation of surface molecular water layers (MWL). So far, the aqueous lubricating layer has proven to reduce the ice adhesion strength even down to ~10 kPa at -10℃.[92–94] Although most of these reported anti-icing surfaces are based on degradable surface grafting and hydrogel networks, polyelectrolytes could potentially be incorporated into more durable coating formulations for future applications in the aviation industry. In this context, the formation and control of MWLs through both polyelectrolyte-based coatings and wettability patterning are investigated in this thesis as key strategies for reducing ice adhesion.

Another promising approach to new low-ice adhesion coatings is known as crack-initiating surfaces or stress-localized surfaces.[97–101] This strategy is based on the formation of local (patterned or not) surface stiffness discontinuities at the ice-substrate interface. As visualized in **Figure 1.5b**, stress-localized surfaces consist of material with two phases: a stiffer phase-I that provides long-term durability for the coating, and a compliant phase-II that is mixed into phase I as small micron-scale particles. During ice adhesion testing, the applied pushing force creates shear stresses at the ice-coating interface. Typically, these shear stresses are centralized at the point where the pushing force is applied. For stress-localized surfaces, the interfacial stresses additionally concentrate at the interfaces between the stiff phase I and the compliant phase II regions due to the mismatch in mechanical properties, generating localized ice detachment points distributed along the ice–coating interface. Due to the multiple simultaneous crack-initiation points, ice can be removed with less force, and ice adhesion values at -25℃ can be reduced to below 10 kPa.[99,100]

Since stress-localized surfaces contain regions of softer material, these areas at the surface are potentially vulnerable to abrasion and other forms of degradation. Nevertheless, this

approach is equally promising as surfaces with an aqueous lubricating layer. Both have proven the ability to lower ice adhesion strength below 30 kPa but have not yet demonstrated long-lasting durability for high-performance applications. Finding the optimal combination of anti-icing and durability performance requires systematic studies dedicated to understanding better how these properties can be controlled by adjusting individual components of the coating formulation. In view of these knowledge gaps, this thesis approaches the design of anti-icing coatings from a different perspective: instead of focusing on optimizing existing coating systems, it systematically investigates how key mechanisms—such as MWL formation and wettability patterning—can be used to control ice nucleation, propagation, and adhesion.

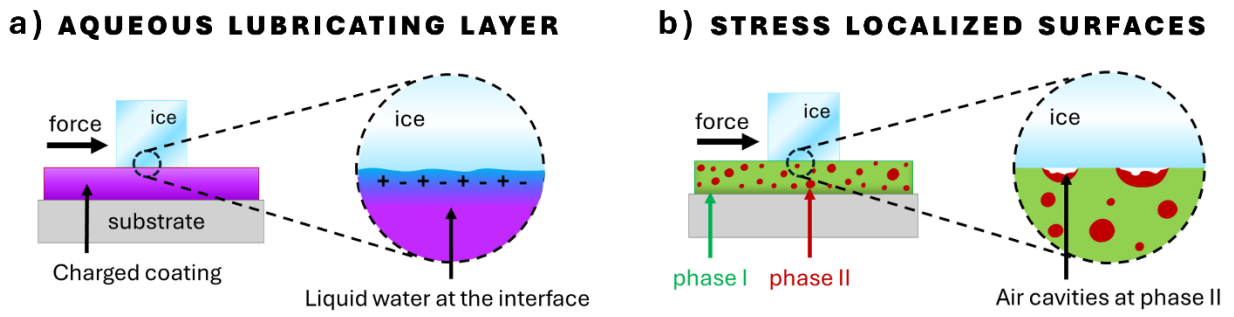

Figure 1.5. a) Coatings functionalized with charged chemical groups can lower ice adhesion by generating an aqueous lubricating layer at the ice-coating interfaces. b) Stress-localized surfaces combining hard (green phase I) and soft (red phase II) materials can lower ice adhesion strength by generating multiple simultaneous ice detachment points that initiate at the soft regions.

THESIS OBJECTIVE AND OUTLINE

To address the objective of understanding and controlling ice nucleation, propagation, and adhesion on surfaces, this thesis is structured to progressively link molecular-scale phenomena to macroscopic anti-icing performance.

Chapters 2 and **3** establish the fundamental role of molecular water layers (MWLs) in surface freezing processes. **Chapter 2** isolates the effect of surface chemistry and environmental humidity on MWL formation and demonstrates how their state and continuity govern freezing onset and propagation on model smooth surfaces. Building on this, **Chapter 3** introduces chemical micropatterning as a strategy to spatially control MWL formation through wettability contrast, thus enabling localized control over freezing behaviour. Together, these chapters provide the mechanistic foundation for manipulating the kinetics of freezing processes on surfaces via the presence and state of MWLs.

Chapters 4 and **5** extend these concepts to more application-relevant icing conditions. **Chapter 4** translates wettability patterning to dynamic scenarios involving impacting supercooled droplets, demonstrating how MWL-mediated wetting asymmetries can influence droplet freezing behaviour and ice accretion morphology. **Chapter 5** further connects MWL formation to ice adhesion by comparing the effect of various surface modification strategies and showing how non-freezing interfacial water layers can significantly reduce adhesion strength. These chapters collectively bridge the gap between controlled frost formation and practical ice accretion and removal.

Finally, **Chapter 6** explores an alternative route to designing passive anti-icing coatings by incorporating ice-binding proteins into surfaces and coatings. This chapter examines how the molecular mobility of antifreeze proteins governs their ability to inhibit freezing propagation, further emphasizing the importance of interfacial processes in controlling ice nucleation and growth.

Overall, this thesis demonstrates that controlling ice formation and adhesion requires a unified understanding of interfacial water behaviour across different length scales and environmental conditions. By systematically investigating MWL formation in relation to local

wettability differences and ice-binging protein mobility at surfaces, this work provides a framework for the rational design of next-generation passive anti-icing materials.

REFERENCES

(1) Wei, K.; Yang, Y.; Zuo, H.; Zhong, D. A Review on Ice Detection Technology and Ice Elimination Technology for Wind Turbine. *Wind Energy*. John Wiley and Sons Ltd March 1, 2020, pp 433–457. https://doi.org/10.1002/we.2427.

(2) Parent, O.; Ilinca, A. Anti-Icing and de-Icing Techniques for Wind Turbines: Critical Review. *Cold Reg. Sci. Technol.* **2011**, *65* (1), 88–96. https://doi.org/https://doi.org/10.1016/j.coldregions.2010.01.005.

(3) Eisenberg, D.; Warner, K. E. Effects of Snowfalls on Motor Vehicle Collisions, Injuries, and Fatalities. *Am. J. Public Health* **2005**, *95* (1), 120–124. https://doi.org/10.2105/AJPH.2004.048926.

(4) DiLorenzo, T.; Yu, X. Use of Ice Detection Sensors for Improving Winter Road Safety. *Accid. Anal. Prev.* **2023**, *191*, 107197. https://doi.org/https://doi.org/10.1016/j.aap.2023.107197.

(5) Lotfi, A.; Virk, M. S. Railway Operations in Icing Conditions: A Review of Issues and Mitigation Methods. *Public Transport* **2023**, *15* (3), 747–765. https://doi.org/10.1007/s12469-023-00327-6.

(6) Laforte, J. L.; Allaire, M. A.; Laflamme, J. State-of-the-Art on Power Line de-Icing. *Atmos. Res.* **1998**, *46* (1), 143–158. https://doi.org/https://doi.org/10.1016/S0169-8095(97)00057-4.

(7) Yamazaki, M.; Jemcov, A.; Sakaue, H. A Review on the Current Status of Icing Physics and Mitigation in Aviation. *Aerospace*. MDPI AG July 1, 2021. https://doi.org/10.3390/aerospace8070188.

(8) Cao, Y.; Tan, W.; Wu, Z. Aircraft Icing: An Ongoing Threat to Aviation Safety. *Aerosp. Sci. Technol.* **2018**, *75*, 353–385. https://doi.org/https://doi.org/10.1016/j.ast.2017.12.028.

(9) Wang, K.; Xue, Y.; Tian, H.; Wang, M.; Wang, X. The Impact of Icing on the Airfoil on the Lift-Drag Characteristics and Maneuverability Characteristics. *Math. Probl. Eng.* **2021**, *2021* (1), 5568740. https://doi.org/https://doi.org/10.1155/2021/5568740.

(10) Rekuviene, R.; Saeidiharzand, S.; Mažeika, L.; Samaitis, V.; Jankauskas, A.; Sadaghiani, A. K.; Gharib, G.; Muganlı, Z.; Koşar, A. A Review on Passive and Active Anti-Icing and de-Icing Technologies. *Appl. Therm. Eng.* **2024**, *250*, 123474. https://doi.org/10.1016/J.APPLTHERMALENG.2024.123474.

(11) Yamazaki, M.; Jemcov, A.; Sakaue, H. A Review on the Current Status of Icing Physics and Mitigation in Aviation. *Aerospace* **2021**, *8* (7). https://doi.org/10.3390/aerospace8070188.

(12) Rodziewicz, J.; Mielcarek, A.; Janczukowicz, W.; Bryszewski, K.; Ostrowska, K. Treatment of Wastewater Containing Runway De-Icing Agents in Biofilters as a Part of Airport

Environment Management System. *Sustainability* **2020**, *12* (9). https://doi.org/10.3390/su12093608.

(13) Kozuba, J.; Pira, J. Impact of De-Icing Substances on Runway and Aircraft Structure. In *ICMT 2019 - 7th International Conference on Military Technologies, Proceedings*; 2019. https://doi.org/10.1109/MILTECHS.2019.8870032.

(14) Freeman, A. I.; Surridge, B. W. J.; Matthews, M.; Stewart, M.; Haygarth, P. M. Understanding and Managing De-Icer Contamination of Airport Surface Waters: A Synthesis and Future Perspectives. *Environ. Technol. Innov.* **2015**, *3*, 46–62. https://doi.org/10.1016/j.eti.2015.01.001.

(15) Gesellschaft für Enteisen und Flugzeugschleppen am Flughafen München mbH. *Aircraft Deicing and Towing Services Munich Airport*; 2025. www.munich-airport.de/efm.

(16) Tanaka, H.; Ahmad, T.; Utsumi, Y.; Yonemoto, S.; Ichikawa, G. Icing on Full-Scale Swept Wings in Flight and Icing Wind Tunnel. *J. Aircr.* **2022**, *59* (6), 1437–1449. https://doi.org/10.2514/1.C036640.

(17) Yang, Q.; Guo, X.; Zheng, H.; Dong, W. Single- and Multi-Objective Optimization of an Aircraft Hot-Air Anti-Icing System Based on Reduced Order Method. *Appl. Therm. Eng.* **2023**, *219*, 119543. https://doi.org/https://doi.org/10.1016/j.applthermaleng.2022.119543.

(18) Huang, X.; Tepylo, N.; Pommier-Budinger, V.; Budinger, M.; Bonaccurso, E.; Villedieu, P.; Bennani, L. A Survey of Icephobic Coatings and Their Potential Use in a Hybrid Coating/Active Ice Protection System for Aerospace Applications. *Progress in Aerospace Sciences*. Elsevier Ltd February 1, 2019, pp 74–97. https://doi.org/10.1016/j.paerosci.2019.01.002.

(19) Strobl, T.; Storm, S.; Ameduri, S. Chapter 26 - Synergic Effects of Passive and Active Ice Protection Systems. In *Morphing Wing Technologies*; Concilio, A., Dimino, I., Lecce, L., Pecora, R., Eds.; Butterworth-Heinemann, 2018; pp 841–864. https://doi.org/https://doi.org/10.1016/B978-0-08-100964-2.00026-5.

(20) Zeng, D.; Li, Y.; Liu, H.; Yang, Y.; Peng, L.; Zhu, C.; Zhao, N. Superhydrophobic Coating Induced Anti-Icing and Deicing Characteristics of an Airfoil. *Colloids Surf. A Physicochem. Eng. Asp.* **2023**, *660*, 130824. https://doi.org/https://doi.org/10.1016/j.colsurfa.2022.130824.

(21) Irajizad, P.; Nazifi, S.; Ghasemi, H. Icephobic Surfaces: Definition and Figures of Merit. *Advances in Colloid and Interface Science*. Elsevier B.V. July 1, 2019, pp 203–218. https://doi.org/10.1016/j.cis.2019.04.005.

(22) Shen, Y.; Wu, X.; Tao, J.; Zhu, C.; Lai, Y.; Chen, Z. Icephobic Materials: Fundamentals, Performance Evaluation, and Applications. *Progress in Materials Science*. Elsevier Ltd June 1, 2019, pp 509–557. https://doi.org/10.1016/j.pmatsci.2019.03.004.

(23) Liu, Y.; Wu, Y.; Liu, S.; Zhou, F. Material Strategies for Ice Accretion Prevention and Easy Removal. *ACS Mater. Lett.* **2022**, *4* (2), 246–262. https://doi.org/10.1021/acsmaterialslett.1c00365.

(24) Kreder, M. J.; Alvarenga, J.; Kim, P.; Aizenberg, J. Design of Anti-Icing Surfaces: Smooth, Textured or Slippery? *Nature Reviews Materials*. Nature Publishing Group January 11, 2016. https://doi.org/10.1038/natrevmats.2015.3.

(25) Hejazi, V.; Sobolev, K.; Nosonovsky, M. From Superhydrophobicity to Icephobicity: Forces and Interaction Analysis. *Sci. Rep.* **2013**, *3* (1), 2194. https://doi.org/10.1038/srep02194.

(26) Dai, X.; Yuan, Y.; Xiao, J.; Jiang, C.; Hua, X.; Xiang, H.; Zhu, T.; Liu, G.; Zhou, J.; Liao, R. Influence of Different Anodised Nanoporous Structures on the Anti-Icing and Electrical Properties of Transmission Al Lines. *High Voltage* **2025**, *10* (1), 167–177. https://doi.org/https://doi.org/10.1049/hve2.12471.

(27) Barthwal, S.; Kang, D.; Lim, S.-H. A Resilient Superhydrophobic Photothermal SiC/Carbon Coating for Enhanced Anti-Icing and Deicing Performance under Extreme Environmental Conditions. *Prog. Org. Coat.* **2025**, *208*, 109523. https://doi.org/https://doi.org/10.1016/j.porgcoat.2025.109523.

(28) Li, C.; Apelt, S.; Feuer, A.; Idrisov, R.; Bergmann, U. Bio-Inspired Surface Modification of Aluminium Heat Exchanger Fins Using Laser Structuring and PDMS Coating for Improved and Scalable Hydrophobic and Ice-Adhesion Performance. *J. Adhes.* **2025**, 1–16. https://doi.org/10.1080/00218464.2025.2511330.

(29) Xu, S.; Huang, X.; Sheng, H.; Wang, X.; Hu, W.; Ji, Z.; Liu, H. Advanced Slippery Coatings Featuring Ternary Photothermal Traps for Superior Anti/De-Icing and Anti/De-Frosting Efficiency in Extreme Dynamic Cold Environment. *Adv. Funct. Mater.* **2025**, *n/a* (n/a), 2505439. https://doi.org/https://doi.org/10.1002/adfm.202505439.

(30) Liu, W.; Li, K.; Shen, Y.; Zhao, H.; Ni, Y.; Cai, Z.; Zhao, L.; Wang, Z. Durable Design of Superhydrophobic Coatings with TiO2 Particles and Al2O3 Whiskers for the Enhanced Anti-Icing Performance. *J. Bionic Eng.* **2024**, *21* (3), 1360–1374. https://doi.org/10.1007/s42235-024-00516-4.

(31) Zhu, T.; Yuan, Y.; Xiang, H.; Song, L.; Wei, X.; Hua, X.; Dai, X.; Liao, R. A Polydimethylsiloxane Coating with Excellent Large-Scale Deicing Property and Durability. *Journal of Industrial and Engineering Chemistry* **2024**, *139*, 492–501. https://doi.org/https://doi.org/10.1016/j.jiec.2024.05.026.

(32) Zhang, R.; Yang, Y.; Zhang, H.; Ma, X.; Li, J. 3D Liquid-Based Porous Coating Integrated with Oleophilic MXene Nanoflakes for Durable Ultra-Low Ice Adhesion and Exceptional Photothermal Slippery Properties. *Chemical Engineering Journal* **2024**, *496*, 154108. https://doi.org/https://doi.org/10.1016/j.cej.2024.154108.

(33) Li, B.; Jie, B.; Fan, L.; Zeng, H.; Mu, H.; Dai, X.; Xiao, J.; Hua, X.; Li, Q.; Yuan, Y.; Liao, R. Experimental Studies of Anodized Al Surface with Composite Nanopore Structures to Enhance the Anti-Icing Properties of Transmission Lines. *J. Phys. Conf. Ser.* **2024**, *2775* (1), 012049. https://doi.org/10.1088/1742-6596/2775/1/012049.

(34) Xuan, S.; Yin, H.; Li, G.; Zhang, Z.; Jiao, Y.; Liao, Z.; Li, J.; Liu, S.; Wang, Y.; Tang, C.; Wu, W.; Li, G.; Yin, K. Trifolium Repens L.-Like Periodic Micronano Structured Superhydrophobic Surface with Ultralow Ice Adhesion for Efficient Anti-Icing/Deicing. *ACS Nano* **2023**, *17* (21), 21749–21760. https://doi.org/10.1021/acsnano.3c07385.

(35) Li, B.; Zeng, H.; Peng, C.; Yang, Q.; Dai, X.; Xiao, J.; Hua, X.; Zhao, Y.; Li, Y.; Yuan, Y.; Liao, R. Preparation and Anti-Icing Properties of Superhydrophobic Bionic Nanopore Structures Aluminum Surface by Anodic Oxidation Technique. In *Proc.SPIE*; 2024; Vol. 13419, p 1341913. https://doi.org/10.1117/12.3051049.

(36) Liu, D.; Liu, R.; Cao, L.; Saeed, S.; Bryanston-Cross, P. J.; Wang, Z. Fabrication of Periodic Hierarchical Structures with Anti-Icing Performance by Direct Laser Interference Lithography and Hydrothermal Treatment. *Surf. Coat. Technol.* **2023**, *471*, 129819. https://doi.org/https://doi.org/10.1016/j.surfcoat.2023.129819.

(37) Zhu, T.; Yuan, Y.; Xiang, H.; Liu, G.; Dai, X.; Song, L.; Liao, R. A Composite Pore-Structured Superhydrophobic Aluminum Surface for Durable Anti-Icing. *Journal of Materials Research and Technology* **2023**, *27*, 8151–8163. https://doi.org/https://doi.org/10.1016/j.jmrt.2023.11.250.

(38) Wang, X.; Huang, X.; Ji, Z.; Hu, W.; Sheng, H.; Li, X. Self-Healing Icephobic Coating with UV Shielding and Removability Based on Biobased Epoxy and Reversible Disulfide Bonds. *Polymer (Guildf).* **2023**, *283*, 126274. https://doi.org/https://doi.org/10.1016/j.polymer.2023.126274.

(39) Chen, T.; Dong, X.; Han, L.; Cong, Q.; Qi, Y.; Jin, J.; Liu, C.; Wang, M. Changing the Freezing Interface Characteristics to Reduce the Ice Adhesion Strength. *Appl. Therm. Eng.* **2023**, *230*, 120796. https://doi.org/https://doi.org/10.1016/j.applthermaleng.2023.120796.

(40) Xiang, H.; Yuan, Y.; Zhu, T.; Dai, X.; Zhang, C.; Gai, Y.; Liao, R. Anti-Icing Mechanism for a Novel Slippery Aluminum Stranded Conductor. *ACS Appl. Mater. Interfaces* **2023**, *15* (28), 34215–34229. https://doi.org/10.1021/acsami.3c04797.

(41) TAS, M.; Memon, H.; Xu, F.; Ahmed, I.; Hou, X. Electrospun Nanofibre Membrane Based Transparent Slippery Liquid-Infused Porous Surfaces with Icephobic Properties. *Colloids Surf. A Physicochem. Eng. Asp.* **2020**, *585*, 124177. https://doi.org/https://doi.org/10.1016/j.colsurfa.2019.124177.

(42) Yang, Q.; Dolatabadi, A.; Golovin, K. Erosion-Resistant Materials Demonstrate Low Interfacial Toughness with Ice and Superior Durability. *Mater. Horiz.* **2023**, *10* (10), 4541–4550. https://doi.org/10.1039/D3MH00885A.

(43) Tas, M.; Musa, U. G.; Ahmed, I.; Xu, F.; Smartt, C.; Hou, X. Functionalised SiO2 Modified Icephobic Nanocomposite Electrospun Membranes for Outdoor Electromagnetic Shielding Applications. *Polymer (Guildf).* **2022**, *240*, 124499. https://doi.org/https://doi.org/10.1016/j.polymer.2021.124499.

(44) Xu, K.; Jiang, W.; Zhou, Z.; Li, Z.; Bai, T.; Yue, H. Shear Adhesion of Ice on Large-Sized Grooved Aluminum Surfaces. *Langmuir* **2023**, *39* (26), 9100–9110. https://doi.org/10.1021/acs.langmuir.3c00833.

(45) Zhu, Z.; Liang, H.; Sun, D.-W. Infusing Silicone and Camellia Seed Oils into Micro-/Nanostructures for Developing Novel Anti-Icing/Frosting Surfaces for Food Freezing Applications. *ACS Appl. Mater. Interfaces* **2023**, *15* (11), 14874–14883. https://doi.org/10.1021/acsami.3c02342.

(46) Li, B.; Bai, J.; Yang, L.; Lu, J.; He, J.; Li, Y.; Xiang, H.; Yuan, Y. Anti-Icing Performance of Lubricant-Infused Surfaces. In *2023 IEEE Conference on Electrical Insulation and Dielectric Phenomena (CEIDP)*; 2023; pp 1–4. https://doi.org/10.1109/CEIDP51414.2023.10410451.

(47) Wei, X.; Zhong, Y.; Feng, Y.; Wei, J.; Wang, J. A Slippery Liquid-Infused Network-like Surface with Anti/De-Icing Properties Constructed Based on the Phosphating Reaction. *Langmuir* **2022**, *38* (46), 14118–14128. https://doi.org/10.1021/acs.langmuir.2c02075.

(48) Hou, Y.; Choy, K. L. Durable and Robust PVDF-HFP/SiO2/CNTs Nanocomposites for Anti-Icing Application: Water Repellency, Icing Delay, and Ice Adhesion. *Prog. Org. Coat.* **2022**, *163*, 106637. https://doi.org/https://doi.org/10.1016/j.porgcoat.2021.106637.

(49) Xie, H.; Zhao, X.; Li, B.; Zhang, J.; Wei, J.; Zhang, J. Waterborne, Non-Fluorinated and Durable Anti-Icing Superhydrophobic Coatings Based on Diatomaceous Earth. *New Journal of Chemistry* **2021**, *45* (23), 10409–10417. https://doi.org/10.1039/D1NJ01307F.

(50) Tan, X.; Zhang, Y.; Liu, X.; Xi, S.; Yan, Z.; Liu, Z.; Shi, T.; Liao, G. Employing Micro Pyramidal Holes and Porous Nanostructures for Enhancing the Durability of Lubricant-Infused Surfaces in Anti-Icing. *Surf. Coat. Technol.* **2021**, *405*, 126568. https://doi.org/https://doi.org/10.1016/j.surfcoat.2020.126568.

(51) Qin, C. (Chris); Mulroney, A. T.; Gupta, M. C. Anti-Icing Epoxy Resin Surface Modified by Spray Coating of PTFE Teflon Particles for Wind Turbine Blades. *Mater. Today Commun.* **2020**, *22*, 100770. https://doi.org/https://doi.org/10.1016/j.mtcomm.2019.100770.

(52) Liu, G.; Yuan, Y.; Jiang, Z.; Youdong, J.; Liang, W. Anti-Frosting/Anti-Icing Property of Nano-ZnO Superhydrophobic Surface on Al Alloy Prepared by Radio Frequency Magnetron

Sputtering. *Mater. Res. Express* **2020**, *7* (2), 026401. https://doi.org/10.1088/2053-1591/ab6e33.

(53) Barthwal, S.; Lee, B.; Lim, S.-H. Fabrication of Robust and Durable Slippery Anti-Icing Coating on Textured Superhydrophobic Aluminum Surfaces with Infused Silicone Oil. *Appl. Surf. Sci.* **2019**, *496*, 143677. https://doi.org/https://doi.org/10.1016/j.apsusc.2019.143677.

(54) Zhu, L.; Xue, J.; Wang, Y.; Chen, Q.; Ding, J.; Wang, Q. Ice-Phobic Coatings Based on Silicon-Oil-Infused Polydimethylsiloxane. *ACS Appl. Mater. Interfaces* **2013**, *5* (10), 4053–4062. https://doi.org/10.1021/am400704z.

(55) Shen, Y.; Wu, Y.; Tao, J.; Zhu, C.; Chen, H.; Wu, Z.; Xie, Y. Spraying Fabrication of Durable and Transparent Coatings for Anti-Icing Application: Dynamic Water Repellency, Icing Delay, and Ice Adhesion. *ACS Appl. Mater. Interfaces* **2019**, *11* (3), 3590–3598. https://doi.org/10.1021/acsami.8b19225.

(56) Fillion, R. M.; Riahi, A. R.; Edrisy, A. Design Factors for Reducing Ice Adhesion. *J. Adhes. Sci. Technol.* **2017**, *31* (21), 2271–2284. https://doi.org/10.1080/01694243.2017.1297588.

(57) Xie, Y.; Chen, H.; Shen, Y.; Tao, J.; Jin, M.; Wu, Y.; Hou, W. Rational Fabrication of Superhydrophobic Nanocone Surface for Dynamic Water Repellency and Anti-Icing Potential. *J. Bionic Eng.* **2019**, *16* (1), 27–37. https://doi.org/10.1007/s42235-019-0003-x.

(58) Rønneberg, S.; He, J.; Zhang, Z. The Need for Standards in Low Ice Adhesion Surface Research: A Critical Review. *J. Adhes. Sci. Technol.* **2020**, *34* (3), 319–347. https://doi.org/10.1080/01694243.2019.1679523.

(59) Zhang, R.; Zhang, H.; Dong, S.; Yang, Y.; Li, J. Photo- and Electro-Responsive Super-Slippery Oleogel Coating for Ultra-Low Temperature Ice-Phobic Applications. *Adv. Funct. Mater.* **2025**, *n/a* (n/a), 2501530. https://doi.org/https://doi.org/10.1002/adfm.202501530.

(60) Li, X.; Tan, X.; Xiao, T.; Li, X.; Jiang, L.; Tan, X.; Liu, S.; Li, T. Superhydrophobic Photothermal Coatings Based on Polyurea for Durable Anti-Icing and Deicing. *Surfaces and Interfaces* **2024**, *54*, 105120. https://doi.org/https://doi.org/10.1016/j.surfin.2024.105120.

(61) Zhu, T.; Yuan, Y.; Song, L.; Wei, X.; Xiang, H.; Dai, X.; Hua, X.; Liao, R. A PDMS Coating with Excellent Durability for Large-Scale Deicing. *Journal of Materials Research and Technology* **2024**, *29*, 4526–4536. https://doi.org/https://doi.org/10.1016/j.jmrt.2024.02.177.

(62) Zhang, R.; Zhang, H.; Dong, S.; Yang, Y.; Li, J. Photo- and Electro-Responsive Super-Slippery Oleogel Coating for Ultra-Low Temperature Ice-Phobic Applications. *Adv. Funct. Mater.* **2025**, *n/a* (n/a), 2501530. https://doi.org/https://doi.org/10.1002/adfm.202501530.

(63) Xu, W.; Shen, J.; Chini, S. F.; Ou, J. Durable Solid Slippery Coating for Ice Adhesion Reduction via Room Temperature Curing. *Mater. Lett.* **2025**, *383*, 137948. https://doi.org/https://doi.org/10.1016/j.matlet.2024.137948.

(64) Wang, G.; Wang, J.; Cheng, K.; Yang, K.; Zhang, W. Nano Hierarchical Hill-like Structure with TA1 Surface Manufactured by LIPSS for Anti-Corrosion and Anti-Icing. *Journal of Materials Research and Technology* **2025**, *35*, 3655–3667. https://doi.org/https://doi.org/10.1016/j.jmrt.2025.02.075.

(65) Zhang, R.; Zhang, H.; Dong, S.; Yang, Y.; Li, J. Photo- and Electro-Responsive Super-Slippery Oleogel Coating for Ultra-Low Temperature Ice-Phobic Applications. *Adv. Funct. Mater.* **2025**, *n/a* (n/a), 2501530. https://doi.org/https://doi.org/10.1002/adfm.202501530.

(66) Mohseni, M.; Recla, L.; Mora, J.; Gallego, P. G.; Agüero, A.; Golovin, K. Quasicrystalline Coatings Exhibit Durable Low Interfacial Toughness with Ice. *ACS Appl. Mater. Interfaces* **2021**, *13* (30), 36517–36526. https://doi.org/10.1021/acsami.1c08740.

(67) Wong, W. S. Y.; Hegner, K. I.; Donadei, V.; Hauer, L.; Naga, A.; Vollmer, D. Capillary Balancing: Designing Frost-Resistant Lubricant-Infused Surfaces. *Nano Lett.* **2020**, *20* (12), 8508–8515. https://doi.org/10.1021/acs.nanolett.0c02956.

(68) Qin, C. (Chris); Mulroney, A. T.; Gupta, M. C. Anti-Icing Epoxy Resin Surface Modified by Spray Coating of PTFE Teflon Particles for Wind Turbine Blades. *Mater. Today Commun.* **2020**, *22*, 100770. https://doi.org/https://doi.org/10.1016/j.mtcomm.2019.100770.

(69) Xu, Y.; Li, A.; Zhang, F.; He, W.; Zhen, W.; Yangyang, J.; Zhang, F.; He, Q. Study on Anti-Icing Performance of Carbon Fiber Composite Superhydrophobic Surface. *Mater. Today Chem.* **2023**, *29*, 101421. https://doi.org/https://doi.org/10.1016/j.mtchem.2023.101421.

(70) Liu, Y.; Sun, W.; Feng, K.; Wu, Y.; Yu, B.; Liu, S.; Zhou, F. Sebaceous Gland-Inspired Self-Lubricated de-Icing Coating by Continuously Secreting Lubricants. *Prog. Org. Coat.* **2023**, *174*, 107311. https://doi.org/https://doi.org/10.1016/j.porgcoat.2022.107311.

(71) Nakamura, S.; Luna, J. A.; Kakiuchida, H.; Hozumi, A. Effective Approach to Render Stable Dynamic Omniphobicity and Icephobicity to Ultrasmooth Metal Surfaces. *Langmuir* **2021**, *37* (40), 11771–11780. https://doi.org/10.1021/acs.langmuir.1c01720.

(72) Liu, Z.; Ye, F.; Tao, H.; Lin, J. Effects of Frost Formation on the Ice Adhesion of Micro-Nano Structure Metal Surface by Femtosecond Laser. *J. Colloid Interface Sci.* **2021**, *603*, 233–242. https://doi.org/https://doi.org/10.1016/j.jcis.2021.06.105.

(73) Chen, D.; Gelenter, M. D.; Hong, M.; Cohen, R. E.; McKinley, G. H. Icephobic Surfaces Induced by Interfacial Nonfrozen Water. *ACS Appl. Mater. Interfaces* **2017**, *9* (4), 4202–4214. https://doi.org/10.1021/acsami.6b13773.

(74) Menini, R.; Farzaneh, M. Production of Superhydrophobic Polymer Fibers with Embedded Particles Using the Electrospinning Technique. *Polym. Int.* **2008**, *57* (1), 77–84. https://doi.org/10.1002/pi.2315.

(75) Ruan, M.; Li, W.; Wang, B.; Deng, B.; Ma, F.; Yu, Z. Preparation and Anti-Icing Behavior of Superhydrophobic Surfaces on Aluminum Alloy Substrates. *Langmuir* **2013**, *29* (27), 8482–8491. https://doi.org/10.1021/la400979d.

(76) Mishchenko, L.; Hatton, B.; Bahadur, V.; Taylor, J. A.; Krupenkin, T.; Aizenberg, J. Design of Ice-Free Nanostructured Surfaces Based on Repulsion of Impacting Water Droplets. *ACS Nano* **2010**, *4* (12), 7699–7707. https://doi.org/10.1021/nn102557p.

(77) Chen, J.; Liu, J.; He, M.; Li, K.; Cui, D.; Zhang, Q.; Zeng, X.; Zhang, Y.; Wang, J.; Song, Y. Superhydrophobic Surfaces Cannot Reduce Ice Adhesion. *Appl. Phys. Lett.* **2012**, *101* (11). https://doi.org/10.1063/1.4752436.

(78) Kulinich, S. A.; Farhadi, S.; Nose, K.; Du, X. W. Superhydrophobic Surfaces: Are They Really Ice-Repellent? *Langmuir*. January 4, 2011, pp 25–29. https://doi.org/10.1021/la104277q.

(79) Farhadi, S.; Farzaneh, M.; Kulinich, S. A. Anti-Icing Performance of Superhydrophobic Surfaces. *Appl. Surf. Sci.* **2011**, *257* (14), 6264–6269. https://doi.org/https://doi.org/10.1016/j.apsusc.2011.02.057.

(80) Jung, S.; Dorrestijn, M.; Raps, D.; Das, A.; Megaridis, C. M.; Poulikakos, D. Are Superhydrophobic Surfaces Best for Icephobicity? *Langmuir* **2011**, *27* (6), 3059–3066. https://doi.org/10.1021/la104762g.

(81) Wu, X.; Silberschmidt, V. V; Hu, Z.-T.; Chen, Z. When Superhydrophobic Coatings Are Icephobic: Role of Surface Topology. *Surf. Coat. Technol.* **2019**, *358*, 207–214. https://doi.org/https://doi.org/10.1016/j.surfcoat.2018.11.039.

(82) Villegas, M.; Zhang, Y.; Abu Jarad, N.; Soleymani, L.; Didar, T. F. Liquid-Infused Surfaces: A Review of Theory, Design, and Applications. *ACS Nano* **2019**, *13* (8), 8517–8536. https://doi.org/10.1021/acsnano.9b04129.

(83) Latthe, S. S.; Sutar, R. S.; Bhosale, A. K.; Nagappan, S.; Ha, C. S.; Sadasivuni, K. K.; Liu, S.; Xing, R. Recent Developments in Air-Trapped Superhydrophobic and Liquid-Infused Slippery Surfaces for Anti-Icing Application. *Progress in Organic Coatings*. Elsevier B.V. December 1, 2019. https://doi.org/10.1016/j.porgcoat.2019.105373.

(84) Wang, G.; Guo, Z. Liquid Infused Surfaces with Anti-Icing Properties. *Nanoscale*. Royal Society of Chemistry December 21, 2019, pp 22615–22635. https://doi.org/10.1039/c9nr06934h.

(85) Samaha, M. A.; Gad-el-Hak, M. Polymeric Slippery Coatings: Nature and Applications. *Polymers (Basel).* **2014**, *6* (5), 1266–1311. https://doi.org/10.3390/polym6051266.

(86) Boinovich, L. B.; Chulkova, E. V; Emelyanenko, K. A.; Domantovsky, A. G.; Emelyanenko, A. M. The Mechanisms of Anti-Icing Properties Degradation for Slippery Liquid-Infused Porous

Surfaces under Shear Stresses. *J. Colloid Interface Sci.* **2022**, *609*, 260–268. https://doi.org/https://doi.org/10.1016/j.jcis.2021.11.169.

(87) Heydarian, S.; Jafari, R.; Momen, G. Recent Progress in the Anti-Icing Performance of Slippery Liquid-Infused Surfaces. *Progress in Organic Coatings*. Elsevier B.V. February 1, 2021. https://doi.org/10.1016/j.porgcoat.2020.106096.

(88) Peppou-Chapman, S.; Hong, J. K.; Waterhouse, A.; Neto, C. Life and Death of Liquid-Infused Surfaces: A Review on the Choice, Analysis and Fate of the Infused Liquid Layer. *Chemical Society Reviews*. Royal Society of Chemistry June 7, 2020, pp 3688–3715. https://doi.org/10.1039/d0cs00036a.

(89) Dou, R.; Chen, J.; Zhang, Y.; Wang, X.; Cui, D.; Song, Y.; Jiang, L.; Wang, J. Anti-Icing Coating with an Aqueous Lubricating Layer. *ACS Appl. Mater. Interfaces* **2014**, *6* (10), 6998–7003. https://doi.org/10.1021/am501252u.

(90) Chen, J.; Luo, Z.; Fan, Q.; Lv, J.; Wang, J. Anti-Ice Coating Inspired by Ice Skating. *Small* **2014**, *10* (22), 4693–4699. https://doi.org/10.1002/smll.201401557.

(91) Chen, D.; Gelenter, M. D.; Hong, M.; Cohen, R. E.; McKinley, G. H. Icephobic Surfaces Induced by Interfacial Nonfrozen Water. *ACS Appl. Mater. Interfaces* **2017**, *9* (4), 4202–4214. https://doi.org/10.1021/acsami.6b13773.

(92) Shamshiri, M.; Jafari, R.; Momen, G. A Novel Hybrid Anti-Icing Surface Combining an Aqueous Self-Lubricating Coating and Phase-Change Materials. *Prog. Org. Coat.* **2023**, *177*, 107414. https://doi.org/https://doi.org/10.1016/j.porgcoat.2023.107414.

(93) Liu, F.; Wang, Z.; Pan, Q. Intelligent Icephobic Surface toward Self-Deicing Capability. *ACS Sustain. Chem. Eng.* **2020**, *8* (2), 792–799. https://doi.org/10.1021/acssuschemeng.9b04570.

(94) Mossayebi, Z.; Jafari, V. F.; Gurr, P. A.; Simons, R.; Qiao, G. G. Reduced Ice Adhesion Using Amphiphilic Poly(Ionic Liquid)-Based Surfaces. *ACS Appl. Mater. Interfaces* **2023**, *15* (5), 7454–7465. https://doi.org/10.1021/acsami.2c21500.

(95) Abasi, S.; Davis, R.; Podstawczyk, D. A.; Guiseppi-Elie, A. Distribution of Water States within Poly(HEMA-Co-HPMA)-Based Hydrogels. *Polymer (Guildf).* **2019**, *185*, 121978. https://doi.org/https://doi.org/10.1016/j.polymer.2019.121978.

(96) Biro, R. A.; Tyrode, E. C.; Thormann, E. Reducing Ice Adhesion to Polyelectrolyte Surfaces by Counterion-Mediated Nonfrozen Hydration Water. *ACS Appl. Mater. Interfaces* **2024**, *16* (16), 21356–21365. https://doi.org/10.1021/acsami.4c02434.

(97) He, Z.; Zhuo, Y.; Wang, F.; He, J.; Zhang, Z. Design and Preparation of Icephobic PDMS-Based Coatings by Introducing an Aqueous Lubricating Layer and Macro-Crack Initiators at

the Ice-Substrate Interface. *Prog. Org. Coat.* **2020**, *147*, 105737. https://doi.org/https://doi.org/10.1016/j.porgcoat.2020.105737.

(98) He, Z.; Xiao, S.; Gao, H.; He, J.; Zhang, Z. Multiscale Crack Initiator Promoted Super-Low Ice Adhesion Surfaces. *Soft Matter* **2017**, *13* (37), 6562–6568. https://doi.org/10.1039/C7SM01511A.

(99) Chen, C.; Fan, P.; Zhu, D.; Tian, Z.; Zhao, H.; Wang, L.; Peng, R.; Zhong, M. Crack-Initiated Durable Low-Adhesion Trilayer Icephobic Surfaces with Microcone-Array Anchored Porous Sponges and Polydimethylsiloxane Cover. *ACS Appl. Mater. Interfaces* **2023**, *15* (4), 6025–6034. https://doi.org/10.1021/acsami.2c15483.

(100) Irajizad, P.; Al-Bayati, A.; Eslami, B.; Shafquat, T.; Nazari, M.; Jafari, P.; Kashyap, V.; Masoudi, A.; Araya, D.; Ghasemi, H. Stress-Localized Durable Icephobic Surfaces. *Mater. Horiz.* **2019**, *6* (4), 758–766. https://doi.org/10.1039/C8MH01291A.

(101) Nazifi, S.; Huang, Z.; Hakimian, A.; Ghasemi, H. Fracture-Controlled Surfaces as Extremely Durable Ice-Shedding Materials. *Mater. Horiz.* **2022**, *9* (10), 2524–2532. https://doi.org/10.1039/D2MH00619G.

2

Role of Molecular Water Layer State on Freezing Front Propagation Rate and Mode

Abstract: In this work, we study the relation between the molecular water layer (MWL) and frost freezing onset and propagation. The progression of frost has been reported to be governed by various localized icing phenomena, including inter-droplet ice bridging, dry zones, and frost halos. Reports studying the state of water on surfaces have revealed the presence of a thin (nm) water layer on a range of surfaces. Regardless of further investigations that show environmental humidity, temperature, and surface energy to affect the thickness of the MWL on surfaces, the influence of the MWL on frost nucleation and propagation has not yet been previously addressed in the literature.

To study the effect of the MWL on surface freezing events, a range of surface-functionalized glass substrates was prepared. In-situ monitoring of freezing events with thermal imaging allowed studying the effect of surface chemistry and environmental relative humidity (RH) on the thickness and continuity of the MWL. We argue that the observed icing nucleation and propagation kinetics are directly related to the presence and continuity of the MWL, which can be manipulated by controlling the environmental humidity and surface chemistry.

INTRODUCTION

The accumulation of ice on solid surfaces can have hazardous consequences, in applications as wide-ranging as aircraft[1-2], power lines[3], marine vessels[4], microelectronics[5], and wind turbines[6-8]. In the aerospace industry, icing affects negatively both the performance and safety of aircraft, whereas, in the production of energy from the kinetic energy of air in motion, ice accumulation on the blades of wind turbines can significantly reduce their power generation efficiency. Ice accretion is currently managed by heating, using de-icing fluids, and/or mechanically removing ice from the exposed surfaces. In spite of being efficient, in most cases, these methods are costly and demand intense labour, excessive amounts of energy, and time.[9-12]

During the past 70 years, researchers have been designing passive anti-icing coatings to overcome the above-mentioned challenges.[13-14] Instead of relentlessly removing ice from a surface, an effective anti-icing coating aims at preventing icing accretion itself, in which case the problematic de-icing methods would remain only as complementary ice removal systems.[15-16] An ideal coating would be one that provides sufficient and long-lasting performance (i.e., low erosion and high UV resistance) with easy application and scalable production. It is calculated that even though an effective anti-icing coating might initially cost more in comparison to the use of de-icing fluids, in the long term, a permanent coating would still reduce the overall costs, effort, and time spent on ice protection.[9,17]

There have already been a variety of attempts to create durable and effective anti-icing coatings.[17-18] Despite these efforts, the incomplete in-depth understanding of the factors necessary to prevent or control ice formation on surfaces and the scatter of relevant information addressing the underlying mechanisms of ice accretion and propagation limit progress. For a more rational anti-icing coating design, it is beneficial to learn more about the factors affecting ice nucleation, propagation, and adhesion on surfaces. Of particular interest in understanding ice nucleation and propagation is the interaction of water molecules in the environment with the surface at a molecular level.

Past research on freezing propagation has mostly attributed freezing propagation to the formation of inter-droplet ice bridges. In this work, we propose an alternative mechanism based on the presence of the so-called molecular water layers (MWL). Continuous layers of molecular water imaged at room temperature were first reported in the 1990s on hydrophilic mica surfaces using atomic force microscopy (AFM).[19] In the early 2010s, while studying the nanoscale condensation of water droplets on COOH-modified hydrophilic silicon surfaces under ambient conditions, it was proposed that these nanoscale water droplets are interconnected through a non-optically detectable thin liquid layer of water.[20]

Despite the initial reports confirming the presence of a MWL on hydrophilic surfaces, its role on ice nucleation and propagation has been widely overlooked in the field of anti-icing surfaces while its presence may explain some of the observations reported in the literature. One plausible reason to overlook its role is the difficulty to detect MWLs under ambient conditions with the most popular and available characterization methods used in icing research, e.g., with optical microscopy. Nanoscale clusters of individual water molecules on solid surfaces have been otherwise systematically studied in ultra-high vacuum conditions and at low temperatures using scanning tunnelling microscopy (STM)[21]. However, in ambient conditions, molecular layers of water have only recently been studied on smooth silica surfaces using AFM[19.20,22], X-ray reflectometry[20], X-ray photoelectron spectroscopy[23], attenuated total reflection infrared spectroscopy (ATR-IR)[24], and sum frequency generation spectroscopy (SFG)[25,26].

In agreement with previous studies, it can be proposed that MWLs between 0.2 and 6 nm may be present on smooth hydrophilic surfaces exposed to ambient conditions. Considering the experimental evidence, the proposed model system of water on surfaces suggests the presence of a homogeneous monolayer of solid hexagonally arranged water molecules followed by a transitional layer of restricted mobility and a sequence of disordered layers of liquid water molecules.[24] Not many reports have been published on the thickness of each of these proposed water layers (solid-like or liquid-like) and the effect of environmental conditions (T, RH) and surface chemistry on such layers. Nevertheless, reports on cleaned smooth glass surfaces in maximum relative humidity (95-100 %) at

ambient temperature (22 ℃) suggest that the solid-like MWL starts to transition into a liquid-like MWL when the solid-like MWL thickness is more than 3 monolayers of water (~1 nm). At that point, the liquid-like MWL grows to a maximum reported thickness of 18 monolayers (~6 nm).[23]

Uniformity of the MWL has attracted even less attention. On hydrophilic mica surfaces, the MWL appears as a uniform layer when the RH is above 40 % or as a discontinuous film with dry holes and/or smaller individual islands of molecular water unevenly distributed on the surface when the RH is below 40 %.[19,22] These observations are compatible with other works reporting MWLs to exist as a solid-like layer below 30 % RH and as a liquid-like layer above 60 % RH on hydrophilic silicon substrates.[20,24] Although most reports did not report MWLs on hydrophobic surfaces at ambient conditions, MWLs of about 2 nm were reported for very hydrophobic surfaces such as halocarbon wax or Teflon at room temperature and 80 % RH.[23] This proves that water can adsorb and/or absorb on hydrophobic surfaces in high-humidity environments, especially when the surfaces have irregularities, defects, or high roughness. On hydrophilic surfaces at room temperature, the measured thickness of MWLs decreases with increasing water contact angle of the surfaces and with increasing temperature (e.g., 65 ℃).[20]

In this work, we systematically study the effect of surface chemistry and relative humidity on the presence of molecular water layers (MWL) and its related role on ice nucleation and propagation at sub-zero temperatures. To this aim, we used smooth and rough glass surfaces functionalized using silane chemistry. Thermal imaging and image correlation protocols were used to monitor and quantify freezing events with high temporal and spatial resolution. The work unveils the role of MWLs on frost ice nucleation and propagation kinetics and its mode of propagation, through hydrophilic and hydrophobic surfaces, as a function of the ambient relative humidity. This confirms the likelihood of freezing events to occur in porous superhydrophobic surfaces.

EXPERIMENTAL

Materials

Standard microscope glass slides purchased from Carl Roth (corners cut, without frosted edge, 26×76×1 mm) were used as substrates across the study. The silanes 11-acetoxyundecyltrichlorosilane (95 %), n-octyltrichlorosilane (97 %), tridecafluoro-1,1,2,2-tetrahydrooctyltrichlorosilane (perfluorooctyltrichlorosilane, 97 %) were purchased from ABCR, and heptadecafluoro-1,1,2,2-tetrahydrodecyltrichlorosilane (perfluoro-decyltrichlorosilane, 97 %) was purchased from Gelest and used as received. All remaining solvents and chemicals used in this study were purchased from Sigma Aldrich and used as received. Silica gel (3.5 mm bead size, for desiccation) was purchased from Sigma Aldrich and heated in the oven at 130 ℃ for 4 hours before use.

Surface activation of the glass slides

Activation of the reactive hydroxyls and removal of any contaminants from the glass surface were done using a wet chemical method based on HCl and MeOH. In the activation procedure, the glass slides were first immersed in a solution containing a 1:1 volume ratio of MeOH:HCl for 30 minutes. In a subsequent step, the slides were rinsed with deionized H_2O and dried under N_2. The activated and dried slides were directly analysed with water contact angle goniometry. Some of the prepared samples were further modified with functional silanes to control the surface water contact angle as explained below.

Surface silanization

Covalent attachment of functional silanes to the cleaned glass slides was carried out with a vapor deposition method in a vacuum chamber.[27] After drying under nitrogen flow, two glass slides and three droplets (150 µL) of one silane were placed in separate dishes inside a custom-made sealed aluminium chamber connected to a vacuum pump. Vapor deposition

of the silane onto the glass slides was carried out at low pressure (20 mbar) for 2 hours at room temperature. Subsequently, the glass slides were removed from the chamber and used for contact angle measurements and icing tests. The procedure was repeated with four different silanes to obtain a representative range of hydrophilic to hydrophobic smooth surfaces.

Sol-gel surface treatment

A sol-gel process leading to a porous silica-based coating was used to develop a superhydrophobic surface on glass. To this aim, methyl trichlorosilane (0.2 mL) was deposited on the top of a glass surface and left to dry at room temperature while being covered with a Petri dish. After drying, the sample was heated for 1 h at 100 °C. The procedure was repeated three times to obtain thicker layers.

Water contact angle measurements

Water contact angles (WCAs) were determined right after the surface activation and the silanization processes. The measurements were made using a KSV CAM 200 optical contact angle goniometer. Static, advancing, and receding water contact angles were recorded using the sessile and needle-in-the-sessile-drop methods. All measurements were repeated three times for each sample. For advancing (A-WCA) and receding (R-WCA) angles, the initial volume of the drop (3 µL) was first increased with a pumping speed of 15 µL s^{-1} until a maximum droplet size of 15 µL. Then the volume of the droplet was decreased from 15 µL back to 3 µL using the same pumping speed of 15 µL s^{-1}. Drop shape analysis of the images was done based on the Young–Laplace equation. All WCA measurements were carried out at an ambient temperature of 21±2 ℃ and relative humidity of 40±5 %.

Measuring and quantifying freezing events with thermal imaging

Freezing events on the substrates were monitored using a FLIR A655sc thermal camera with a close-up lens (1.5 magnifying factor and 25 µm lateral resolution). The thermal camera was calibrated according to the manufacturer's instructions, including emissivity correction, and the measured temperatures were cross-checked against thermocouple measurements during experimental setup. An emissivity value of 0.9 was used during the recordings to avoid reflections from influencing the results. To induce and control freezing, the samples were cooled on two Peltier elements set in parallel (40x40 mm each) to obtain a uniform temperature distribution. The Peltier elements were connected to a heat sink and a small fan for heat dissipation. Each thermal video recording started shortly before switching on the Peltier plates where the glass samples were set to reach -20 °C at 15 °C min^{-1} and ended 1 minute after the freezing event was observed to have propagated across the surface. Each measurement was repeated at least 3 times per sample. Two types of experiments were conducted: (i) monitoring frost formation in the absence of water droplets, and (ii) monitoring freezing of water droplets previously deposited on the sample surfaces. In the former, the surfaces were kept at -20 °C until a freezing event was observed. Image analysis was used to quantify freezing onset times and kinetics of the freezing propagation front. Due to the complex geometry of the freezing fronts, the propagation rates were determined by tracking the local displacement of the front between consecutive thermal video frames at multiple locations along the freezing interface, followed by averaging over several measurements (see Supporting Information, **Figure S2.3**). The second set of experiments was carried out similarly, but with a single 5 µL deionized water droplet placed on top of the sample before the Peltier plates were cooled down. Image analysis was used to quantify the freezing kinetics of the droplet and its surroundings. To study the effect of environmental humidity on the freezing events, the thermal camera and Peltier elements were placed inside a glove box. The humidity inside was lowered to 25 % RH with dried silica gel and increased to 50 % RH and 70 % RH by placing a beaker of $CaCl_2$ solution in the closed environment.[28,29] A humidity equilibrium inside the glove box was reached within three days each time the humidity was adjusted. All the images were

analysed with the analysis program FLIR Research Studio, and the image processing program ImageJ.

RESULTS AND DISCUSSION

Water contact angles

Table 2.1 and **Figure 2.1** summarize the measured static (WCA), advancing (A-WCA), and receding (R-WCA) water contact angles and hysteresis (CAH) as a function of the surface chemistry obtained after surface cleaning and silanization. As expected, the surface-activated glass slides show more hydrophilic surface chemistry (WCA=21±3°) than the degreased bare glass slides (WCA=49±2°) as a result of a larger presence of active hydroxyl groups[30]. The WCA of the silane-treated samples follows the expected growing hydrophobic nature: acid end group < hydrocarbon chain < fluorocarbon content. Amongst the smooth surfaces, the glass slides covered with perfluorinated decyl carbon chains show the most hydrophobic WCA (109±2°). Of all studied samples, the porous sol-gel coatings showed, as intended, superhydrophobic WCA (150±5°). A-WCA and R-WCA followed a similar trend to WCA with surface chemistry. Interestingly, the surface-activated and silanized smooth surfaces showed comparable CAH values (18-23°) lower than the CAH of the degreased bare glass surface (36±4°). The surface activation removes topological differences caused by contaminants, which can explain the lower CAH values on the surface-activated and silanized glass slides. The superhydrophobic surfaces, on the other hand, showed a significantly lower CAH (4±10°); a distinctive mark of a superhydrophobic and self-cleaning surface as a result of roughness porosity entrapping air[31]. **Figure 2.2** shows Confocal Laser Scanning Microscopy (CLSM) images of the superhydrophobic surfaces and a smooth hydrophobic surface for comparison. The micrographs confirm the presence of porosity in the superhydrophobic surface responsible for air entrapment beneath water droplets.

Altogether, these results confirm a successful obtaining of a range of surfaces with varying hydrophilic/hydrophobic nature and justifies the use of static contact angle (WCA) for the subsequent comparisons with the freezing events.

Table 2.1. A series of smooth and rough samples with varying surface chemistry and related WCAs. The red scale bar corresponds to 1 mm for all images shown here.

Sample	Chemistry	Structure	WCA	A-WCA	R-WCA	CAH	Image
A	Surface activated	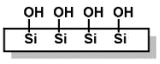	21±3°	26±2°	4±2°	22±4°	
B	Degreased	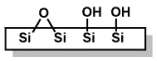	38±6°	49±2°	13±2°	36±4°	
C	11-Acetoxyundecyl trichlorosilane	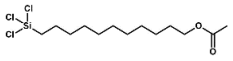	54±6°	56±1°	38±1°	18±2°	
D	n-Octyltrichlorosilane	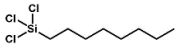	89±6°	91±1°	73±4°	18±5°	
E	Perfluoro-octyltrichlorosilane	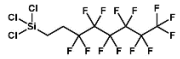	106±3°	115±3°	92±4°	23±7°	
F	Perfluoro-decyltrichlorosilane		109±2°	117±2°	95±4°	22±6°	
G	Sol-gel treatment with methyltrichlorosilane	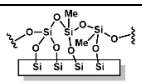	150±5°	152±3°	148±7°	4±10°	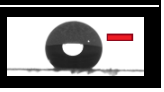

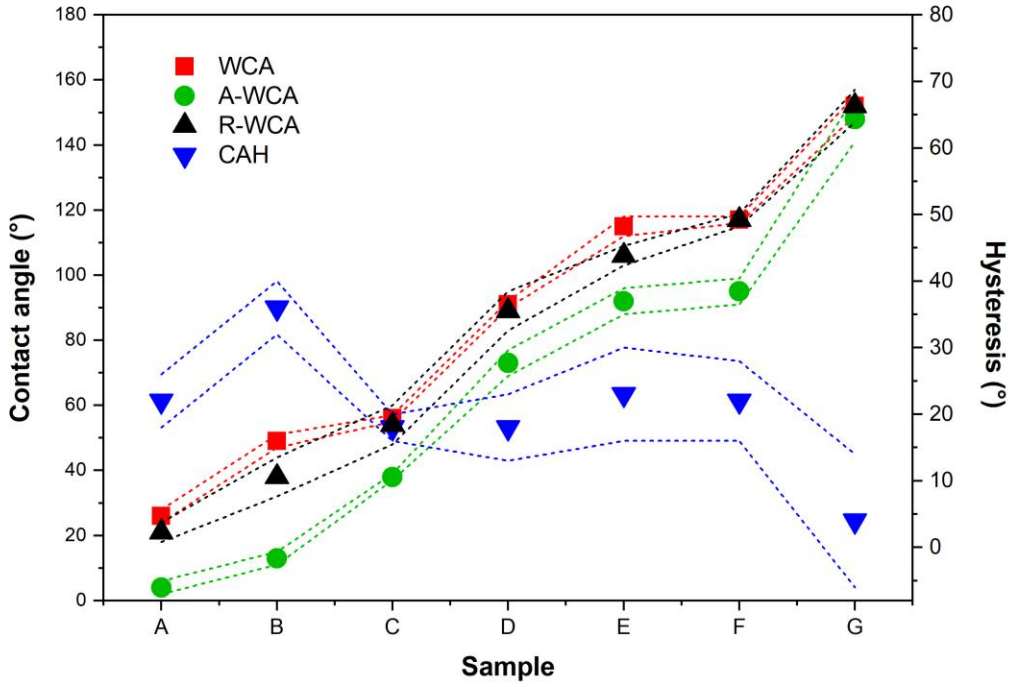

Figure 2.1. Water contact angles as a function of surface chemistry. The static (WCA), advancing (A-WCA), and receding (R-WCA) water contact angles of samples A to G show a similar increasing trend. The hysteresis (CAH) values are comparable for all smooth samples (A to F) and show a local minimum for the superhydrophobic sample (G).

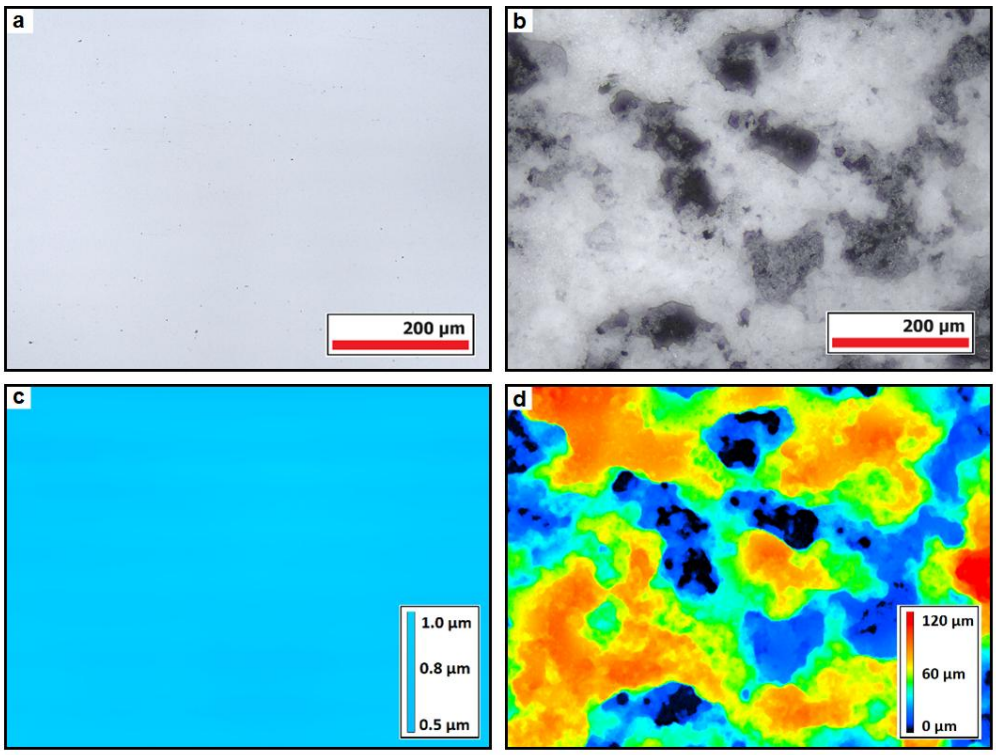

Figure 2.2. CLSM images show optical images (top row) and their corresponding height maps (bottom row) of the smooth glass surfaces functionalized with perfluorodecyltrichlorosilane (a and c) and the superhydrophobic surfaces prepared via sol-gel treatment (b and d).

Frost propagation in the absence of water droplets

Figure 2.3 shows representative snapshots from the recorded thermal imaging videos as a function of the relative humidity (25 %, 50 %, and 70 %) for surfaces (12 mm x 16 mm) without a droplet. The rest of the snapshots and videos can be found in the Supporting Information (**Tables S2.1-S2.3**). In this experiment, thermal imaging reveals the latent heat release during the freezing of supercooled surface water. In practice, this allows following the freezing propagation front throughout the surface with high spatial and temporal resolution once a freezing event starts somewhere on the sample surfaces.

In the video snapshots, the dark purple colour corresponds to a lower temperature, and the bright yellow to a higher temperature. As liquid water freezes on the sample surface, a

sudden temperature increase pinpoints the location of the freezing event. The higher the volume of water freezing, the more heat is released, and the brighter the colour change is in the video. In the case of a water droplet freezing, the abrupt temperature increase is eye-catching. On the other hand, it is much more difficult to follow the freezing front propagating on a surface with little or no water condensation present. Hence, in **Figures 2.3a-b**, the freezing front propagation fronts are highlighted with a white line, and the direction of the freezing front is specified with black arrows. After the latent heat has been released, the frozen areas keep cooling down and appear with a darker colour in the thermal videos.

At 25 % RH, the propagation front line looks similar on all samples (**Figure 2.3a** and **Table S2.1**) except for the superhydrophobic surface (**Figure 2.3d**). There is no condensation visible on the surface (absence of small growing round dots with darker colour compared to the substrate), and the freezing front line is clearly fractal-like in shape. In contrast, the superhydrophobic sample is covered with condensation and as seen in **Figure 2.3d**, the freezing front line is only detectable by following individual condensed droplets lighting up as they freeze (marked with white circles).

At 50 % and 70 % RH, small droplets of condensation can be observed on all samples (**Figures 2.3 b-c** and **Tables S2.2**-**S2.3**). Instead of fractal-like freezing front lines, most of the samples show much smoother propagation fronts. The front line on the activated glass surface at 70 % RH is almost perfectly round. Conversely, there were no changes in the freezing propagation pattern of the superhydrophobic surface, regardless of the humidity (**Tables S2.1**-**S2.3**), and the same freezing mechanism was observed on all hydrophobic silane-treated surfaces at 50% RH (**Table S2.2**).

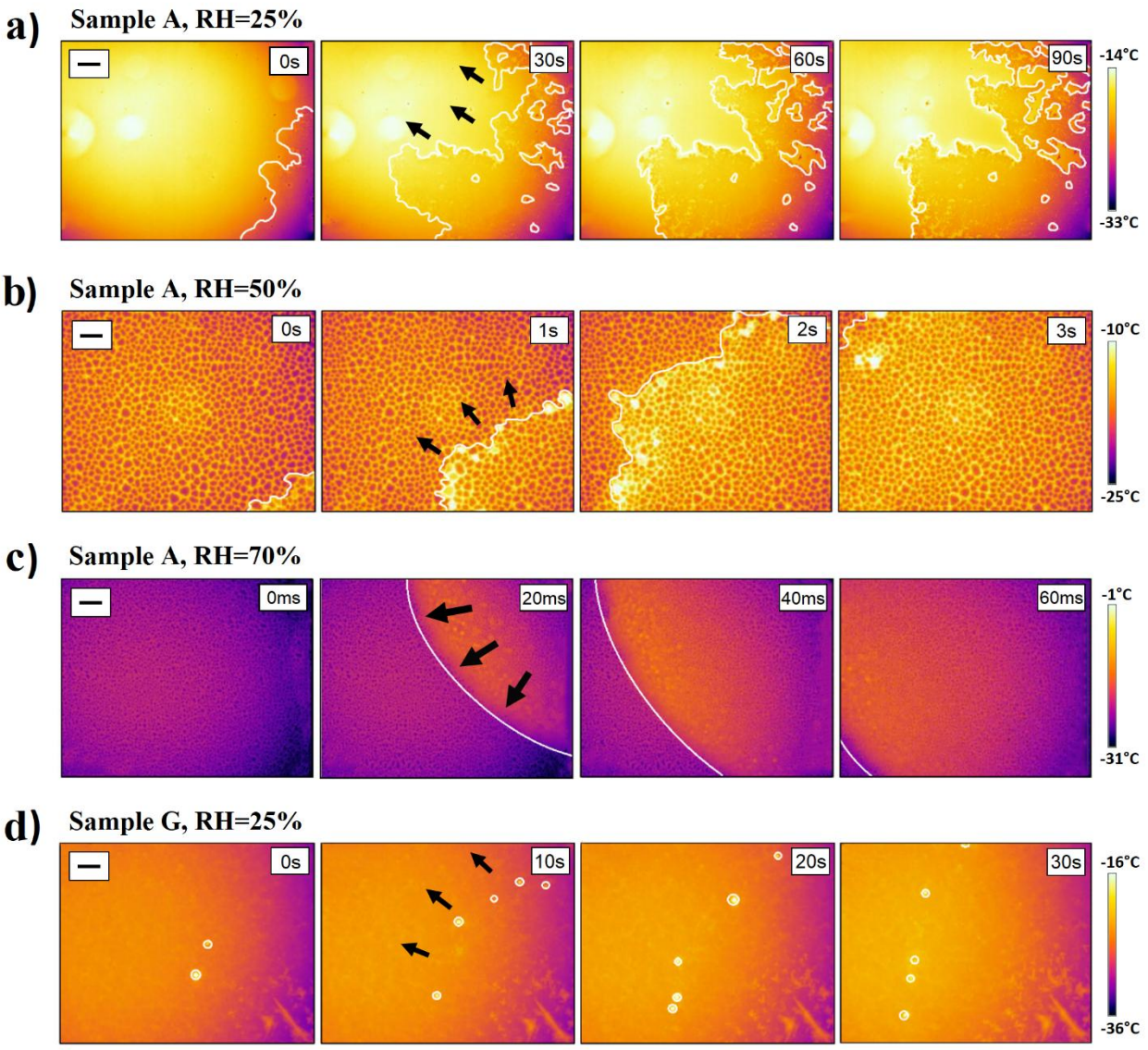

Figure 2.3. Time snapshots from thermal videos showing a freezing front propagating on the activated glass slides (sample A) as a function of relative humidity **(a-c)** and on superhydrophobic surfaces at 25% RH **(d)**. The cooling rate in these experiments was set so that the sample surface reaches -20 °C at 15 °C min^{-1}. In **a-c**, the propagation front line is highlighted with a white line, and, in **d**, the isolated freezing events are marked with white circles. The black arrows indicate the direction of the freezing front propagation, and black scale bars shown in the top left corners are 1 mm. The time indicated in the top right corner of each image shows the timestep between each snapshot and, therefore, does not correspond to the freezing onset time. The vertical colour bars indicate the temperature at the surface measured by the IR camera.

Frost propagation in the presence of deposited water microdroplets

Figure 2.4 shows representative snapshots from the recorded thermal imaging videos as a function of the relative humidity (25 %, 50 %, and 70 %) in the presence of a water droplet (5 µL) deposited in the centre of each sample. The complete set of samples is in **Tables S2.4-S2.6**. The main distinctive feature of these image snapshots is the presence of a large round supercooled droplet in the centre lighting up when freezing. Notably, the droplet begins freezing only when the propagation front line meets it, as clearly seen in **Figure 2.4c** at 20 ms snapshot. The presence of the droplet seems to not have influenced the freezing propagation modes discussed in the previous section.

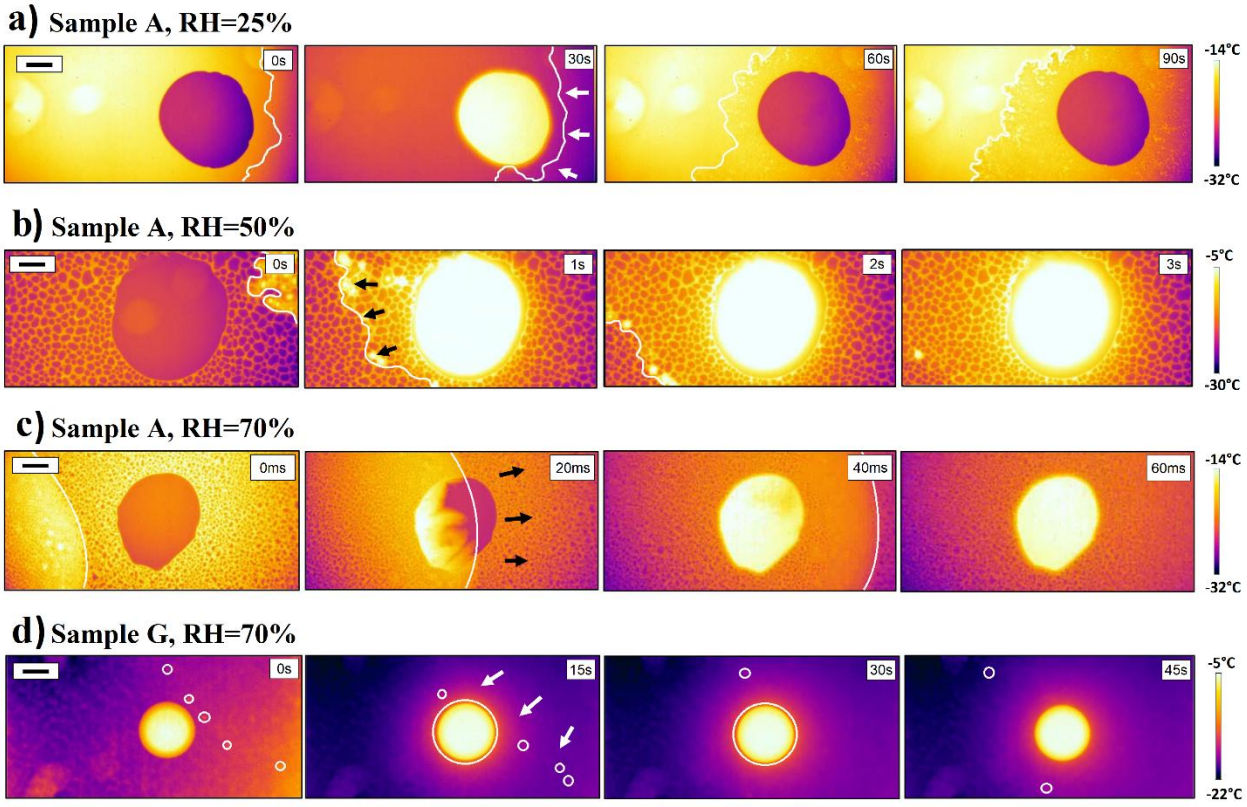

Figure 2.4. Time snapshots from thermal videos showing a freezing front propagating in the presence of a 5 µL water droplet on the activated glass slides as a function of relative humidity **(a-c)** and on superhydrophobic surfaces in 25% RH **(d)**. The cooling rate in these experiments was set so that the sample surface reaches -20 °C at 15 °C min^{-1}. In **a** to **c**, the front line of each freezing event is highlighted with a white line, and, in **d**, the isolated freezing events are marked by white circles. The white and black arrows indicate the direction of the freezing front propagation. The time indicated in the top right corner of each image shows the timestep between each snapshot and, therefore, does not correspond to the freezing onset time. The black scale bars shown in the top left corners are 1 mm. The vertical colour bars indicate the temperature at the surface measured by the IR camera.

Freezing of the microdroplets

The high accuracy of thermal imaging allows extracting local temperature at any location and time, for instance, at a water droplet present at the surface, as shown in **Figure 2.4**. **Figure 2.5a** plots the temperature of supercooled droplets on the different studied samples as a function of the freezing experiment time. Independently of the surface chemistry, all droplets show the same temperature profile during freezing: (i) supercooling to the temperature around -15 °C; (ii) sudden temperature increase to around -5 °C (t_{onset}); (iii) isothermal at that temperature for varying times; (iv) rapid temperature drop (t_{end}), and (v) stabilization to the initial temperature before the freezing event.

The sudden temperature increase (ii) originates from the latent heat released in the phase change from liquid to solid. Some of this heat release is observed as a temperature increase in the videos, yet a part of it is dissipated into the substrate. **Figure 2.5b** shows the extracted duration of the freezing event of individual droplets (t_{onset} until t_{end}) as a function of the WCA. Even though the water droplets have the same volume in all of the experiments, the plot reveals a linear increase of the freezing event duration (length of stage iii) with the WCA. In general, the higher the contact area (the lower the contact angle), the earlier the freezing event ends (shorter stage iii). The superhydrophobic sample keeps the general trend and shows the longest freezing event duration, presumably due to having the lowest contact area and therefore slowest latent heat dissipation into the substrate and surrounding environment.

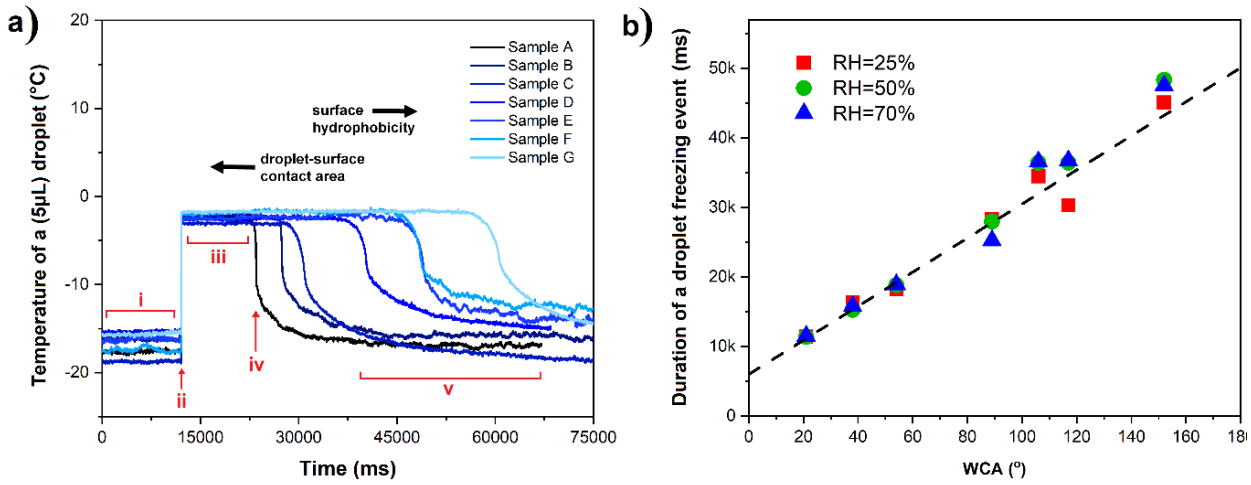

Figure 2.5. a) Time-temperature plots from a 5 µL droplet freezing at 50 % relative humidity. For sample A, the different stages of freezing are marked with red numerals i, ii, iii, iv, and v. The plots are set to overlap each other at t_{onset} (ii) to demonstrate the increase in freezing duration time with increasing hydrophobicity of the samples. **b)** Shows the duration of the freezing event (t_{end} - t_{onset}) plotted as a function of the static WCA in 3 different humidities. A linear dependence between the droplet freezing and the static WCA is observed.

Freezing onset time at the surface with and without a droplet

From each freezing experiment recorded using the thermal camera (**Figures 2.3-2.4** and **Tables S2.1-S2.6**), a freezing onset time (t_{fo}) was extracted and plotted in **Figure 2.6a** as a function of the surface chemistry (represented by the WCA) and the relative humidity (RH). The freezing onset time is described as the time from when the cooling plates are turned on to the moment at which the first freezing event is captured by the observation window of the thermal camera.

In **Figure 2.6a**, the freezing experiments done with and without a droplet show the same trend shape for every relative humidity. The freezing onset times grow exponentially with increasing WCA until reaching an apparent plateau at WCA>120°, with the superhydrophobic samples showing much lower freezing onset times than expected. However, without additional data points at WCA>150°, it is not possible to confirm what happens to the trend in the case of superhydrophobic surfaces.

Similarly, freezing onset times also decrease as RH increases. The presence of the droplet did not seem to have a large effect on the results at RH 25 % and 70 % nor on the freezing onset values of any of the hydrophilic surfaces at any RH. In the case of RH 50 %, the presence of the droplet seems to have delayed the freezing onset times of the hydrophobic samples; however, all freezing onset measurements at RH 50 % fit between rather wide error bars.

A similar exponential growth towards a plateau has been found for the dependence of the supersaturation degree (SSD) and nucleation pressure on WCA, following the mathematical procedure by Nath and Boreyko[32] (**Equations S2.1-S2.6** in SI). In the experiments therein, there are two possible mechanisms that explain frost development on the sample surfaces: (i) water first condenses on the sample surfaces and then freezes via condensation frosting, or (ii) water deposits directly from vapor to solid ice. The phase change of water vapor to liquid (condensation) or to solid ice (deposition) on a substrate requires either an undercooling of the substrate temperature or a supersaturation of the surrounding vapor pressure. SSD is a parameter that describes the extent of supersaturation needed for condensation or deposition to occur on the substrate at a given temperature, whereas nucleation pressure gives the pressure required for each phase change. The values of SSD and nucleation pressure are both dependent on substrate wettability and have, therefore, different values for each of the samples.

In **Figure 2.6b**, the SSD and nucleation pressure have been plotted as a function of WCA for both condensation and deposition at -20 ℃. The similarities between plots **2.6a** and **2.6b** can be understood since both SSD and freezing onset times can be used to describe the energy barrier of nucleation on surfaces. It is also notable that, in **Figure 2.6b**, the nucleation pressure required for deposition becomes lower than the nucleation pressure required for condensation at WCA<47° indicating that deposition is theoretically a more favourable mode of nucleation on the hydrophilic surfaces at -20 ℃.

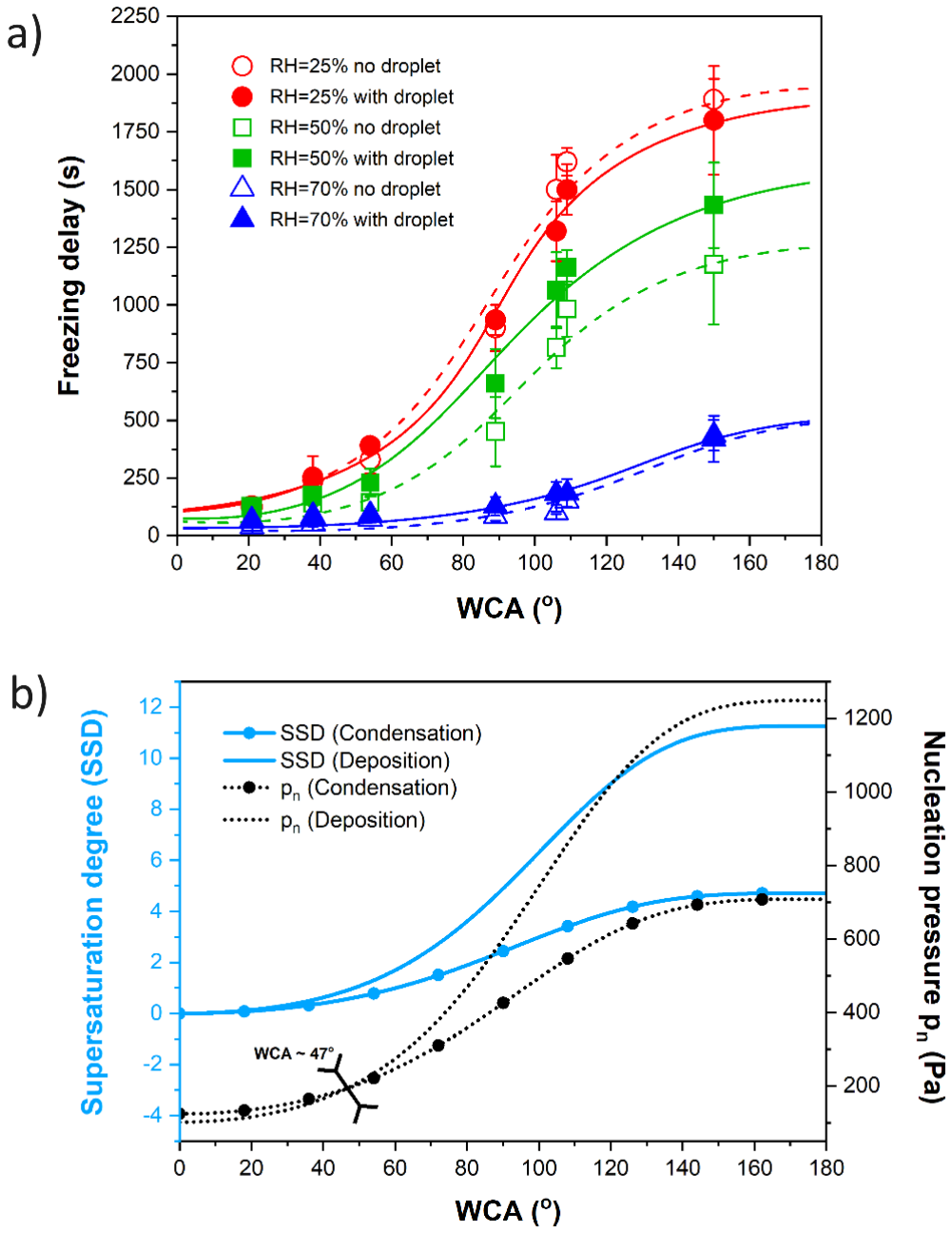

Figure 2.6. a) Freezing onset times as a function of the static WCA of the sample surfaces in the experiments conducted with a 5 µL water droplet placed in the centre of the sample (filled symbols, solid line) and without a water droplet (open symbols, dashed line) in three RHs. The continuous and dashed lines serve as a guide to the eye. **b)** Supersaturation degree (SSD) and nucleation pressure (p_n) respectively plotted as a function of the static WCA for condensation (vapor-to-liquid, marked with circle symbols) and deposition (vapor-to-solid, no symbols). The functions are calculated for -20 °C surface temperature using 10^{29} m^{-2} s^{-1} as a fixed kinetic constant for embryo formation for both condensation and deposition using **Equations S2.1-S2.6** in SI. The black inverted arrows indicate the WCA intersection point of nucleation pressure curves below which deposition is thermodynamically favoured (WCA < 47°).

Relation between freezing front propagation, surface chemistry, and MWL

Previous research dedicated to freezing propagation phenomena on surfaces mostly focused on frost growth using optical microscopy under experimental conditions leading to visible water droplet condensation[33-44]. Under these circumstances, individual droplets sequentially freeze when optically detectable ice bridges, formed at a frozen droplet, propagate and reach a neighbouring liquid droplet. In line with these observations, freezing propagation on surfaces has been related to the formation of inter-droplet ice bridges (i.e., percolation-induced frost propagation). Experimental evidence[35-41] suggests that the propagation rate of such inter-droplet bridges occurs at ~0.01 mm s^{-1}, 4 to 5 orders of magnitude slower than the reported intra-droplet freezing propagation rate (10-100 mm s^{-1})[45-48]. As a consequence, the overall frost propagation rate on surfaces has been reported to be around 0.01 mm s^{-1} based on a (relatively) limited number of substrates and environmental conditions studied. In this work, we identified different freezing front propagation mechanisms and rates as a function of the relative humidity and substrate hydrophilicity and topology. **Figures 2.3** and **2.4**, **Tables S2.1-S2.6,** show snapshots of the freezing experiments monitored by thermal imaging used in this work to calculate freezing front propagation rates and to identify freezing propagation mechanisms as a function of RH and surface energy. Analysis of the images and identification of the freezing front propagation lines was performed using the image processing program ImageJ. This allowed identifying different freezing front lines depending on the experimental conditions (front lines marked as white lines in **Figures 2.3** and **2.4**, and **Tables S2.1-S2.6** in SI). Replicates of the freezing experiments allowed obtaining average freezing propagation rates with deviation for each experimental (RH) and sample surface energy (WCA) as shown in **Figure 2.7** and **Figure S2.3** in SI.

Figure 2.7 shows how, independently of the front-line geometry and propagation mechanism, the freezing fronts propagate faster at higher environmental humidities. Larger differences are nevertheless seen at low surface energies (WCA in the range 20° to 60°) and high relative humidities (50 % and 70 %). This trend seems to hold true for all of the experimental conditions except for the superhydrophobic surfaces (WCA~150°) for which

the freezing front propagation rates increase at all RHs slightly above the most hydrophobic of all smooth surfaces (both perfluorinated samples with WCA around 105-110°). The increase in the freezing propagation rate for the superhydrophobic sample is here attributed to moisture entrapment within the porous structure of the superhydrophobic samples shown in **Figure 2.2**.

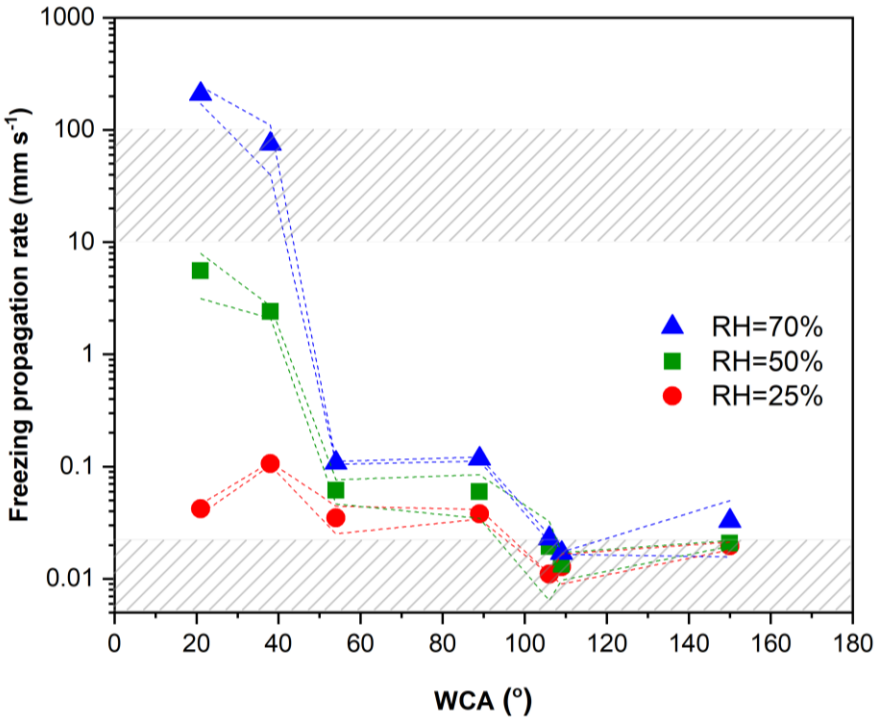

Figure 2.7. Freezing front propagation rates (mm s^{-1}) as a function of the static WCA measured at three RHs in the absence of a droplet. The error bars of the freezing front propagation rates are indicated by the dashed lines for each RH. The upper and bottom grey pattern blocks mark the range of propagation rates previously reported for intra-droplet freezing (10-100 mm s^{-1}) and percolation-induced frost growth (~0.01 mm s^{-1}), respectively.

In addition to the values of propagation rates, valuable information about the freezing propagation mechanisms can be obtained by visual examination of the thermal imaging videos. As seen in **Figures 2.3-2.4** and **Tables S2.1-S2.6**, the shape of the freezing front can vary dramatically from a smooth round line (e.g., sample A with WCA~21° at 70 % RH) to a complicated fractal border (e.g., sample C with WCA~54° at 25 % RH). When examining

simultaneously the propagation rates and the shape of the propagation front line, it appears that the smoothness of the freezing front is directly related to faster freezing front propagation rates. Droplet condensation density, on the other hand, did not have a measurable effect on the mode and kinetics of ice propagation. When analysing the freezing propagation fronts under all conditions (WCA and RH) four freezing front propagation modes can be identified. **Table 2.2** summarizes the characteristics of these propagation modes and the conditions at which they were observed. The specific freezing front propagation rates for all RHs and WCAs and their relation to the freezing propagation mode are shown in **Table 2.3.**

Table 2.2. Characteristics of the four freezing propagation modes observed via thermal imaging and the conditions at which they are observed.

Mode I (Movie S2.1)	**Mode II** (Movie S2.2)	**Mode III** (Movie S2.3)	**Mode IV** (Movie S2.4)
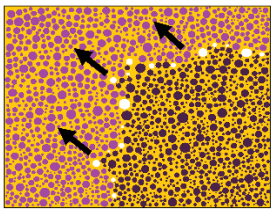	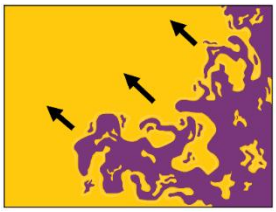	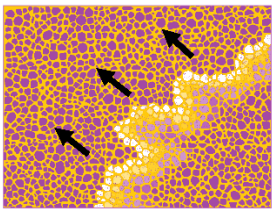	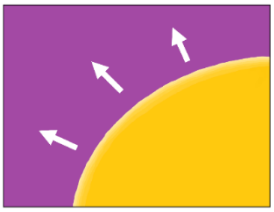
Freezing onset 1.2—34 min Propagation rates 0.01—0.1 mm s^{-1} Visible condensation; Ice-bridge formation.	Freezing onset 1.7—28 min Propagation rates 0.01—0.1 mm s^{-1} No visible condensation; Fractal-like front line.	Freezing onset 1.0—3.0 min Propagation rates 2—10 mm s^{-1} Visible condensation; Wavy fluctuating front.	Freezing onset 0.6—1.5 min Propagation rates 50—400 mm s^{-1} With or w/o condensation; Smooth front line.
All RHs WCA 54°—154°	RH 25 % WCA 21°—117°	RH 50 % WCA 21°—38°	RH 70 % WCA 21°—38°

Table 2.3. The table shows the quantified freezing propagation rates (mm s^{-1}) in relation to RH and surface WCA, and their relation to freezing propagation mode. Grey background marks propagation mode I, light blue mode II, medium blue mode III, and dark blue mode IV.

Relative Humidity (%) →

Static Water Contact Angle (°) ↓

	25 ±2	**50** ±2	**70** ±3
21 ±3	**0.052** ±0.004	**5.54** ±2.4	**208** ±36
38 ±6	**0.106** ±0.004	**2.40** ±0.3	**75.2** ±35
54 ±6	**0.035** ±0.010	**0.061** ±0.015	**0.108** ±0.003
89 ±6	**0.038** ±0.004	**0.060** ±0.025	**0.117** ±0.005
106 ±3	**0.011** ±0.0001	**0.019** ±0.013	**0.023** ±0.002
117 ±2	**0.013** ±0.004	**0.013** ±0.004	**0.017** ±0.0004
152 ±5	**0.020** ±0.002	**0.021** ±0.001	**0.033** ±0.017

As summarized in **Tables 2.2** and **2.3**, freezing propagation Mode I and Mode II show propagation rates in the same ballpark (0.01-0.1 mm s^{-1}). The lower limit of this range (0.01 mm s^{-1}) is well aligned with values previously reported for percolation-induced freezing, as shown in **Figure 2.7**. However, the upper limit (0.1 mm s^{-1}) observed in samples with both propagation modes is about one order of magnitude faster than percolation-induced freezing. This suggests the influence of another surface factor appearing at certain RH and surface hydrophilicity that homogeneously affects the surface without visibly detectable water condensation. As summarized in **Table 2.2**, mode II (low-speed fractal propagation) appears to be limited to low relative humidity (25 % RH) and smooth surfaces (independently of their hydrophilicity). The fractal-like propagation observed for mode II is well aligned with

previous studies at low humidity (RH ≤ 35 %) on hydrophobic PMMA and hydrophilic metallic substrates attributed to a visibly detectable deposition-limited frost growth.[49-50]

A detailed look at the thermal imaging video recordings (**Tables S2.2, S2.3**, **S2.5,** and **S2.6**) reveals the presence of small ice bridges in all the samples showing mode I propagation (e.g. see snapshots in **Figure 2.8**). The ice bridges' presence is in good agreement, together with the average propagation rates around 0.01-0.1 mm s^{-1}, with ice-bridge controlled frost propagation observed in samples freezing in the presence of condensation droplets.

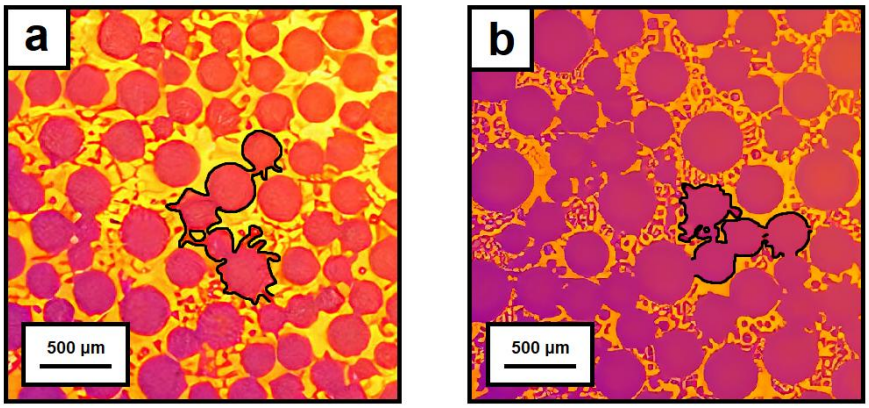

Figure 2.8. Time snapshot from a thermal imaging video showing the surface freezing of a) sample E (WCA=106°) at 50 % RH and b) sample D (WCA=90°) at 70 % RH with frozen condensation on top. The numerous connecting pathways between the frozen droplets (highlighted with a black line) are here identified as inter-droplet ice bridges.

The identification of these two propagation modes (mode I corresponding to ice-bridge-limited frost growth, and mode II corresponding to deposition-limited frost growth) at all RHs and most surface energies (WCAs) hints at a relation between the propagation mode and the presence of water at the surface. In line with this, higher amounts of water at the surface should lead to faster and more homogeneous propagation front lines as discussed hereon.

Frost propagation modes III and IV show significantly earlier freezing onset times (1-3 min) and faster propagation rates (2-400 mm s^{-1}) than modes I and II, and more continuous

propagation fronts instead of fractal lines. These two modes (III and IV) are observed only for the most hydrophilic samples (samples A and B with WCAs below 40°) at the highest RHs (50 % and 70 %). In general, a clear trend from a fractal frontline with a slow propagation rate to a continuous frontline with a fast propagation rate is observed when the RH and the hydrophilic nature of the surface increase. It is remarkable to note that the flash-like (see **Movie S2.4**) freezing propagation rates observed in mode IV for high RH and hydrophilic surfaces are one order of magnitude faster (up to 400 mm s^{-1}) than the reported values of bulk water freezing (50 mm s^{-1})[51] and several orders of magnitude slower than the speed of sound in water (1000 m s^{-1})[52]. The freezing propagation rate is similar to the speed of rapidly released vapor bolus (500 mm s^{-1}) observed during cascade freezing in reduced pressure (~3 mbar) reported in the literature.[53] In our work, the freezing experiments were conducted at normal atmospheric pressure, which would reduce the diffusion speed due to cascade freezing to a maximum of 3 mm s^{-1}. These factors and the observation of the freezing front in the presence of non-frozen individual water droplets from condensation (see **Tables S2.2** and **S2.5**) rule out freezing propagation dominated by regular water freezing of a thick continuous water film layer created by condensation as well as the acceleration of the freezing propagation by an acoustic wave traveling in water or a vapor bolus released during droplet freezing cascade. However, comparable freezing propagation rates (200-400 mm s^{-1}) have been reported for the intra-droplet freezing of impacting supercooled water droplets on surfaces.[47-48] Moreover, the experimental values obtained by us and those reported for supercooled droplets freezing are comparable and just one order of magnitude lower than those calculated with numerical simulations for freezing of supercooled water on ice (1000-10000 mm s^{-1} at RH 100 % and WCA~0°).[54]

Altogether, the above considerations suggest that freezing in modes III and IV took place through a supercooled water layer and pave the way to the relation between surface freezing and the presence of molecular water layers (MWL) whose thickness and continuity affect the freezing front propagation mode and rate. Even though we did not measure the thickness of the water layers for the samples showing mode III and IV propagation (i.e., hydrophilic surfaces, samples A and B, at high relative humidities (RH 50-70 %)), a MWL of around 1 nm

can be assumed based on previous experimental studies[19-26] reporting MWLs of more than 1 nm thick on hydrophilic silicon surfaces at RH 60 %. We hypothesize that, since the thickness decrease accelerates freezing propagation rates, propagation delays observed in mode III compared to conditions leading to mode IV cannot be explained by the lower thickness induced by lower RH but by discontinuities in the MWL causing a wavy fluctuating propagation front line, with overall propagation rate decrease, due to local differences in freezing propagation rates.

In line with the above, and as reported by others in the case of hydrophilic and hydrophobic chemically modified silicon wafers[20], there should be no liquid-like molecular water present on the sample surfaces in the case of modes I and II. However, there is one order of magnitude difference in the propagation kinetics of modes I and II (between 0.1 and 0.01 mm s^{-1}). Based on the literature, the highest propagation rates measured in conditions leading to propagation mode I and mode II (0.1 mm s^{-1}) can be explained by the presence of a solid-like MWL of around 0.5 nm, as identified for similar conditions in previous works.[19,20,22,23] According to reports on MWL, these thin solid-like MWLs are not smooth even layers, but rather non-continuous depositions of solid-like molecular water on the hydrophilic sites. Since the presence of liquid-like MWL is dramatically affecting the freezing propagation rates in modes III and IV, the presence of a more or less continuous solid-like MWL is arguably influencing the observed freezing propagation rates in modes I and II as well.

Figure 2.9 summarizes the proposed relation between the presence and state of molecular water layers (MWL) and the freezing mechanisms, onset times, and propagation rates observed in this work. At RH 25 %, both hydrophilic and hydrophobic surfaces exhibit deposition–controlled frost, although the presence of solid-like MWL on the hydrophilic samples promotes faster freezing propagation rates. Similarly, at RH 50 % and 70 %, all surfaces with WCA≥54° froze via percolation-limited frost propagation, while among them, the hydrophilic samples with solid-like molecular water showed ten times faster freezing propagation rates. On the two most hydrophilic samples (WCA≤38°) at RH 50 % and 70 %,

the freezing events propagate via a discontinuous or continuous layer of supercooled liquid-like water, respectively.

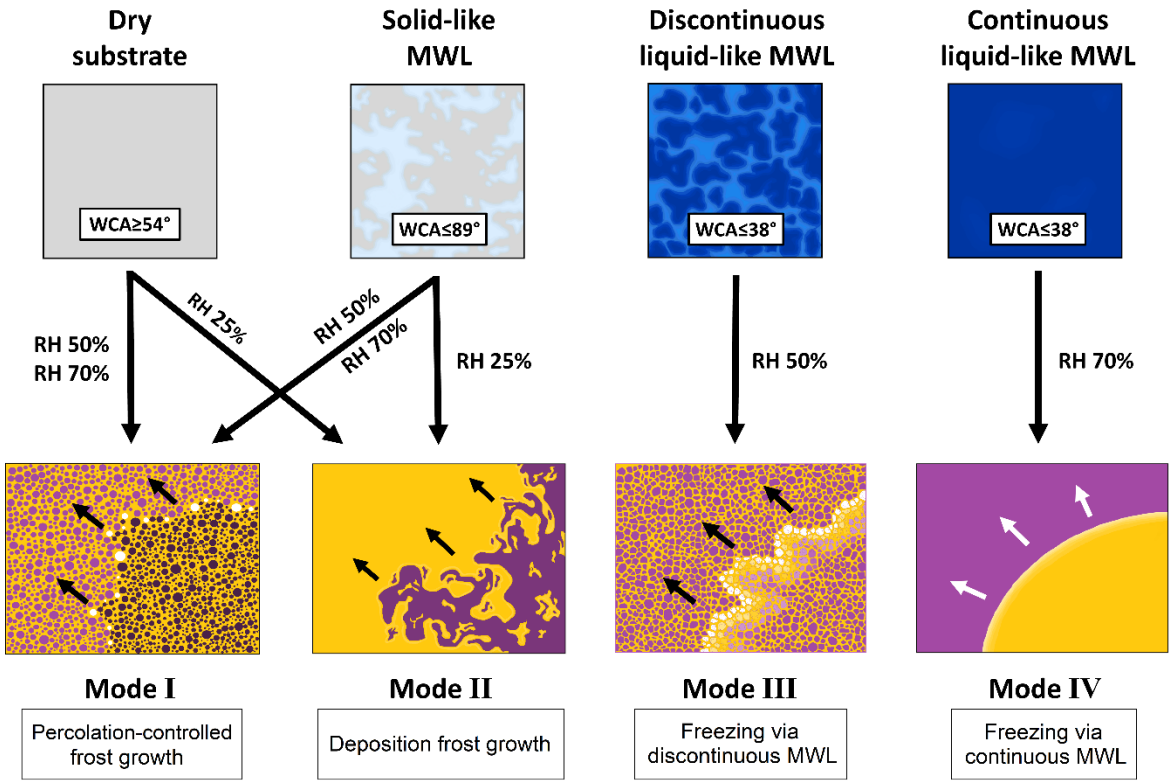

Figure 2.9. Overview of the relation between relative humidity, surface energy, and the resulting molecular water layer state and the freezing propagation mode.

CONCLUSIONS

In this work, the role of molecular water layer (MWL) on frost propagation rate and propagation front mode has been identified and studied using high-resolution thermal imaging. To do so, glass slides were functionalized to obtain a broad range of hydrophilic and hydrophobic surfaces. Exposure to selected relative humidities (RHs) and in-situ monitoring of freezing at –20 °C in the presence and absence of a pre-deposited water droplet were monitored using infrared imaging. The systematic results obtained, and previously reported literature, allow establishing for the first time a direct relation between MWL and freezing kinetics (ranging from 0.01 to 500 mm s^{-1}) and mode (from fractal to continuous front line). Depending on the MWL state, four frost propagation modes are described: ice-bridge percolation-controlled (in the presence of solid-like MWL), deposition-controlled (in the presence of solid-like continuous MWL), and continuous and discontinuous supercooled water layer-controlled freezing (in the presence of liquid-like MWL). The observations confirm freezing in porous superhydrophobic surfaces can occur due to the presence of surface MWLs even at low RHs. The results here reported bring new insights into surface freezing and establish guidelines for the development of novel ice-controlling passive strategies using surface energy local variations.

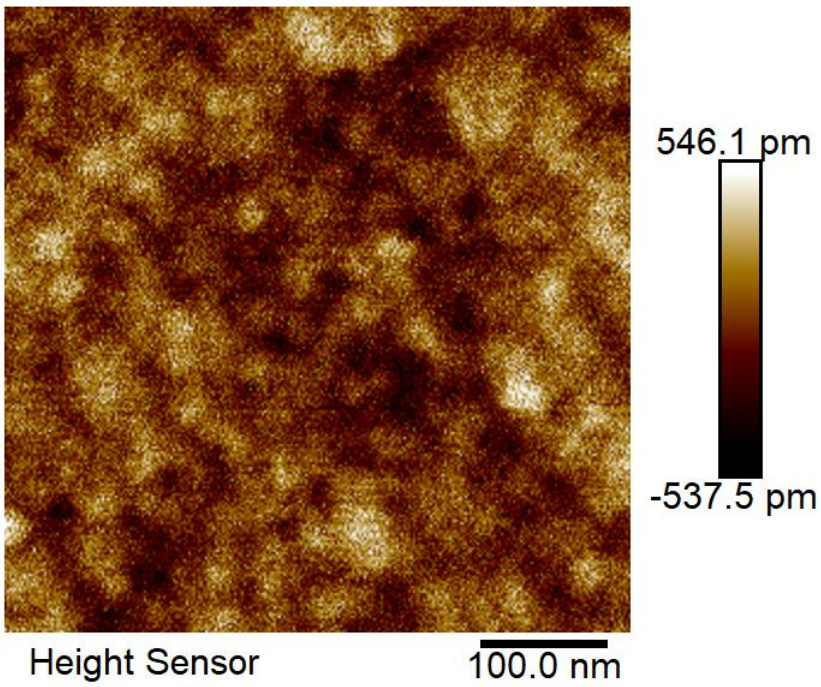

Figure S2.1. An AFM image of the glass slide functionalized with n-octyltrichlorosilane shows uniformity in the smooth silanized glass slides with an average roughness (R_a) of 0.125 nm.

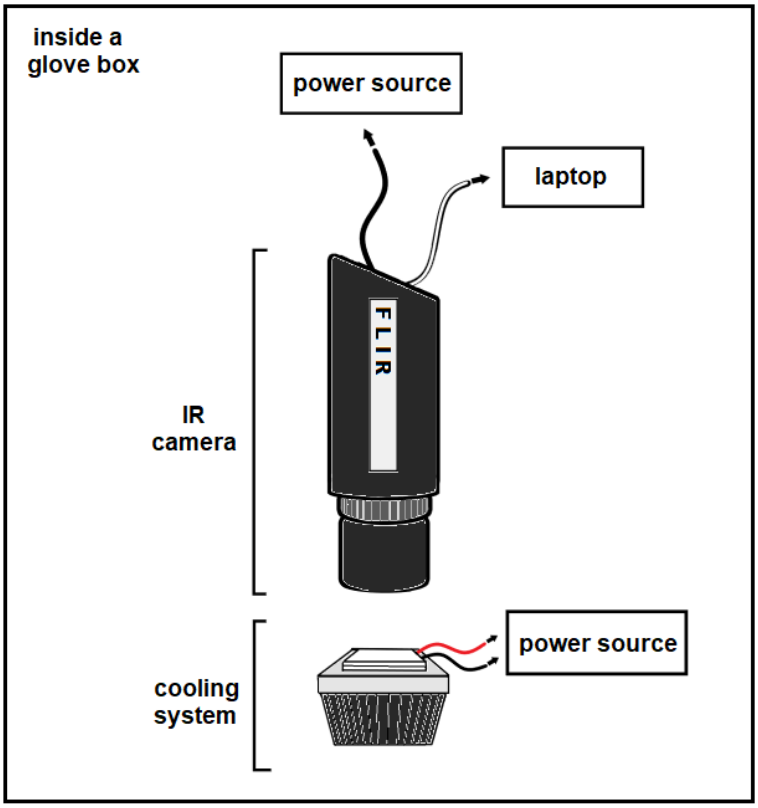

Figure S2.2. Schematic presentation of the experimental setup for monitoring freezing events on surfaces. Freezing events on the substrates were monitored using a FLIR A655sc thermal camera with a close-up lens (1.5 magnifying factor and 25 µm lateral resolution). The cooling system consists of two Peltier elements set in parallel (40x40 mm each) connected to a heat sink and a small fan for heat dissipation. The sample surfaces were placed on top of the two stacked Peltier plates.

Table S2.1. Time snapshots from thermal videos* showing a freezing front propagating on the different samples exposed to **25 %** RH.

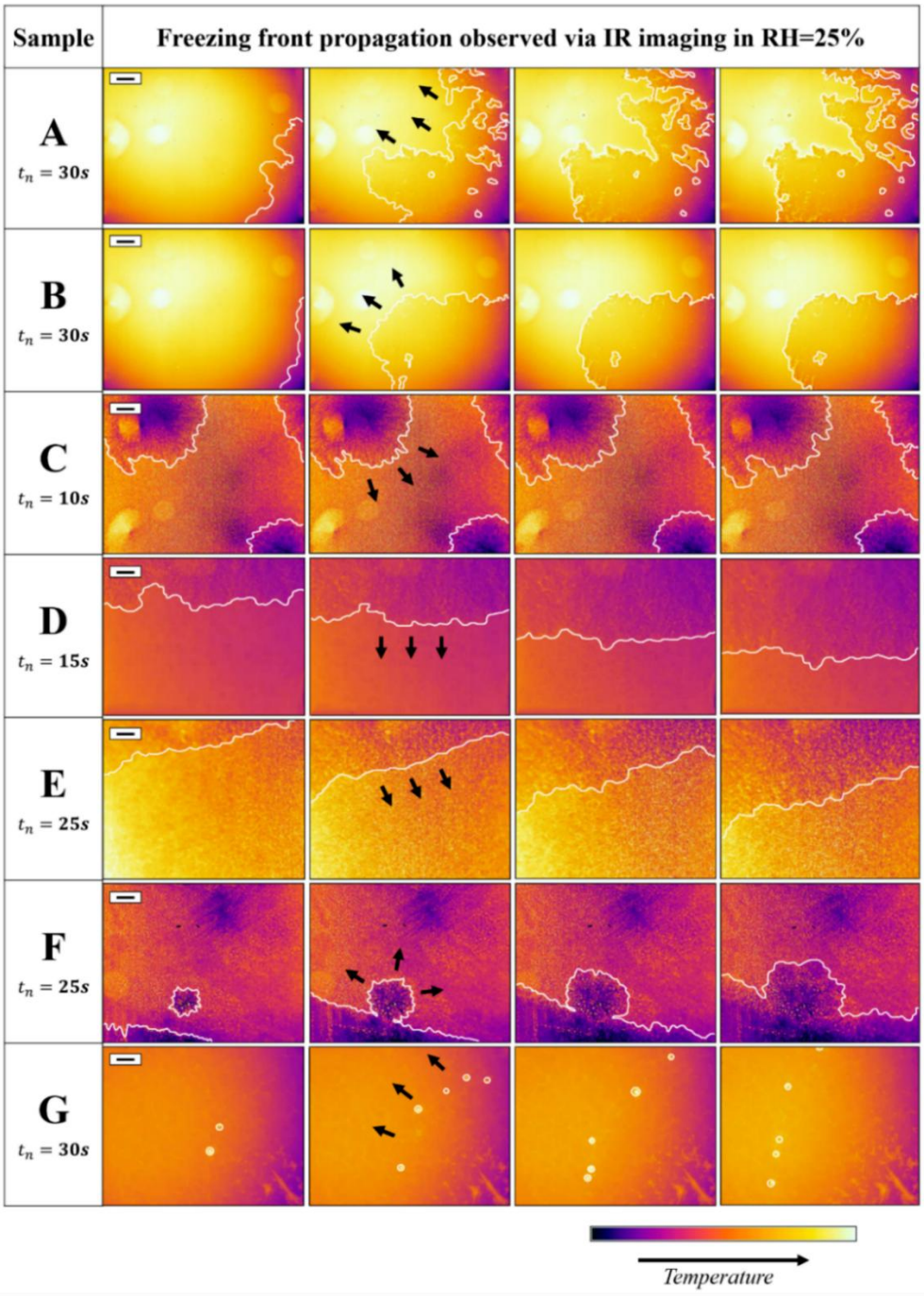

**The images are snapshots from the recorded thermal imaging videos. The cooling rate in these experiments was set so that the sample surface reaches -20 ℃ at 15 ℃ min^{-1}. The time step t_n between the frames is indicated separately for each sample due to variability in the frost propagation velocity. The front line of each freezing event is highlighted with a white line. Isolated freezing events are marked with white circles (sample G). The black arrows indicate the direction of the freezing front propagation. The black scale bar shown in the top corner of the first images is 1 mm. No set values were given to the temperature scale since it needed to be automatically adjusted for each video to better detect the freezing events (optimal contrast).*

Table S2.2. Time snapshots from thermal videos showing a freezing front propagating on the different samples exposed to 50 % RH.

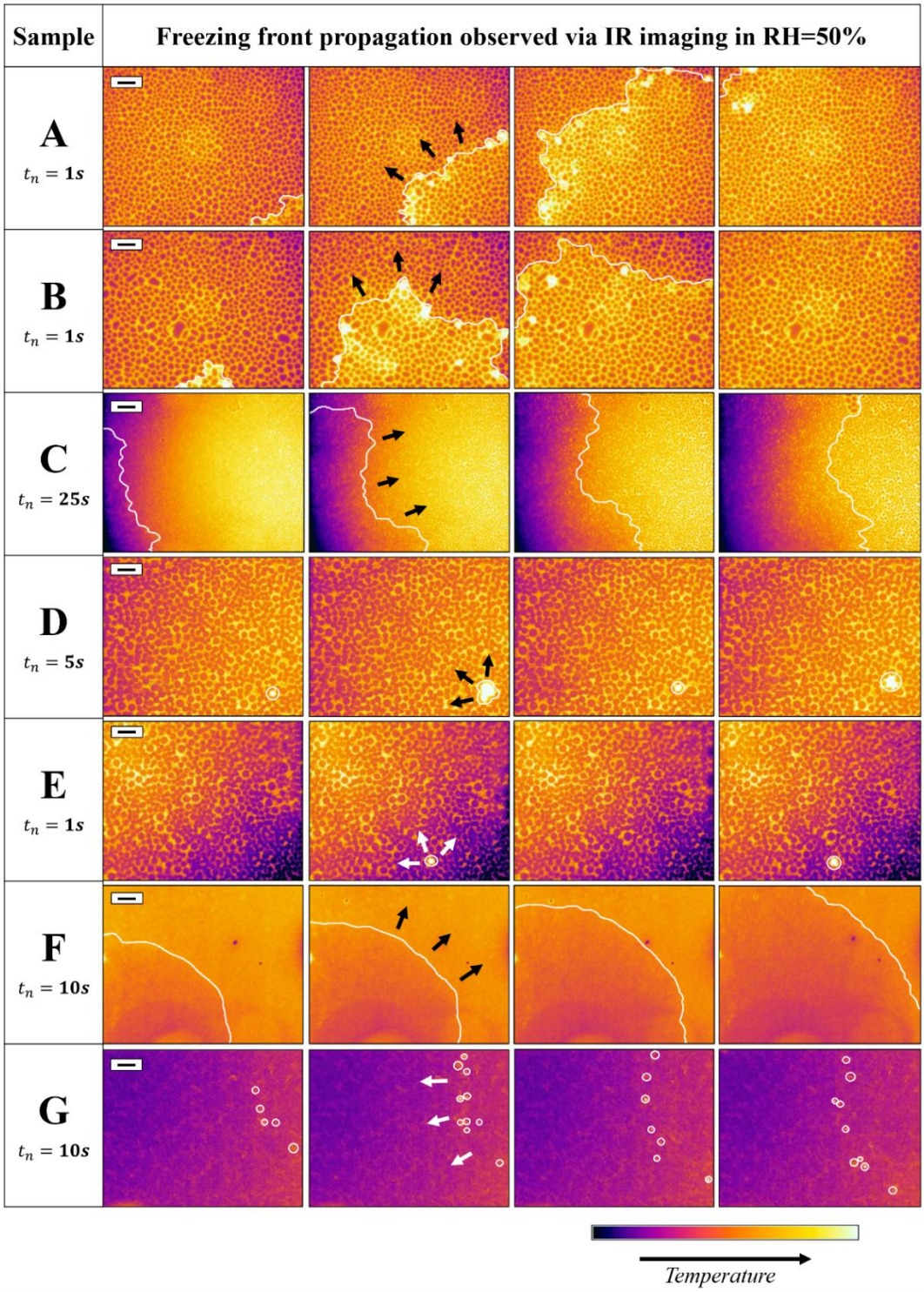

Table S2.3. Time snapshots from thermal videos showing a freezing front propagating on the different samples exposed to **70 %** RH.

Sample	Freezing front propagation observed via IR imaging in RH=70%
A $t_n = 20ms$	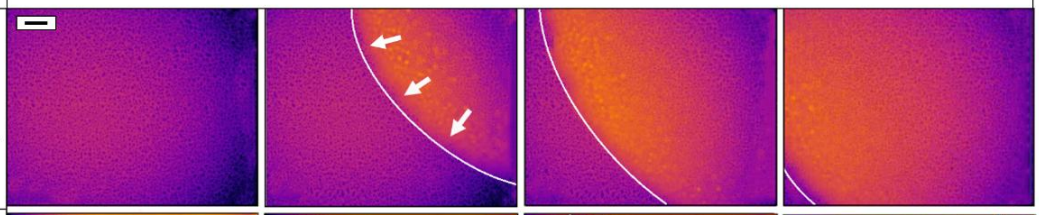
B $t_n = 40ms$	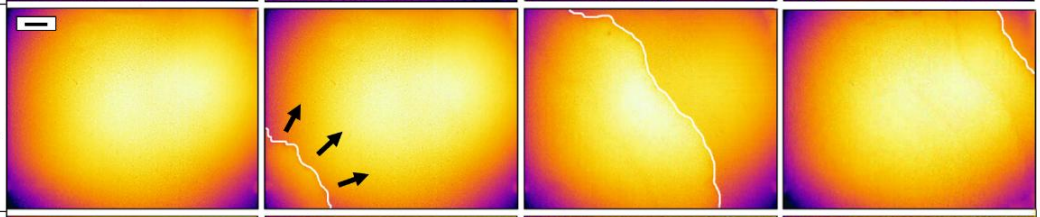
C $t_n = 30s$	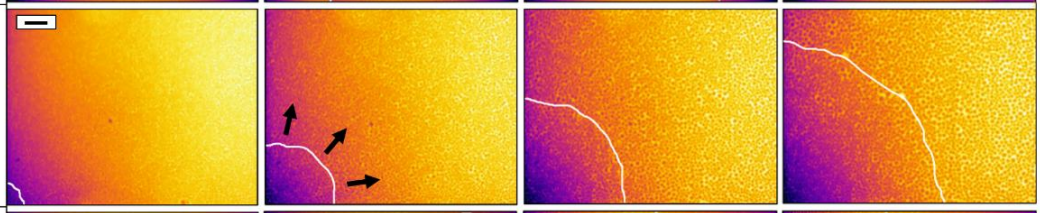
D $t_n = 20s$	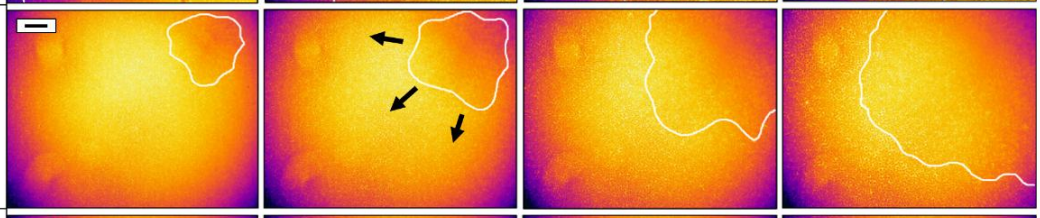
E $t_n = 25s$	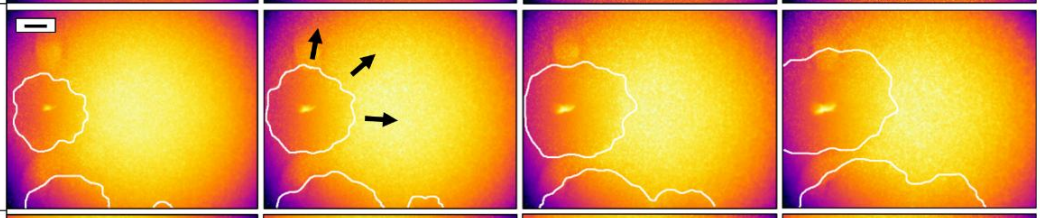
F $t_n = 40s$	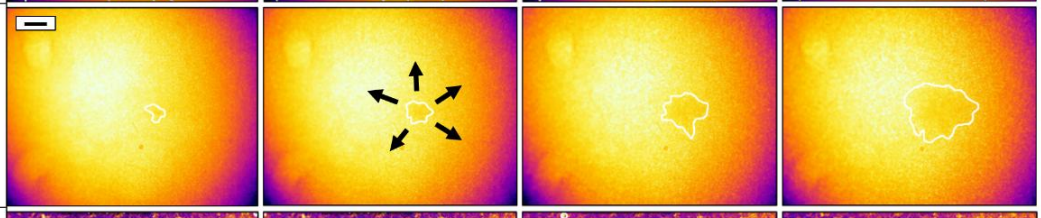
G $t_n = 15s$	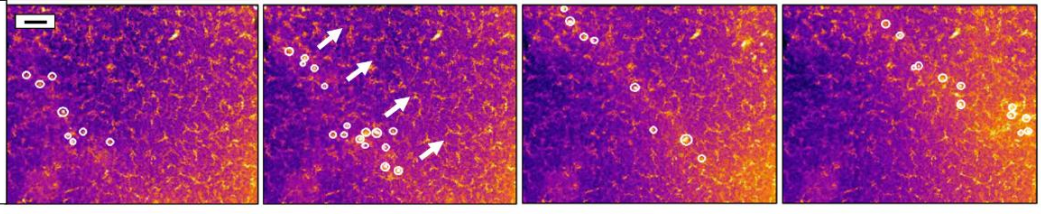

Table S2.4. Time snapshots from thermal videos* showing a freezing front propagating on the different samples exposed to **25 %** RH in the presence of a 5 μL water droplet

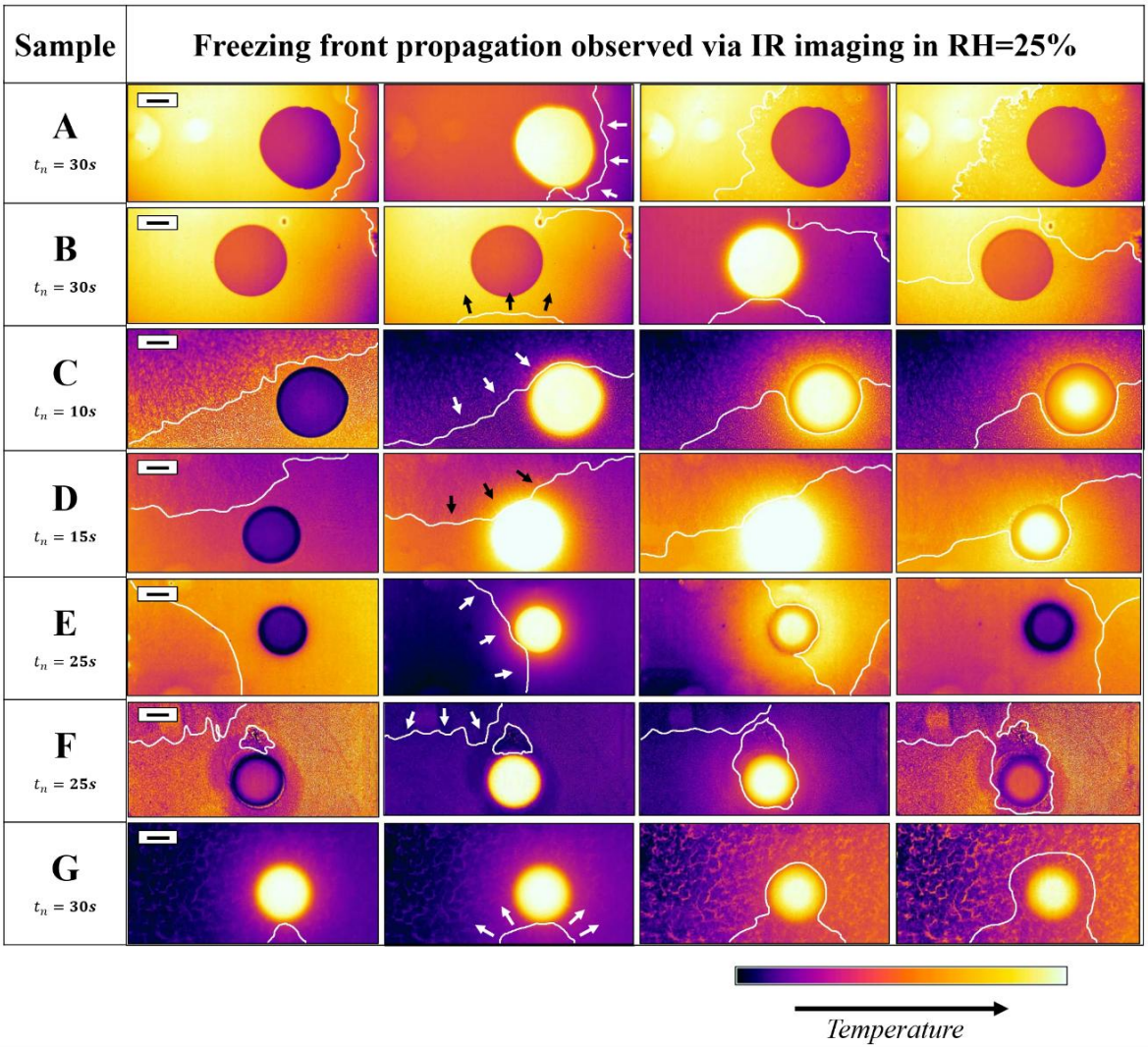

**The images were saved from a recorded thermal imaging video and the time step t_n between the frames is indicated separately for each sample due to variability in the frost propagation velocity. The cooling rate in these experiments was set so that the sample surface reaches -20 ℃ at 15 ℃ min^{-1}. The front line of each freezing event is highlighted with a white line, and the black arrows indicate the direction of the freezing front propagation. The black scale bar shown in the top corner of the first image is 1mm. The temperature scale was automatically adjusted for each video to gain better contrast.*

Table S2.5. Time snapshots from thermal videos showing a freezing front propagating on the different samples exposed to **50 %** RH in the presence of a 5 µL water droplet

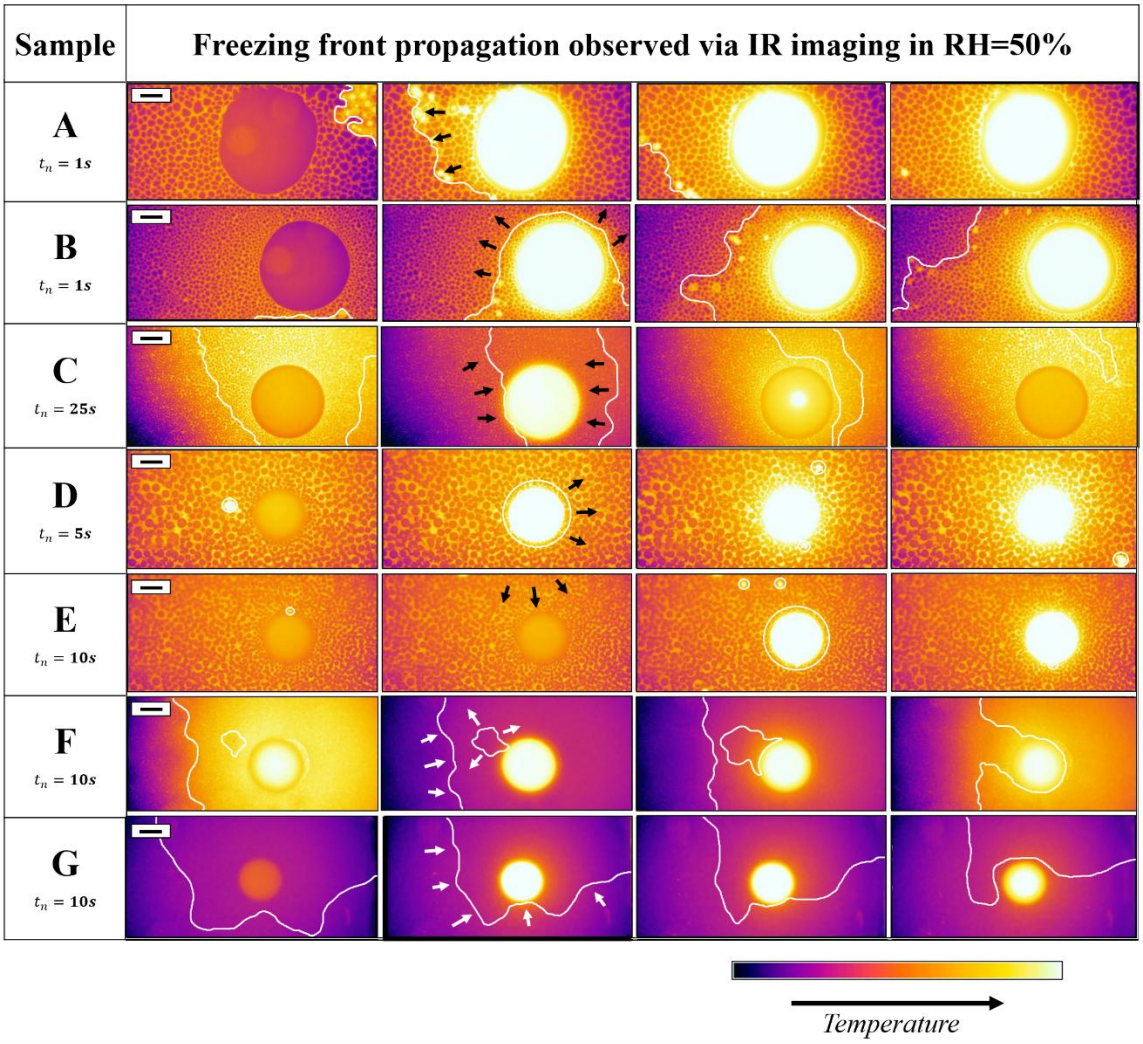

Table S2.6. Time snapshots from thermal videos showing a freezing front propagating on the different samples exposed to **70 %** RH in the presence of a 5 µL water droplet

Sample	Freezing front propagation observed via IR imaging in RH=70%
A $t_n = 20ms$	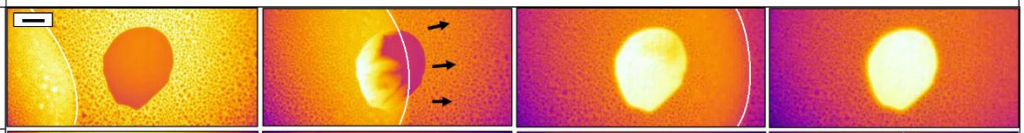
B $t_n = 40mss$	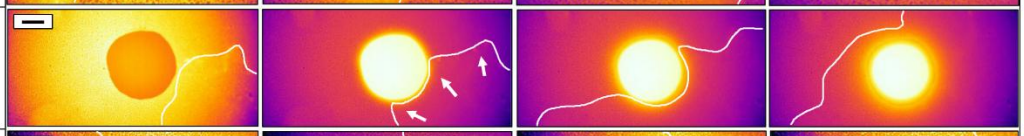
C $t_n = 30s$	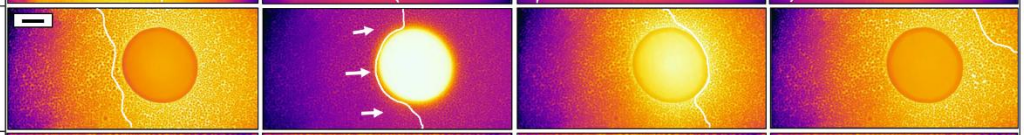
D $t_n = 20s$	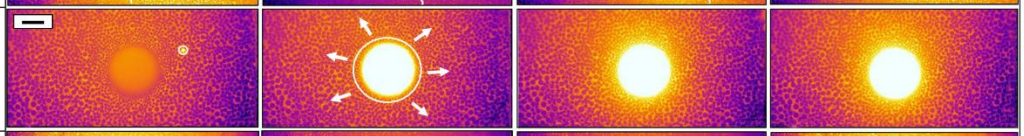
E $t_n = 25s$	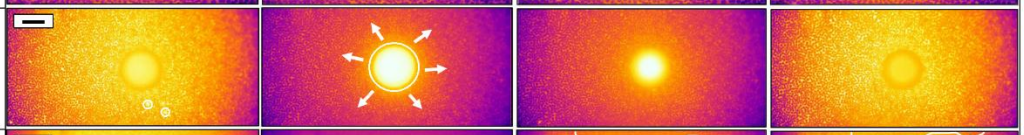
F $t_n = 40s$	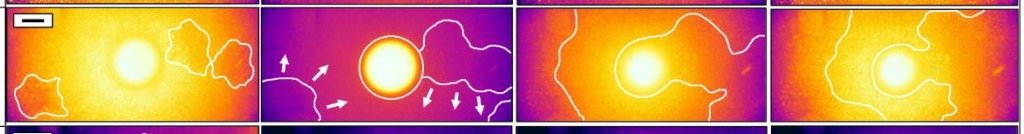
G $t_n = 15s$	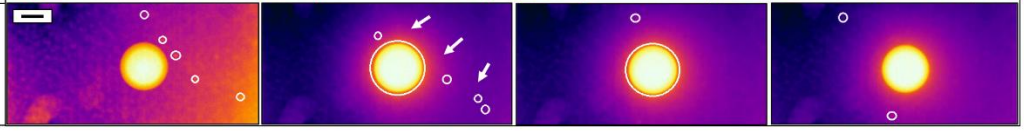

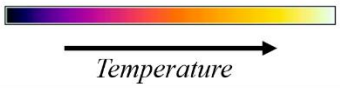

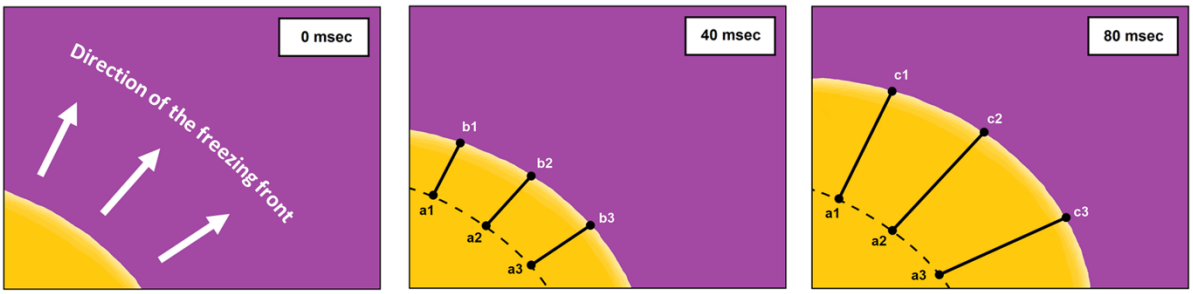

Figure S2.3. Calculation of the freezing front propagation rates (mm s^{-1}) from the thermal video snapshots using ImageJ. The distance that the freezing front propagates between two snapshots (distance between points a-b and a-c) is divided by the time difference between the two snapshots (40 msec and 80 msec). This method is repeated for the video for a series of snapshots and points along the freezing front line to obtain an average propagation rate.

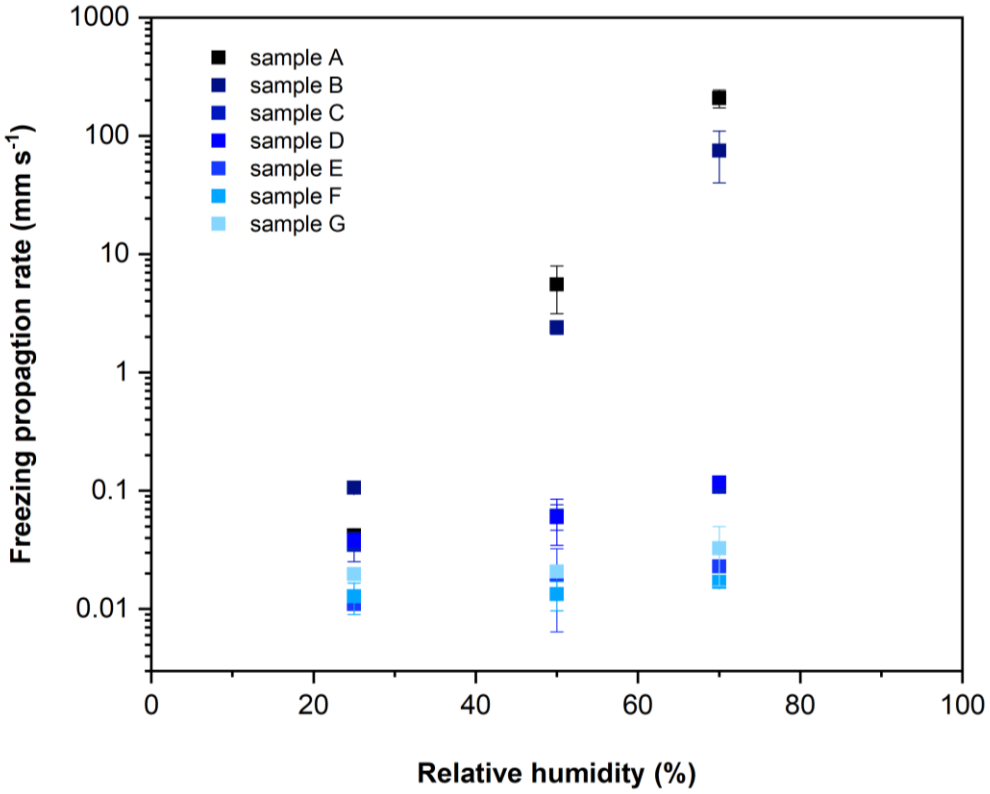

Figure S2.4. The measured freezing front propagation rates (mm s^{-1}) are plotted as a function of the environmental relative humidity. Note that the freezing front propagation rates are set on a logarithmic scale.

Equation to calculate SSD and nucleation pressure

The critical extent of supersaturation needed for nucleation to occur on a surface can be described with the supersaturation degree (SSD) as follows:

$$SSD = \frac{p_n - p_s}{p_s} \qquad (S2.1)$$

Where p_n is the critical supersaturation vapor pressure required for embryo formation on the surface and p_s is the saturation vapor pressure at a given temperature. The critical supersaturation vapor pressure can be calculated from the following equation:

$$p_n = p_s\, exp\left(\frac{v}{RT_s}\sqrt{\frac{4\pi}{3}\frac{\sigma^3}{kT_s\, ln\left(\frac{I_0}{I_c}\right)}(2 + cos\,(\theta))(1 - cos\,(\theta))^2}\right) \qquad (S2.2)$$

Where v is the molar volume of water ($1.8 \times 10^{-5}\, m^3/mol$), R is the gas constant in $J\,/\,mol \times K$, T_s is the temperature of the surface in K, σ is the surface energy in J/m^2, k is the is the Boltzmann constant in J/K, I_0 is the kinetic constant in $m^{-2} \times s^{-1}$, I_c is the critical embryo formation rate in $m^{-2} \times s^{-1}$, and θ is the water contact angle of the surface. Here we chose $I_0 \sim 10^{29}\, m^{-2} \times s^{-1}$ and $I_c \sim 10^{4}\, m^{-2} \times s^{-1}$.
The saturation water vapor pressure p_s in Pa and the surface energy σ in J/m^2 at a given temperature T in K are estimated using the Goff–Gratch equation and the surface tension of liquid water or ice respect to its vapor.

For condensation:

$$p_{sc} = 10^{-7.902\left(\frac{373.15}{T}-1\right)+5.028\,\lg\left(\frac{375.15}{T}\right)-1.382\times10^{-7}\left(10^{11.344\left(\frac{1-T}{373.15}\right)}-1\right)+8.1328\times10^{-3}\left(10^{-3{,}491\left(\frac{373.15}{T-1}\right)}-1\right)+\lg(1013.25)} \times 100 \qquad (S2.3)$$

$$\sigma_c = \left(75{,}7 - 0{,}1775(T - 273.15)\right) \times 10^{-3} \qquad (S2.4)$$

For desublimation:

$$p_{sd} = 10^{-9.097\left(\frac{273.15}{T}-1\right)+3.57\,lg\left(\frac{273.15}{T}\right)+0.877\left(1-\frac{T}{273.15}\right)+lg(6.1173)} \times 100 \qquad (S2.5)$$

$$\sigma_d = \left(99.5 - 0{,}075(T - 273.15)\right) \times 10^{-3} \qquad (S2.6)$$

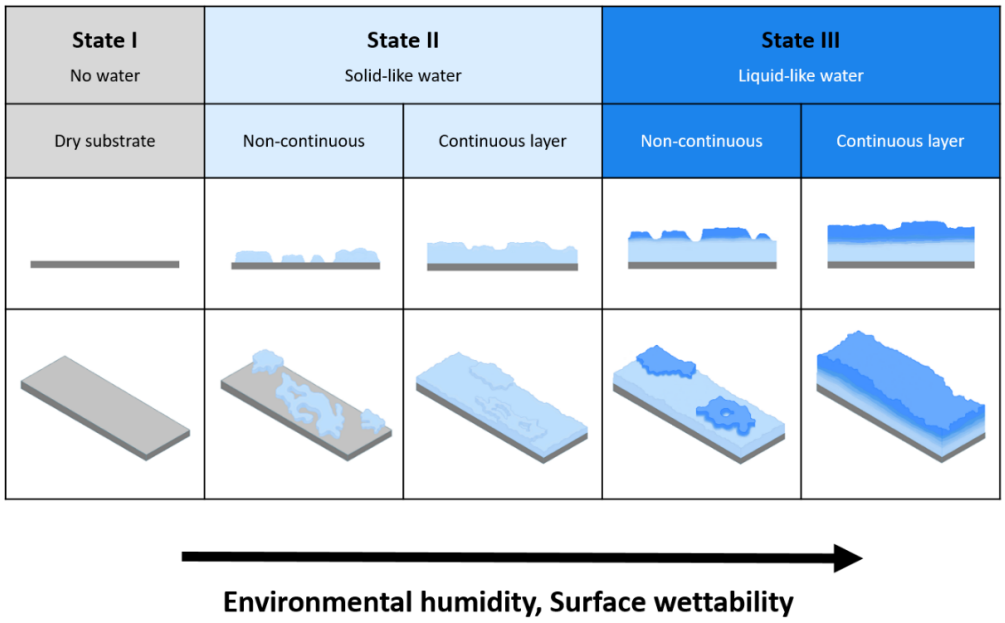

Figure S2.5. Illustrations of the three states of molecular water on the sample surfaces as proposed to the observed in previous research[19-24].

Movie S2.1. QR code to access a thermal video of percolation-controlled frost propagation (mode I) on sample G (superhydrophobic surface) in 70 % RH.

Movie S2.2. QR code to access a thermal video of deposition-driven frost propagation (mode II) on sample A (hydrophilic surface) in 25 % RH.

Movie S2.3. QR code to access a thermal video of MWL-promoted frost propagation (mode III) on sample A (hydrophilic surface) in 50 % RH.

Movie S2.4. QR code to access a thermal video of MWL-promoted frost propagation (mode IV) on sample A (hydrophilic sample) in 70 % RH.

REFERENCES

(1) Gent, R. W.; Dart, N. P.; Cansdale, J. T. Aircraft Icing. *Philosophical Transactions of the Royal Society of London. Series A: Mathematical, Physical and Engineering Sciences* **2000**, *358*, 2873–2911.

(2) Cao, Y.; Tan, W.; Wu, Z. Aircraft Icing: An Ongoing Threat to Aviation Safety. *Aerosp. Sci. Technol.* **2018**, *75*, 353–385. https://doi.org/https://doi.org/10.1016/j.ast.2017.12.028.

(3) Laforte, J. L.; Allaire, M. A.; Laflamme, J. State-of-the-Art on Power Line de-Icing. *Atmos. Res.* **1998**, *46* (1), 143–158. https://doi.org/https://doi.org/10.1016/S0169-8095(97)00057-4.

(4) Dehghani-Sanij, A. R.; Dehghani, S. R.; Naterer, G. F.; Muzychka, Y. S. Marine Icing Phenomena on Vessels and Offshore Structures: Prediction and Analysis. *Ocean Engineering* **2017**, *143*, 1–23. https://doi.org/https://doi.org/10.1016/j.oceaneng.2017.07.049.

(5) Yin, Z.; Yuan, F.; Zhou, D.; Xue, M.; Luo, Y.; Hong, Z.; Xie, C. Ultra Dynamic Water Repellency and Anti-Icing Performance of Superhydrophobic ZnO Surface on the Printed Circuit Board (PCB). *Chem. Phys. Lett.* **2021**, *771*, 138558. https://doi.org/https://doi.org/10.1016/j.cplett.2021.138558.

(6) Tarhan, C.; Çil, M. A. The Use of Wind Turbines and the Problem of Icing. *Wind Engineering* **2021**, *45*, 1680–1688.

(7) Wei, K.; Yang, Y.; Zuo, H.; Zhong, D. A Review on Ice Detection Technology and Ice Elimination Technology for Wind Turbine. *Wind Energy*. John Wiley and Sons Ltd March 1, 2020, pp 433–457. https://doi.org/10.1002/we.2427.

(8) Parent, O.; Ilinca, A. Anti-Icing and de-Icing Techniques for Wind Turbines: Critical Review. *Cold Reg. Sci. Technol.* **2011**, *65* (1), 88–96. https://doi.org/10.1016/j.coldregions.2010.01.005.

(9) Lin, Y.; Chen, H.; Wang, G.; Liu, A. Recent Progress in Preparation and Anti-Icing Applications of Superhydrophobic Coatings. *Coatings* **2018**, *8*, 208. https://doi.org/10.3390/coatings8060208.

(10) Wang, Y.; Xu, Y.; Su, F. Damage Accumulation Model of Ice Detach Behavior in Ultrasonic De-Icing Technology. *Renew. Energy* **2020**, *153*, 1396–1405. https://doi.org/10.1016/j.renene.2020.02.069.

(11) Shi, Z.; Zhao, Y.; Ma, C.; Zhang, J. Parametric Study of Ultrasonic De-Icing Method on a Plate with Coating. *Coatings* **2020**, *10* (7). https://doi.org/10.3390/coatings10070631.

(12) Freeman, A. I.; Surridge, B. W. J.; Matthews, M.; Stewart, M.; Haygarth, P. M. Understanding and Managing De-Icer Contamination of Airport Surface Waters: A Synthesis and Future Perspectives. *Environ. Technol. Innov.* **2015**, *3*, 46–62. https://doi.org/https://doi.org/10.1016/j.eti.2015.01.001.

(13) Shen, Y.; Wu, X.; Tao, J.; Zhu, C.; Lai, Y.; Chen, Z. Icephobic Materials: Fundamentals, Performance Evaluation, and Applications. *Progress in Materials Science*. Elsevier Ltd June 1, 2019, pp 509–557. https://doi.org/10.1016/j.pmatsci.2019.03.004.

(14) Brassard, J. D.; Laforte, C.; Guerin, F.; Blackburn, C. Icephobicity: Definition and Measurement Regarding Atmospheric Icing. In *Advances in Polymer Science*; Springer, 2019; Vol. 284, pp 123–143. https://doi.org/10.1007/12_2017_36.

(15) Strobl, T.; Storm, S.; Thompson, D.; Hornung, M.; Thielecke, F. Feasibility Study of a Hybrid Ice Protection System. *J. Aircr.* **2015**, *52* (6), 2064–2076. https://doi.org/10.2514/1.C033161.

(16) Fortin, G.; Adomou, M.; Perron, J. Experimental Study of Hybrid Anti-Icing Systems Combining Thermoelectric and Hydrophobic Coatings. In *SAE Technical Papers*; SAE International, 2011. https://doi.org/10.4271/2011-38-0003.

(17) Huang, X.; Tepylo, N.; Pommier-Budinger, V.; Budinger, M.; Bonaccurso, E.; Villedieu, P.; Bennani, L. A Survey of Icephobic Coatings and Their Potential Use in a Hybrid Coating/Active Ice Protection System for Aerospace Applications. *Progress in Aerospace Sciences* **2019**, *105*, 74–97. https://doi.org/https://doi.org/10.1016/j.paerosci.2019.01.002.

(18) Jamil, M. I.; Ali, A.; Haq, F.; Zhang, Q.; Zhan, X.; Chen, F. Icephobic Strategies and Materials with Superwettability: Design Principles and Mechanism. *Langmuir* **2018**, *34* (50), 15425–15444. https://doi.org/10.1021/acs.langmuir.8b03276.

(19) Hu, J.; Xiao, X.-D.; Ogletree, D. F.; Salmeron, M. Imaging the Condensation and Evaporation of Molecularly Thin Films of Water with Nanometer Resolution. *Science (1979).* **1995**, *268* (5208), 267. https://doi.org/10.1126/science.268.5208.267.

(20) James, M.; Darwish, T. A.; Ciampi, S.; Sylvester, S. O.; Zhang, Z.; Ng, A.; Gooding, J. J.; Hanley, T. L. Nanoscale Condensation of Water on Self-Assembled Monolayers. *Soft Matter* **2011**, *7* (11), 5309–5318. https://doi.org/10.1039/c1sm05096f.

(21) Shimizu, T. K.; Maier, S.; Verdaguer, A.; Velasco-Velez, J.-J.; Salmeron, M. Water at Surfaces and Interfaces: From Molecules to Ice and Bulk Liquid. *Prog. Surf. Sci.* **2018**, *93* (4), 87–107. https://doi.org/https://doi.org/10.1016/j.progsurf.2018.09.004.

(22) Spagnoli, C.; Loos, K.; Ulman, A.; Cowman, M. K. Imaging Structured Water and Bound Polysaccharide on Mica Surface at Ambient Temperature. *J. Am. Chem. Soc.* **2003**, *125* (23), 7124–7128. https://doi.org/10.1021/ja029721j.

(23) Sumner, A. L.; Menke, E. J.; Dubowski, Y.; Newberg, J. T.; Penner, R. M.; Hemminger, J. C.; Wingen, L. M.; Brauers, T.; Finlayson-Pitts, B. J. The Nature of Water on Surfaces of Laboratory Systems and Implications for Heterogeneous Chemistry in the Troposphere. *Physical Chemistry Chemical Physics* **2004**, *6* (3), 604–613. https://doi.org/10.1039/B308125G.

(24) Asay, D. B.; Kim, S. H. Evolution of the Adsorbed Water Layer Structure on Silicon Oxide at Room Temperature. *Journal of Physical Chemistry B* **2005**, *109* (35), 16760–16763. https://doi.org/10.1021/jp053042o.

(25) Bluhm, H.; Inoue, T.; Salmeron, M. Formation of Dipole-Oriented Water Films on Mica Substrates at Ambient Conditions. *Surf. Sci.* **2000**, *462* (1–3), L599–L602. https://doi.org/10.1016/S0039-6028(00)00595-1.

(26) Miranda, P. B.; Xu, L.; Shen, Y. R.; Salmeron, M. Icelike Water Monolayer Adsorbed on Mica at Room Temperature. *Phys. Rev. Lett.* **1998**, *81* (26), 5876–5879. https://doi.org/10.1103/PhysRevLett.81.5876.

(27) Dong, J.; Wang, A.; Ng, K. Y. S.; Mao, G. Self-Assembly of Octadecyltrichlorosilane Monolayers on Silicon-Based Substrates by Chemical Vapor Deposition. *Thin Solid Films* **2006**, *515* (4), 2116–2122. https://doi.org/10.1016/j.tsf.2006.07.041.

(28) O'Brien, F. E. M. The Control of Humidity by Saturated Salt Solutions. *J. Sci. Instrum.* **1948**, *25* (3), 73–76. https://doi.org/10.1088/0950-7671/25/3/305.

(29) Young, J. Humidity Control in the Laboratory Using Salt Solutions—A Review. *Journal of Applied Chemistry* **1967**, *17*, 241–245. https://doi.org/10.1002/jctb.5010170901.

(30) Han, Y.; Mayer, D.; Offenhäusser, A.; Ingebrandt, S. Surface Activation of Thin Silicon Oxides by Wet Cleaning and Silanization. *Thin Solid Films* **2006**, *510* (1), 175–180. https://doi.org/https://doi.org/10.1016/j.tsf.2005.11.048.

(31) Erbil, H. Y. Practical Applications of Superhydrophobic Materials and Coatings: Problems and Perspectives. *Langmuir* **2020**, *36* (10), 2493–2509. https://doi.org/10.1021/acs.langmuir.9b03908.

(32) Nath, S.; Boreyko, J. B. On Localized Vapor Pressure Gradients Governing Condensation and Frost Phenomena. *Langmuir* **2016**, *32* (33), 8350–8365. https://doi.org/10.1021/acs.langmuir.6b01488.

(33) Boreyko, J. B.; Hansen, R. R.; Murphy, K. R.; Nath, S.; Retterer, S. T.; Collier, C. P. Controlling Condensation and Frost Growth with Chemical Micropatterns. *Sci. Rep.* **2016**, *6*. https://doi.org/10.1038/srep19131.

(34) Guadarrama-Cetina, J.; Mongruel, A.; González-Viñas, W.; Beysens, D. Percolation-Induced Frost Formation. *EPL* **2013**, *101* (1). https://doi.org/10.1209/0295-5075/101/16009.

(35) Nath, S.; Ahmadi, S. F.; Boreyko, J. B. How Ice Bridges the Gap. *Soft Matter* **2020**, *16* (5), 1156–1161. https://doi.org/10.1039/C9SM01968E.

(36) Paulovics, D.; Raufaste, C.; Frisch, T.; Claudet, C.; Celestini, F. Dynamics of Frost Propagation on Breath Figures. *Langmuir* **2022**, *38* (9), 2972–2978. https://doi.org/10.1021/acs.langmuir.1c03463.

(37) Zhao, Y.; Yang, C. Frost Spreading on Microscale Wettability/Morphology Patterned Surfaces. *Appl. Therm. Eng.* **2017**, *121*, 136–145. https://doi.org/https://doi.org/10.1016/j.applthermaleng.2017.04.063.

(38) Zhao, Y.; Wang, R.; Yang, C. Interdroplet Freezing Wave Propagation of Condensation Frosting on Micropillar Patterned Superhydrophobic Surfaces of Varying Pitches. *Int. J. Heat Mass Transf.* **2017**, *108*, 1048–1056. https://doi.org/10.1016/j.ijheatmasstransfer.2016.12.112.

(39) Zhao, Y.; Yang, C. Retarded Condensate Freezing Propagation on Superhydrophobic Surfaces Patterned with Micropillars. *Appl. Phys. Lett.* **2016**, *108* (6), 061605. https://doi.org/10.1063/1.4941927.

(40) Haque, M. R.; Das, S. R.; Betz, A. R. Experimental Investigation of Condensation and Freezing Phenomena on Hydrophilic and Hydrophobic Graphene Coating. *Appl. Therm. Eng.* **2019**, *160*, 113987. https://doi.org/10.1016/j.applthermaleng.2019.113987.

(41) Hauer, L.; Wong, W. S. Y.; Donadei, V.; Hegner, K. I.; Kondic, L.; Vollmer, D. How Frost Forms and Grows on Lubricated Micro- and Nanostructured Surfaces. *ACS Nano* **2021**, *15* (3), 4658–4668. https://doi.org/10.1021/acsnano.0c09152.

(42) Shen, Y.; Zou, H.; Wang, S. Condensation Frosting on Micropillar Surfaces - Effect of Microscale Roughness on Ice Propagation. *Langmuir* **2020**.

(43) Chavan, S.; Park, D.; Singla, N.; Sokalski, P.; Boyina, K.; Miljkovic, N. Effect of Latent Heat Released by Freezing Droplets during Frost Wave Propagation. *Langmuir* **2018**, *34* (22), 6636–6644. https://doi.org/10.1021/acs.langmuir.8b00916.

(44) Yang, S.; Wu, C.; Zhao, G.; Sun, J.; Yao, X.; Ma, X.; Wang, Z. Condensation Frosting and Passive Anti-Frosting. *Cell Rep. Phys. Sci.* **2021**, *2* (7). https://doi.org/10.1016/j.xcrp.2021.100474.

(45) Castillo, J. E.; Huang, Y.; Pan, Z.; Weibel, J. A. Quantifying the Pathways of Latent Heat Dissipation during Droplet Freezing on Cooled Substrates. *Int. J. Heat Mass Transf.* **2021**, *164*, 120608. https://doi.org/https://doi.org/10.1016/j.ijheatmasstransfer.2020.120608.

(46) Meng, Z.; Zhang, P. Dynamic Propagation of Ice-Water Phase Front in a Supercooled Water Droplet. *Int. J. Heat Mass Transf.* **2020**, *152*. https://doi.org/10.1016/j.ijheatmasstransfer.2020.119468.

(47) Schremb, M.; Roisman, I.; Tropea, C. Different Outcomes after Inclined Impacts of Water Drops on a Cooled Surface; 2015.

(48) Schremb, M.; Roisman, I. V; Tropea, C. Normal Impact of Supercooled Water Drops onto a Smooth Ice Surface: Experiments and Modelling. *J. Fluid Mech.* **2018**, *835*, 1087–1107. https://doi.org/DOI: 10.1017/jfm.2017.797.

(49) Jeong, H.; Byun, S.; Kim, D. R.; Lee, K. S. Frost Growth Mechanism and Its Behavior under Ultra-Low Temperature Conditions. *Int. J. Heat Mass Transf.* **2021**, *169*, 120941. https://doi.org/10.1016/j.ijheatmasstransfer.2021.120941.

(50) Jung, S.; Tiwari, M. K.; Poulikakos, D. Frost Halos from Supercooled Water Droplets. *Proceedings of the National Academy of Sciences* **2012**, *109* (40), 16073. https://doi.org/10.1073/pnas.1206121109.

(51) Pasieka, J.; Nanua, R.; Coulombe, S.; Servio, P. The Crystallization of Sub-Cooled Water: Measuring the Front Velocity and Mushy Zone Composition via Thermal Imaging. *Int. J. Heat Mass Transf.* **2014**, *77*, 940–945. https://doi.org/https://doi.org/10.1016/j.ijheatmasstransfer.2014.06.009.

(52) Attenborough, K. Chapter 3. Fundamentals of Acoustics in Liquids. *Studies in Interface Science* **2002**, *15* (C), 75–99. https://doi.org/10.1016/S1383-7303(02)80014-X.

(53) Graeber, G.; Dolder, V.; Schutzius, T. M.; Poulikakos, D. Cascade Freezing of Supercooled Water Droplet Collectives. *ACS Nano* **2018**, *12* (11), 11274–11281. https://doi.org/10.1021/acsnano.8b05921.

(54) Wang, T.; Chen, M. Determining Interface Temperature During Rapid Freezing of Supercooled Water. *J. Aircr.* **2017**, *55* (3), 1269–1275. https://doi.org/10.2514/1.C034572.

3

Controlling Frost Propagation on Polymeric Surfaces Using SI-ATRP Chemical Micropatterning

Abstract: Micro-patterned surfaces with both hydrophilic and hydrophobic regions are relevant for a wide range of applications from fuel cells to water harvesting systems. The preferential nucleation of water on hydrophilic regions can also be used to control frost nucleation on chemically patterned surfaces. So far, this concept has been tested on brittle silicon surfaces with only a few different sizes and shapes of hydrophilic regions. In this work, the concept of controlled icing is investigated on five polymeric surfaces with different surface energies modified by micro-patterning them with three types of hydrophilic polymer brushes. Frost formation and propagation on the resulting patterned surfaces with regions of varying wettability was monitored and quantified using high-resolution thermal imaging. The study proves that control over frost nucleation and propagation using regions of varying wettability can be achieved on commodity polymers (PC, PP, PMMA, PVC, PU). In addition to influencing the time and location of ice nucleation, the local patterning affects the freezing propagation mode and rate due to its impact on the continuity and thickness of molecular water layers (MWL). These results show that local control over the state of MWLs is key to controlling both ice nucleation and propagation of freezing events on surfaces.

INTRODUCTION

To combat ice accretion on surfaces, two strategies have received most of the attention: (i) the development of active de-icing systems and (ii) the fabrication of passive low ice-adhesion surfaces.[1-3] Unfortunately, these strategies have intrinsic disadvantages and are often combined to be able to reach good performance in real-life applications.[4-5] A less explored alternative is to influence ice nucleation and growth.[6-7] In this strategy, instead of removing already accreted ice from surfaces, surfaces could be fabricated to direct ice growth towards the formation of brittle ice structures that can be continuously removed by environmental factors such as wind, of relevance in applications as wind turbines, electric cables, and airplanes.

The first step towards controlling ice formation is to gain a better understanding of the early freezing mechanisms at surfaces and to investigate them at a molecular level. In this regard, it is important to consider the role of adsorbed interfacial water in the initial nucleation events. The presence of submicron molecular water layers (MWL) has been reported on all dry surfaces as long as there is some humidity in the environment. However, its state varies in continuity and thickness depending on the surface wettability and environmental conditions.[8-17] In general, the MWL thickness and continuity increase with higher hydrophilicity of the surface (lower water contact angle) and higher environmental humidity.

In Chapter 2, we connected the presence and state of MWL to various freezing events observed on smooth functionalized glass surfaces via high-resolution thermal imaging.[17] The presence of solid-like MWL was found to promote the speed of inter-droplet ice bridging and deposition frost growth, whereas, very hydrophilic surfaces at high humidity showed rapid freezing propagation via a continuous liquid-like MWL. Since MWLs clearly affect the type and rate of freezing propagation on surfaces[17], spatial control over the state and thickness of MWLs may also lead to localized control over freezing mechanisms on surfaces with both hydrophilic and hydrophobic regions.

Even though surfaces with wettability patterns, also known as contrast wettability surfaces, have been a popular topic among researchers working on water-harvesting applications[18-23]

and microfluidics[24-27], there are very few studies investigating their effect on freezing[28-33]. In one of the first reports, the spatial control of water condensation and freezing was observed using fluorinated Si micropillars with hydrophilic PVA tips.[28] When the samples were cooled to -15 ℃ the water droplets froze one by one via ice-bridge formation on the hydrophilic tips of the pillars. Similar freezing propagation based on ice-bridging was also reported on smooth fluorinated Si surfaces with hydrophilic silicon oxide micropatterning.[30] A follow-up study using the same smooth patterned Si surfaces found that introducing ice-nucleating proteins on top of the hydrophilic silicon oxide micropatterns results in the formation of dry zones around frozen hydrophilic regions.[31] The same effect has also been observed on gold substrates patterned with hydrophilic polyelectrolyte brushes in low supersaturation freezing conditions (S<1.5).[32] This phenomenon has been explained by the formation of a humidity sink as described already in 1981 during the investigation of water condensation around salt crystals.[34] Once the hydrophilic areas freeze in low supersaturation conditions, the frozen regions act as humidity sinks and prevent nucleation events on the hydrophobic surrounding areas.[34-39] This is a result of the saturation vapor pressure over ice being slightly lower than over liquid water.[35]

So far, preferential freezing onset and frost growth on patterned wettability surfaces have been successfully presented either on brittle silicon surfaces and/or in low supersaturation environments with reduced nucleation density of condensation.[30-33,35] However, there is no information on how this phenomenon would occur on mechanically robust polymeric coatings, as opposed to the idealized model surfaces commonly studied in the literature, particularly when environmental conditions fluctuate between high and low supersaturation. There is also a lack of systematic studies on the role of chemistry of the pattern, the size, shape, or distribution of the hydrophilic regions, and how changes in these parameters influence the type of frost or ice accretion on the surfaces.

To address the aspects above, in this work, we create polymeric surfaces with patterned wettability by modifying various hydrophobic polymeric substrates with three different hydrophilic polymer brushes. The effect of the substrate (local) wettability and the pattern

chemistry on the freezing onset and propagation is investigated in a high supersaturation environment (S>6.5) using a digital microscope and high-resolution thermal imaging.

EXPERIMENTAL SECTION

Reagents and Materials

PC, PP, PMMA, PU, and PVC were used as substrates in this work. PU substrates were prepared as described elsewhere.[40] All other polymer substrates (PC, PP, PMMA, and PVC) used in this work were purchased from S-Polytec GmbH. Glycidyl methacrylate (GMA, 97%), 2-hydroxyethyl methacrylate (HEMA, 97%), 2-(dimethylamino)ethyl methacrylate (DMAEMA, 98%), 4-cyano-4-(phenylcarbonothioylthio)pentanoic acid (CTA), 2,2'-azobis(isobutyronitrile) (AIBN, 98%), sodium azide (NaN_3, 99.5%), triethylamine (TEA, 99.7%), copper(I)bromide (CuBr, 98%), copper(II) bromide ($CuBr_2$, 99%), and 2-bromoisobutyrylbromide (BIBB, 98%) were purchased from Merck Sigma. Poly(ethylene glycol) methacrylate (PEGMA, M_n=500), and N,N,N0,N0,N0-Pentamethyldiethylenetriamine (PMDETA, 99%) were purchased from TCl Europe. All solvents used in this study were of analytical grade and used as received.

Synthesis of PGMA backbone

Poly(glycidyl methacrylate) (PGMA) was synthesized via reversible-addition-fragmentation chain transfer (RAFT) polymerization using 4-cyano-4-(phenylcarbonothioylthio)pentanoic acid (CTA) as a chain transfer agent.[41] First, GMA (3mL, 23mmol), AIBN (9.27mg, 0.056mmol), and CTA (63.1mg, 0.23mmol) were transferred into a 50ml round-bottomed reaction flask using 1,4-dioxane (2 ml) as a solvent.[42] The molar feed ratio of the reagents [GMA]:[AIBN:[CTA] was 100:0.25:1. After oxygen was removed from the reaction flask by 5 freeze-pump-thaw cycles, the reaction was carried out under a nitrogen atmosphere at 65℃ while stirring at 250rpm. The reaction was stopped after 24h by opening the reaction flask to

air. To decrease the viscosity of the reaction mixture, 5ml of THF was added into the flask, after which, the product was extracted from the reaction mixture by dropwise addition to 300ml of cold methanol under vigorous stirring. The mixture was filtered under reduced pressure, and the filtered product was redissolved to THF to purify it with two reprecipitations.[43] The purified pink-coloured PGMA was dried overnight under reduced pressure (5mbar) at RT. Based on the mass of the purified and dried PGMA, the yield of the product was calculated as 79%. All synthesis steps were monitored by FTIR and ^{1}H-NMR (**Figures S3.2** and **S3.3** in SI).

Introduction of azide groups onto PGMA (PAzMA)

An azide functionality was introduced to the polymer chain via a ring-opening reaction between the epoxide groups of the PGMA and sodium azide (NaN_3).[44,45] Dried PGMA (1.5g), sodium azide (2.06g), and ammonium chloride (1.7g) were dissolved into DMF (25ml) in a 100 ml round-bottomed reaction flask. The reaction was carried out in a 50 ℃ oil bath while stirring at 250rpm for 24h. Afterwards, the product was extracted from the reaction mixture by dropwise addition to 400ml of cold deionized water under vigorous stirring. The mixture was filtered under reduced pressure, and the filtered product was redissolved to THF to purify it with two reprecipitations. The purified colourless PAzMA was dried overnight under reduced pressure (5mbar) at RT. The yield of the product was calculated as 92%.

Introduction of bromide groups onto PAzMA (PAzBrMA)

A bromide functionality was added to the polymer chain via an esterification reaction between the OH-groups of the PAzMA and 2-bromoisobutyrylbromide (BIBB).[45] Dried PAzMA (1.0g) and TEA (1.5ml) were first dissolved into THF (40ml) in a 250ml three-necked round-bottomed reaction flask. The reaction flask was kept in an ice bath while 2.5mL of BIBB in 20mL of THF was added dropwise into the reaction mixture over a 45-minute period in continuous magnetic stirring. The reaction was allowed to proceed at room temperature for 24h, after which TEA hydrobromide salt was removed from the reaction mixture by filtering

under reduced pressure. Before precipitation, the filtrate was concentrated to <10ml by removing most of the THF with a rotary evaporator. Finally, the product was extracted from the concentrate by dropwise addition to 400ml of cold deionized water under vigorous stirring. The mixture was filtered under reduced pressure, and the filtered product was redissolved to THF to purify it with two reprecipitations. The purified slightly-orange-coloured PAzBrMA was dried overnight under reduced pressure (5mbar) at RT. The yield of the product was calculated as 93%.

Surface functionalization with PAzBrMA

The polymeric substrates (20x20x3mm) were spin-coated with PAzBrMA solution (60µl of 10mg/ml in ethanol-acetone 6:1 mixture) at 1000rpm for 20 sec. Right after spin coating, the panels were exposed to a UV-light lamp (<400nm, 5min) to initiate the covalent attachment of the PAzBrMA macroinitiator through the azide group. After UV exposure, the samples were washed with an ethanol-acetone (6:1) mixture solution to remove the unreacted polymer chains from the sample surfaces.[46] For the preparation of the patterned surfaces, a suitably patterned UV mask was placed on top of the substrates during the UV-light exposure, followed by the same washing procedure. The UV masks were created by laser-cutting predesigned patterns (100µm wide stripes with 0.5mm distance between stripes) into a 0.8mm thin polyester sheet.

Grafting of hydrophilic monomers on PAzBrMA-modified polymer substrates

To modify the surface chemistry of the Br-functionalized surfaces, SI-ATRP of three hydrophilic monomers (HEMA, PEGMA, and DMAEMA) was carried out in a 50mL round-bottom flask.[46,47] All reagents and their amounts in the three different polymerizations can be found in **Table S3.1** in the Supporting Information. For example, HEMA (4mL), CuBr2 (14.7mg), PMDETA (69µL), and four of the PAzBrMA-functionalized surfaces (2cmx2cm) were placed in 4 mL of deionized water. After degassing the mixture with nitrogen for 30 minutes, CuBr (47.3mg) was added to the mixture. The polymerization was terminated after

stirring at RT for 4 h by opening the reaction flask to air. Finally, the samples were extracted from the flask and washed in aqueous ethylenediaminetetraacetic acid disodium salt (EDTA) solution, followed by rinsing with deionized water.

Water contact angle measurements

Water contact angles (WCAs) of the bare and grafted polymer surfaces were determined using a KSV CAM 200 optical contact angle goniometer. Static, advancing, and receding water contact angles were recorded using the sessile and needle-in-the-sessile-drop methods. All measurements were repeated three times for each sample. For advancing (A-WCA) and receding (R-WCA) angles the initial volume of the drop (3μL) was first increased with a pumping speed of 15 μL/s until a maximum droplet size of 15μL. Then the volume of the droplet was decreased from 15μL back to 3μL using the same pumping speed of 15μL/s. All WCA measurements were carried out at an ambient temperature of 21±2 ℃ and relative humidity of 40±5 %.

Surface Imaging

The polymeric substrates were imaged before and after the surface functionalization using Laser Scanning Confocal Microscopy (Keyence VK-X1000) and micro-FTIR (PerkinElmer Spotlight 400). The 3D Laser Scanning Confocal images were further analysed to determine area roughness values (S_a) for the sample surfaces.

Measuring and quantifying freezing events with thermal imaging

Freezing events on the substrates were monitored using a thermal imaging setup described in Chapter 2.[17] The cooling system of the setup was modified with a liquid-cooled thermoelectric cold plate (102x102mm, LHP-300CP, ThermoElectric Cooling America Corporation). A small acrylic environmental chamber (10x10x10mm) was built to fit on top of the cooling system for humidity control during the experiments. The relative humidity was

lowered with a flow of nitrogen gas and increased with a flow of humid air from a bubbler system. The temperature inside the chamber was monitored throughout the experiments as close to the sample surface as possible. After turning the cooling stage on at the beginning of each experiment, the in-chamber temperature dropped slowly from 21℃ to 4℃.

RESULTS AND DISCUSSION

Preparation of patterned and non-patterned surfaces

To investigate systematically the effect of patterned wettability on freezing onset and propagation on the hydrophilic/hydrophobic surfaces, five different polymeric substrates were grafted with three different hydrophilic polymer brushes. The polymeric brushes were linked covalently to the substrates using a bifunctional macroinitiator PAzBrMA. **Figure 3.1** shows the chemical structures of the PAzBrMA and the three hydrophilic polymer brushes used in this study. The synthesis of PAzBrMA consisted of a RAFT polymerization of GMA[41-43], a ring-opening reaction between the epoxide groups of the PGMA and sodium azide (NaN_3)[44,45], and an esterification reaction between the OH-groups of the PAzMA and 2-bromoisobutyryl bromide (BIBB)[45,46] (see **Figure S3.1** in Supporting Information).

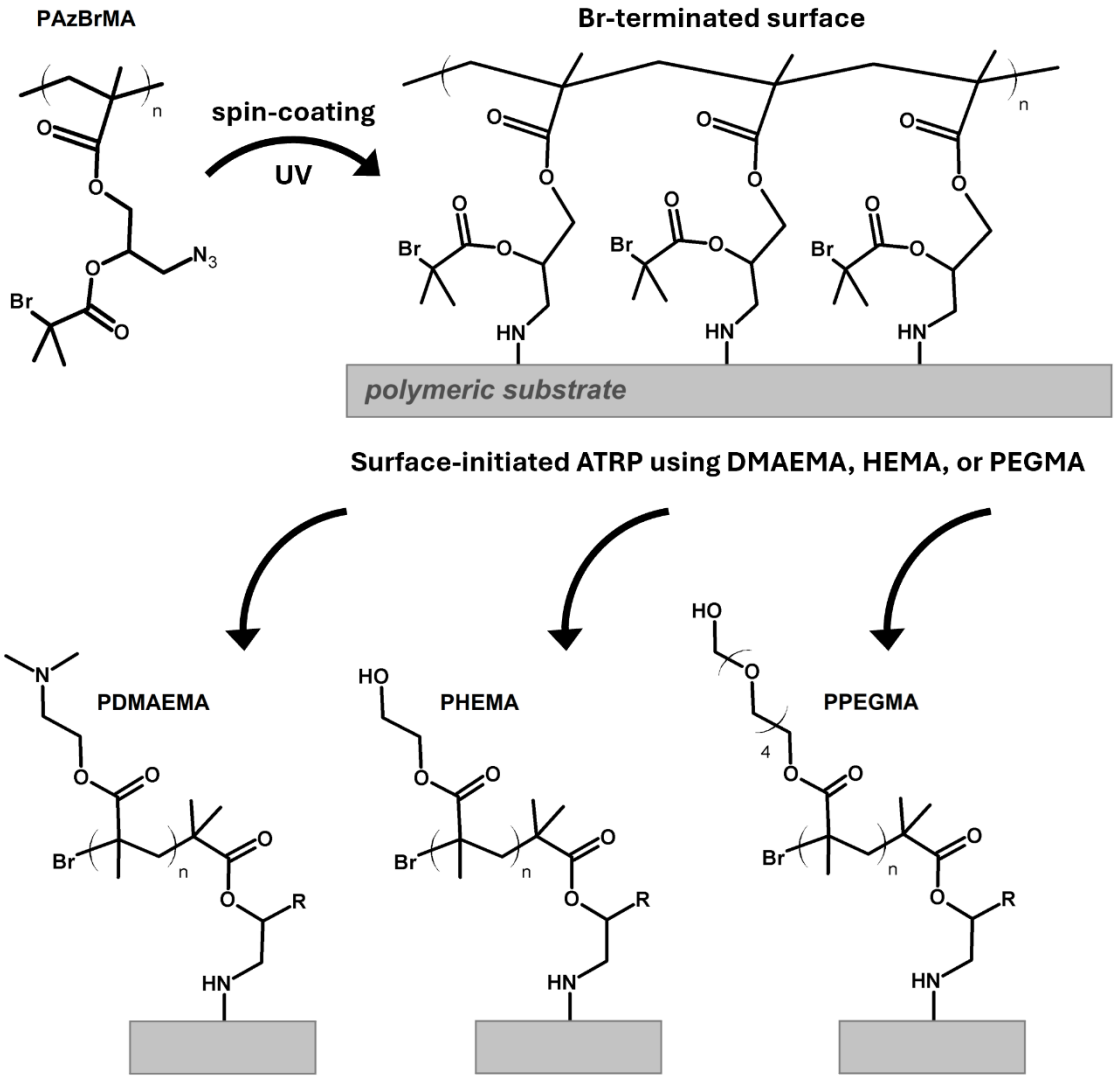

Figure 3.1. Chemical structures of the bifunctional macroinitiator poly[3-azido-2-(2-bromo-2-methylpropanoyloxy)propyl methacrylate] (PAzBrMA), and the three polymer brush structures poly[2-(dimethylamino)ethyl methacrylate] (PDMAEMA), poly(2-hydroxyethyl methacrylate) (PHEMA), and poly[poly(ethylene glycol) methacrylate] (PPEGMA).

To obtain the functionalized polymeric substrates, as visualized in **Figure 3.2**, sample preparation started with spin-coating PAzBrMA (10mg/ml) on each polymer surface (PC, PP, PMMA, PU, and PVC). After spin-coating, the surface was exposed to UV light (<400nm, 5min) which initiated a reaction between the azide groups of the PAzBrMA and the hydrocarbon chain of the polymeric substrates, thus covalently linking the macroinitiator to the polymer surface.[46] To remove any unreacted PAzBrMA, the samples were rinsed with EtOH-Acetone (6:1) mixture and dried under nitrogen flow (**Figure 3.2**, step 3). When a striped mask (100µm wide stripes with 0.5mm spacing) was covering the surface during the UV exposure, only the areas exposed to UV allowed for the fixation of PAzBrMA on the surface; rinsing removed then the unreacted PAzBrMA at the areas covered by the mask and not exposed to UV light (**Figure 3.2**, step 2 –left). In the last step of sample preparation, the areas functionalized with PAzBrMA were rendered hydrophilic via surface-initiated atom transfer radical polymerization (SI-ATRP) of the monomers HEMA, DMAEMA, or PEGMA followed by washing (**Figure 3.2**, steps 4-5). Similarly to the azide groups attaching PAzBrMA to the sample surfaces, the Br-functionalities were used as initiation points for the surface-initiated polymerization of the polymer brushes on the (patterned) surfaces.[46-48]

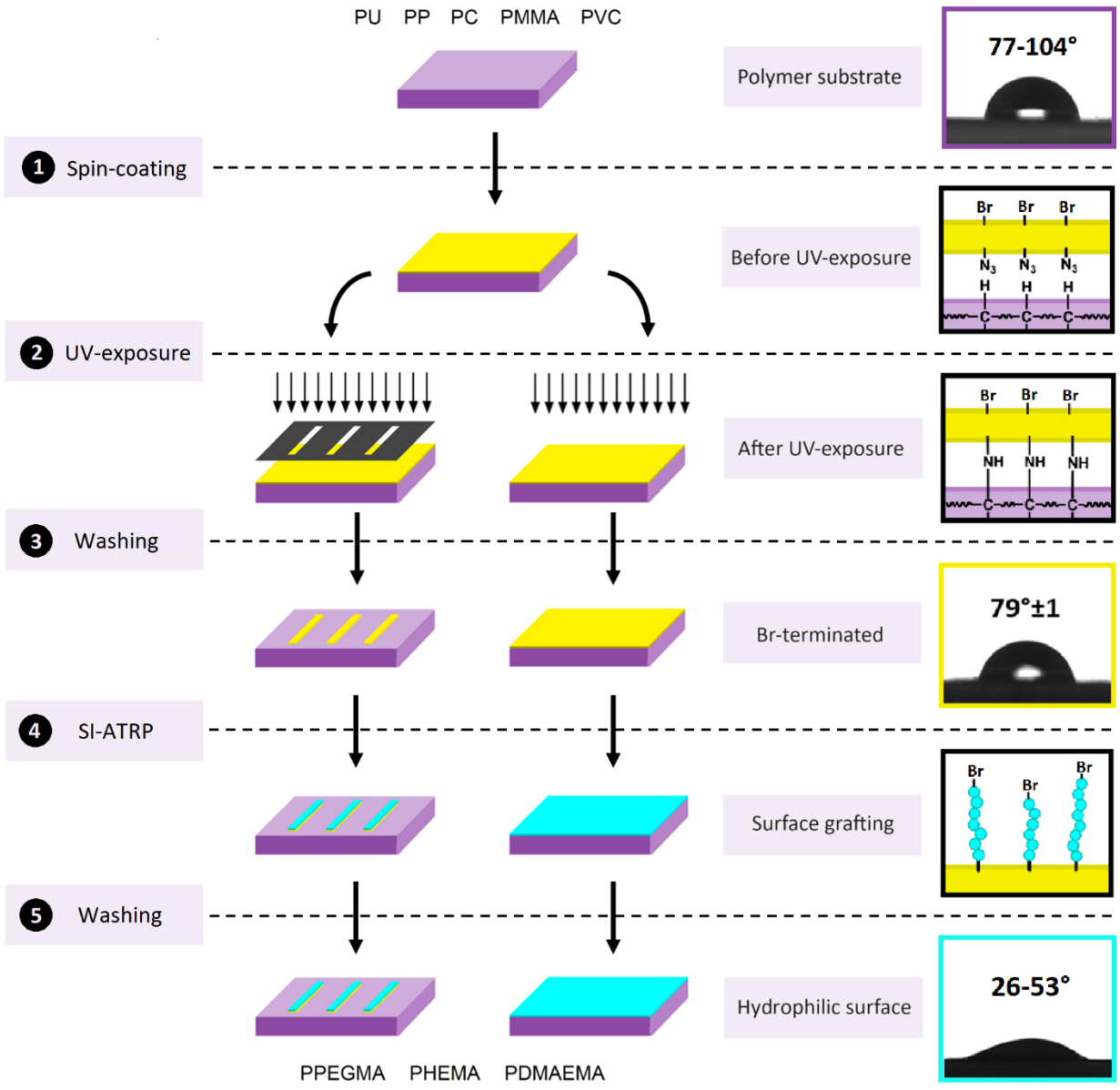

Figure 3.2. Step-wise representation of the patterned and non-patterned samples preparation: 1) The polymer substrate (purple) is spin-coated with a solution of PAzBrMA (yellow); 2) UV light attaches the PAzBrMA covalently to the substrate through the azide group; 3) The UV-exposed substrate is rinsed to remove all unreacted PAzBrMA. If a striped mask is used during UV exposure, only the exposed areas are attached to the polymer substrate; 4) The Br-terminated surface is grafted with a hydrophilic polymer (blue) via SI-ATRP; 5) The grafted substrate is removed from the reaction flask, cleaned, and dried before confirming surface modification through contact angle and IR.

To confirm patterning, FTIR and optical microscopy analysis were performed. As a representative example, **Figure 3.3** shows a confocal scanning microscopy and micro-FTIR images of a PHEMA stripe on PP. The thickness of the stripes was measured to be approximately 200nm as seen in the roughness profile of the stripe in **Figure 3.3c**. The successful functionalization at the optically detectable patterns with the intended chemical groups was confirmed using micro-FTIR by mapping the absorbance intensity of C=O vibration at 1720 cm^{-1} as seen in **Figure 3.3b**. Although the micro-FTIR mapping reveals local variations in the intensity of the carbonyl absorption band within the grafted region, this is likely related to the limited spatial resolution and sensitivity of the measurement for ultrathin grafted polymer layers rather than complete absence of PHEMA in those regions.

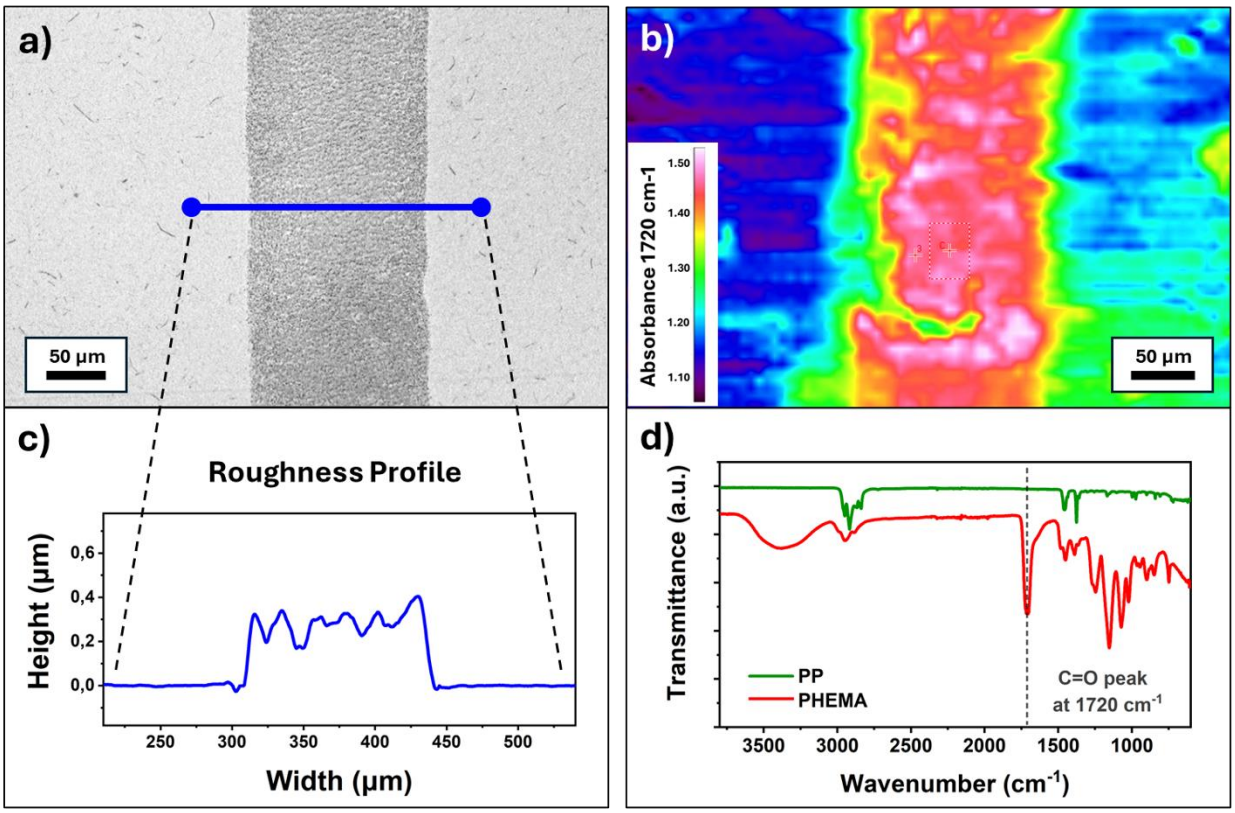

Figure 3.3. Representative images of patterning for the case of PHEMA stripes on a PP substrate using: a) Confocal Scanning Microscope and b) Micro-FTIR imaging. Roughness profile of the PHEMA stripe (c) extracted from the CSM image shows the thickness of the stripe to be approximately 200nm. The red colour in the micro-FTIR image visualizes the presence of carbonyl groups present in the repeating unit of PHEMA as shown in the corresponding FTIR spectra (d) and the C=O vibrational peak at 1720 cm^{-1}.

Surface wettability and roughness

To assess the wettability of the patterned hydrophilic/hydrophobic surfaces, water contact angle measurements were conducted on all bare polymeric substrates and the substrates fully covered with the hydrophilic polymer grafts (i.e. no patterns). **Figure 3.4a** shows the static (S-WCA), advancing (A-WCA), and receding water contact angles (R-WCA) on all bare polymer substrates (PC, PP, PMMA, PVC, and PU), as well as their water contact angle hysteresis (CAH). The S-WCAs of the substrates vary between 77° and 104°, PP having the highest and PMMA the lowest S-WCA of the polymers. The substrates vary particularly in their CAH values, with PC having the lowest CAH at 25° and PU the highest CAH at 74°. The roughness values of the bare substrates (**Figure 3.4b**) follow a similar trend as the CAH values, with PC having the lowest mean area roughness (S_a= 0.06µm) and PU having the highest S_a (S_a =0.5µm).

As seen in **Figure 3.4c**, after the surface grafting, the S-WCAs of the PDMAEMA, PHEMA, and PPEGMA-covered substrates decreased from 77-104° corresponding to the substrate polymers to 53°, 41°, and 26°, respectively. Since all fully grafted surfaces were strongly hydrophilic, their receding contact angles approached the lower detection limit of the sessile-drop measurement method and were measured as approximately 0°, resulting in CAH values that were effectively comparable to their S-WCAs. Additionally, the underlying polymeric substrates did not seem to affect the wettability of grafted samples, confirming a homogeneous surface coverage with hydrophilic polymer grafts. The roughness values of the hydrophilic surfaces, as represented in **Figure 3.4d** for the case of PP and PU substrates, are similar regardless of the chemistry of the polymeric graft. Since the thickness of the polymer grafting is approximately 200nm (**Figure 3.3c**) the overall roughness values of the hydrophilic samples did not change significantly compared to the bare polymeric substrates.

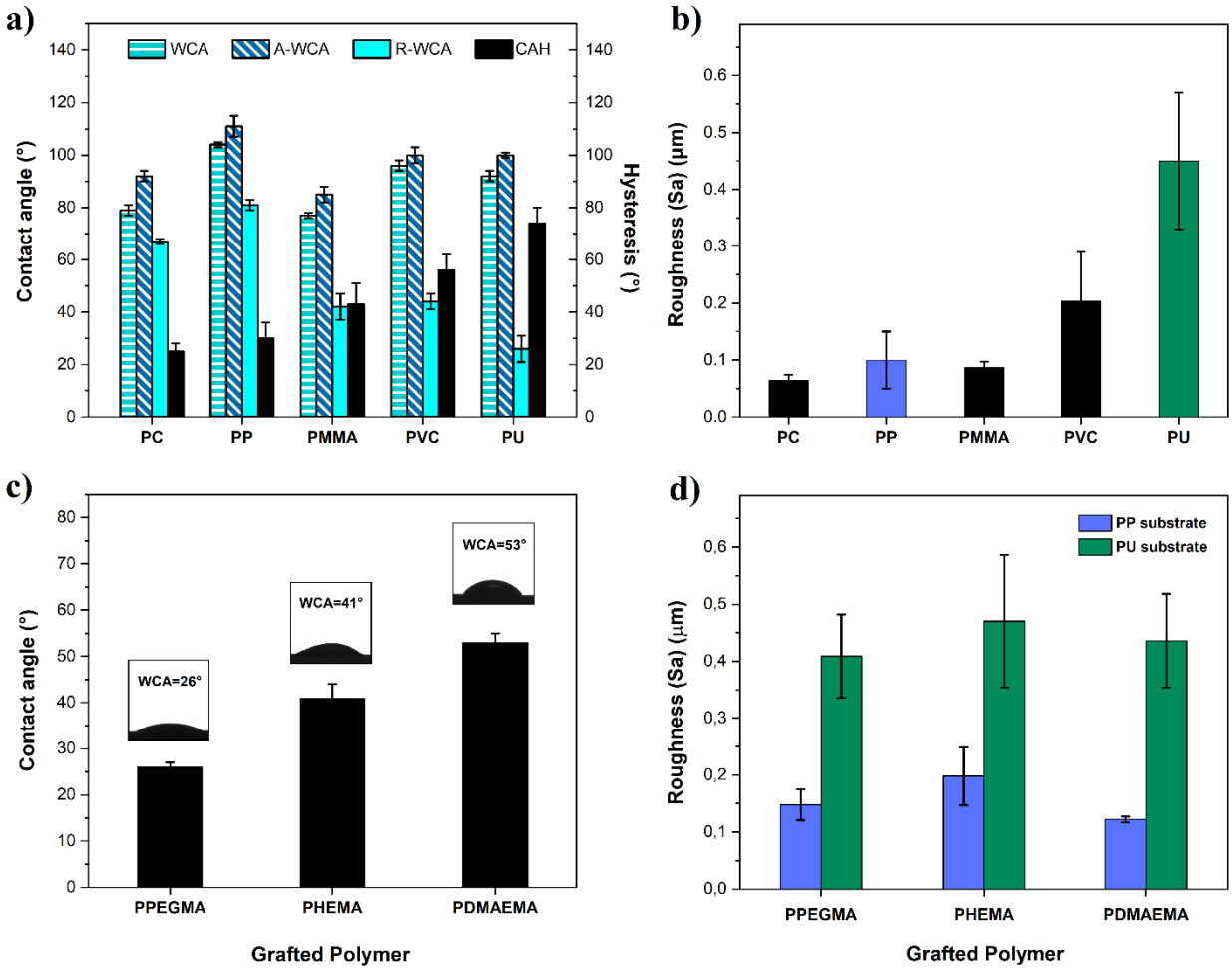

Figure 3.4. Water contact angle (S-WCA, A-WCA, R-WCA, and CAH) and roughness (S_a) values of the bare substrates (a,b) and the samples fully covered with a hydrophilic graft (c,d). The static contact angle of substrates coated with hydrophilic grafts (PPEGMA, PHEMA, PDMAEMA) shown in 4c did not depend on the substrate used (PC, PP, PMMA, PVC, PU). The hydrophilic surface grafting also did not significantly influence the roughness of the different polymeric substrates as shown by the consistently different S_a values of PP (blue colour) and PU (green colour) before (b) and after grafting (d).

Frost propagation on non-patterned polymer substrates

To investigate the freezing onset and propagation on homogeneous surfaces, the non-patterned polymeric samples were cooled to -20℃ at a rate of 8℃/min using a liquid-cooled Peltier plate inside an environmental chamber at RH 50%. The polymer surfaces were monitored during the cooling and freezing propagation experiment from above with a high-resolution thermal camera. In this experiment, thermal imaging reveals the latent heat release during the freezing of supercooled surface water. In practice, this allows following the freezing propagation front throughout the surface with high spatial and temporal resolution once a freezing event starts somewhere on the sample surface.

Figure 3.5 shows selected snapshots from the thermal videos representative of the freezing propagation on the five different bare polymeric substrates and one PHEMA-grafted PMMA substrate. Example videos of the different samples can be found in **Movies S3.1-S3.3**. In the video snapshots, the dark purple colour corresponds to a lower temperature, and the bright yellow to a higher temperature. As liquid condensation freezes on the sample surface, a sudden temperature increase (local yellow colour in the snapshots) pinpoints the location of the freezing event. Thus, the front line of the freezing propagation on the bare polymeric substrates in **Figure 3.5** can be detected as a rim of bright yellow dots corresponding to the freezing of condensed water droplets on the sample surfaces. The white arrows indicate the direction of the freezing front-line propagation. In **Figure 3.5**, the freezing propagation front lines on the (slightly)hydrophobic non-patterned polymeric substrates (WCA>80°) are composed of condensed water droplets individually and sequentially freezing (see **Movie S3.1**). A closer examination of the video snapshots reveals small ice bridges interconnecting the frozen droplets (**Figure S3.8** in SI). This is in good agreement with an ice-bridging process driving the freezing propagation as reported for percolation-induced frost formation.[49,50]

Freezing onset and propagation rates were also monitored for the substrates fully covered with the hydrophilic PHEMA grafting. The last row in **Figure 3.5** shows one example of the freezing front propagation on the hydrophilic surfaces. In this case, the freezing propagation is captured as a bright yellow rapid wave that eventually fills the entire window of observation. This propagation mode was similar for all the PHEMA-grafted polymeric

surfaces, independent of the underlying polymeric substrate (**Figure S3.4** in SI). Based on Chapter 2 connecting the presence and state of molecular water layer (MWL) to various freezing events observed on smooth functionalized glass surfaces[17], the extremely fast freezing frontlines are consistent with freezing events that propagate via a continuous liquid-like MWL.

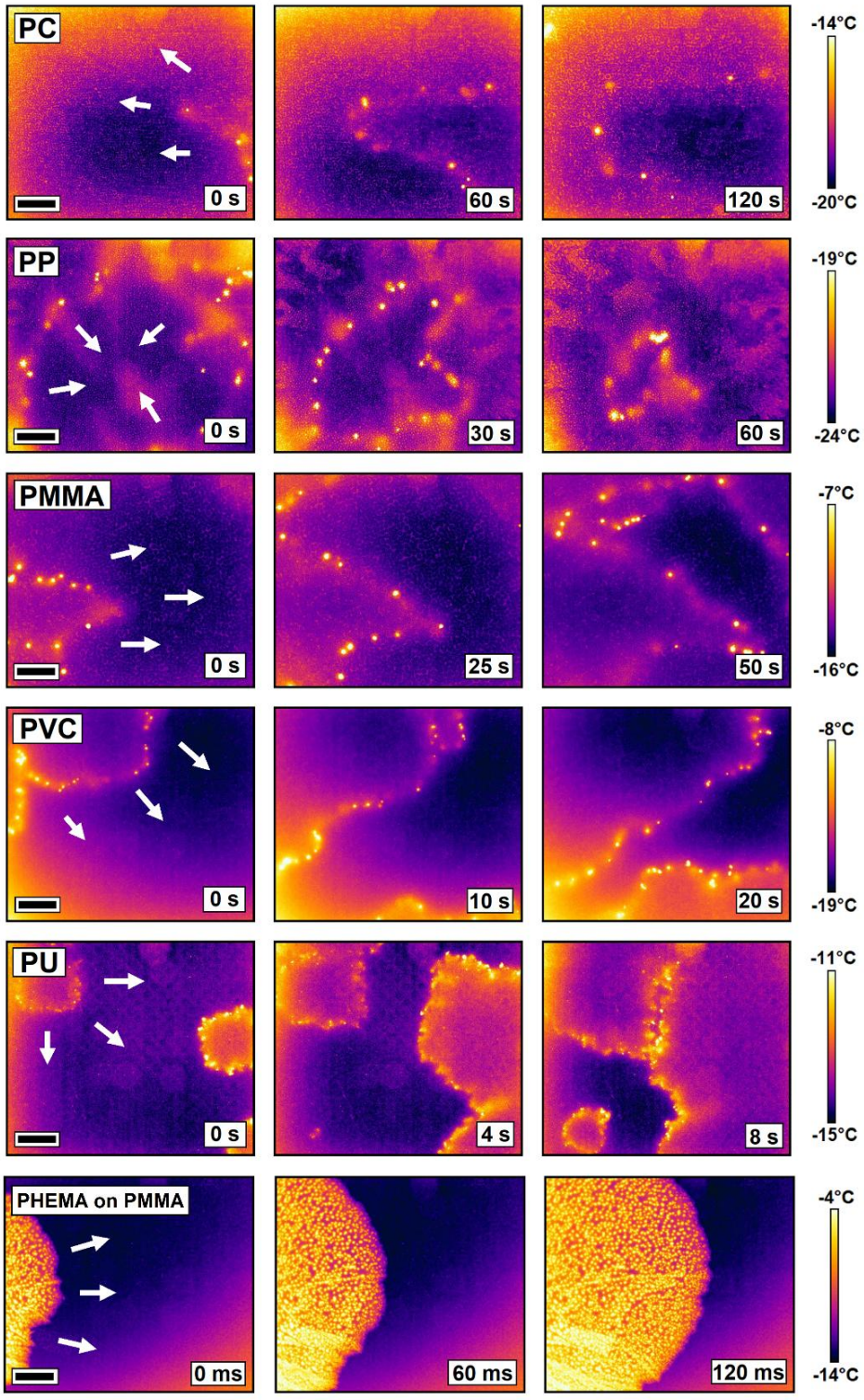

Figure 3.5. Thermal video snapshots showing freezing propagation on the five non-patterned polymer substrates (PC, PP, PMMA, PVC, PU) and one PHEMA-grafted PMMA substrate (PHEMA) in RH 50%. The white arrows indicate the direction of the freezing propagation frontline. The black scale bars in the first column of images correspond to 2 mm. Note the time scale for the PHEMA-PMMA sample is in ms (three orders of magnitude faster than the rest of the polymers).

The thermal snapshots like those shown in **Figure 3.5** were analysed using the image processing program ImageJ to obtain freezing propagation rates as shown in **Figure S3.7** in SI. The average freezing propagation rates with error bars obtained for all non-patterned samples are shown in **Figure 3.6** as a function of the substrate WCA hysteresis (CAH).

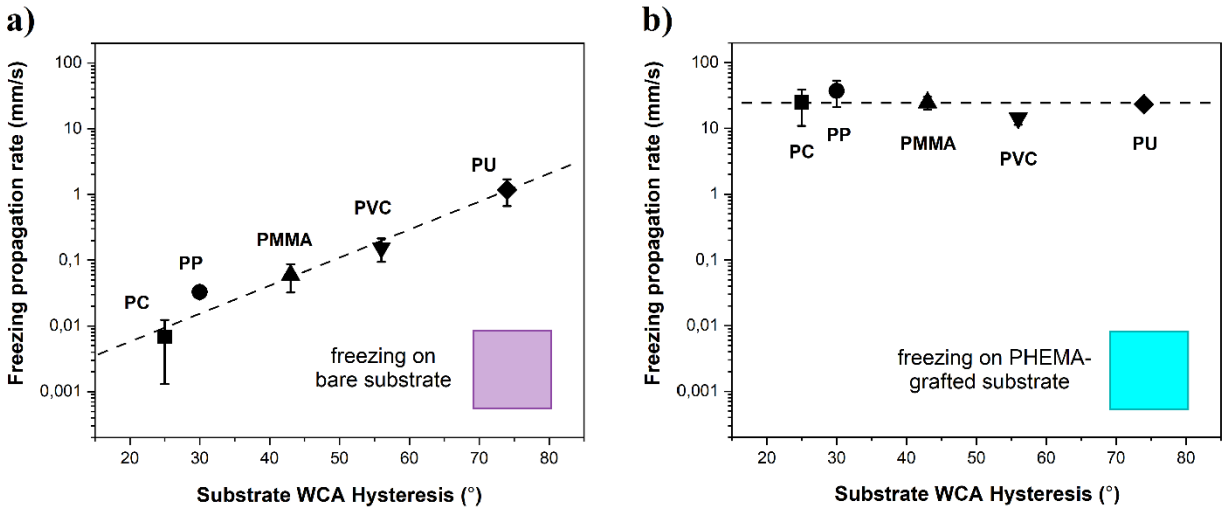

Figure 3.6. Calculated freezing propagation rates of (a) the bare polymers plotted as a function of the substrate CAH; and (b) the PHEMA-grafted surfaces plotted as a function of the underlying bare substrate CAH. The same x-axis is used in both graphs to highlight the independence of the PHEMA freezing propagation rate from the underlying substrate type.

Despite showing a propagation pattern corresponding to percolation-induced freezing, the measured average propagation rates of the hydrophobic samples (**Figure 3.6a**) are significantly higher (between 0.03 mm/s for PP and 1.2 mm/s for PU) than those propagation rates previously reported for inter-droplet ice bridging characteristic of percolation-induced freezing (0.001-0.01 mm/s)[49-55], with the exception of the PC sample (0.007 mm/s). The results reported here (**Figure 3.6a**) therefore extend the previously reported propagation rates for ice-bridging and show for the first time a linear relation between contact angle hysteresis (CAH) and, to a lower extent surface roughness (**Figure 3.4b**), with the

propagation rate: the higher the difference between advancing and receding angles (higher CAH) the faster the global freezing propagation rate is.

As seen in **Figure 3.5**, and different to the hydrophobic surfaces, the freezing propagation frontline on the hydrophilic PHEMA-grafted polymeric surfaces (**Movie S3.2** in SI) shows a rapid flash-like freezing propagation (e.g. PHEMA on PP) in the scale of ~20mm/s (**Figure 3.6b**), regardless of the underlying substrate. The slight variation in the freezing propagation rates results from different degrees of supercooling of the PHEMA-covered substrates at the time of nucleation. The cooling stage was set to reach -20℃ at the start of the experiments, but the initial nucleation event can occur before the sample surface has cooled down to this temperature. Freezing events initiated at slightly higher temperatures (lower degree of supercooling) have a slightly lower freezing propagation rate.

Despite the small deviation between experiments, the freezing propagation rates on the hydrophilic surfaces (~20mm/s) are in good agreement with the reported values for freezing propagation in bulk water (~1-100mm/s)[56-59] and suggest that the freezing event is propagating through a continuous layer of molecular water layer (MWL). This hypothesis is in line with Chapter 2 on MWL-promoted freezing propagation on surface-modified glass[17] and confirms a good homogeneous surface coverage with hydrophilic moieties (e.g. PHEMA) in all cases despite the eventual presence of water droplet freezing.

Frost propagation on patterned polymer substrates

Thermal video snapshots of the freezing propagation on the polymer substrates patterned with hydrophilic PHEMA stripes can be seen in **Figure 3.7** for three polymer substrates (PC, PMMA, PU) and in **Figures S3.5** and **S3.6** in SI. In all cases the freezing events initiate at the hydrophilic stripes as seen by the 0ms snapshots, to rapidly propagate longitudinally along the PHEMA stripes (MWL freezing controlled). Once the PHEMA stripes are frozen, the freezing propagation continues laterally outbound from the frozen stripe with the familiar, yellow-dotted front line, highlighting individually freezing of condensed water droplets (interdroplet freezing controlled process).

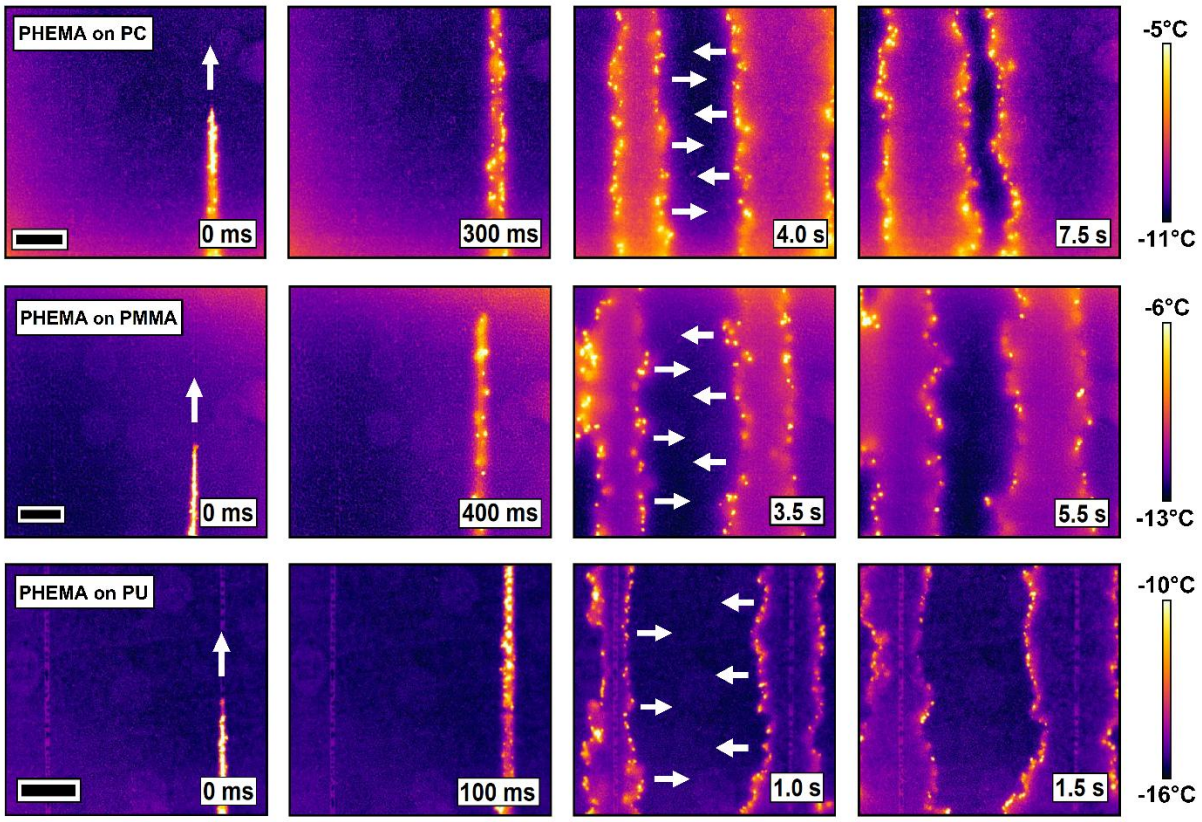

Figure 3.7. Thermal video snapshots showing freezing propagation in RH 50% on three different polymer substrates (PC, PMMA, PU) patterned with hydrophilic PHEMA stripes. The white arrows indicate the direction of the freezing propagation. The black scale bar equals 2mm. Note the similar patterns but at different nucleation times and propagation rates.

To study the effect of the hydrophilic stripe chemistry on the freezing onset and propagation, freezing propagation tests on PP substrates with PHEMA, PDMAEMA, or PPEGMA grafted stripes were monitored separately. As seen in **Figure 3.8**, changing the stripe chemistry did not influence the overall freezing propagation mechanism of the patterned wettability surfaces: freezing events still onset and propagate at the hydrophilic stripe(s) first to further expand transversally onto the PP surface.

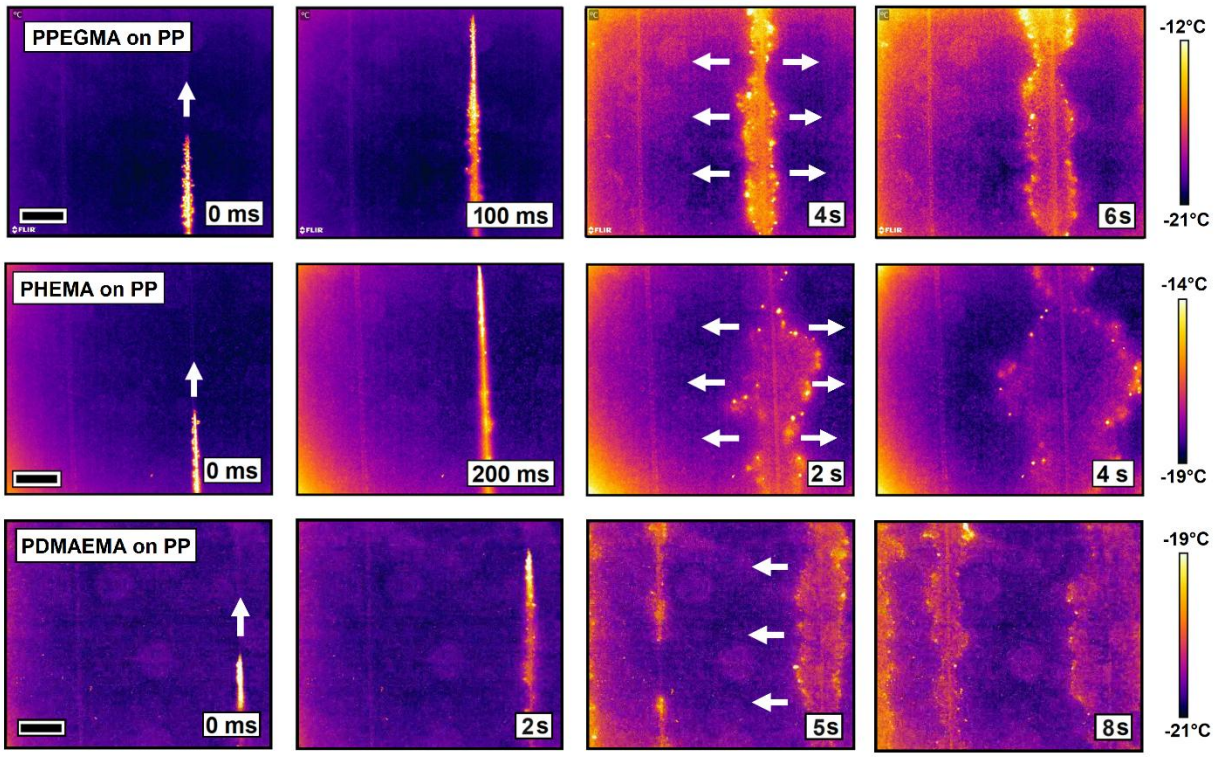

Figure 3.8. Thermal video snapshots showing freezing propagation in RH 50% on PP substrates patterned with PPEGMA, PHEMA, and PDMAEMA stripes. The white arrows indicate the direction of the freezing propagation. The scale bar equals 2mm. Note the different nucleation times and propagation rates.

When analysing the freezing mechanisms involved in the freezing of the patterned wettability surfaces (**Figures 3.7, 3.8, S3.5, S3.6**, and **Movie S3.3**), two separate freezing propagation rates were calculated for the two contrasting freezing propagation steps and

modes: (i) rapid freezing initiation and propagation along the hydrophilic stripes (**Figures 3.9a** and **3.9c**), and (ii) slower lateral freezing front propagation from the stripes into the more hydrophobic substrates (**Figures 3.9b** and **3.9d**).

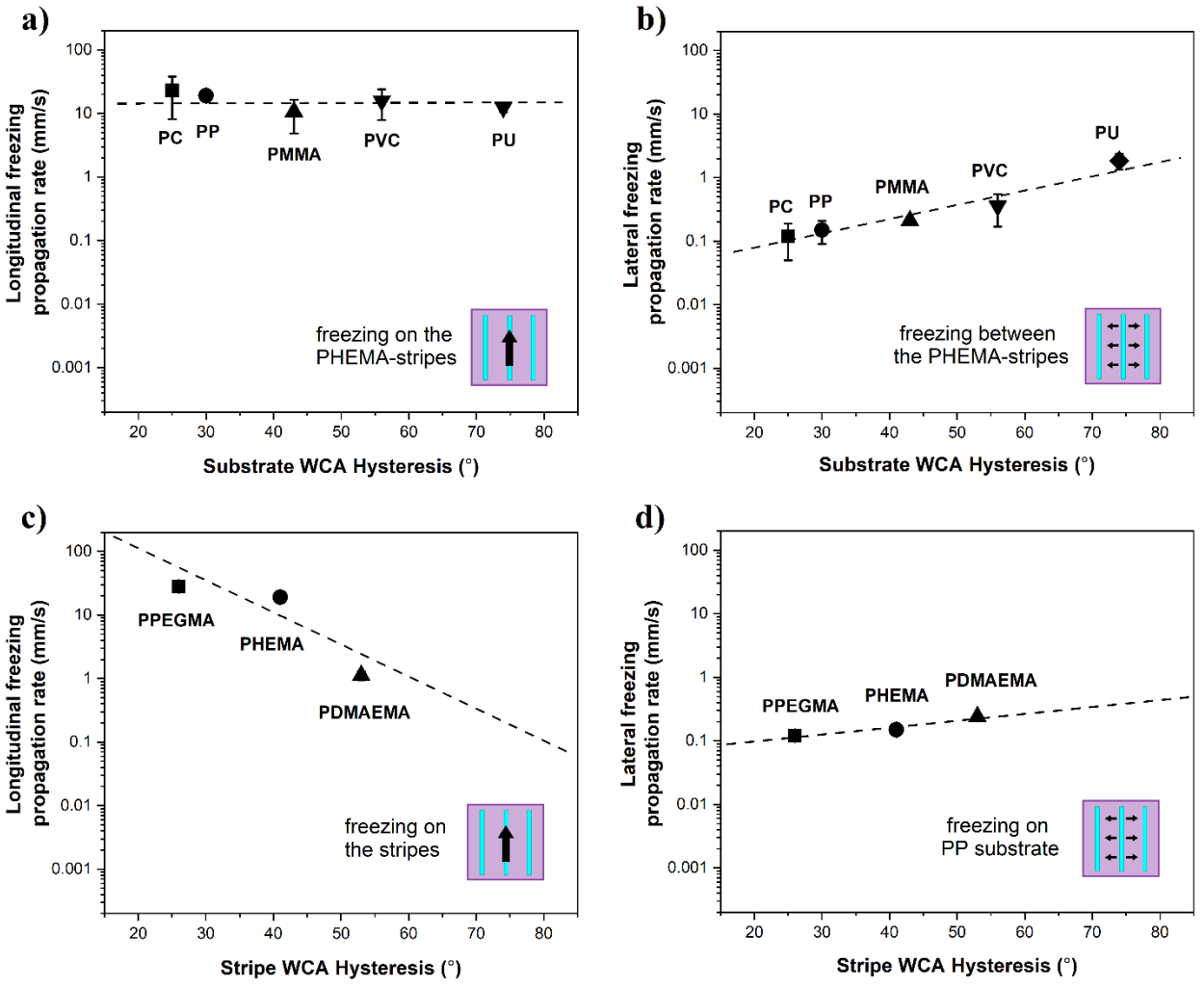

Figure 3.9. Freezing propagation rates on the patterned surfaces with PHEMA stripes and varying wettability of the hydrophobic substrate (a and b), and the PP substrates with varying wettability of the hydrophilic stripes (c and d). The propagation rates were calculated separately for the freezing events propagating longitudinally along the hydrophilic stripes (a and c) and for the freezing events propagating laterally from the stripes onto the substrate (b and d).

When comparing **Figure 3.6b** and **3.9a** it becomes clear that the propagation mode and speed on the stripes (10mm/s, **Figure 3.9a**) resemble those seen on the polymers homogeneously covered with PHEMA (20mm/s, **Figure 3.6b**). A similar comparison can be made for the freezing propagation rates for the hydrophobic polymers (**Figure 3.6a**) and the lateral freezing propagation mode on the patterned surfaces perpendicular to the stripes (**Figure 3.9b**). In this case, we report an order of magnitude faster propagation rates on the hydrophobic surfaces when the surfaces are patterned with hydrophilic stripes.

An explanation to this difference can be found in the theory of ice-bridge kinetics based on Kinetic Monte Carlo simulations which predicted that the rate of ice-bridge formation increases with decreasing inter droplet distance, increasing temperature, or increasing surface wettability.[60] Since the experimental procedure did not change at any point, the influence of temperature i.e. higher degree of supercooling cannot explain the observed faster propagation rates. Also, the wettability of the polymer substrates at areas that were covered during the UV exposure did not change after the grafting procedure, as shown in **Figure S3.9** in SI. Therefore, changes in both surface temperature and wettability of the substrates can be excluded, and the increased frost propagation rate is likely due to shorter distances between condensed water droplets.

On the patterned surfaces, the freezing events initiate on the hydrophilic stripes where the nucleation events are energetically more favourable and therefore happen earlier than on the more hydrophobic bare polymers. The earlier the initial nucleation event occurs, the less time the existing condensed water droplets have to grow in size and coalesce with each other. Droplet coalescing leads to longer inter-droplet distances since depressed vapor pressure over larger droplets promotes evaporation of its smaller neighbouring droplets.[35] Therefore, during an earlier nucleation event on the patterned surfaces, the condensed water droplets are smaller and closer together which accounts for the faster inter-droplet ice bridging rates.

In addition to the faster frost propagation rates in the patterned surfaces, the same linear dependency with the hysteresis contact angle (CAH) can be observed; i.e. connection of the

lateral freezing propagation rate to the wettability of the polymeric substrate and the role of the MWL on local freezing propagation along the stripes. Earlier research measuring the thickness and continuity of MWLs with FTIR, AFM, thermal imaging, and X-ray reflectometry has shown a clear difference in the presence and state of MWL between hydrophilic and hydrophobic surfaces.[9,12,17] In general, liquid-like MWL was found on all hydrophilic surfaces (WCA<80°) at ambient conditions, while the hydrophobic samples (WCA>80°) showed either no water adsorption at all or some water adsorption at surface defects depending on RH.

Considering the previous measurements on hydrophobic methyl-terminated monolayer surfaces[9], it can be assumed that there is no water adsorption on the PP substrates at RT in 50% RH. On the other hand, the polymeric substrates grafted with hydrophilic polymers are expected to adsorb a continuous liquid-like MWL with a thickness >0.4 nm, as previously reported for hydrophilic COOH-terminated monolayers[9]. On the patterned surfaces, following the same logic, the hydrophilic stripes are expected to be covered with a continuous liquid-like MWL, whereas the surrounding bare polymeric substrate should have no MWL.

In Chapter 2, we connected the presence and state of MWLs to different freezing propagation modes on surface-functionalized glass slides with varying wettability.[17] On the dry hydrophobic surfaces in 50% RH, the freezing events propagated slowly (<0.05mm/s) via ice-bridge formation. In the same environmental conditions, freezing events propagated rapidly (>2mm/s) on very hydrophilic surfaces via a thin continuous liquid-like MWL. These same freezing propagation modes were detected here on the bare polymeric substrates (**Figure 3.5**) and the substrates grafted with hydrophilic polymers (**Figures 3.5** and **S3.4**). The faster freezing propagation rates on the bare PU, PVC, and PMMA (0.1-1.0mm/s in **Figure 3.6a**) are likely the result of some minor water adsorption at surface defects/higher surface roughness, as previously suggested for chloro-terminated monolayers and Teflon surfaces[9,12].

As seen in **Figure 3.9a**, changing the chemistry of the hydrophilic stripes seems to also influence the rate of the rapid longitudinal freezing propagation on the patterned surfaces. The fast freezing propagation mode along the stripes still corresponds to freezing via a continuous MWL, however, the propagation rate decreases with increasing wettability of the stripe. Similar to the bare polymer substrate, lowering the hydrophilicity of the polymer brush can result in less continuous MWL and a slower freezing propagation rate on the stripes.

The presence of the two distinctively different freezing propagation mechanisms on the patterned wettability surfaces (**Figures 3.7** and **3.8**) strongly indicates that localized wettability difference can induce localized variability in MWL which, moreover, can lead to localized variability in the freezing propagation speeds. As shown in **Figure 3.10**, the freezing events first propagate rapidly on the stripe through the continuous liquid-like MWL, after which the freezing propagation continues much more slowly on the dry polymeric substrate via ice-bridge formation being this process faster at higher hysteresis values of the hydrophobic substrate. This is attributed to the lower receding contact angles measured for the samples with the highest hysteresis which arguably contribute to a faster propagation of the MWL from the hydrophilic regions, hence accelerating the propagation rate in one order of magnitude with respect to the bare (slightly)hydrophobic polymers (**Figure 3.6a** vs **3.9b**).

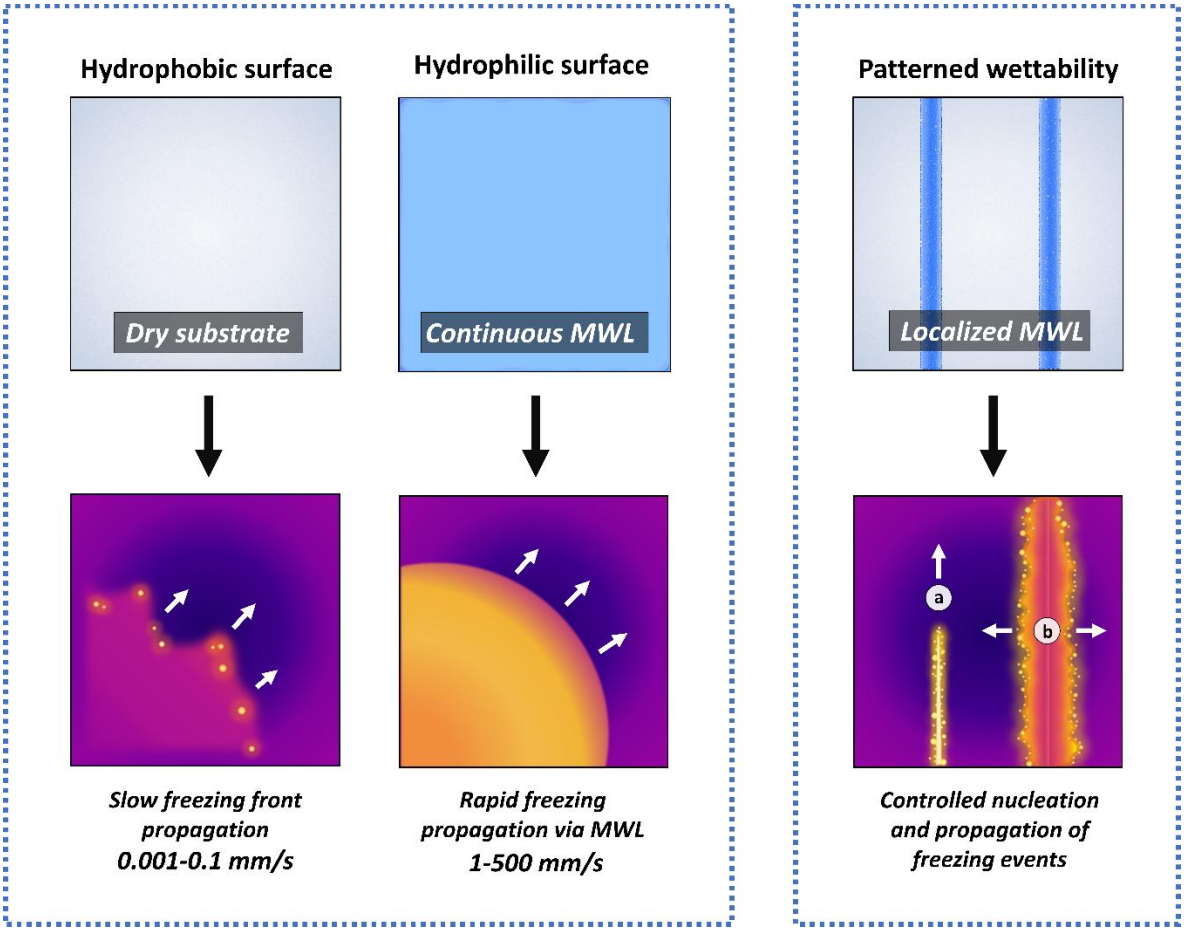

Figure 3.10. Illustration representing how local variations in the state of MWL can be used to control nucleation and propagation of freezing events on patterned wettability surfaces. On hydrophobic surfaces with hydrophilic stripes, the initial freezing events nucleate on the hydrophilic areas and propagate rapidly along the hydrophilic stripes (a) via liquid-like MWL. After local hydrophilic stripes are frozen, the freezing event continues to propagate laterally on the hydrophobic areas from the stripes at a significantly lower propagation rate (b).

CONCLUSIONS

In this work, a set of five slightly hydrophobic polymers (PP, PU, PVC, PMMA, PC) was surface-modified to create stripped hydrophilic patterns on hydrophobic surfaces using SI-ATRP. This allowed studying the effect of pattern and substrate wettability local differences on surface freezing propagation mechanism. The condensation frost onset and propagation rate and mode were monitored in a high supersaturation environment (S>6.5) using high-resolution thermal imaging. Local wettability differences on the polymeric substrates grafted with hydrophilic stripes were linked to local variations in the presence and state of MWL: the presence of localized liquid-like MWL was related to the fast-freezing events on the hydrophilic stripes and to the acceleration of the freezing propagation rate across the more hydrophobic substrate for the studied patterns and environmental conditions. A linear relation between inter-droplet ice propagation rate and CAH was found for the hydrophobic surfaces, revealing propagation rates one order of magnitude faster than those reported for ice-droplet freezing. In the future, these insights could be used to develop new ice-controlling surfaces based on the idea of local ice nucleation and propagation control. The findings here reported may also contribute to a better understanding of freezing mechanisms on surfaces with defects and impurities with varying molecular water layers.

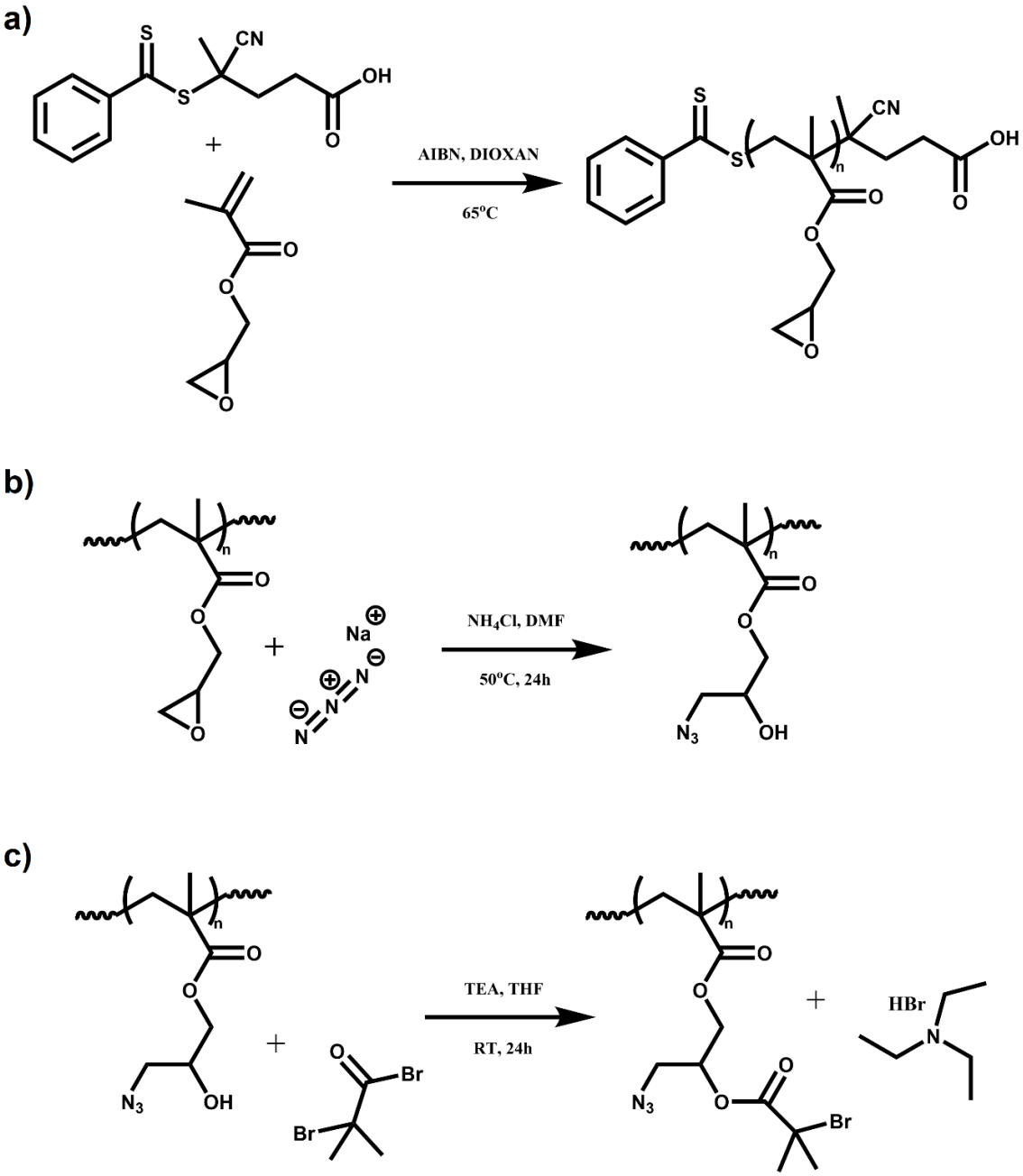

Figure S3.1. Reaction schemes of the three synthesis steps in the preparation of the bifunctional macroinitiator: a) RAFT polymerization of glycidyl methacrylate (GMA), b) ring-opening reaction between the epoxide groups of the PGMA and sodium azide (NaN3), and c) esterification reaction between the OH-groups of the PAzMA and 2-bromoisobutyrylbromide (BIBB).

Table S3.1. Reagent table for the SI-ATRP of HEMA, PEGMA, and DMAEMA

Reagent	Mass	Volume	M (g/mol)	ρ (kg/m^3)	n (mmol)
HEMA	4.29 g	4 ml	130.14	1.073	33
DI-water	-	4 ml	-	0.997	-
$CuBr_2$	14.7 mg	-	223.37	-	0.066
PMDETA	57.1 mg	69 µl	173.3	0.83	0.33
CuBr	47.3 mg	-	143.45	-	0.33
PEGMA	4.43 g	4 ml	360	1.105	12.3
DI-water	-	4 ml	-	0.997	-
$CuBr_2$	4.5 mg	-	223.37	-	0.02
bpy	18.7 mg	-	156.18	-	0.12
CuBr	17.2 mg	-	143.45	-	0.12
DMAEMA	3.73 g	4 ml	157.21	0.933	23.7
DI-water	-	2 ml	-	0.997	-
MeOH	-	2 ml	-	0.792	-
$CuBr_2$	10.5 mg	-	223.37	-	0.047
bpy	37.0 mg	-	156.18	-	0.237
CuBr	34.0 mg	-	143.45	-	0.237

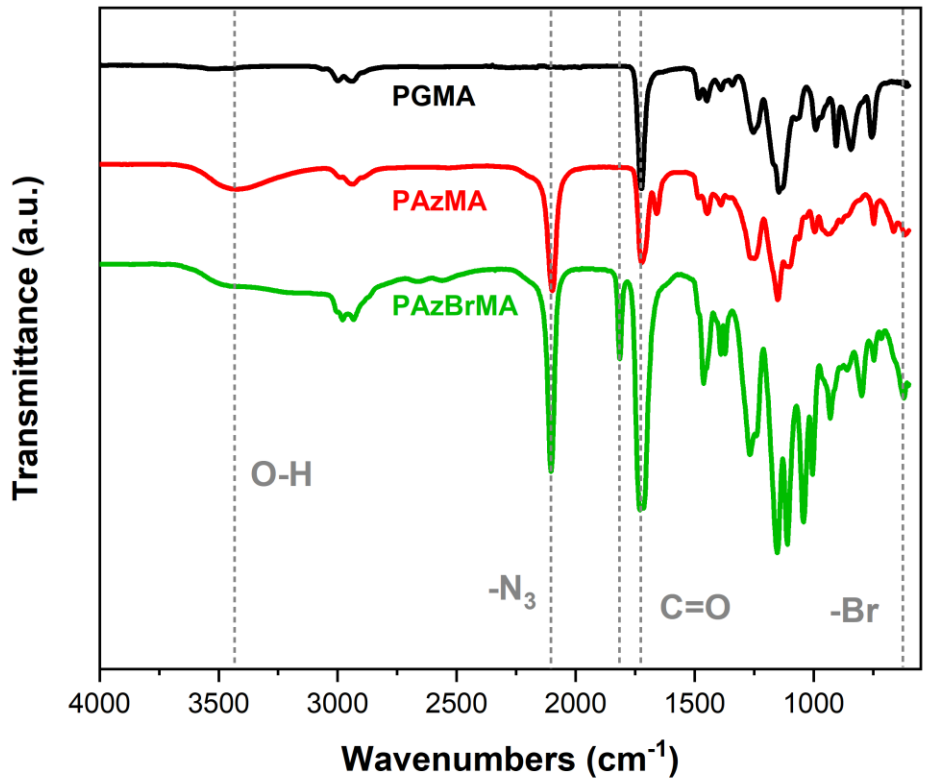

Figure S3.2. FTIR spectra of PGMA (black), PAzMA (red), and PAzBrMA (green). The signals from OH ($3400cm^{-1}$) and N_3 ($2110m^{-1}$) differentiate the spectrum of PAzMA from PGMA. Additional signals from a second carbonyl and Br-groups are present on the spectrum of PAzBrMA.

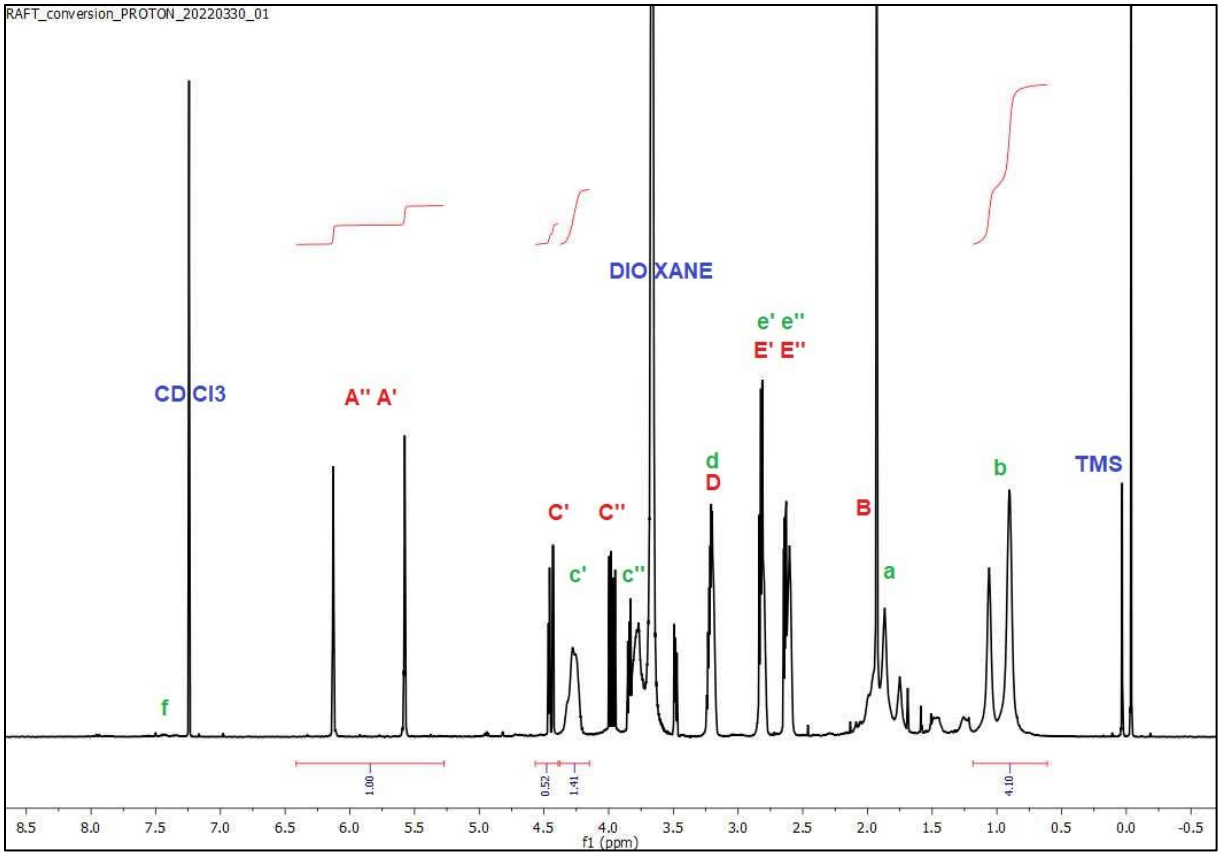

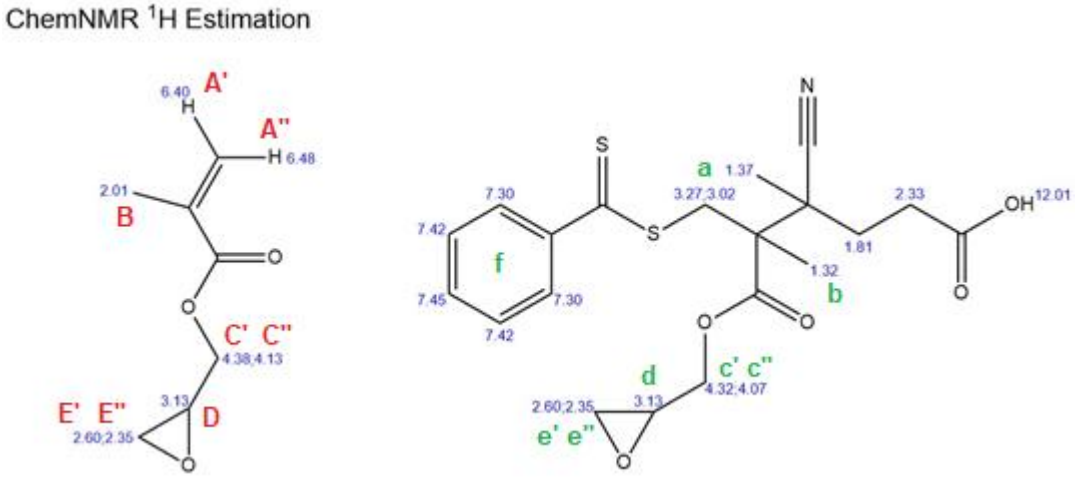

Figure S3.3. [1]H-NMR spectrum of the conversion sample from RAFT polymerization of PGMA. The red capital letters correspond to signals from the monomer and the green letters to signals from the polymer. Conversion of the reaction was calculated from the areas under peaks b at ~1ppm (3 protons) and A at ~6ppm (2 protons).

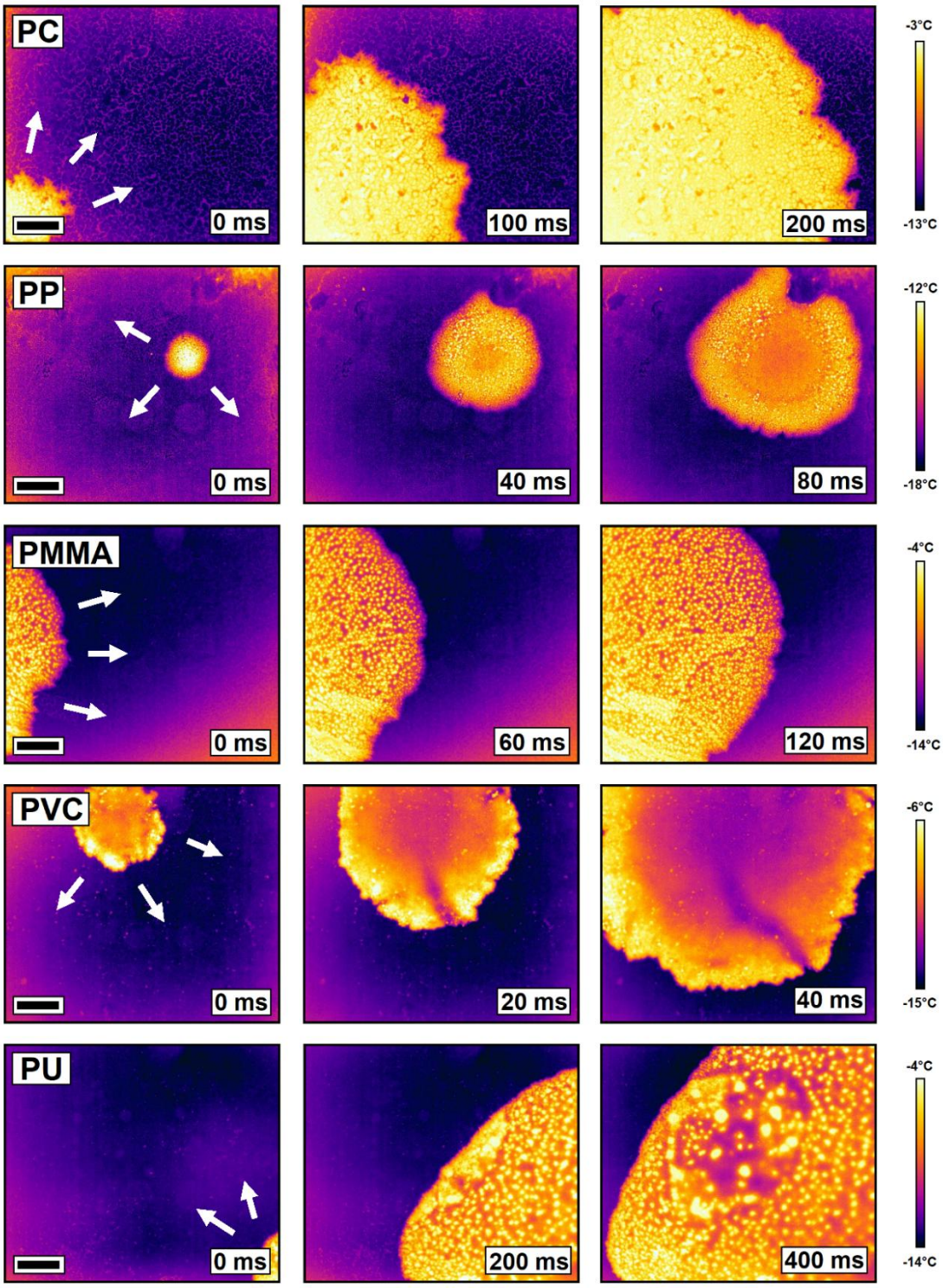

Figure S3.4. Time snapshots from thermal videos showing a freezing front propagating on the PHEMA-covered polymer substrates exposed to **50 %** RH. The white arrows indicate the direction of the freezing front propagation. The black scale bar shown in the bottom left corner of the first images is 2 mm.

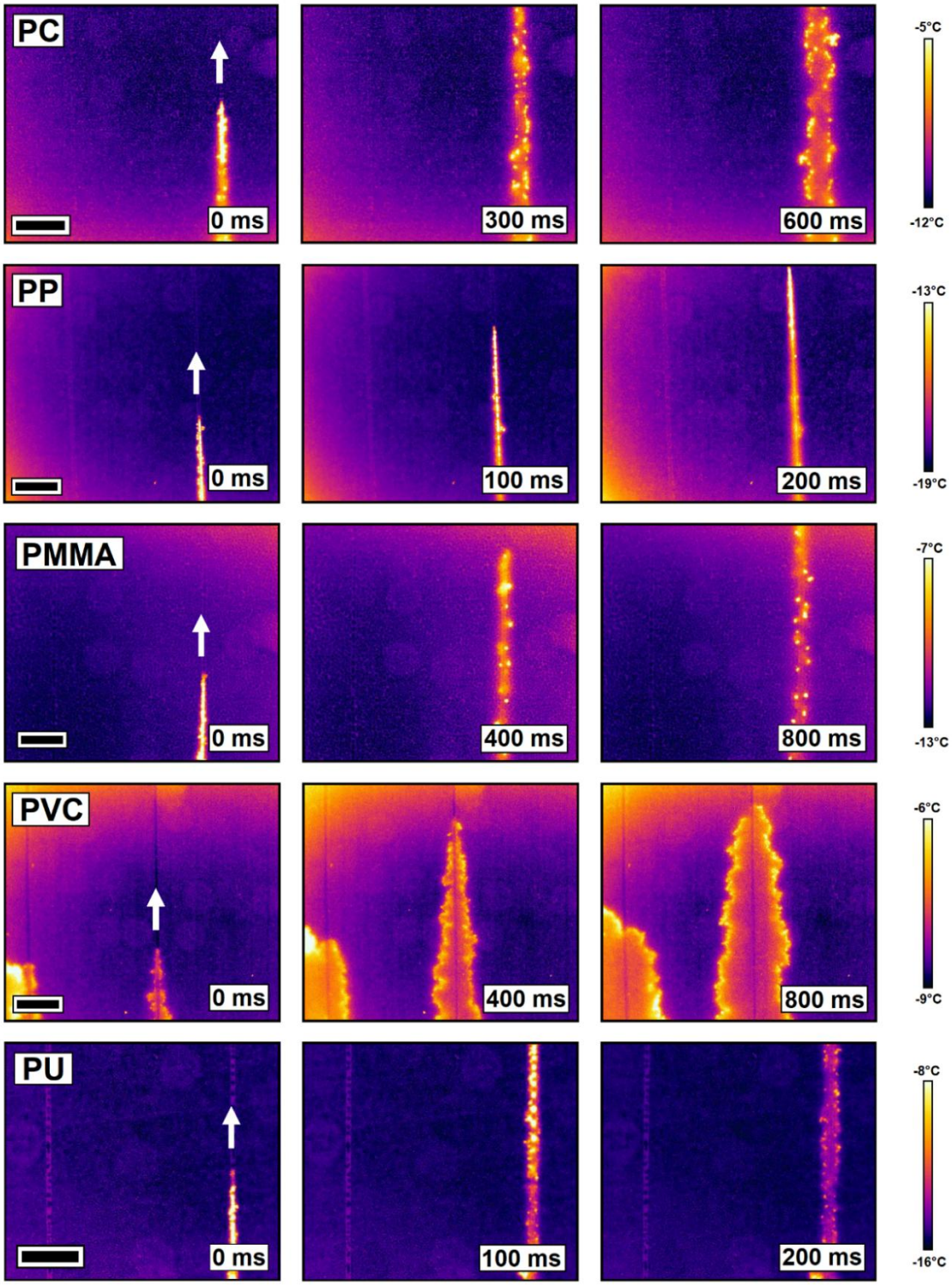

Figure S3.5. Time snapshots from thermal videos showing a freezing front propagating on the polymer substrates modified with PHEMA-stripes exposed to **50 %** RH. The white arrows indicate the direction of the freezing front propagation on the hydrophilic PHEMA-stripe. The black scale bar shown in the bottom left corner of the first images is 2 mm.

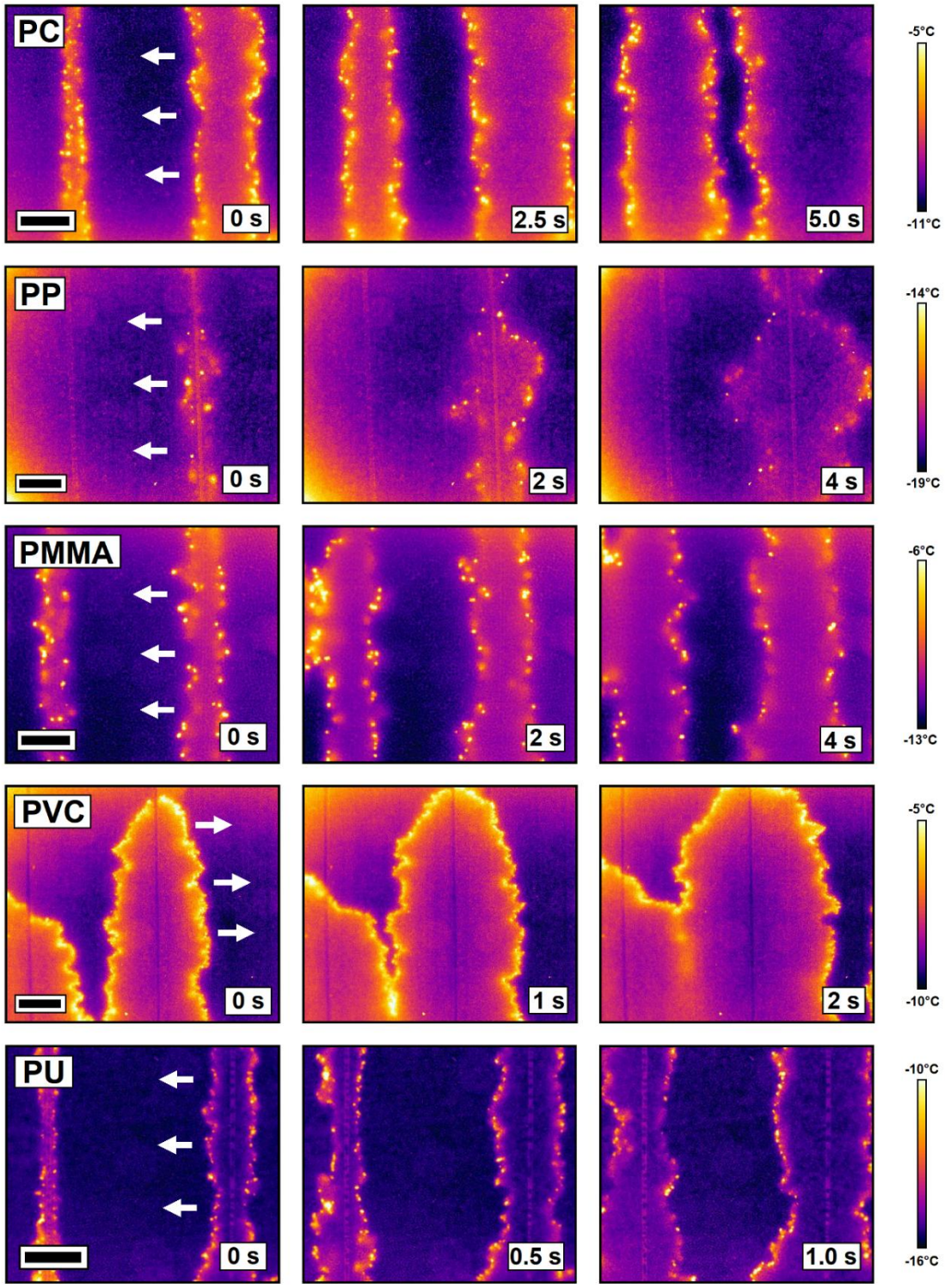

Figure S3.6. Time snapshots from thermal videos showing a freezing front propagating on the polymer substrates modified with PHEMA-stripes exposed to **50 %** RH. The white arrows indicate the direction of the freezing front propagation on hydrophobic polymer substrate. The black scale bar shown in the bottom left corner of the first images is 2 mm.

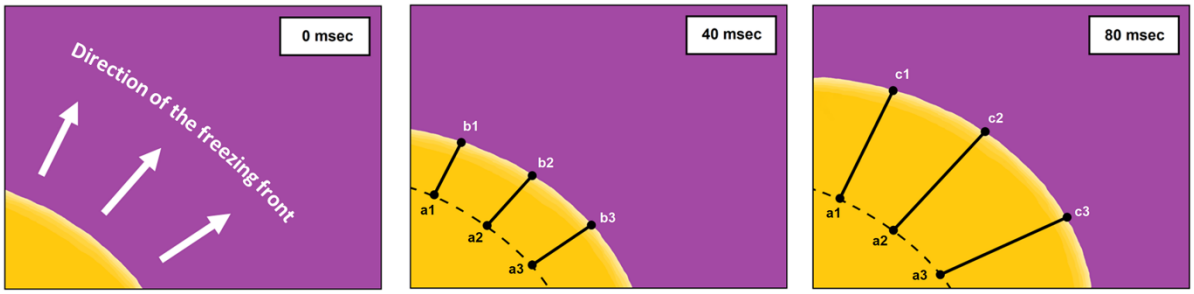

Figure S3.7. Calculation of the freezing front propagation rates (mm s^{-1}) from the thermal video snapshots using ImageJ. The distance that the freezing front propagates between two snapshots (distance between points a-b and a-c) is divided by the time difference between the two snapshots (40 msec and 80 msec). This method is repeated for the video for a series of snapshots and points along the freezing front line to obtain an average propagation rate.

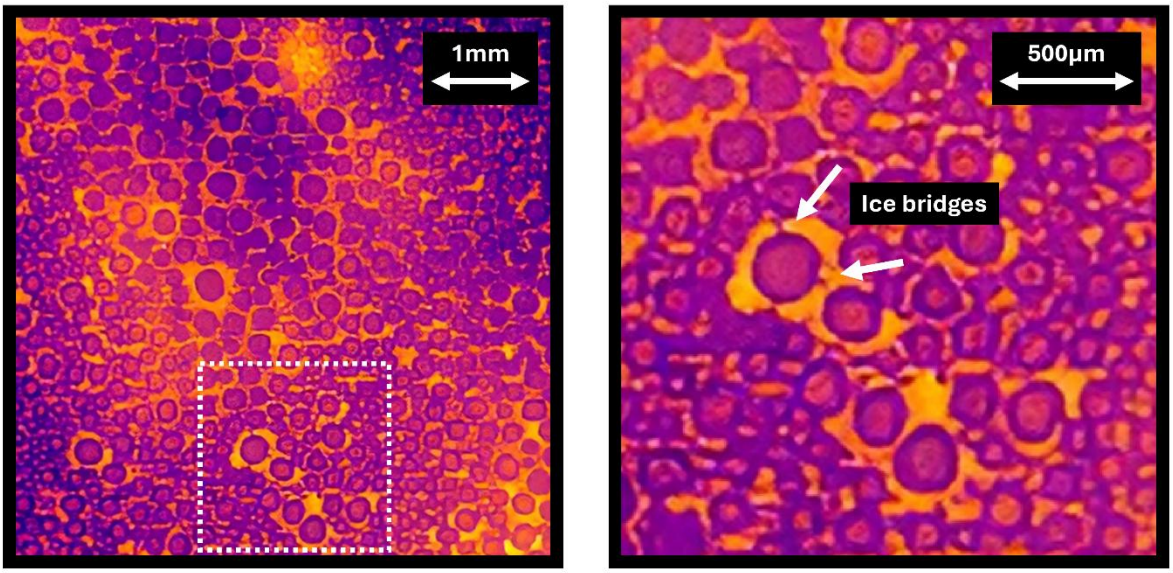

Figure S3.8. Time snapshot (left) and its close-up image (right) from a thermal imaging video showing the surface freezing of PC substrate at 50 % RH with frozen condensation on top. The numerous connecting pathways between the frozen droplets are here identified as inter-droplet ice bridges.

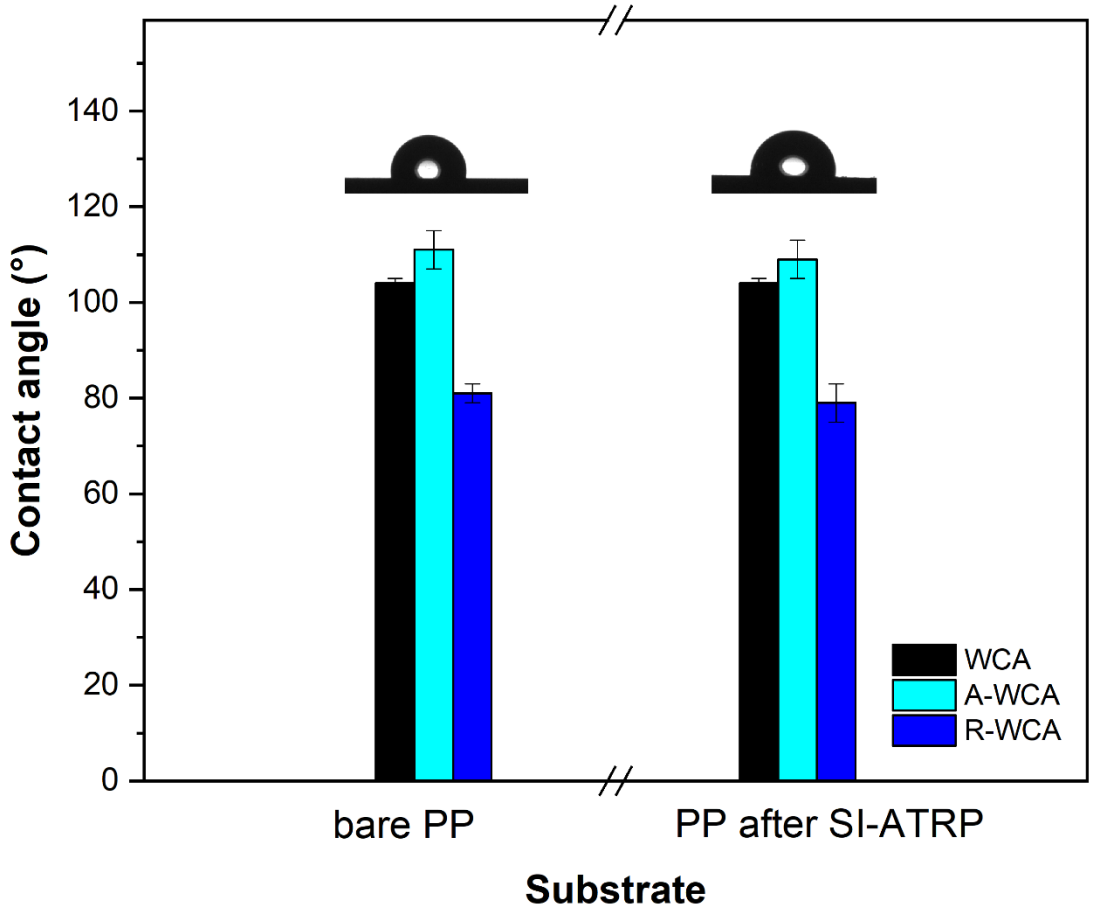

Figure S3.9. Water contact angle (S-WCA, A-WCA, R-WCA) values of PP before and after the patterning process. The patterning process did not influence the wettability of the PP substrate in areas that were not exposed to the UV light.

Movie S3.1. QR code to access a thermal video of percolation-controlled frost growth on PC.

Movie S3.2. QR code to access a thermal video of MWL-promoted frost propagation on PHEMA-grafted PP.

Movie S3.3. QR code to access a thermal video of freezing propagation on PP with PHEMA stripes.

REFERENCES

(1) Lin, Y.; Chen, H.; Wang, G.; Liu, A. Recent Progress in Preparation and Anti-Icing Applications of Superhydrophobic Coatings. *Coatings* **2018**, *8*, 208. https://doi.org/10.3390/coatings8060208.

(2) Shen, Y.; Wu, X.; Tao, J.; Zhu, C.; Lai, Y.; Chen, Z. Icephobic Materials: Fundamentals, Performance Evaluation, and Applications. *Progress in Materials Science*. Elsevier Ltd June 1, 2019, pp 509–557. https://doi.org/10.1016/j.pmatsci.2019.03.004.

(3) Huang, X.; Tepylo, N.; Pommier-Budinger, V.; Budinger, M.; Bonaccurso, E.; Villedieu, P.; Bennani, L. A Survey of Icephobic Coatings and Their Potential Use in a Hybrid Coating/Active Ice Protection System for Aerospace Applications. *Progress in Aerospace Sciences*. Elsevier Ltd February 1, 2019, pp 74–97. https://doi.org/10.1016/j.paerosci.2019.01.002.

(4) Hernández Rodríguez, G.; Fratschko, M.; Stendardo, L.; Antonini, C.; Resel, R.; Coclite, A. M. Icephobic Gradient Polymer Coatings Deposited via ICVD: A Novel Approach for Icing Control and Mitigation. *ACS Appl. Mater. Interfaces* **2024**, *16* (9), 11901–11913. https://doi.org/10.1021/acsami.3c18630.

(5) Hernández Rodríguez, G.; Gastaldo, G.; Stendardo, L.; Rafik, Y.; Pothin, J.; Budinger, M.; Antonini, C.; Pommier-Budinger, V.; Coclite, A. M. Icephobic Gradient Polymer Coatings Coupled with Electromechanical De-Icing Systems: A Promising Ice Repellent Hybrid System. *Adv. Eng. Mater.* **2025**, *27* (13), 2401532. https://doi.org/https://doi.org/10.1002/adem.202401532.

(6) Zhou, X.; Sun, Y.; Liu, J. Designing Anti-Icing Surfaces by Controlling Ice Formation. *Advanced Materials Interfaces*. John Wiley and Sons Inc September 1, 2021. https://doi.org/10.1002/admi.202100327.

(7) Liu, Y.; Wu, Y.; Liu, S.; Zhou, F. Material Strategies for Ice Accretion Prevention and Easy Removal. *ACS Mater. Lett.* **2022**, *4* (2), 246–262. https://doi.org/10.1021/acsmaterialslett.1c00365.

(8) Hu, J.; Xiao, X.-D.; Ogletree, D. F.; Salmeron, M. Imaging the Condensation and Evaporation of Molecularly Thin Films of Water with Nanometer Resolution. *Science (1979).* **1995**, *268* (5208), 267. https://doi.org/10.1126/science.268.5208.267.

(9) James, M.; Darwish, T. A.; Ciampi, S.; Sylvester, S. O.; Zhang, Z.; Ng, A.; Gooding, J. J.; Hanley, T. L. Nanoscale Condensation of Water on Self-Assembled Monolayers. *Soft Matter* **2011**, *7* (11), 5309–5318. https://doi.org/10.1039/c1sm05096f.

(10) Shimizu, T. K.; Maier, S.; Verdaguer, A.; Velasco-Velez, J. J.; Salmeron, M. Water at Surfaces and Interfaces: From Molecules to Ice and Bulk Liquid. *Prog. Surf. Sci.* **2018**, *93* (4), 87–107. https://doi.org/10.1016/j.progsurf.2018.09.004.

(11) Spagnoli, C.; Loos, K.; Ulman, A.; Cowman, M. K. Imaging Structured Water and Bound Polysaccharide on Mica Surface at Ambient Temperature. *J. Am. Chem. Soc.* **2003**, *125* (23), 7124–7128. https://doi.org/10.1021/ja029721j.

(12) Sumner, A. L.; Menke, E. J.; Dubowski, Y.; Newberg, J. T.; Penner, R. M.; Hemminger, J. C.; Wingen, L. M.; Brauers, T.; Finlayson-Pitts, B. J. The Nature of Water on Surfaces of Laboratory Systems and Implications for Heterogeneous Chemistry in the Troposphere. *Physical Chemistry Chemical Physics* **2004**, *6* (3), 604–613. https://doi.org/10.1039/B308125G.

(13) Asay, D. B.; Kim, S. H. Evolution of the Adsorbed Water Layer Structure on Silicon Oxide at Room Temperature. *Journal of Physical Chemistry B* **2005**, *109* (35), 16760–16763. https://doi.org/10.1021/jp053042o.

(14) Bluhm, H.; Inoue, T.; Salmeron, M. Formation of Dipole-Oriented Water Films on Mica Substrates at Ambient Conditions. *Surf. Sci.* **2000**, *462* (1–3), L599–L602. https://doi.org/10.1016/S0039-6028(00)00595-1.

(15) Miranda, P. B.; Xu, L.; Shen, Y. R.; Salmeron, M. Icelike Water Monolayer Adsorbed on Mica at Room Temperature. *Phys. Rev. Lett.* **1998**, *81* (26), 5876–5879. https://doi.org/10.1103/PhysRevLett.81.5876.

(16) Santos, S.; Verdaguer, A. Imaging Water Thin Films in Ambient Conditions Using Atomic Force Microscopy. *Materials* **2016**, *9* (3). https://doi.org/10.3390/ma9030182.

(17) Tavaststjerna, M. J.; Picken, S. J.; Garcia, S. J. Role of Molecular Water Layer State on Freezing Front Propagation Rate and Mode Studied with Thermal Imaging. *Langmuir* **2024**, *40* (25), 12888–12898. https://doi.org/10.1021/acs.langmuir.4c00323.

(18) Garrod, R. P.; Harris, L. G.; Schofield, W. C. E.; McGettrick, J.; Ward, L. J.; Teare, D. O. H.; Badyal, J. P. S. Mimicking a Stenocara Beetle's Back for Microcondensation Using Plasmachemical Patterned Superhydrophobic-Superhydrophilic Surfaces. *Langmuir* **2007**, *23* (2), 689–693. https://doi.org/10.1021/la0610856.

(19) Varanasi, K. K.; Hsu, M.; Bhate, N.; Yang, W.; Deng, T. Spatial Control in the Heterogeneous Nucleation of Water. *Appl. Phys. Lett.* **2009**, *95* (9). https://doi.org/10.1063/1.3200951.

(20) Yu, Z.; Yun, F. F.; Wang, Y.; Yao, L.; Dou, S.; Liu, K.; Jiang, L.; Wang, X. Desert Beetle-Inspired Superwettable Patterned Surfaces for Water Harvesting. *Small* **2017**, *13* (36), 1701403. https://doi.org/https://doi.org/10.1002/smll.201701403.

(21) Bai, H.; Wang, L.; Ju, J.; Sun, R.; Zheng, Y.; Jiang, L. Efficient Water Collection on Integrative Bioinspired Surfaces with Star-Shaped Wettability Patterns. *Advanced Materials* **2014**, *26* (29), 5025–5030. https://doi.org/10.1002/adma.201400262.

(22) Dimitriadis, T.; Stendardo, L.; Tagliaro, I.; Coclite, A. M.; Antonini, C.; Maitra, T. Capillary-Driven Water Transport by Contrast Wettability-Based Durable Surfaces. *ACS Appl. Mater. Interfaces* **2023**, *15* (22), 27206–27213. https://doi.org/10.1021/acsami.3c03840.

(23) Chen, Z.; Zhang, Z. Recent Progress in Beetle-Inspired Superhydrophilic-Superhydrophobic Micropatterned Water-Collection Materials. *Water Science and Technology* **2020**, *82* (2), 207–226. https://doi.org/10.2166/wst.2020.238.

(24) Oliveira, N. M.; Vilabril, S.; Oliveira, M. B.; Reis, R. L.; Mano, J. F. Recent Advances on Open Fluidic Systems for Biomedical Applications: A Review. *Materials Science and Engineering: C* **2019**, *97*, 851–863. https://doi.org/10.1016/j.msec.2018.12.040.

(25) Segawa, Y.; Kinoshita, K.; Kai, H. Efficient Collection of Oil Microdroplets by Hyperbranched, Space-Filling Open Microfluidic Channels. *Adv. Mater. Interfaces* **2023**, *10* (36), 2300340. https://doi.org/https://doi.org/10.1002/admi.202300340.

(26) Gao, C.; Zhang, L.; Hou, Y.; Zheng, Y. A UV-Resistant Heterogeneous Wettability-Patterned Surface. *Advanced Materials* **2023**, *35* (42), 2304080. https://doi.org/https://doi.org/10.1002/adma.202304080.

(27) Li, Y.; Liu, B. F.; Zhang, X. Wettability-Patterned Microchip for Emerging Biomedical Materials and Technologies. *Materials Today* **2021**, *51*, 273–293. https://doi.org/10.1016/j.mattod.2021.10.008.

(28) Mishchenko, L.; Khan, M.; Aizenberg, J.; Hatton, B. D. Spatial Control of Condensation and Freezing on Superhydrophobic Surfaces with Hydrophilic Patches. *Adv. Funct. Mater.* **2013**, *23* (36), 4577–4584. https://doi.org/10.1002/adfm.201300418.

(29) Kirillova, A.; Ionov, L.; Roisman, I. V.; Synytska, A. Hybrid Hairy Janus Particles for Anti-Icing and de-Icing Surfaces: Synergism of Properties and Effects. *Chemistry of Materials* **2016**, *28* (19), 6995–7005. https://doi.org/10.1021/acs.chemmater.6b02765.

(30) Boreyko, J. B.; Hansen, R. R.; Murphy, K. R.; Nath, S.; Retterer, S. T.; Collier, C. P. Controlling Condensation and Frost Growth with Chemical Micropatterns. *Sci. Rep.* **2016**, *6*. https://doi.org/10.1038/srep19131.

(31) O'Brien, J. L.; Ahmadi, S. F.; Failor, K. C.; Bisbano, C. E.; Mulroe, M. D.; Nath, S.; Vinatzer, B. A.; Boreyko, J. B. Spatial Control of Condensation and Desublimation Using Ice Nucleating Proteins. *Appl. Phys. Lett.* **2018**, *113* (15), 153701. https://doi.org/10.1063/1.5046187.

(32) Jin, Y.; Wu, C.; Yang, Y.; Wu, J.; He, Z.; Wang, J. Inhibiting Condensation Freezing on Patterned Polyelectrolyte Coatings. *ACS Nano* **2020**, *14* (4), 5000–5007. https://doi.org/10.1021/acsnano.0c01304.

(33) Lo, C.-W.; Sahoo, V.; Lu, M.-C. Control of Ice Formation. *ACS Nano* **2017**, *11* (3), 2665–2674. https://doi.org/10.1021/acsnano.6b07348.

(34) Williams, R.; Blanc, J. Inhibition of Water Condensation by a Soluble Salt Nucleus. *J. Chem. Phys.* **1981**, *74* (8), 4675–4677. https://doi.org/10.1063/1.441658.

(35) Nath, S.; Boreyko, J. B. On Localized Vapor Pressure Gradients Governing Condensation and Frost Phenomena. *Langmuir* **2016**, *32* (33), 8350–8365. https://doi.org/10.1021/acs.langmuir.6b01488.

(36) Nath, S.; Bisbano, C. E.; Yue, P.; Boreyko, J. B. Duelling Dry Zones around Hygroscopic Droplets. *J. Fluid Mech.* **2018**, *853*, 601–620. https://doi.org/DOI: 10.1017/jfm.2018.579.

(37) Guadarrama-Cetina, J.; Narhe, R. D.; Beysens, D. A.; González-Viñas, W. Droplet Pattern and Condensation Gradient around a Humidity Sink. *Phys. Rev. E* **2014**, *89* (1), 12402. https://doi.org/10.1103/PhysRevE.89.012402.

(38) Guadarrama-Cetina, J.; Mongruel, A.; González-Viñas, W.; Beysens, D. Frost Formation with Salt. *EPL* **2015**, *110* (5). https://doi.org/10.1209/0295-5075/110/56002.

(39) Sun, X.; Damle, V. G.; Uppal, A.; Linder, R.; Chandrashekar, S.; Mohan, A. R.; Rykaczewski, K. Inhibition of Condensation Frosting by Arrays of Hygroscopic Antifreeze Drops. *Langmuir* **2015**, *31* (51), 13743–13752. https://doi.org/10.1021/acs.langmuir.5b03869.

(40) Montano, V.; Wempe, M. M. B.; Does, S. M. H.; Bijleveld, J. C.; van der Zwaag, S.; Garcia, S. J. Controlling Healing and Toughness in Polyurethanes by Branch-Mediated Tube Dilation. *Macromolecules* **2019**, *52* (21), 8067–8078. https://doi.org/10.1021/acs.macromol.9b01554.

(41) Zhu, J.; Zhou, D.; Zhu, X.; Chen, G. Reversible Addition–Fragmentation Chain Transfer Polymerization of Glycidyl Methacrylate with 2-Cyanoprop-2-Yl 1-Dithionaphthalate as a Chain-Transfer Agent. *J. Polym. Sci. A Polym. Chem.* **2004**, *42* (10), 2558–2565. https://doi.org/https://doi.org/10.1002/pola.20119.

(42) Gudipati, C. S.; Tan, M. B. H.; Hussain, H.; Liu, Y.; He, C.; Davis, T. P. Synthesis of Poly(Glycidyl Methacrylate)-Block-Poly(Pentafluorostyrene) by RAFT: Precursor to Novel Amphiphilic Poly(Glyceryl Methacrylate)-Block-Poly(Pentafluorostyrene). *Macromol. Rapid Commun.* **2008**, *29* (23), 1902–1907. https://doi.org/https://doi.org/10.1002/marc.200800515.

(43) Cheng, Z.; Zhu, X.; Fu, G. D.; Kang, E. T.; Neoh, K. G. Dual-Brush-Type Amphiphilic Triblock Copolymer with Intact Epoxide Functional Groups from Consecutive RAFT Polymerizations and ATRP. *Macromolecules* **2005**, *38* (16), 7187–7192. https://doi.org/10.1021/ma050536a.

(44) Thankappan, H.; Semsarilar, M.; Li, S.; Chang, Y.; Bouyer, D.; Quemener, D. Synthesis of Block Copolymer Brush by RAFT and Click Chemistry and Its Self-Assembly as a Thin Film. *Molecules* **2020**, *25* (20). https://doi.org/10.3390/molecules25204774.

(45) Zhao, C.; Wu, D.; Lian, X.; Zhang, Y.; Song, X.; Zhao, H. Amphiphilic Asymmetric Comb Copolymer with Pendant Pyrene Groups and PNIPAM Side Chains: Synthesis, Photophysical Properties, and Self-Assembly. *J. Phys. Chem. B* **2010**, *114* (19), 6300–6308. https://doi.org/10.1021/jp1007494.

(46) Pranantyo, D.; Xu, L. Q.; Neoh, K. G.; Kang, E. T.; Yang, W.; Teo, S. L. M. Photoinduced Anchoring and Micropatterning of Macroinitiators on Polyurethane Surfaces for Graft Polymerization of Antifouling Brush Coatings. *J. Mater. Chem. B* **2014**, *2* (4), 398–408. https://doi.org/10.1039/c3tb21201g.

(47) Panzarasa, G.; Aghion, S.; Marra, G.; Wagner, A.; Liedke, M. O.; Elsayed, M.; Krause-Rehberg, R.; Ferragut, R.; Consolati, G. Probing the Impact of the Initiator Layer on Grafted-from Polymer Brushes: A Positron Annihilation Spectroscopy Study. *Macromolecules* **2017**, *50* (14), 5574–5581. https://doi.org/10.1021/acs.macromol.7b00953.

(48) Zhang, Y.; He, H.; Gao, C. Clickable Macroinitiator Strategy to Build Amphiphilic Polymer Brushes on Carbon Nanotubes. *Macromolecules* **2008**, *41* (24), 9581–9594. https://doi.org/10.1021/ma801696z.

(49) Nath, S.; Ahmadi, S. F.; Boreyko, J. B. How Ice Bridges the Gap. *Soft Matter* **2020**, *16* (5), 1156–1161. https://doi.org/10.1039/C9SM01968E.

(50) Guadarrama-Cetina, J.; Mongruel, A.; González-Viñas, W.; Beysens, D. Percolation-Induced Frost Formation. *EPL (Europhysics Letters)* **2013**, *101* (1), 16009. https://doi.org/10.1209/0295-5075/101/16009.

(51) Paulovics, D.; Raufaste, C.; Frisch, T.; Claudet, C.; Celestini, F. Dynamics of Frost Propagation on Breath Figures. *Langmuir* **2022**, *38* (9), 2972–2978. https://doi.org/10.1021/acs.langmuir.1c03463.

(52) Zhao, Y.; Yang, C. Frost Spreading on Microscale Wettability/Morphology Patterned Surfaces. *Appl. Therm. Eng.* **2017**, *121*, 136–145. https://doi.org/https://doi.org/10.1016/j.applthermaleng.2017.04.063.

(53) Zhao, Y.; Wang, R.; Yang, C. Interdroplet Freezing Wave Propagation of Condensation Frosting on Micropillar Patterned Superhydrophobic Surfaces of Varying Pitches. *Int. J. Heat Mass Transf.* **2017**, *108*, 1048–1056. https://doi.org/10.1016/j.ijheatmasstransfer.2016.12.112.

(54) Zhao, Y.; Yang, C. Retarded Condensate Freezing Propagation on Superhydrophobic Surfaces Patterned with Micropillars. *Appl. Phys. Lett.* **2016**, *108* (6), 061605. https://doi.org/10.1063/1.4941927.

(55) Haque, M. R.; Das, S. R.; Betz, A. R. Experimental Investigation of Condensation and Freezing Phenomena on Hydrophilic and Hydrophobic Graphene Coating. *Appl. Therm. Eng.* **2019**, *160*, 113987. https://doi.org/10.1016/j.applthermaleng.2019.113987.

(56) Schremb, M.; Roisman, I. V; Tropea, C. Normal Impact of Supercooled Water Drops onto a Smooth Ice Surface: Experiments and Modelling. *J. Fluid Mech.* **2018**, *835*, 1087–1107. https://doi.org/DOI: 10.1017/jfm.2017.797.

(57) Castillo, J. E.; Huang, Y.; Pan, Z.; Weibel, J. A. Quantifying the Pathways of Latent Heat Dissipation during Droplet Freezing on Cooled Substrates. *Int. J. Heat Mass Transf.* **2021**, *164*, 120608. https://doi.org/https://doi.org/10.1016/j.ijheatmasstransfer.2020.120608.

(58) Meng, Z.; Zhang, P. Dynamic Propagation of Ice-Water Phase Front in a Supercooled Water Droplet. *Int. J. Heat Mass Transf.* **2020**, *152*. https://doi.org/10.1016/j.ijheatmasstransfer.2020.119468.

(59) Schremb, M.; Roisman, I.; Tropea, C. Different Outcomes after Inclined Impacts of Water Drops on a Cooled Surface; 2015.

(60) Curiotto, S.; Paulovics, D.; Raufaste, C.; Celestini, F.; Frisch, T.; Leroy, F.; Cheynis, F.; Müller, P. Atomistic Description of Interdroplet Ice-Bridge Formation during Condensation Frosting. *Langmuir* **2023**, *39* (1), 579–587. https://doi.org/10.1021/acs.langmuir.2c02860.

4

The Influence of Chemical Surface Patterning on the Freezing Behaviour of Impacting Supercooled Water Droplets

Abstract: Impacting supercooled water droplets commonly cause in-flight ice accumulation on aircraft surfaces. Ice accretion can lead to dangerous situations such as disturbance of airflow around the aircraft wings, breakdown of vital antennae, or even malfunction of the engines. The adverse effects of aircraft icing could be avoided by designing passive anti-icing surfaces that either delay ice nucleation after droplet impact and/or reduce ice adhesion to promote its shedding. Among potential passive anti-icing strategies, smooth surfaces with patterned hydrophilic and hydrophobic regions have shown good potential to control local frost formation. In this study, we investigate how hydrophilic 150µm wide stripes influence the impact and freezing of supercooled water droplets on two polymeric substrates (Polyvinylchloride and Polypropylene). In addition to varying the wettability difference between the stripes and the substrate, the distance between the stripes (1.25—10 mm) and the impact velocity of the water droplet (4.1—6.5 m/s) were varied. High-speed video analysis of the impacting droplets shows that the presence of the hydrophilic patterns can lower ice nucleation rates and direct the shape of the droplet spreading after impact. However, a low wettability difference between the substrate and the patterns can lead to the opposite scenario with higher nucleation rates.

INTRODUCTION

Due to significant safety hazards and increased fuel consumption, ice accretion on aircraft wings, engines, and antennae is a substantial concern for aviation[1-3]. Currently, in-flight ice accretion is managed using various active de-icing methods that rely on external energy, including thermal protection through heating wing surfaces, chemical protection by spraying the surfaces with de-icing fluids, or mechanical protection by attaching inflatable pneumatic boots onto the wings. Since these active methods increase energy consumption and add weight to the aircraft, an alternative strategy could be to create passive anti-icing coatings that inherently delay ice nucleation and/or reduce ice adhesion, thus promoting its shedding[3-6]. The most researched passive anti-icing strategies rely on water-repelling superhydrophobic surfaces or slippery liquid-infused surfaces, while concepts combining stiffness and chemical patterning are gaining attention.

Although some passive anti/low icing technologies effectively reduce condensation frosting and ice adhesion strength, their performance in dynamic icing conditions, more relevant from the in-flight perspective, requires further research. The case of supercooled impact droplets is even less studied due to its complexity. When an aircraft passes through cold cloud formations, supercooled water droplets within the clouds impact the aircraft's surface at high velocities. In the particular case of water-repelling superhydrophobic surfaces and slippery liquid-infused surfaces, the impacting water droplets freeze quickly upon impact and generate fast-growing layers of ice that mechanically interlock with the rough superhydrophobic surface structures, leading to higher ice adhesion or wear out the lubricating liquids from the surface, hence reducing the long-term efficiency[7-12].

Alternatively, surfaces combining hydrophilic and hydrophobic regions have shown some success in controlling static frost propagation and condensation in high and low supersaturation conditions[13-15]. These patterned wettability surfaces have also attracted interest for applications related to dynamic icing conditions with the aim of controlling where and what type of ice forms on the aircraft's surface[4,16,17]. However, to construct a rational design for a chemically patterned anti-icing coating, it is imperative to understand

the physics of supercooled water droplet impact on uniform and patterned surfaces, an aspect so far not investigated.

The state-of-the-art in supercooled droplet impact studies make use of high-speed imaging and the interpretation of the videos through thermodynamics and hydrodynamics to study the mechanisms involved in the impact and solidification of supercooled water droplets[18-21]. Once a supercooled water droplet impacts a smooth surface, the droplet spreads and then recedes, forming a thin film over the surface. During this process, air bubbles can become entrapped within the film, introducing localized instabilities in the liquid and creating favourable conditions for ice nucleation and subsequent solidification[20].

Since nucleation events in the film are stochastic, multiple experiments of the same sample under the same conditions must be analysed to understand the droplet freezing behaviour. To compare the freezing behaviour of different samples in different environments quantitatively, a statistical model[22] can be used to derive the rate of heterogeneous nucleation per unit area $J_s(t)$. During video analysis, the droplet freezing onset time is recorded individually for each experiment. For each recorded freezing onset time (t), the average number of nucleation sites per unit area at time t, $\lambda_s(t)$, can be estimated by[20,22]

$$\lambda_{\mathrm{s}}(t) = \frac{1}{A_{\mathrm{c}}(t)} \ln\left(\frac{N_0}{N_{\mathrm{liq}}(t)}\right) \equiv \int_0^t J_{\mathrm{s}} dt \tag{4.1}$$

where $A_c(t)$ is the wetted surface area of the droplet at freezing onset time (t), $N_{\mathrm{liq}}(t)$ is the number of experiments where the freezing onset time is higher than time (t), and N_0 is the overall number of experiments. Even though this statistical model has been used to compare droplet nucleation rates on various uniform aluminium and superhydrophobic surfaces in different environmental conditions[20,22,23] it has not yet been applied to patterned wettability surfaces.

So far, only a few studies have investigated the dynamic behaviour of impacting water droplets on patterned wettability surfaces[24-29]. However, these studies rely on computational modelling and focus on droplet impact and wetting in a room temperature environment, instead of supercooled conditions. One of these simulates the impact of

glycerol droplets (diameter D_0 = 2.45 mm and impact velocity 0.2 m/s ≤ U_0 ≤ 2 m/s) on hydrophobic surfaces (static water contact angle WCA~95°) patterned with four hydrophilic squares (WCA~15°) using an immersed boundary-based framework[25]. The results show how the droplet breaks into four sections at impact, followed by selective wetting of the four hydrophilic areas. Although this work focuses on glycerol droplets at room temperature conditions, it demonstrates the ability of hydrophilic patterning to influence the shape of the thin film after droplet impact by sufficient dewetting at the hydrophobic substrate combined with easy wetting of the hydrophilic square patterns.

A similar study models the impact of water droplets (diameter D_0 = 0.025 mm) on hydrophilic glass (WCA~45°) patterned with cross-shaped or inverted cross-shaped hydrophobic areas (WCA~120°) using a multiphase lattice Boltzmann method[24]. This simulation also showed the water droplet splitting and transporting toward the hydrophilic regions, with experimental results supporting the numerical models. While the impacting water droplets have been shown to deform, split, and spread according to the hydrophilic pattern design in ambient conditions, the ability of the patterning to influence dynamic droplet freezing behaviour is yet unknown. Potentially, patterned wettability surfaces could help direct the freezing of impacting droplets to a specific shape or spatial distribution in dynamic icing conditions, which may help to reduce airflow disruption around aircraft wings or simply lower the ice adhesion or facilitate ice separation.

So far, the influence of wettability patterns on droplet impact has promising computational results; however, only a few experimental studies support these numerical models. Furthermore, neither numerical simulations nor experimental studies have been reported for droplet impact on patterned wettability surfaces in cooled or supercooled conditions. Although patterned wettability surfaces have already been suggested as a solution for impact icing conditions, the literature lacks any systematic experimental evidence to support this proposition. This work presents the first systematic investigation of the influence of patterned wettability on supercooled water droplet impact, wetting, and freezing behaviour on surfaces. The supercooled droplet impact experiments were carried out with three different impact velocities on polymeric substrates patterned with hydrophilic

stripes. Two types of commodity polymers (PP and PVC) were functionalized with hydrophilic poly(2-hydroxyethyl methacrylate) (PHEMA) brushes to prepare the patterned samples. Samples with varying numbers of hydrophilic stripes were used to examine the influence of stripe-to-stripe distance on the dynamic droplet impact behaviour. The droplet impact, wetting, and freezing dynamics are here related to the substrate type, hydrophilic stripe distance, and droplet impact velocity using high-speed camera imaging and statistical analysis of the high-speed videos.

MATERIALS AND METHODS

Sample Preparation

The polymeric substrates PP and PVC (20 x 20 x 1 mm) used in this work were purchased from S-Polytec GmbH, and were functionalized with poly(2-hydroxyethyl methacrylate) (PHEMA) grafted with the help of bifunctional macroinitiator PAzBrMA as reported in Chapter 3.[15] To create the stripes, UV masks with constant stripe width of 150 µm and varying stripe distances of 1.2 mm, 2.5 mm, 5 mm, and 10 mm were used to allow covalently fixing the macroinitiator only at stripe locations on the PVC and PP substrates upon exposure to a UV lamp (OmniCure S2000 UV Curing System, 320-500 nm) with 30 W/cm^2 for 5 min. This was followed by rinsing to remove the unreacted PAzBrMA, exposure to PHEMA for reaction with the macroinitiator at the stripe locations and rinsing again to remove the excess PHEMA. The resulting samples are polymeric substrates (PP or PVC) patterned with hydrophilic polymer brushes (PHEMA), which are covalently anchored to the substrate surface.

.

Water contact angle measurements

Water contact angles (WCA) of the bare and grafted polymer surfaces were determined using a KSV CAM 200 optical contact angle goniometer. Static, advancing, and receding contact angles were recorded using the sessile and needle-in-the-sessile-droplet methods. All measurements were repeated three times for each sample. For advancing and receding contact angles, the initial volume of the droplet (3 µL) was first increased with a pumping speed of 15 µL/s until a maximum droplet size of 15 µL. Then, the volume of the droplet was decreased from 15 µL back to 3 µL using the same pumping speed of 15 µL/s. All contact angle measurements were carried out at an ambient temperature of 21±2 ℃ and relative humidity of 40±5 %.

Surface Imaging

The polymeric substrates were imaged before and after the surface functionalization using Laser Scanning Confocal Microscopy (Keyence VK-X1000) and micro-FTIR (PerkinElmer Spotlight 400). The 3D Laser Scanning Confocal images were further analysed to determine area roughness values (Sa) for the sample surfaces.

Supercooled Water Droplet Impact Test

The droplet impact tests were conducted inside an L-shaped wind tunnel in isothermal conditions (-10 ℃) with airflow set to vary between 0, 10, and 20 m/s. A schematic presentation of the experimental setup for investigating supercooled droplet impact on the patterned surfaces is presented in **Figure 4.1**. The supercooled droplet was generated with a syringe needle on top of the wind tunnel, from where the droplet was directed to fall on top of the sample substrate placed at the test section of the vertical wind tunnel. To ensure that the impacting droplets were in a supercooled state, a thin thermocouple was kept inside the needle to monitor the droplet temperature during the experiments. Additionally, the samples were kept inside the wind tunnel for a minimum of 30 minutes before each experiment to cool them down to the desired surface temperature of -10 °C. The droplet

impact onto the sample surface was recorded with a high-speed camera (Photron SA-X2 k1080, 8000 fps, 52.91 µm/pixel). Since the droplet impact was imaged at an angle of 40°, a calibration algorithm was used to calculate distances during image processing. The droplet impact tests were repeated a minimum of 10 times for each sample per air flow condition. A detailed description of the experimental setup is provided elsewhere[20].

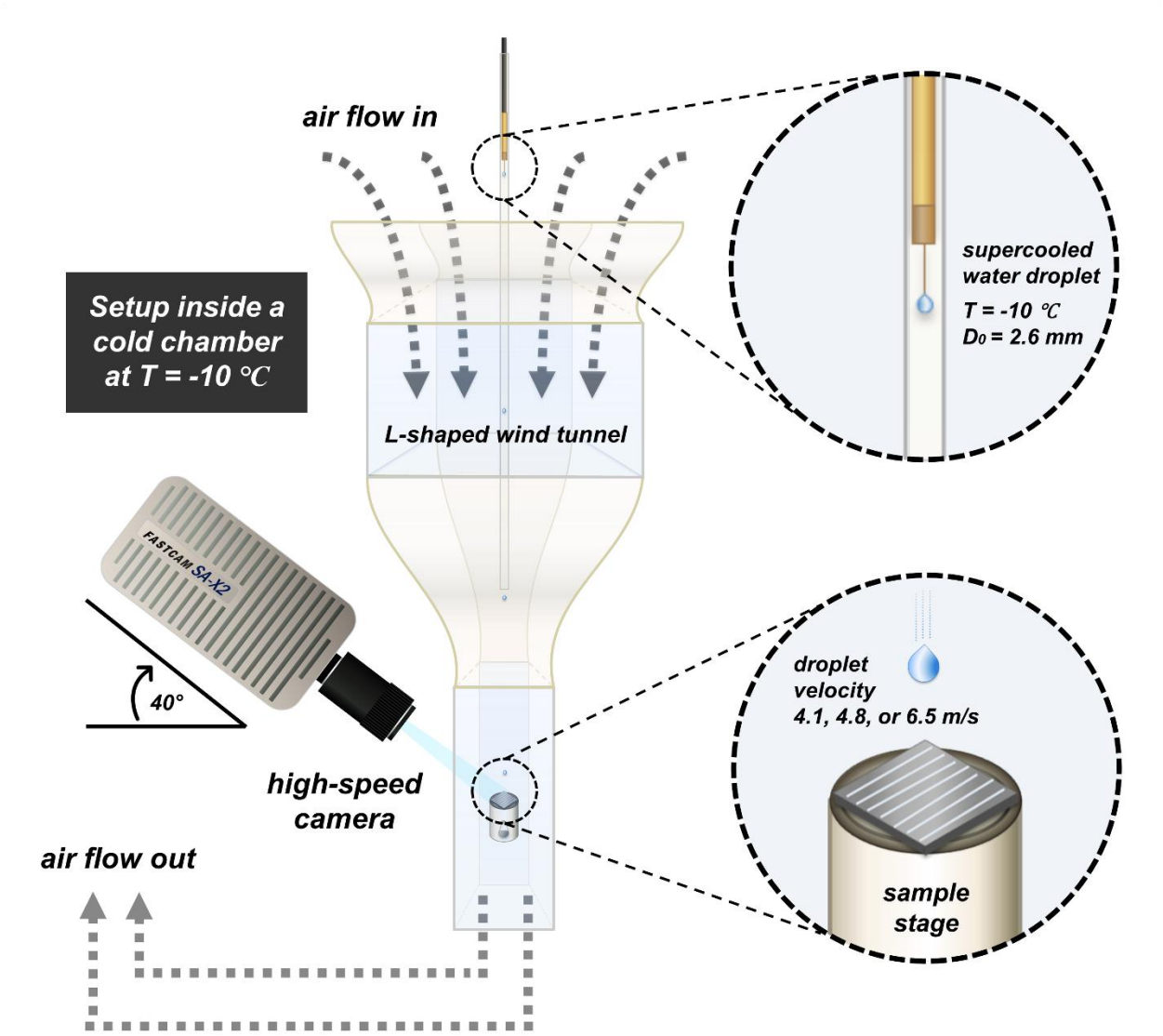

Figure 4.1. A schematic presentation of the experimental setup used for the supercooled droplet impact tests.

RESULTS AND DISCUSSION

Sample preparation

Two commodity polymeric substrates (PP and PVC) were functionalized with hydrophilic poly(2-hydroxyethyl methacrylate) (PHEMA) stripes to investigate supercooled droplet impact on patterned wettability surfaces. PP and PVC were selected as model polymeric substrates because they are widely used commodity polymers with substantially different wetting characteristics, as demonstrated in Chapter 3, enabling investigation of how substrate wettability influences freezing propagation behaviour. To ensure the durability of the patterning during repeated droplet impact tests on the same location, the hydrophilic PHEMA polymer was covalently linked to the substrates via a bifunctional macroinitiator PAzBrMA[15]. The azide functionalities of PAzBrMA enabled the covalent attachment of the macroinitiator to the substrate under UV light exposure, while the remaining bromide functionalities act as initiation points for surface-initiated atom transfer radical polymerization (SI-ATRP) of hydrophilic monomer HEMA.

To create the patterns, UV masks cut with 100 μm thin slits were placed on top of the substrates covered with PAzBrMA. Upon UV exposure, the PAzBrMA located at the areas where the slit is located becomes covalently bound to the surface, while the unreacted PAzBrMA chains beyond the slit openings can be rinsed away. This is followed by exposure to HEMA to polymerize where the fixed PAzBrMA is located (i.e., at the stripes). The distance between the stripes was varied from 1.25 mm to 10 mm by changing the design of the UV mask. As a result, 10 different types of samples: bare PP and PVC substrates with no stripes and PP and PVC patterned with a stripe distribution of 1.2 mm, 2.5 mm, 5 mm, and 10 mm.

As shown in **Figure 4.2**, PP shows about two times higher roughness (1.50 μm > 0.8 μm), slightly higher static water contact angle (101° > 96°) and lower contact angle hysteresis (30° < 59°) than is the case for PVC.

Confocal imaging and micro-FTIR confirmed fixation, stripe size, conformality, and roughness of the PHEMA patterns. The hydrophilic polymer brushes should be thin enough to avoid significantly changing the roughness of the sample surface, which could interfere with the droplet spreading behaviour and freezing probability. As seen in **Figures 4.2** and **S4.1**, the width of the stripes is approximately 150 µm, and the thickness is lower than 0.3 µm after 4 h of polymerization in HEMA solutions. Analysis of samples fully covered with PHEMA (without a mask during UV exposure) showed that the surface functionalization did not influence the overall roughness of the substrates. In contrast, the wettability of the PHEMA-covered areas was lowered to a static water contact angle of 41° (from initial 101° and 96° of PP and PVC, respectively).

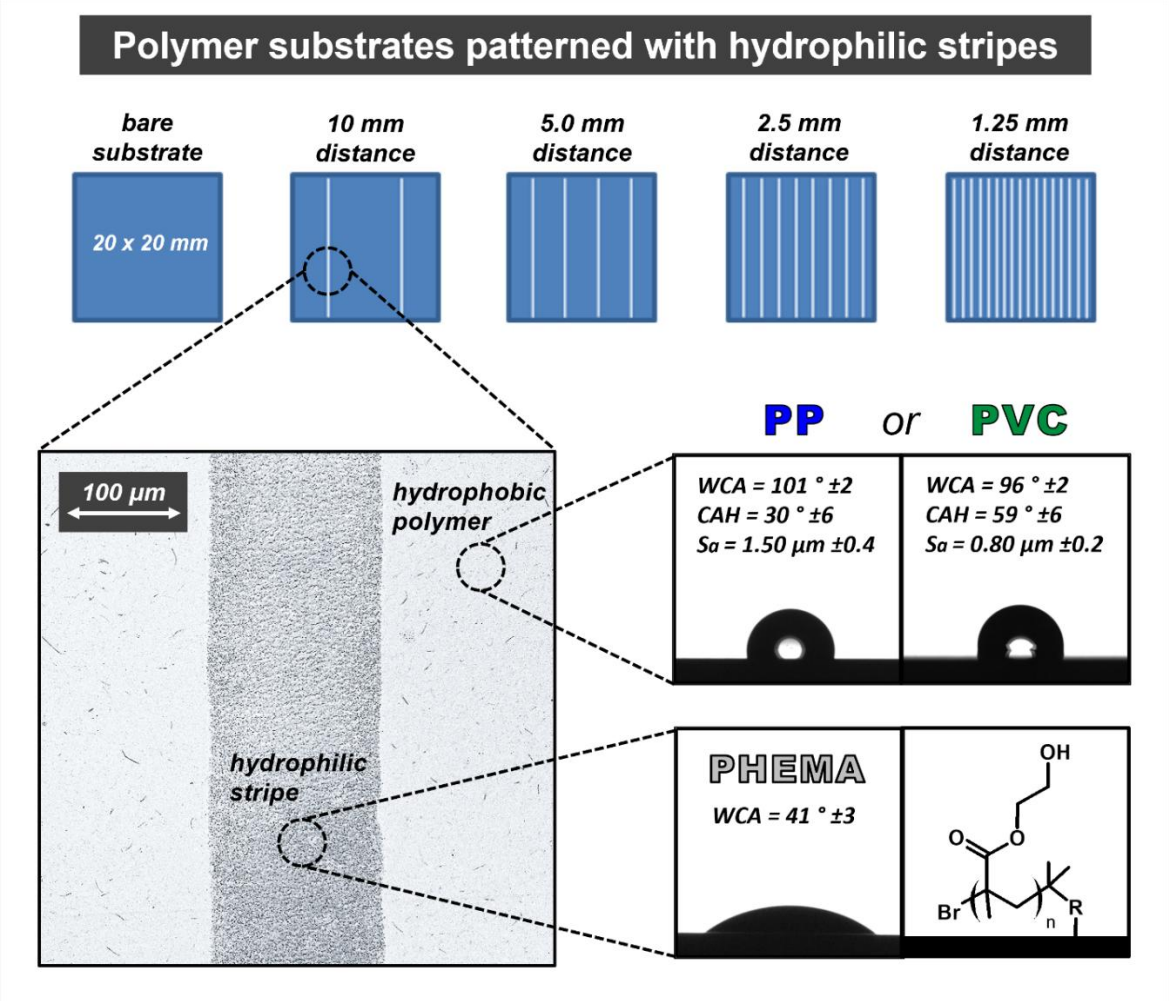

Figure 4.2. The PP and PVC substrates patterned with hydrophilic PHEMA stripes were imaged using confocal microscopy (left) to determine the stripe dimensions and the substrate roughness (S_a). Static water contact angle (WCA) and contact angle hysteresis (CAH) of the bare substrates and the hydrophilic stripes were determined using contact angle goniometry (right). The chemical structure of the hydrophilic PHEMA brushes can be seen in the bottom right corner.

Influence of hydrophilic patterns on droplet impact

In Supercooled droplet impact on the patterned surfaces was investigated in an L-shaped wind tunnel built inside a cold chamber (see **Figure 4.1**). Before each experiment, the sample was attached to a round sample stage positioned in the middle of the wind tunnel. The temperature inside the cold chamber was set to -10 °C, and the airflow inside the wind tunnel was varied between 0, 10, and 20 m/s, corresponding to droplet impact velocities of 4.1, 4.8, and 6.5 m/s, respectively. The droplet impact velocity is not linearly proportional to

the variation of airflow inside the wind tunnel because the droplet is pulled more efficiently toward the airflow at high wind speeds. At low wind speeds, the incremental benefit is small because the drop is still mostly gravity driven.

Figures 4.3 and **S4.2-S4.7** show time snapshots from four example videos, including droplet impact at a velocity of 6.5 m/s on both bare substrates (PP and PVC) and the same substrates patterned with PHEMA stripes (1.25 mm stripe distance). For each sample, the first image at t = -1 ms shows the square-shaped sample on the round stage holder and the falling supercooled droplet just above the sample. The second image at t = 0.3 ms shows the initial impact of the droplet, followed by an impact to represent droplet spread at t = 1 ms, and the receding process of the droplet at t = 30 ms. The fifth snapshot, at t = 150 ms, visualizes a high degree of receding (approximately maximum receding before freezing), while the last snapshot at t = 4000 ms shows frozen droplets. The exact time at which each transition takes place depends on the droplet, substrate, and test as discussed here.

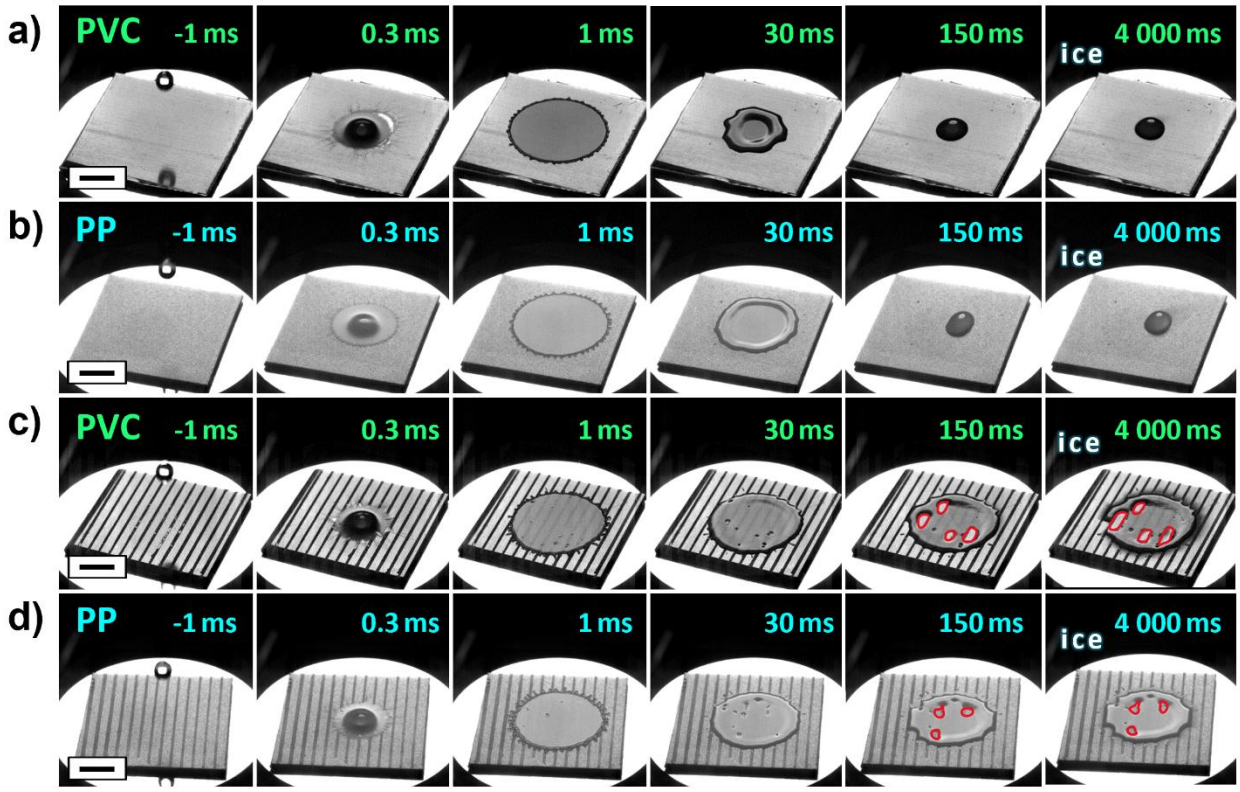

Figure 4.3. A series of high-speed video snapshots showing supercooled droplet impacting, receding, and freezing stages on a) bare PVC, b) bare PP, c) patterned PVC with 1.25 mm stripe distance, and d) patterned PP with 1.25 mm stripe distance. The marked red areas highlight dry voids between the hydrophilic stripes on the patterned surfaces. All four videos were conducted under isothermal conditions at -10 ℃ with a droplet impact velocity of 6.5 m/s. The black scale bars at the bottom left corners correspond to 5 mm.

The droplet impact tests were repeated a minimum of 10 times for each substrate and airflow speed combination. An image processing program (ImageJ) was used to determine droplet spreading rates, freezing onset times, and freezing propagation rates from the recorded videos. For the quantification of the droplet spreading after impact, the dimensionless diameter β (t) of the droplet spread on the surface and the dimensionless time τ, defined as follows, were used:

$$\beta(t) = \frac{D(t)}{D_0} \tag{4.2}$$

$$\tau = t\frac{U_0}{D_0} \tag{4.3}$$

where D (t) is the spreading diameter, D_0 is the initial diameter of the droplet, and U_0 is the impact velocity of the droplet.

In **Figure 4.4**, the dimensionless diameter β (t) is plotted as a function of the time after droplet impact for all PP and PVC samples in two different droplet impact velocities. In all four plots, the dimensionless diameter β (t) increases rapidly after droplet impact until it reaches its maximum spreading between τ = 2-3. After maximum spreading, the wetting area recedes at a slower pace than it spreads until an equilibrium static contact angle is reached and/or the droplet begins to freeze. This holds true for all dark blue and dark green plots corresponding to bare PP and PVC (β decreases with τ after reaching a maximum). Opposite to this trend, and unlike common droplet behaviour in homogeneous samples, the spreading diameter remains steady after reaching maximum spread for all striped samples at all droplet impact velocities (β remains constant with τ after reaching a maximum). Additionally, at the lowest droplet impact velocity of 4.1 m/s (zoomed-in section in **Figures 4.4a-b** and **S4.8**), the maximum spreading diameter of the droplet decreases with the increasing number of hydrophilic stripes.

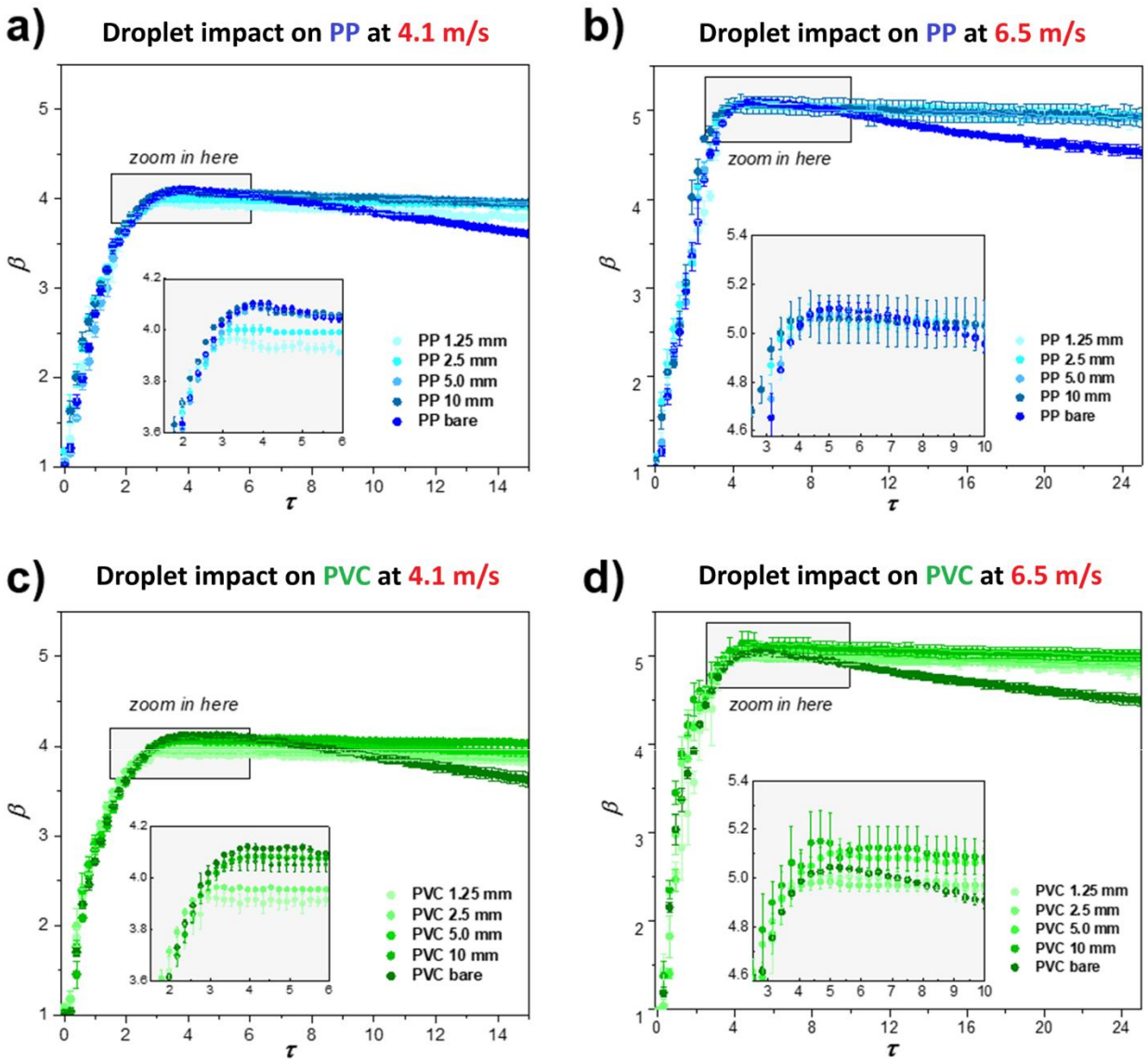

Figure 4.4. The dimensionless droplet spreading diameter scaled by original droplet diameter β is plotted as a function of dimensionless time τ after droplet impact for: a) PP substrate at 4.1 m/s impact velocity; b) PP substrate at 6.5 m/s impact velocity; c) PVC substrate at 4.1 m/s impact velocity; and d) PVC substrate at 6.5 m/s impact velocity with and without stripes.

The behaviour observed for the striped samples can be explained by the droplet being pinned as it comes in contact with the hydrophilic stripes when spreading on the surface. If the droplet covers 10 hydrophilic stripes in the moment of maximum spreading, it will remain wetting these 10 stripes while receding slowly on the hydrophobic areas. Since the image analysis aims to calculate the evolution of the droplet diameter over time, rather than

the overall wetted area, the dimensionless β values in **Figure 4.4** remain constant after the maximum droplet spreading on the patterned surfaces. This is in good agreement with previously conducted numerical simulations for patterned surfaces[24-27], in which the droplet is simultaneously wetting the hydrophilic stripes and slowly dewetting the hydrophobic polymer substrate.

At the highest impact velocity (6.5 m/s), the dewetting occasionally results in dry areas between the stripes, as shown in **Figures 4.3c** and **4.3d**. It is argued that during the dry void formation, bubbles form in both hydrophilic and hydrophobic regions due to air entrainment during impact. However, hydrophilic stripes, with higher wettability and strong pinning forces, anchor the contact line, causing localized lamella thinning and rupture to be more likely. Once initiated at the hydrophilic strips, the rupture propagates into hydrophobic regions due to their lower adhesion and faster water recession. Hydrophobic areas, therefore, amplify rupture through accelerated liquid withdrawal, exposing larger dry voids.

To study this local dewetting better, a close-up analysis is needed. **Figure 4.5a** shows representative screenshots of frozen droplets on the patterned surfaces with dry voids indicated with red circles. Although the droplets froze before the water fully receded from the hydrophobic areas, the occasional dry voids between the stripes suggest that the patterning directs the final water distribution. **Figure 4.5b** presents the sum of all detected void areas per sample for quantitative assessment of each sample's void formation tendency at a given speed of 6.5 m/s (i.e. dewetted area added together from all the impacts for a specific speed and substrate). This approach was selected because it better captures the cumulative effects of repeated droplet impacts over larger surface areas compared to isolated single-droplet analyses.

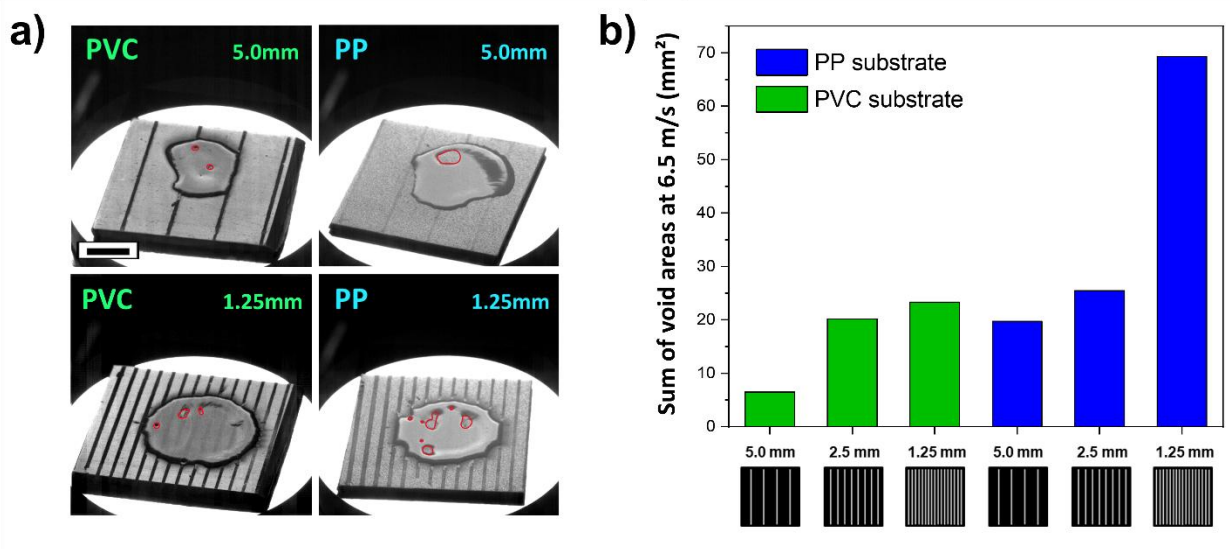

Figure 4.5. a) Video snapshots showing regions of dry voids (circled with a red line) on PVC and PP substrates with 5.0 mm and 1.25 mm stripe distance impacted at 6.5 m/s. The black scale bar on the bottom left corner of the first image corresponds to 5 mm. b) Sum of all detected void areas on the patterned PVC and PP substrates with varying distances between the hydrophilic stripes at 6.5 m/s impact velocity.

Since the void formation was observed only at the highest impact velocity (6.5 m/s), the probability of void formation is expected to increase with increasing droplet impact velocity. **Figure 4.5b** also shows that the probability of void formation seems to increase with decreasing stripe distance, with the PP substrate showing more void areas than the PVC samples. This is likely due to the combination of lower wettability and slightly higher roughness of the PP substrate. By increasing droplet impact velocity and by maximizing the wetting contrast between the stripes and the substrate (i.e., stripes with a lower static contact angle on a substrate with a higher static contact angle), the impacted droplet would recede faster towards the hydrophilic patterns, and the final shape of the frozen area would mimic the predetermined surface patterning.

Influence of hydrophilic patterns on droplet freezing after impact

Ice nucleation can occur at any time after droplet impact; however, high-speed recordings longer than 18 s produce unreasonably large video files that are impractical to generate and store in large quantities. Consequently, droplets that did not freeze within the 18 s recording window were classified as "not frozen" for the freezing probability analysis shown in **Figure 4.6**. The resulting freezing probabilities therefore represent the fraction of droplets that froze within the experimental observation window.

Figure 4.6 shows the freezing probabilities for each sample with the three different droplet impact velocities. As expected, the droplet freezing probabilities increase with higher impact velocities due to more small air bubbles generated at the liquid-solid interface during impact[20]. On the other hand, the samples with PVC substrate show higher freezing probabilities even though **Figure 4.2** shows that the PP substrates have slightly higher roughness (S_a = 1.50 µm > 0.80 µm). Since these experiments were conducted in isothermal conditions, differences in thermal conductivities (0.12 W/mK for PP and 0.19 W/mK for PVC)[30], are unlikely to account for the higher freezing probability of PVC. On the other hand, the higher wettability of PVC compared to PP (**Figure 4.2** showing CAH values 59°>30°) likely leads to more continuous molecular water layers on PVC, which have in turn been proven to promote earlier freezing onset times in surface frosting[31] and could be the underlying reason for more rapid droplet freezing observed in this work. An existing layer of interfacial ice-like water, which has previously been identified and described even on surfaces modified with hydrophobic alkyl silanes and halocarbon wax[32], provides thermodynamically ideal hydrophilic surfaces for nucleation events[33]. The presence of these hydrophilic MWLs promote earlier nucleation on the PVC substrate, leading to higher freezing probability in the supercooled droplet impact tests.

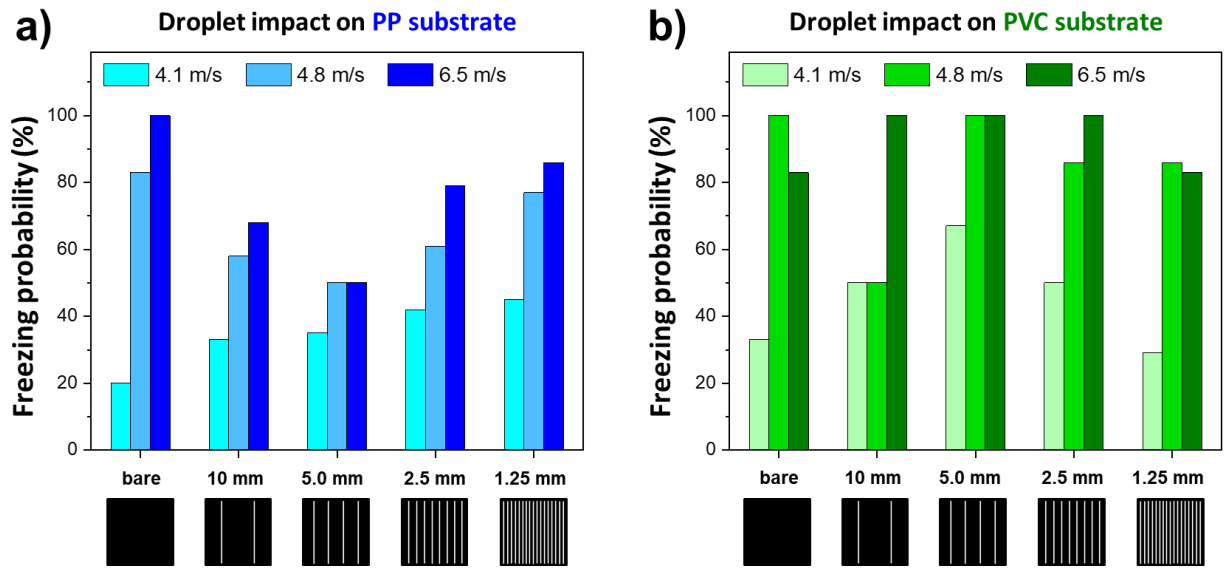

Figure 4.6. Freezing probabilities with a droplet impact velocity of 4.1 m/s, 4.8 m/s, and 6.5 m/s for the various patterned samples with a) a PP substrate (blue colour) or b) a PVC substrate (green colour).

The surface coverage of each frozen droplet was analysed from the recorded videos using ImageJ and plotted as a function of the nucleation onset time after droplet impact. In **Figure 4.7a**, the frozen droplet areas decrease exponentially with increasing time after the droplet impact. After t = 1 s, the frozen area coverage remains below 40 mm^2 (less than a third of the maximum droplet spreading ~150 mm^2) regardless of the substrate type or droplet impact velocity. As mentioned earlier, complete receding of the droplet before freezing onset is necessary for controlling the shape of the frozen area with better precision. Therefore, the freezing onset time for these samples should ideally be higher than one second.

Since freezing after droplet impact is a stochastic process, reporting average freezing onset times for each sample is irrelevant in this context. Instead, the freezing onset times for each sample were plotted as the fraction of liquid droplets $Q_{liq}(t)$ at the given onset time after the droplet impact.

$$Q_{\mathrm{liq}}(t) = \frac{N_{\mathrm{liq}}(t)}{N_0} \tag{4.4}$$

As shown in **Figure 4.7b**, the resulting plot shows the fraction of liquid droplets freezing at longer times decays exponentially. By fitting an exponential power function to this plot, it is possible to extract the theoretical time after droplet impact at which there is a 50 % chance that the droplet has already frozen. This parameter will be denoted as the median freezing onset time (MFOT). The MFOTs for each sample with the three different droplet impact velocities are shown in **Figure 4.7c-d**. Similarly to the freezing probabilities in **Figure 4.6**, the MFOTs are significantly higher for droplet impact on PP substrates and decrease with increasing droplet impact velocity for most samples. The MFOTs on PP substrate are also mostly above 1 s, indicating that the droplets impacting PP substrate have more time to recede and form larger dry voids than droplets impacting PVC substrate before they freeze.

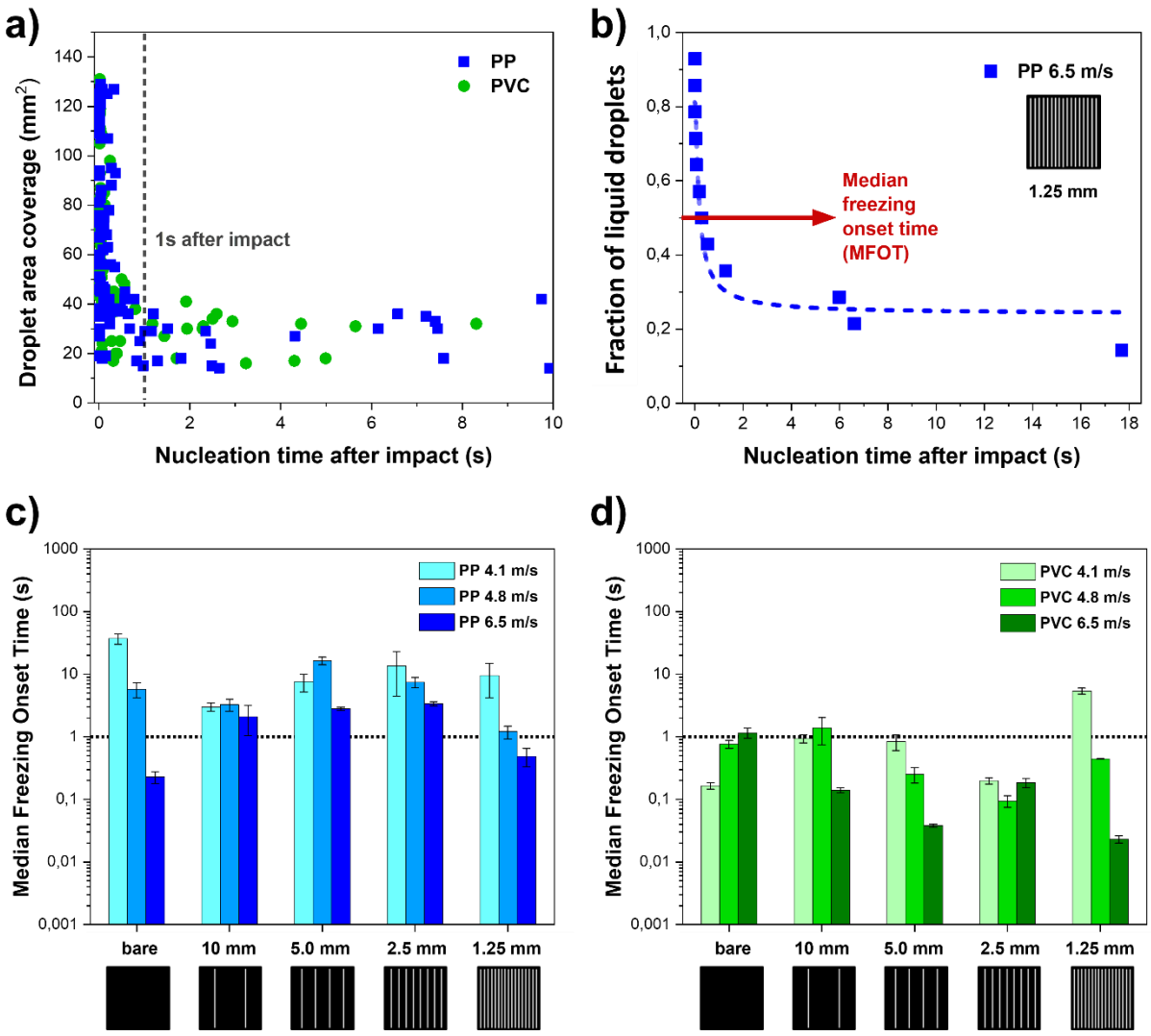

Figure 4.7. a) The surface coverage of each frozen droplet plotted as a function of droplet nucleation time after impact. b) Fraction of liquid droplets plotted as a function of all nucleation onset times of droplets impacting a PP substrate with 1.25 mm stripe distance at a velocity of 6.5 m/s. The nucleation onset time corresponding to the half point of frozen and liquid droplets (red arrow) is denoted as the median freezing onset time (MFOT). The MFOTs are shown for all samples with c) PP substrate (blue) and d) PVC substrate (green). The dotted black line indicates t = 1 s after the impact.

In addition to the freezing probabilities and MFOTs, the droplet areas at freezing onset times $A_c(t)$ and the fraction of liquid droplets $N_{liq}(t)/N_0$ were used to calculate the average number of nucleation sites $\lambda_s(t)$ and average nucleation rates per unit area $J_s(t)$ for each sample, as shown in **Equation 4.1**.

Figure 4.8a shows examples of $\lambda_s(t)$ plotted as a function of the droplet nucleation time after impact for the patterned samples. For all samples, the $\lambda_s(t)$ values increase linearly over time, with the slope corresponding to the average nucleation rate $J_s(t)$. As shown in **Figure 4.8b,** the initial nucleation rate at t < 50 ms is significantly higher compared to the second nucleation rate thereafter. The higher nucleation rate at t < 50 ms is attributed to the air bubbles generated at droplet impact. For droplets freezing after 50 ms, the nucleation rate decreases, attributed to the impact of trapped bubbles disappearing.

The average nucleation rates for all samples can be seen in **Figure 4.8c-d**. As expected, the initial nucleation rates at t < 50 ms (**Figure 4.8c**) are higher for all samples compared to the second nucleation rate at t > 50 ms (**Figure 4.8d**); i.e., nucleation happens at higher speeds when droplets freeze within 50 ms after impact. Following the same trend of freezing probability and MFOTs, the nucleation rates are also much higher for PVC substrates (green color) than for PP (blue color), again attributed to the presence of MWL on PVC. The differences between droplet impact velocities and stripe distances are less obvious, especially at t < 50 ms in **Figure 4.8c.** However, the striped PVC samples in **Figure 4.8d** show higher nucleation rates at t > 50 ms compared to the bare PVC sample. An opposite trend can be seen in **Figure 4.8d** for the striped PP samples, which show lower nucleation rates at t > 50 ms compared to the bare PP substrate. This reinforces the idea that the wettability difference between the substrate and the patterns should be maximised to lower nucleation rates, which increases the median freezing onset time MFOT, which, in turn, creates more time for the droplet to recede towards the hydrophilic patterning.

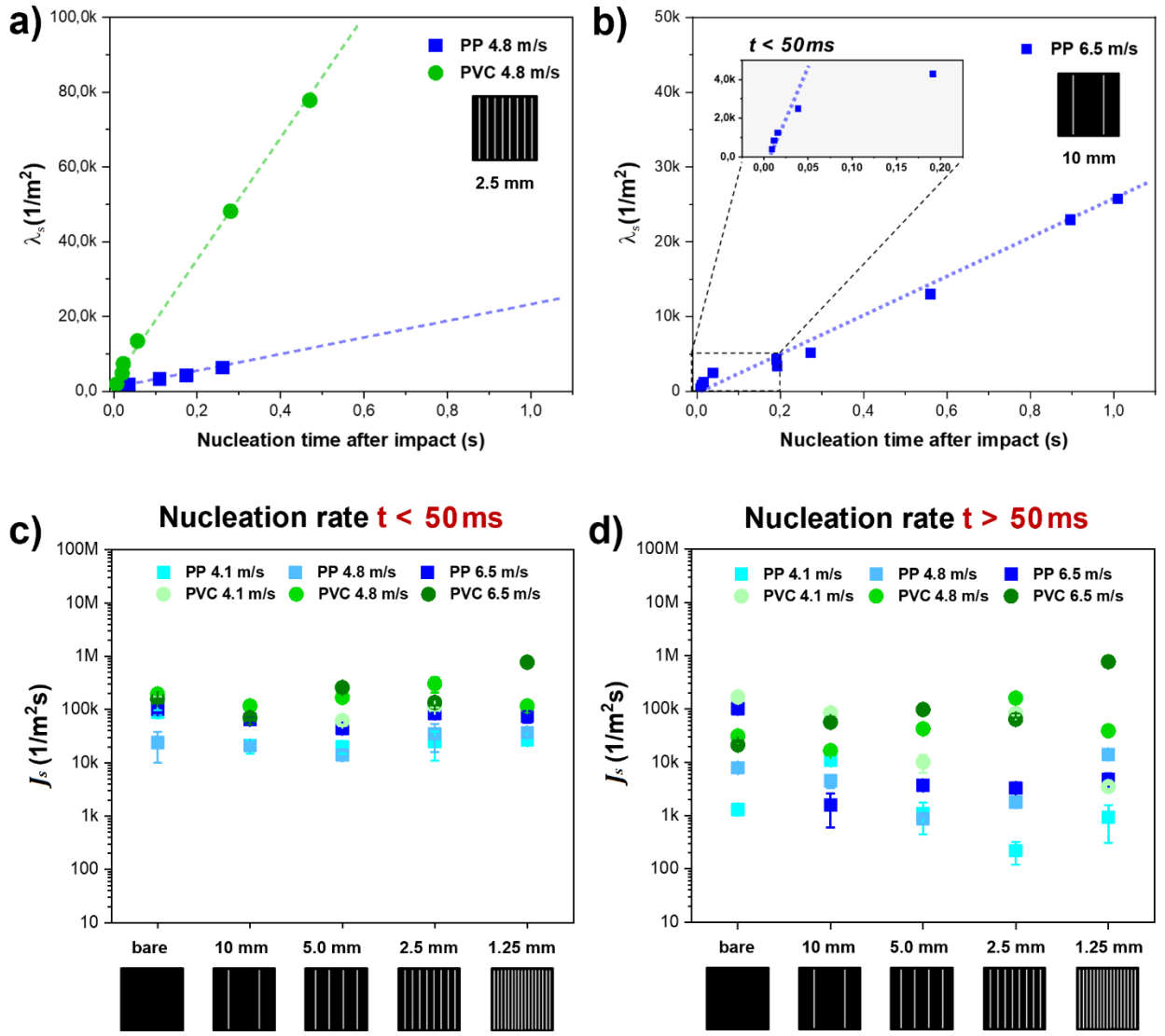

Figure 4.8. Average number of nucleation sites per unit area (λ_s) as a function of the nucleation time after droplet impact for samples a) PP and PVC with 2.5 mm stripe distance and 4.8 m/s droplet velocity, and b) PP with 10 mm stripe distance and 6.5 m/s droplet velocity. From the slopes of the $\lambda_s(t)$ plots nucleation rates (J_s) for the samples at c) t < 50 ms and d) t > 50 ms can be obtained.

Once a freezing event initiates after the droplet impact, its propagation within the supercooled droplet can also be followed in the recorded videos. The rate of freezing propagation within the droplet was analysed using ImageJ for all of the experiments, and their values were plotted in **Figure 4.9**. All propagation rates were found to be between 50

and 100 mm/s with no variation between the two substrates, distance between the hydrophilic stripes, or droplet impact velocity. These values are comparable to those reported for bulk water freezing[31,34-36] being between 10 and 100 mm/s, as expected since the freezing propagation within the supercooled droplet is bulk water freezing, given the dimensions of the droplet. The droplet freezing mechanism after impact is therefore confirmed to be governed by bulk water freezing dynamics, independent of surface effects.

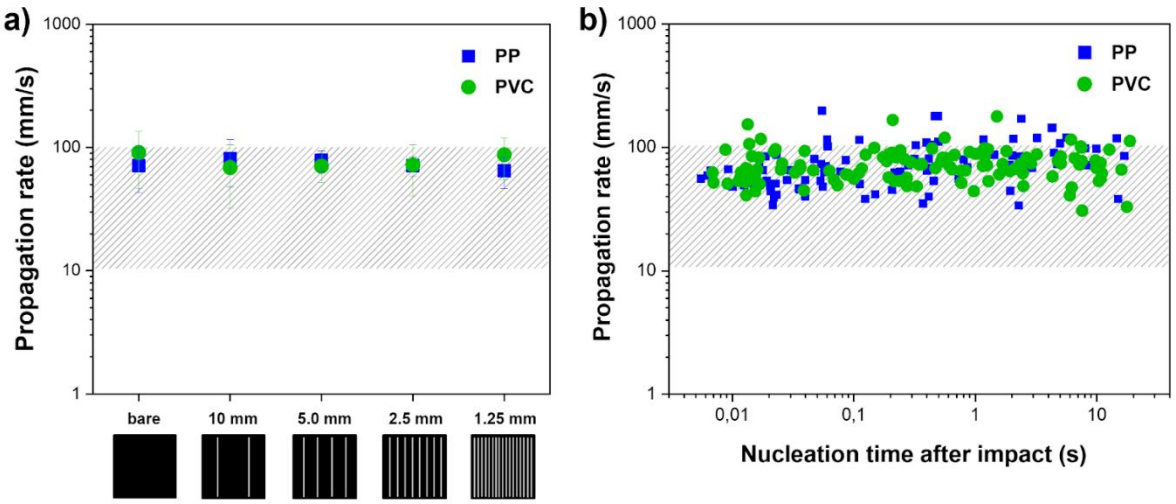

Figure 4.9. a) Freezing propagation rate within the droplet after impact for all of the patterned PP (blue) and PVC (green) samples and all droplet velocities as a function of a) the distance between the hydrophilic stripes; b) represents the relation between nucleation time after impact and the propagation rate. The gray dashed grid indicates the range of propagation rates previously reported for bulk water freezing [31,34-36].

As a mode of summary of the different observations made during supercooled water droplet impact, **Figure 4.10** shows a comparison of the droplet wetting and freezing behaviour on the two different polymeric substrates (PP and PVC). For both substrates, dry voids were detected when the patterning distance was lower than 5 mm, with the probability of void formation increasing with decreasing stripe distance. **Figure 4.10a-b** shows the overall average nucleation rates (t > 50 ms) on both substrates at all impact velocities to highlight the differences as a function of the underlying polymer substrate. Both substrates show the

lowest nucleation rates for stripe distances between 2.5 and 5 mm, although the patterned PP substrates had significantly lower nucleation rates compared to the PVC samples.

Overall, the patterned PVC samples show increased nucleation rates compared to the bare PVC substrate, whereas the patterned PP samples show an opposite trend. We hypothesize that this behaviour is due to the wettability contrast between substrate and stipes (higher for PP samples), as well as the presence of MWL on PVC. Although further testing on more hydrophobic substrates with higher wettability contrast could lead to faster droplet receding and bigger dry areas, this study provides important initial insights into the performance of patterned wettability surfaces as passive anti-icing coatings in dynamic icing conditions. During in-flight icing conditions, supercooled water droplets can impact the aircraft surfaces with velocities up to 500 m/s, which is an order of magnitude higher than the impact velocities used in this work (up to 6.5 m/s). Since dry void formation was observed only at the highest impact velocity, higher droplet impact velocities in real-life icing conditions could potentially significantly increase the droplet receding rate toward the hydrophilic patterns, thus leading to better control over where ice is formed on the surface.

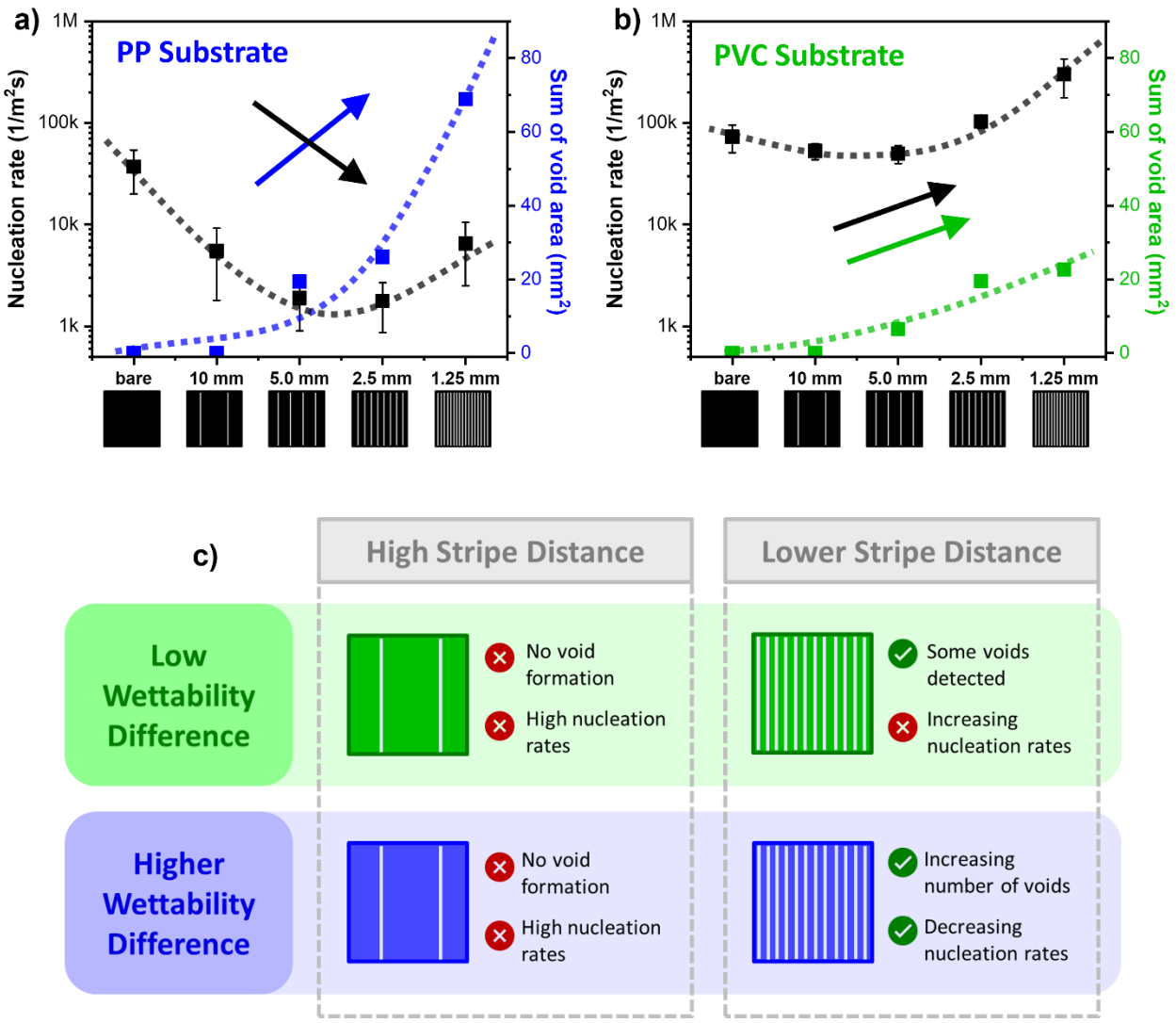

Figure 4.10. Average nucleation rates (t > 50 ms) and the dry void areas as a function of the stripe density for samples with a) PP substrate (blue) and b) PVC substrate (green). The dotted lines are a guide for the eye. c) Summary of the trends seen in plots a) and b).

CONCLUSIONS

The impact behaviour of supercooled droplets (D_0 = 2.6 mm) on homogeneous and patterned wettability surfaces was investigated in an L-shaped wind tunnel at isothermal conditions of -10 ℃ at three different impact velocities. Two commodity polymers (PP and PVC) with different CAH (30° and 59°) were covered with hydrophilic stripes (150 µm wide PHEMA stripes) to create patterned samples with two different wettability regions. A high-speed camera was used to monitor the droplet impact on the hydrophilic stripes, with stripe distance varying from 1.25 mm to 10 mm, and the droplet impact velocities adjusted at 4.1, 4.8, and 6.5 m/s.

The captured high-speed videos show occasional dry voids between the hydrophilic stripes during the receding of impacted supercooled droplets at the highest impact velocity (6.5 m/s). Image analysis of the frozen droplets reveals that the void formation is more likely to occur with a higher wettability difference (PP substrate) and with a lower patterning distance. The higher wettability difference on PP was also linked to a reduced nucleation probability and rate after droplet impact. Even though the freezing onset occurs on both substrates before the droplet has fully receded towards the hydrophilic stripes, the numerous dry voids on PP suggest that an even higher wettability difference between the hydrophilic patterns and the hydrophobic substrate could help control the shape and location of the final frozen area after droplet impact.

Unlike the patterned PVC substrates, the hydrophilic patterning on PP leads to overall better performance in terms of nucleation rates and wetting behaviour compared to bare PP. Specifically, PP samples with a patterning distance of 2.5-5.0 mm exhibit the lowest freezing probabilities and nucleation rates under the experimental conditions used in this work (a droplet diameter of 2.6 mm, impact velocities of 4.1-6.5 m/s, and an isothermal temperature of -10 °C). While lower freezing probability is more critical for anti-icing surfaces from a practical point of view, freezing onset time after impact can play a crucial role in the aim of controlling where and in what shape ice accumulates on patterned surfaces. The later the freezing onset occurs, the more time the droplet has to recede

towards the hydrophilic patterning, thus generating dry areas that grow between the patterns.

This work is the first experimental study that investigates systematically the influence of wettability patterns on supercooled water droplet impact, wetting, and freezing behaviour. The results indicate that patterned wettability surfaces could be potentially beneficial under impact icing conditions, especially when considering the higher impact velocities and using a lower patterning distance that can aid in faster and more frequent dry void formation. Although the droplet impact velocities used in this study (4.1-6.5 m/s) are much lower than what anti-icing coatings would experience in potential real-life applications (e.g. supercooled droplet impact on aircraft at 50-500 m/s), the dry void formation in the highest tested impact velocity is an encouraging sign for further systematic tests in more challenging environmental conditions. Finally, to develop rational designs for future patterned anti-icing surfaces, a more in-depth investigation is needed into the role of patterning distance, shape, chemistry, and topology on the freezing of impacting supercooled droplets, particularly in connection with varying droplet diameter and impact velocity.

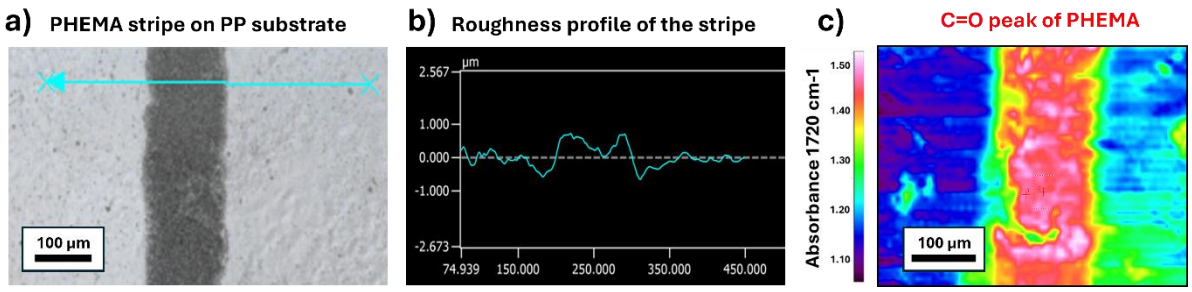

Figure S4.1. The PHEMA patterns on PP portrayed in a) confocal microscopy imaging, b) roughness profilometry, and c) micro-FTIR imaging.

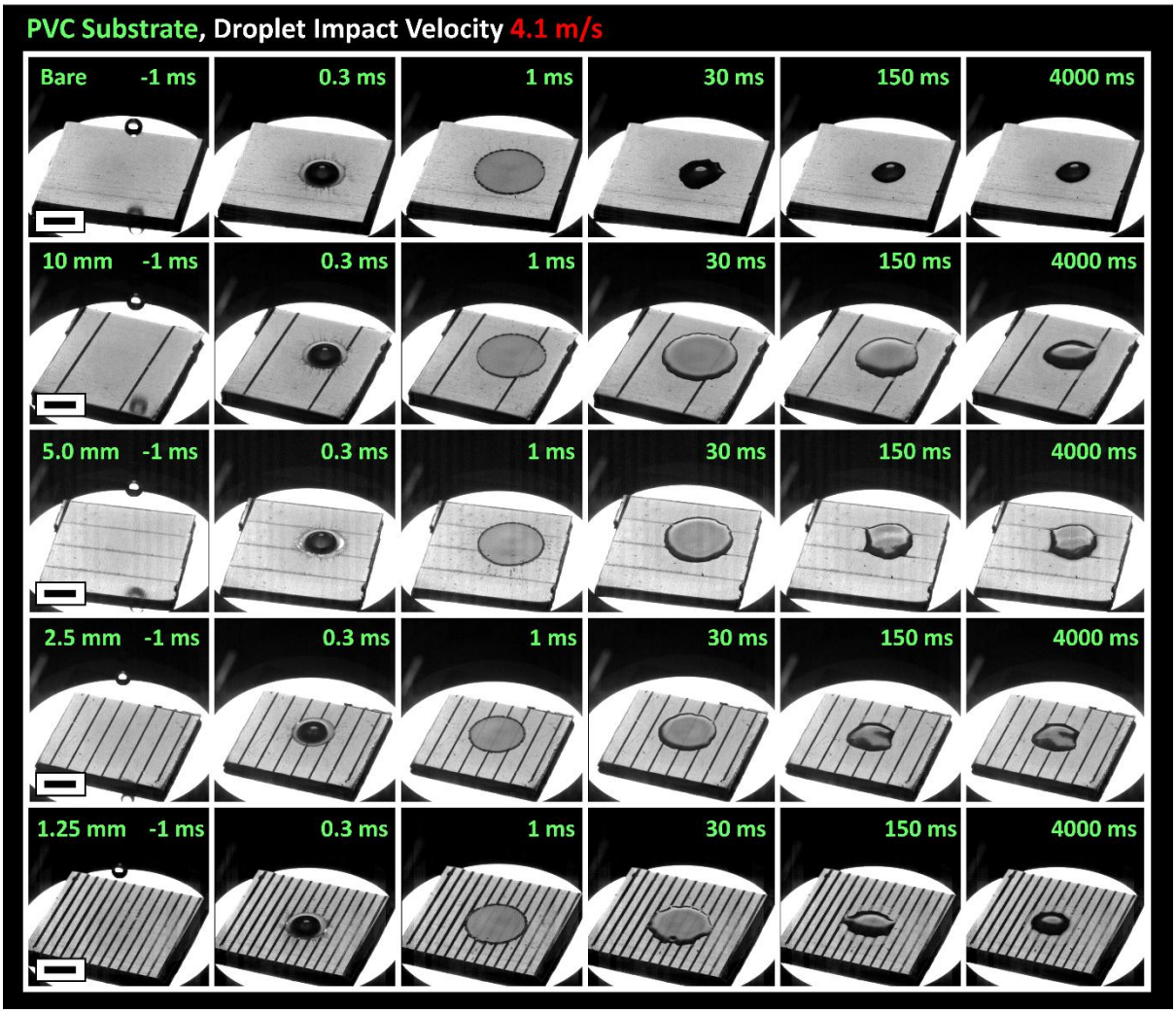

Figure S4.2. A series of high-speed video snapshots showing supercooled droplet impacting, receding, and freezing stages on all PVC samples with droplet impact velocity of 4.1 m/s. All videos were conducted in isothermal conditions at -10 ℃. The black scale bars at the bottom left corners correspond to 5 mm.

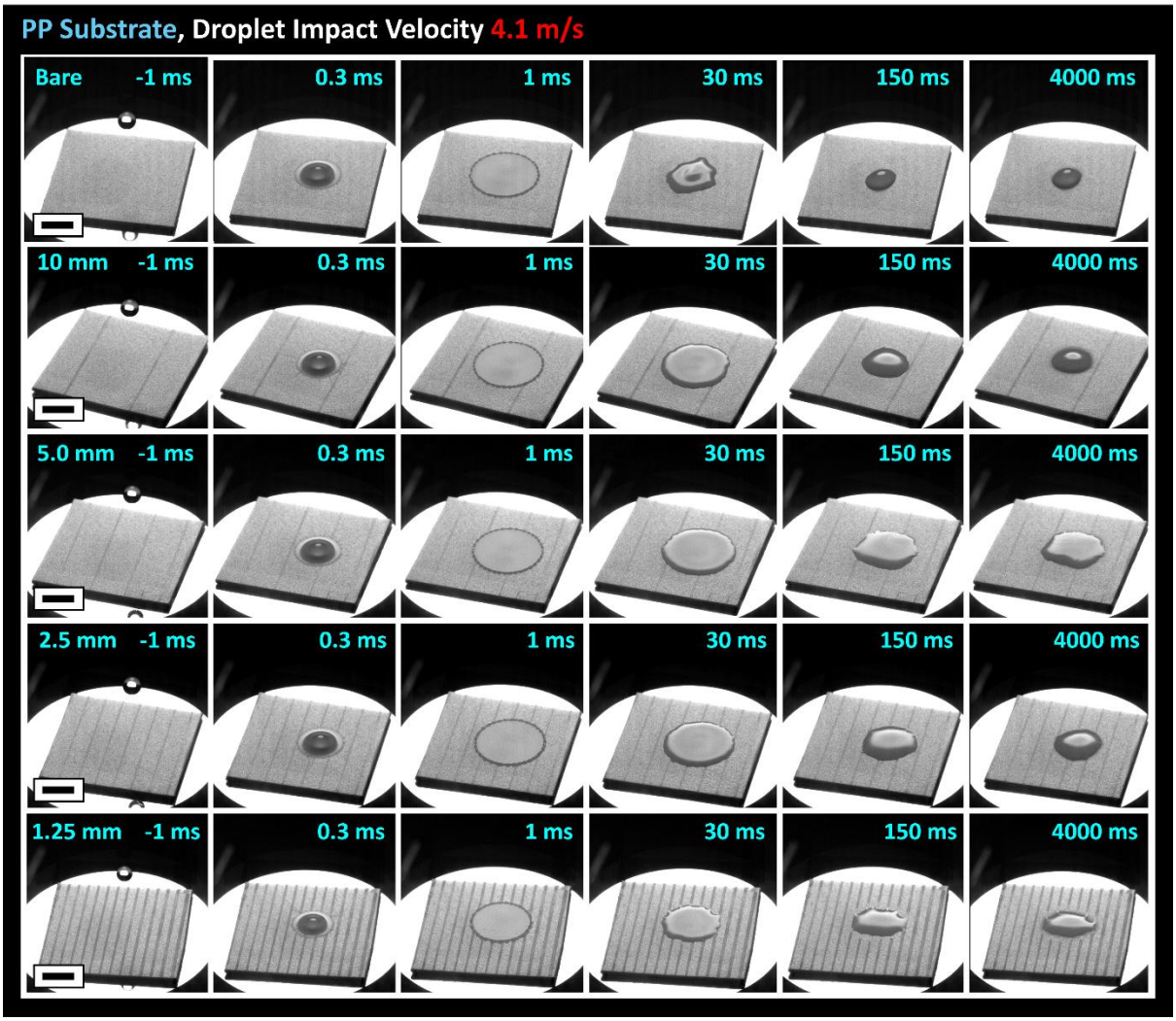

Figure S4.3. A series of high-speed video snapshots showing supercooled droplet impacting, receding, and freezing stages on all PP samples with droplet impact velocity of 4.1 m/s. All videos were conducted in isothermal conditions at -10 °C. The black scale bars at the bottom left corners correspond to 5 mm.

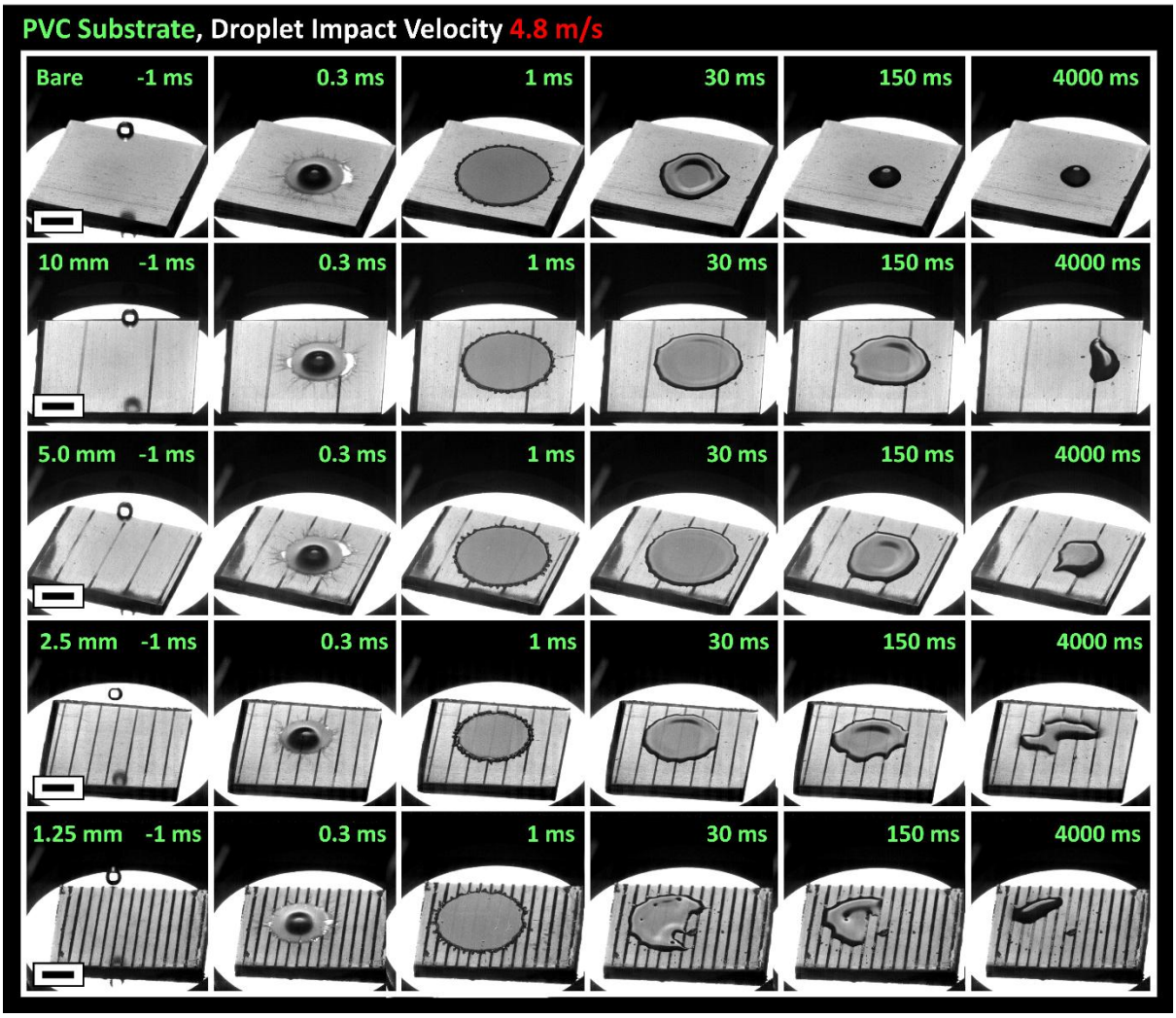

Figure S4.4. A series of high-speed video snapshots showing supercooled droplet impacting, receding, and freezing stages on all PVC samples with droplet impact velocity of 4.8 m/s. All videos were conducted in isothermal conditions at -10 ℃. The black scale bars at the bottom left corners correspond to 5 mm.

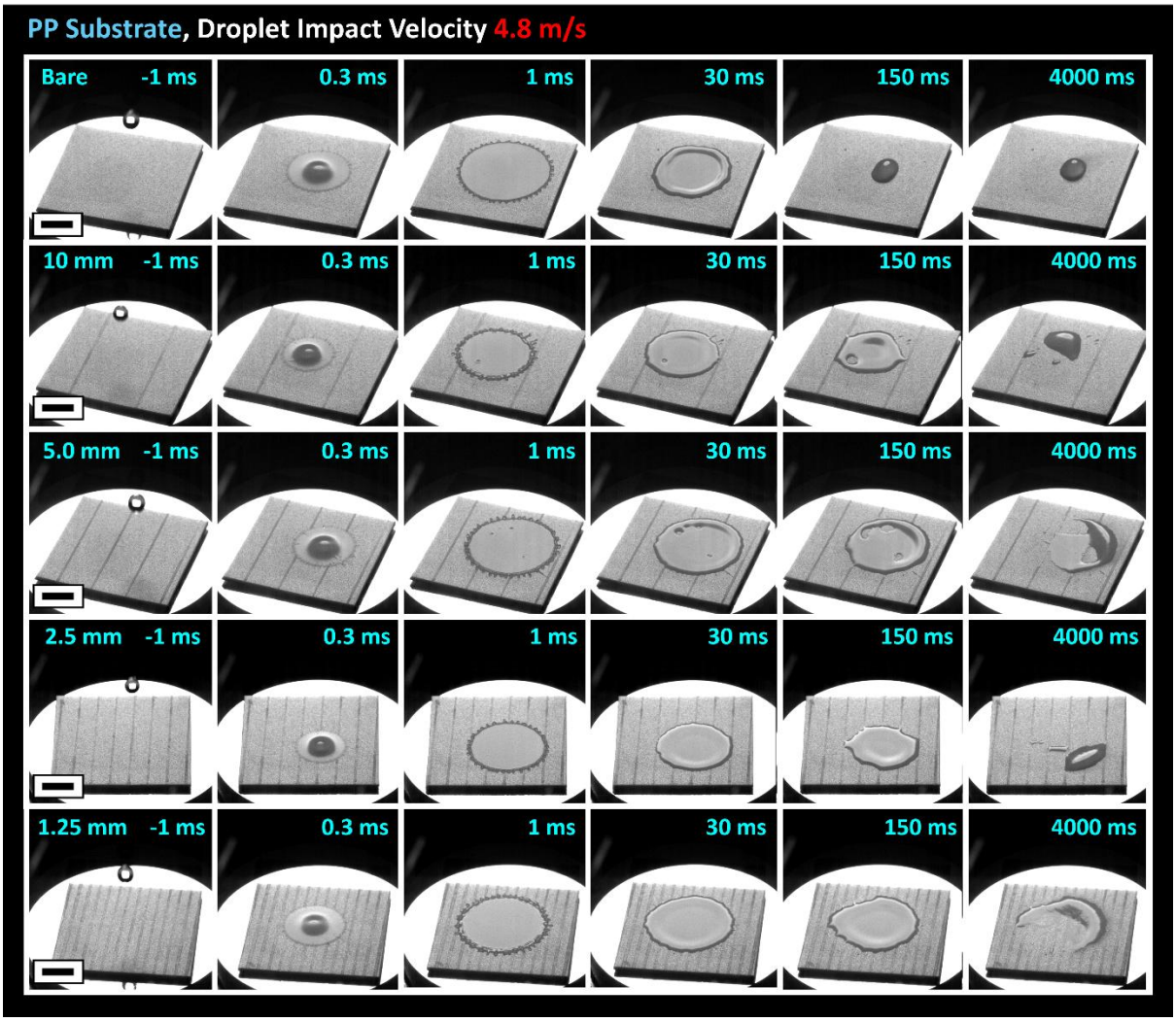

Figure S4.5. A series of high-speed video snapshots showing supercooled droplet impacting, receding, and freezing stages on all PP samples with droplet impact velocity of 4.8 m/s. All videos were conducted in isothermal conditions at -10 °C. The black scale bars at the bottom left corners correspond to 5 mm.

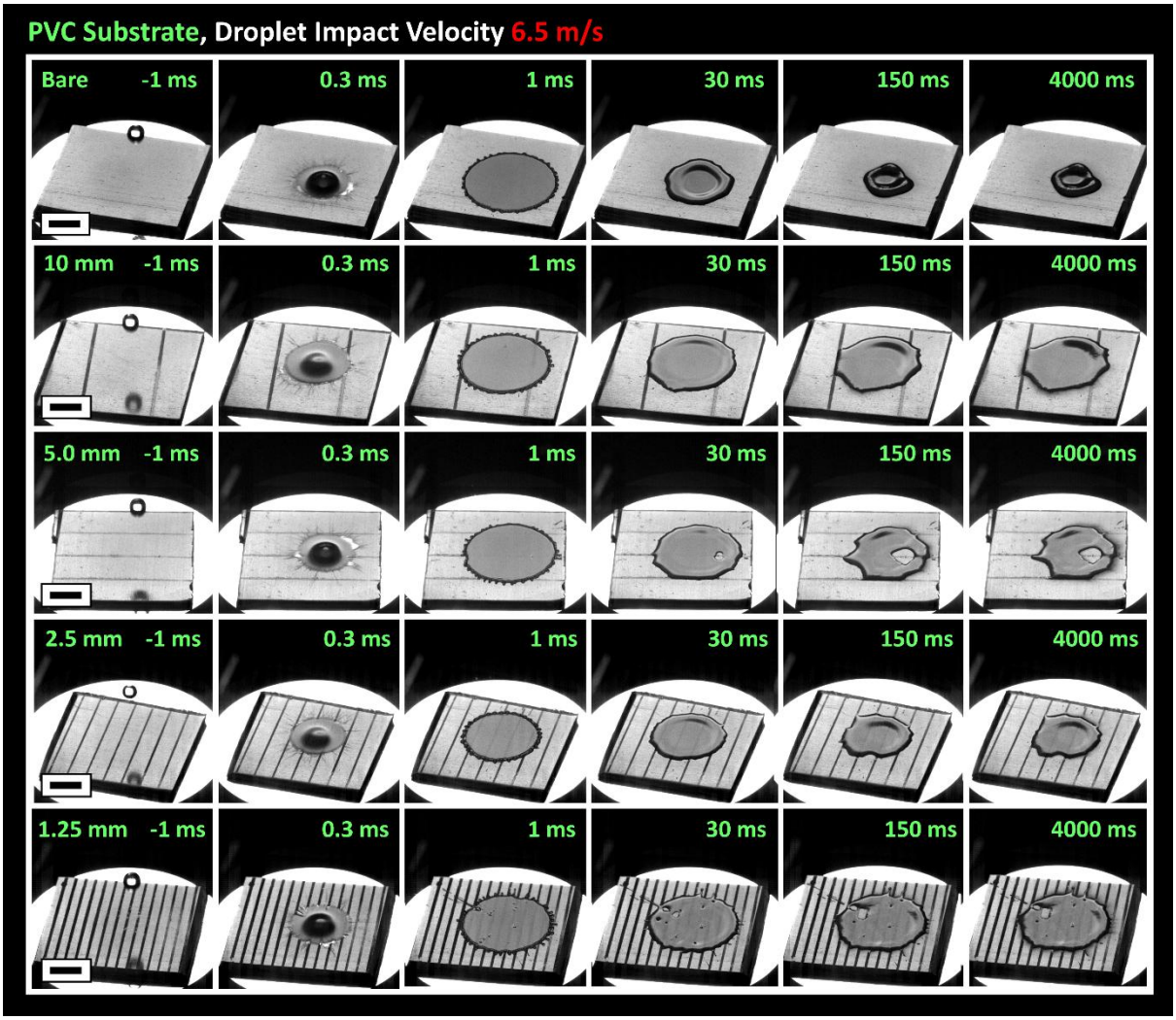

Figure S4.6. A series of high-speed video snapshots showing supercooled droplet impacting, receding, and freezing stages on all PVC samples with droplet impact velocity of 6.5 m/s. All videos were conducted in isothermal conditions at -10 ℃. The black scale bars at the bottom left corners correspond to 5 mm.

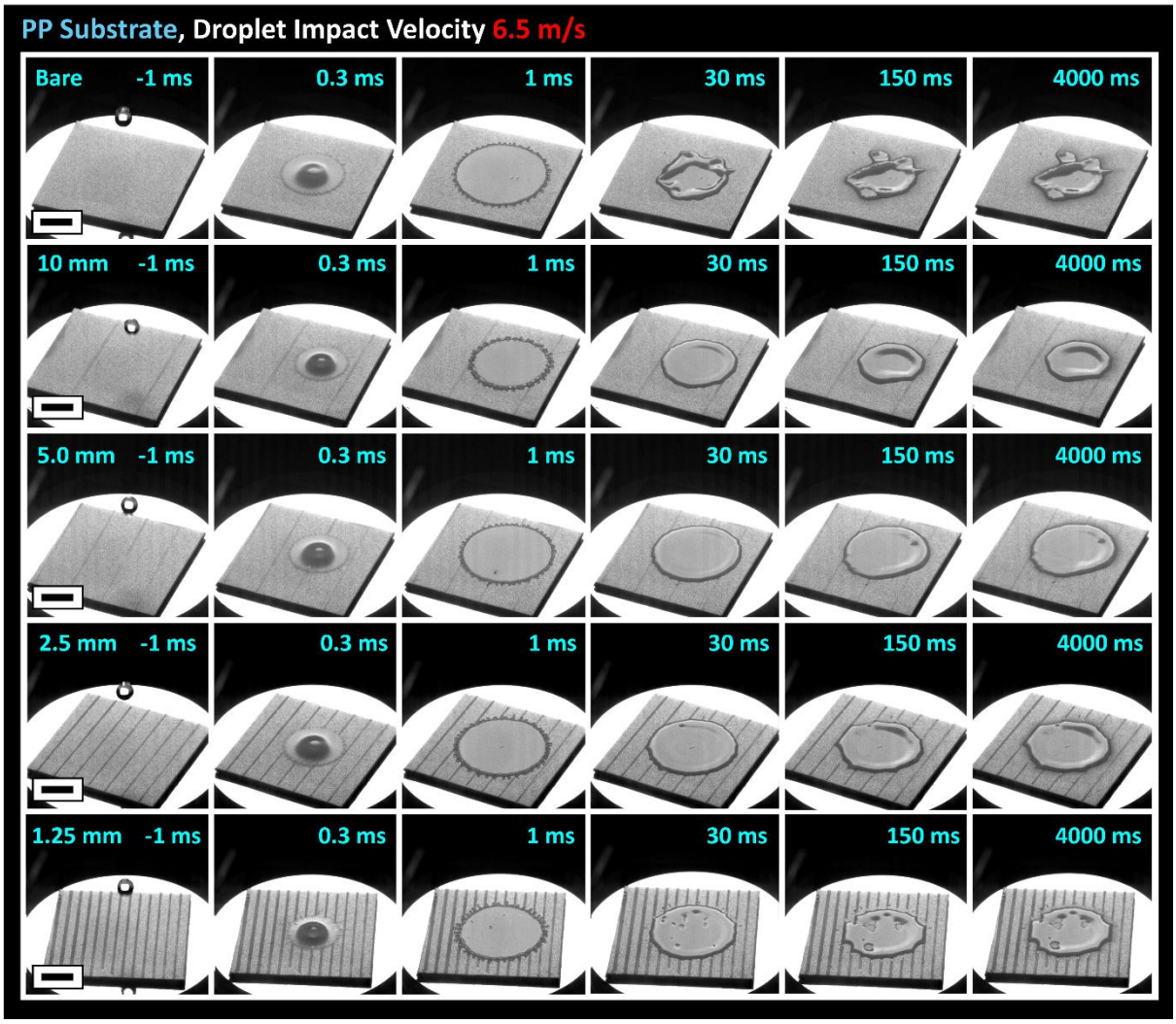

Figure S4.7. A series of high-speed video snapshots showing supercooled droplet impacting, receding, and freezing stages on all PP samples with droplet impact velocity of 6.5 m/s. All videos were conducted in isothermal conditions at -10 ℃. The black scale bars at the bottom left corners correspond to 5 mm.

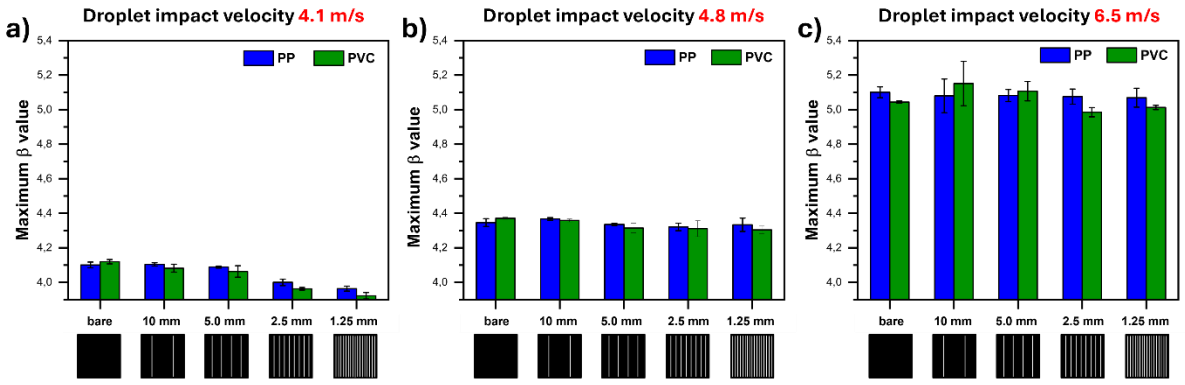

Figure S4.8. The maximum values of the dimensionless droplet spreading diameter scaled by original droplet diameter (max β) are plotted as a function of stripe distance for PP (blue) and PVC (green) at a) 4.1 m/s, b) 4.8 m/s, and c) 6.5 m/s droplet impact velocity.

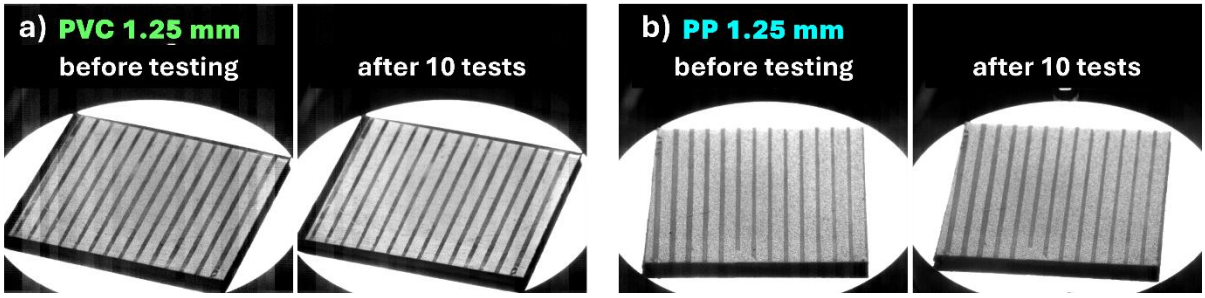

Figure S4.9. a) PVC and b) PP samples with 1.25 mm stripe distance shown before and after 10 repetitive droplet impact tests.

REFERENCES

(1) Cao, Y.; Tan, W.; Wu, Z. Aircraft Icing: An Ongoing Threat to Aviation Safety. *Aerosp. Sci. Technol.* **2018**, *75*, 353–385. https://doi.org/https://doi.org/10.1016/j.ast.2017.12.028.

(2) Yamazaki, M.; Jemcov, A.; Sakaue, H. A Review on the Current Status of Icing Physics and Mitigation in Aviation. *Aerospace*. MDPI AG July 1, 2021. https://doi.org/10.3390/aerospace8070188.

(3) Huang, X.; Tepylo, N.; Pommier-Budinger, V.; Budinger, M.; Bonaccurso, E.; Villedieu, P.; Bennani, L. A Survey of Icephobic Coatings and Their Potential Use in a Hybrid Coating/Active Ice Protection System for Aerospace Applications. *Progress in Aerospace Sciences*. Elsevier Ltd February 1, 2019, pp 74–97. https://doi.org/10.1016/j.paerosci.2019.01.002.

(4) Irajizad, P.; Nazifi, S.; Ghasemi, H. Icephobic Surfaces: Definition and Figures of Merit. *Advances in Colloid and Interface Science*. Elsevier B.V. July 1, 2019, pp 203–218. https://doi.org/10.1016/j.cis.2019.04.005.

(5) Wang, F.; Zhuo, Y.; He, Z.; Xiao, S.; He, J.; Zhang, Z. Dynamic Anti-Icing Surfaces (DAIS). *Advanced Science* **2021**, *8* (21), 2101163. https://doi.org/https://doi.org/10.1002/advs.202101163.

(6) Shen, Y.; Wu, X.; Tao, J.; Zhu, C.; Lai, Y.; Chen, Z. Icephobic Materials: Fundamentals, Performance Evaluation, and Applications. *Progress in Materials Science*. Elsevier Ltd June 1, 2019, pp 509–557. https://doi.org/10.1016/j.pmatsci.2019.03.004.

(7) Susoff, M.; Siegmann, K.; Pfaffenroth, C.; Hirayama, M. Evaluation of Icephobic Coatings—Screening of Different Coatings and Influence of Roughness. *Appl. Surf. Sci.* **2013**, *282*, 870–879. https://doi.org/https://doi.org/10.1016/j.apsusc.2013.06.073.

(8) Peppou-Chapman, S.; Hong, J. K.; Waterhouse, A.; Neto, C. Life and Death of Liquid-Infused Surfaces: A Review on the Choice, Analysis and Fate of the Infused Liquid Layer. *Chem. Soc. Rev.* **2020**, *49* (11), 3688–3715. https://doi.org/10.1039/D0CS00036A.

(9) Jung, S.; Dorrestijn, M.; Raps, D.; Das, A.; Megaridis, C. M.; Poulikakos, D. Are Superhydrophobic Surfaces Best for Icephobicity? *Langmuir* **2011**, *27* (6), 3059–3066. https://doi.org/10.1021/la104762g.

(10) Chen, J.; Liu, J.; He, M.; Li, K.; Cui, D.; Zhang, Q.; Zeng, X.; Zhang, Y.; Wang, J.; Song, Y. Superhydrophobic Surfaces Cannot Reduce Ice Adhesion. *Appl. Phys. Lett.* **2012**, *101* (11). https://doi.org/10.1063/1.4752436.

(11) Kulinich, S. A.; Farhadi, S.; Nose, K.; Du, X. W. Superhydrophobic Surfaces: Are They Really Ice-Repellent? *Langmuir*. January 4, 2011, pp 25–29. https://doi.org/10.1021/la104277q.

(12) Erbil, H. Y. Practical Applications of Superhydrophobic Materials and Coatings: Problems and Perspectives. *Langmuir* **2020**, *36* (10), 2493–2509. https://doi.org/10.1021/acs.langmuir.9b03908.

(13) O'Brien, J. L.; Ahmadi, S. F.; Failor, K. C.; Bisbano, C. E.; Mulroe, M. D.; Nath, S.; Vinatzer, B. A.; Boreyko, J. B. Spatial Control of Condensation and Desublimation Using Ice Nucleating Proteins. *Appl. Phys. Lett.* **2018**, *113* (15). https://doi.org/10.1063/1.5046187.

(14) Jin, Y.; Wu, C.; Yang, Y.; Wu, J.; He, Z.; Wang, J. Inhibiting Condensation Freezing on Patterned Polyelectrolyte Coatings. *ACS Nano* **2020**, *14* (4), 5000–5007. https://doi.org/10.1021/acsnano.0c01304.

(15) Tavaststjerna, M. J.; Picken, S. J.; Garcia, S. J. Controlling Frost Propagation on Polymeric Surfaces Using SI-ATRP Chemical Micropatterning. *Adv. Mater. Interfaces* **2025**, *n/a* (n/a), 2400838. https://doi.org/https://doi.org/10.1002/admi.202400838.

(16) Zhou, X.; Sun, Y.; Liu, J. Designing Anti-Icing Surfaces by Controlling Ice Formation. *Advanced Materials Interfaces*. John Wiley and Sons Inc September 1, 2021. https://doi.org/10.1002/admi.202100327.

(17) Mousavi, S. M.; Sotoudeh, F.; Chun, B.; Lee, B. J.; Karimi, N.; Faroughi, S. A. The Potential for Anti-Icing Wing and Aircraft Applications of Mixed-Wettability Surfaces - A Comprehensive Review. *Cold Regions Science and Technology*. Elsevier B.V. January 1, 2024. https://doi.org/10.1016/j.coldregions.2023.104042.

(18) Zhang, X.; Liu, X.; Wu, X.; Min, J. Impacting-Freezing Dynamics of a Supercooled Water Droplet on a Cold Surface: Rebound and Adhesion. *Int. J. Heat Mass Transf.* **2020**, *158*. https://doi.org/10.1016/j.ijheatmasstransfer.2020.119997.

(19) Tang, C.; Qin, M.; Weng, X.; Zhang, X.; Zhang, P.; Li, J.; Huang, Z. Dynamics of Droplet Impact on Solid Surface with Different Roughness. *International Journal of Multiphase Flow* **2017**, *96*, 56–69. https://doi.org/10.1016/j.ijmultiphaseflow.2017.07.002.

(20) Ding, M.; Hussong, J.; Roisman, I. V. Freezing of a Supercooled Water Drop after an Impact onto a Solid Wall. *Cold Reg. Sci. Technol.* **2024**, *229*.

(21) Sun, M.; Kong, W.; Wang, F.; Liu, H. Impact Freezing Modes of Supercooled Droplets Determined by Both Nucleation and Icing Evolution. *Int. J. Heat Mass Transf.* **2019**, *142*. https://doi.org/10.1016/j.ijheatmasstransfer.2019.07.081.

(22) Schremb, M.; Roisman, I.; Tropea, C. Transient Effects in Ice Nucleation of a Water Drop Impacting onto a Cold Substrate. *Phys. Rev. E* **2017**, *95*, 022805.

(23) Wu, H.; Kong, W.; Bian, P.; Liu, H. The Coupled Impact-Freezing Mechanism of Supercooled Droplet on Superhydrophobic Surface. *Aerospace Systems* **2024**, *7* (1), 11–28. https://doi.org/10.1007/s42401-023-00192-y.

(24) Pravinraj, T.; Patrikar, R. A Droplet Actuation Technique for a Lab-on-Chip Device Using Partial Wetting Surface without External Force. *Sens. Actuators A Phys.* **2019**, *285*, 482–490. https://doi.org/https://doi.org/10.1016/j.sna.2018.11.039.

(25) Göhl, J.; Mark, A.; Sasic, S.; Edelvik, F. An Immersed Boundary Based Dynamic Contact Angle Framework for Handling Complex Surfaces of Mixed Wettabilities. *International Journal of Multiphase Flow* **2018**, *109*, 164–177. https://doi.org/10.1016/j.ijmultiphaseflow.2018.08.001.

(26) Yuan, Z.; Matsumoto, M.; Kurose, R. Directional Migration of an Impinging Droplet on a Surface with Wettability Difference. *Phys. Rev. Fluids* **2020**, *5* (11). https://doi.org/10.1103/PhysRevFluids.5.113605.

(27) Huang, J.; Wang, L.; He, K. Three-Dimensional Study of Double Droplets Impact on a Wettability-Patterned Surface. *Comput. Fluids* **2022**, *248*. https://doi.org/10.1016/j.compfluid.2022.105669.

(28) Sotoudeh, F.; Kamali, R.; Mousavi, S. M.; Karimi, N.; Lee, B. J.; Khojasteh, D. Understanding Droplet Collision with Superhydrophobic-Hydrophobic–Hydrophilic Hybrid Surfaces. *Colloids Surf. A Physicochem. Eng. Asp.* **2021**, *614*. https://doi.org/10.1016/j.colsurfa.2021.126140.

(29) Russo, A.; Icardi, M.; Elsharkawy, M.; Ceglia, D.; Asinari, P.; Megaridis, C. M. Numerical Simulation of Droplet Impact on Wettability-Patterned Surfaces. *Phys. Rev. Fluids* **2020**, *5* (7). https://doi.org/10.1103/PhysRevFluids.5.074002.

(30) Ngo, I.-L.; Jeon, S.; Byon, C. Thermal Conductivity of Transparent and Flexible Polymers Containing Fillers: A Literature Review. *Int. J. Heat Mass Transf.* **2016**, *98*, 219–226. https://doi.org/https://doi.org/10.1016/j.ijheatmasstransfer.2016.02.082.

(31) Tavaststjerna, M. J.; Picken, S. J.; Garcia, S. J. Role of Molecular Water Layer State on Freezing Front Propagation Rate and Mode Studied with Thermal Imaging. *Langmuir* **2024**, *40* (25), 12888–12898. https://doi.org/10.1021/acs.langmuir.4c00323.

(32) Sumner, A. L.; Menke, E. J.; Dubowski, Y.; Newberg, J. T.; Penner, R. M.; Hemminger, J. C.; Wingen, L. M.; Brauers, T.; Finlayson-Pitts, B. J. The Nature of Water on Surfaces of Laboratory Systems and Implications for Heterogeneous Chemistry in the Troposphere. *Physical Chemistry Chemical Physics* **2004**, *6* (3), 604–613. https://doi.org/10.1039/B308125G.

(33) Nath, S.; Boreyko, J. B. On Localized Vapor Pressure Gradients Governing Condensation and Frost Phenomena. *Langmuir* **2016**, *32* (33), 8350–8365. https://doi.org/10.1021/acs.langmuir.6b01488.

(34) Castillo, J. E.; Huang, Y.; Pan, Z.; Weibel, J. A. Quantifying the Pathways of Latent Heat Dissipation during Droplet Freezing on Cooled Substrates. *Int. J. Heat Mass Transf.* **2021**, *164*, 120608. https://doi.org/https://doi.org/10.1016/j.ijheatmasstransfer.2020.120608.

(35) Meng, Z.; Zhang, P. Dynamic Propagation of Ice-Water Phase Front in a Supercooled Water Droplet. *Int. J. Heat Mass Transf.* **2020**, *152*. https://doi.org/10.1016/j.ijheatmasstransfer.2020.119468.

(36) Schremb, M.; Roisman, I. V; Tropea, C. Normal Impact of Supercooled Water Drops onto a Smooth Ice Surface: Experiments and Modelling. *J. Fluid Mech.* **2018**, *835*, 1087–1107. https://doi.org/DOI: 10.1017/jfm.2017.797.

5

From Patterned to Continuous Hydrophilic Surface Lubrication as Strategies to Decrease Ice Adhesion

Abstract: In aviation, ice removal from surfaces primarily relies on energy-intensive active de-icing systems and anti-icing fluids with significant operational and environmental impact. Alternatively, passive low-icing or low-ice-adhesion surfaces may be used. However, existing passive anti-icing and low-ice adhering materials often lack durability, rely on complex fabrication methods, or cannot be integrated into certified coating systems. Similar challenges are faced in other fields such as communications, ships, and cryogenic preservation. In this work, we introduce and compare several scalable PFAS-free surface-modification strategies based on surface lubrication to obtain low ice adhesion. A robust home-made multichannel ice adhesion testing device was further developed and used across the study. The strategies, applied to three polymeric substrates (a commercial aircraft polyurethane (PU) topcoat, polyvinyl chloride (PVC), and polypropylene (PP)), were: (i) controlled UV exposure, (ii) silicone-oil microdroplet contamination, (iii) hydrophilic micropatterns based on covalently grafted Poly(2-hydroxyethyl methacrylate) (PHEMA), and (iv) a UV-curable hydrophilic spray coating based on 2-(Methacryloyloxy)ethyltrimethylammonium chloride (DMC). UV degradation showed a minor yet measurable effect on the reduction of ice adhesion. On the other hand, surfaces

coated with molecular water layer-forming treatments (PHEMA patterns and DMC) significantly lowered ice adhesion at -10 °C, outperforming oil microdroplets. Together with homogeneous PHEMA-grafts, the DMC coating achieved the lowest adhesion strengths—consistently below 20 kPa in cyclic testing—attributed to the formation of a non-freezing surface water layer. These results demonstrate that PFAS-free water-lubricating hydrophilic coatings offer a promising pathway toward a new generation of effective passive anti-icing materials.

INTRODUCTION

Ice accretion and frost formation on surfaces present persistent safety and operational challenges across numerous sectors, including energy production[1,2], telecommunications[3,4], transportation[5], and refrigeration[6]. Among these, the aviation industry is particularly vulnerable due to the severe consequences that even small amounts of ice can impose on aerodynamic performance[7–11]. Ice buildup on aircraft wings, propellers, and sensors alters airfoil geometry, increases drag, reduces lift, and increases the aircraft's weight, ultimately compromising both efficiency and safety. Because aircraft routinely operate in mixed-phase clouds, freezing rain, and cold and humid atmospheres, any surface exposed to the airflow becomes susceptible to repeated icing events. As global air traffic continues to expand, mitigating icing risks efficiently and sustainably has become an increasingly important engineering challenge.

Commercial aircraft currently rely almost exclusively on active anti-icing systems, the most common being electro-thermal heating.[12-13] Embedded heating elements supply continuous or cyclic thermal energy to maintain surface temperatures above freezing. Although effective and reliable, such systems impose considerable penalties in terms of energy consumption, fuel use, and maintenance requirements. For modern passenger aircraft, thermal anti-icing can account for several percent of overall fuel burn, corresponding to increased carbon emissions and operational costs. Furthermore, adding heaters and power lines increases both structural complexity and aircraft weight. These limitations have motivated a growing interest in passive anti-icing materials, which aim to prevent or mitigate icing without requiring external energy input.[14-16]

One promising passive strategy is the development of surface coatings with ultra-low ice adhesion strength.[15,17] If the adhesion between ice and the aircraft coating is sufficiently small—often cited in the literature as approaching values below approximately 30 kPa—then aerodynamic forces may become sufficient to continuously remove accreted ice during flight, hence preventing dangerous ice accumulation without the need for heating or chemical de-icing.[16,18,19] Although numerous materials and surface treatments with low ice

adhesion have been reported in the literature, none have yet reached commercial implementation on aircraft. Coatings with promising laboratory performance often fail due to issues with scalability, durability, surface contaminations, and/or complex fabrication routes. From an industrial standpoint, an ideal passive anti-icing solution should be inexpensive, fast to apply, compatible with existing aerospace coatings, and mechanically robust under UV exposure, abrasion, dust contamination, and chemical stressors.

To design such coatings, it is essential to consider how ice adhesion can be minimized. Several strategies have been explored extensively: hydrophobic and superhydrophobic coatings, soft elastic substrates, and oil-infused polymers (also referred to as liquid-infused surfaces). Superhydrophobic materials utilize structured and nano-fabricated surface topologies to reduce ice adhesion by minimizing ice-substrate contact area.[20] However, superhydrophobic surfaces typically depend on delicate micro- or nano-textured topographies that are susceptible to abrasion and contamination.[21] Moreover, under humid or icing conditions, liquid penetration into the nano-features can also drastically increase ice adhesion due to mechanical interlocking.[22,23] Elastic PDMS-based surfaces[24], which deform at the ice–substrate interface, can also lower adhesion by dissipating shear stresses during detachment; however, their inherent softness makes them vulnerable to mechanical damage and abrasion. Oil-infused polymers[25,26] create an effective lubricating oil film between the ice and the solid substrate, but the infused oils (typically silicone, perfluoropolyether (PFPE), or mineral oils) tend to deplete over time, leading to increased ice adhesion[27]. In all these strategies, durability remains the biggest limiting factor for industrial applications.

An emerging alternative approach relies on the formation of a stable aqueous lubricating layer at the ice–substrate interface.[18,19,28-34] This concept is also described in the literature using terms such as quasi-liquid layer (QLL), non-freezing water layer, or liquid-like molecular water layer (MWL). Such layers arise when water molecules form strong interactions with certain chemical groups at the surface, preventing them from crystallizing at typical freezing temperatures.[35-37] On a molecular level, this behaviour is typically attributed to strong hydrogen-bonding interactions with charged or hydrophilic groups that

inhibit the cooperative rearrangement of water molecules required for ice nucleation. These non-freezing water layers function as atmospheric self-replenishing lubricants, dramatically reducing interfacial shear strength. Several studies[28,29,31], using this principle applied on hydrogels, polyelectrolyte networks, and PEG-modified elastomers, have reported ice adhesion strengths well below 30 kPa— values commonly regarded as promising for passive aircraft anti-icing applications. However, most such materials lack the mechanical robustness, environmental resistance, or application simplicity required for aviation and other fields. The development of aqueous lubricating surfaces made from durable and scalable coating chemistries appears as an interesting development with potential implementation in critical application domains.

While material innovation is a key challenge, a parallel issue complicates progress in the field of passive anti-icing coatings: a lack of standardized ice adhesion testing.[38] Ice adhesion is most commonly measured using a shear force-based push test, but different laboratories employ widely varying apparatus designs, loading geometries, ice formation protocols, pushing speeds, pushing heights, and temperature–humidity conditions. Recently, several studies have demonstrated that parameters such as actuator pushing speed and pushing height can significantly influence the measured adhesion strength.[41-43] Yet most published reports do not fully disclose these parameters, making cross-comparison of results difficult. The absence of standardization has led to large discrepancies in reported adhesion values for inherently similar materials, obscuring which anti-icing strategies are genuinely most effective hence highlighting the need to properly report and compare surfaces under well controlled testing and environmental conditions.

In this study, we address both the materials challenge and the testing challenge in the development of low-ice adhesion coatings. First, we designed a horizontal shear (push) test setup with accurate temperature and humidity control and multiple sample holders, thereby significantly increasing experimental output speed relative to conventional single-sample designs. This system enables more reproducible, transparent, and systematic testing of ice adhesion under well-defined conditions. Second, we evaluated several surface modification strategies on three polymeric substrates of practical relevance: a commercial

aircraft polyurethane (PU) topcoat, poly(vinyl chloride) (PVC), and polypropylene (PP). The selected surface modifications aimed at studying and comparing the impact on ice adhesion of hydrophobic and hydrophilic continuous and patterned surface lubrication, and the impact of UV exposure on the surface ice adhesion properties. To this aim, selected polymers were treated in different manners: (i) exposed to UV light, (ii) covered with silicone oil droplets, mimicking potential maintenance-related contamination, (iii) surface modified with hydrophilic micropatterns following our recent reports showing their potential to control frost nucleation and propagation[39] as well as ice nucleation during supercooled droplet impact[40] and (iv) coating the surfaces with a UV-curable hydrophilic (2-methacryloyloxyethyl) trimethyl ammonium chloride (DMC)-based spray coating, designed to create a durable, charged surface capable of supporting the formation of a stable non-freezing water layer.

Together, these experiments in very well-controlled testing and environmental conditions aim to provide new insight into how aqueous lubricating layers, surface chemistry, and environmental exposures affect ice adhesion to polymeric materials and demonstrate the potential of aqueous lubricating scalable, durable, and energy-efficient passive anti-icing strategies for future aircraft technologies.

MATERIALS AND METHODS

Materials

The polyurethane coating evaluated in this study is a commercial topcoat currently used in aviation. While the product identity and formulation details are proprietary and therefore undisclosed, its widespread use ensures that the findings are directly applicable to real-world scenarios. The polyurethane was received as part of the full coating system on an AA2024-T3 metallic panel (surface treatment-epoxy primer-polyurethane). The PP and PVC (20 x 20 x 2 mm) polymeric substrates used in this work were purchased from S-Polytec GmbH. Glycidyl methacrylate (GMA, 97%), 2-hydroxyethyl methacrylate (HEMA, 97%), hydrophilic (2-methacryloyloxyethyl) trimethyl ammonium chloride (DMC, 75 wt. % in H_2O), 4-cyano-4-(phenylcarbonothioylthio)pentanoic acid (CTA), 2,2'-azobis(isobutyronitrile) (AIBN, 98%), sodium azide (NaN3, 99.5%), triethylamine (TEA, 99.7%), copper(I)bromide (CuBr, 98%), copper(II) bromide (CuBr2, 99%), 2-bromoisobutyrylbromide (BIBB, 98%), trimethylolpropane triacrylate (TMPTA, technical grade) and the silicone oil were purchased from Merck Sigma. 2-Hydroxy-2-methylpropiophenone (Darocur 1173, >96%) was purchased from TCI Europe.

Preparation of samples exposed to UV

All substrates (PU, PP, and PVC) were exposed to a UV-A lamp (OmniCure S2000 UV Curing System, 320-500 nm) with an irradiance of 30 W/cm^2 for 5 h and 10 h. This treatment exposes the substrates to an irradiance 3,000 to 30,000 times higher than that of natural sunlight (0.001-0.01 W/cm^2) and can be considered an accelerated degradation test simulant of UV aging.

Preparation of samples with hydrophobic oil droplets

All substrates (PU, PP, PVC) were coated with eight droplets of approximately 1 µL silicone oil (an aircraft contaminant) using a micropipette.

Preparation of PHEMA-coated Surfaces

PU, PP, and PVC were coated with poly(2-hydroxyethyl methacrylate) (PHEMA) stripped patterns via surface-initiated atom transfer radical polymerization (SI-ATRP) as reported in Chapter 3.[39] Briefly, to create the stripes, the substrates were first spin-coated with a bifunctional macroinitiator (PAzBrMA). Since the macroinitiator is covalently attached to the surface via UV exposure, a UV mask with a constant stripe width of 150 µm and a stripe distance of 1.2 mm was used to fix the macroinitiator only at stripe locations upon exposure to a UV lamp (OmniCure S2000 UV Curing System, 320-500 nm) with 30 W/cm^2 for 5 min. This was followed by (i) rinsing to remove the unreacted PAzBrMA, (ii) a SI-ATRP of the hydrophilic 2-hydroxyethyl methacrylate (HEMA) monomer from the macroinitiator at the stripe locations, and (iii) rinsing again to remove the excess HEMA. The resulting samples are polymeric substrates (PU, PP, or PVC) patterned with hydrophilic polymer brushes (PHEMA), which are covalently anchored to the substrate surface. Samples uniformly coated with PHEMA were fabricated using the same protocol, omitting the patterned mask during the UV-exposure step.

Preparation of DMC-coated Surfaces

To evaluate the concept of water-enriched surfaces on ice adhesion, a UV coating (DMC) was designed. The hydrophilic DMC-coating formulation was prepared by mixing DMC (4 g, monomer), Darocur 1173 (0.16 g, type I photoinitiator), and TMPTA (2.88 g, cross-linker) in EtOH (20 g, solvent). The mixture was applied to the polymeric substrates using a spray gun with a nozzle diameter of 1.4 mm, followed by UV exposure (OmniCure S2000 UV Curing System, 320-500 nm) at 30 W/cm^2 for 15 min.

Water contact angle measurements

Water contact angle (WCA) measurements of the bare, UV-exposed, PHEMA-grafted, and DMC-coated polymer surfaces were performed using an optical contact angle goniometer (KSV CAM 200). Silicone-oil-contaminated samples are excluded from WCA measurements, as the liquid oil phase exhibits an intrinsically high-water repellency. Static contact angles were determined using the sessile drop (10 µL) method. Each measurement was repeated three times per sample. All contact angle measurements were conducted at an ambient temperature of 21 ± 2 °C and a relative humidity of 40 ± 5 %.

Surface Characterization

Laser scanning confocal microscopy (LSCM, Keyence VK-X1000) was used to obtain the areal surface roughness (Sa) using a 20x magnification lens for all samples except for the oil-contaminated surfaces. Silicone-oil-contaminated samples are excluded from roughness characterization, as the liquid oil phase exhibits an effectively zero surface roughness. LSCM was also used to determine the thickness of the PHEMA stripes and DMC coating via line profile analysis. For PHEMA-patterned samples, profiles were taken across individual stripes to measure the height difference between grafted and unmodified regions. For the DMC coating, a step edge was created by masking the substrate with adhesive tape prior to spray coating. After UV curing and tape removal, the coating thickness was obtained from the height difference across the step edge. Micro–FTIR (µ-FTIR, PerkinElmer Spotlight 400) was employed specifically to analyse the chemically micropatterned PHEMA-grafted surfaces. In addition, the effect of UV exposure on the chemical composition of PU, PVC, and PP substrates was investigated using an FTIR spectrometer (Spectrum 100, PerkinElmer). Spectra were collected in the range of 4000–600 cm^{-1}, with each spectrum obtained by averaging 32 scans.

Ice Adhesion Tests

The ice adhesion strength of the samples was measured using a custom-built horizontal push-off test setup (**Figure 5.1**). The setup consists of a temperature- and humidity-controlled environmental chamber, an external circulating cooling unit (LAUDA ECO RE1050), a humidity control system, a set of five sample holders, and a linear actuator (LTA-HL with CONEX-CC controller) equipped with a calibrated load cell that can be displaced to the selected sample holder for multiple measurements under comparable environmental conditions. The chamber humidity was maintained below 10% relative humidity (5 ± 3 %) using a low nitrogen flow to prevent unwanted frost formation. Prior to testing, the substrates were cooled to −10 ± 1 °C inside the environmental chamber, with the surface temperature monitored using thermocouples. Teflon moulds were then positioned on top of the samples using the alignment block, and 400 µL of deionized water was slowly injected into each mould using a syringe equipped with a long needle to form cylindrical ice pillars (8 mm diameter, 8 mm height). After water injection, the chamber was allowed to re-equilibrate to the target temperature and humidity conditions, and the water pillars were left to freeze for approximately 30–35 min before testing. Ice adhesion was measured by advancing the actuator at a constant speed of 0.01 mm/s, with the pushing tip positioned 2 mm above the substrate surface. The applied force was recorded as a voltage–time curve, from which the peak force required to detach the ice was extracted with the help of a calibration force-voltage calibration curve. The ice adhesion strength was calculated by dividing this peak force by the ice–substrate contact area (**Equation 5.1**). Each measurement was repeated at least five times per sample.

$$\tau_{ave} = \frac{F}{A} = \frac{g \times V_{peak}}{A} = \frac{9{,}80665\,\frac{m}{s^2} \times V_{peak}}{0.0503\ cm^2} \tag{5.1}$$

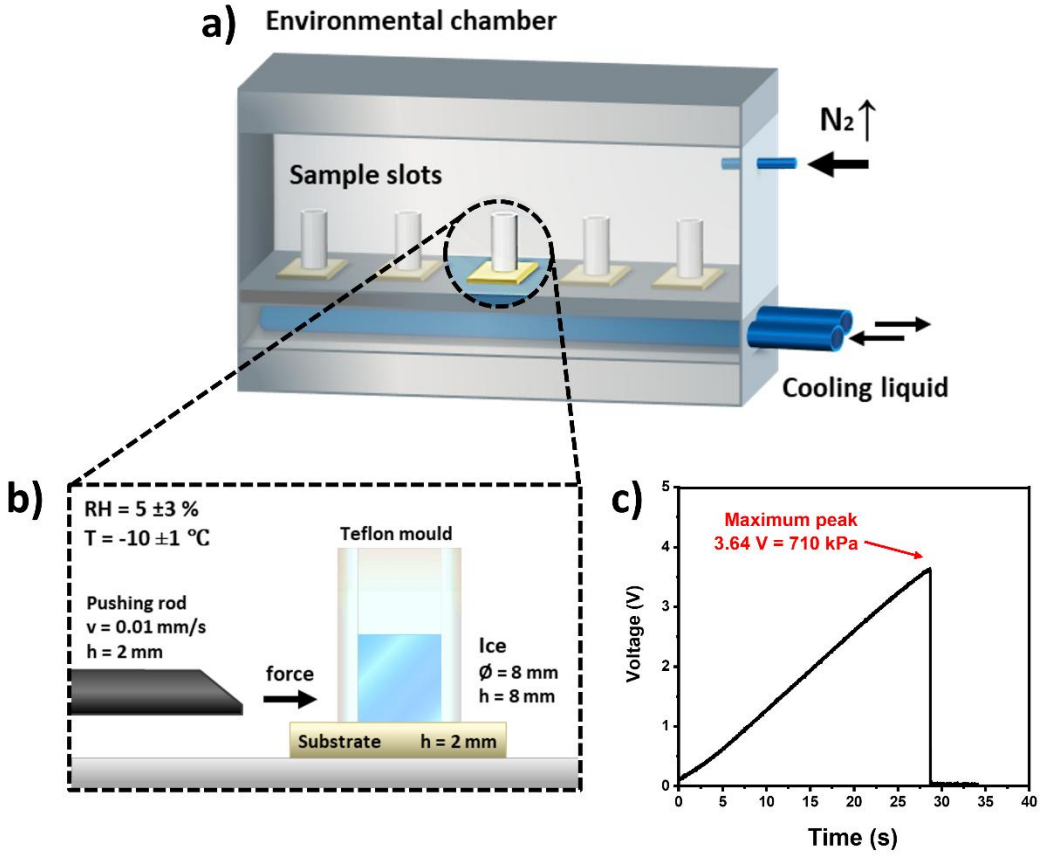

Figure 5.1. Schematic representation of the ice adhesion experimental setup: (a) the environmental chamber with 5 sample holders, (b) the environmental and experimental parameters used in the push test in this work, and (c) an example of a voltage-time curve, which shows the peak voltage value at ice detachment and the corresponding ice adhesion strength derived from a voltage-force curve.

RESULTS AND DISCUSSION

Design, Construction, and Validation of the Ice Adhesion Test Setup

Ice-adhesion measurements reported in the literature comprise a wide range of experimental configurations, including centrifugal tests, vertical shear setups, and various custom-built horizontal push or pull -test rigs.[38] This diversity complicates direct comparison between studies, particularly because the ice failure mechanism, environmental conditions, and mechanical test parameters strongly influence the measured ice adhesion strength. To ensure comparability with the majority of reported results, we designed and constructed a horizontal shear test (push test) setup, which remains the most widely used testing configuration in the literature.

Although conceptually straightforward, the push test is sensitive to several critical parameters that can dramatically affect the measured adhesion strength. Previous works have demonstrated that pushing height, pushing speed, and testing temperature can shift the measured adhesion strength values by tens of kilopascals.[41-43] Based on these insights, our setup was designed to operate in a quasi-static regime, with the pushing height fixed at 2 mm and the pushing speed at 0.01 mm/s (out of a potential range of 0.01-1 mm/s). These settings minimize dynamic or inertial contributions, ensuring that fracture occurs in a controlled manner dominated by interfacial failure.

A second major design goal was to obtain strict control of environmental testing conditions (humidity and temperature). The final setup (illustrated in **Figure 5.1**) consists of a fully enclosed environmental chamber with independent control of temperature and humidity. The temperature inside the chamber and on the sample surfaces is regulated via a cooling-fluid channel beneath the sample holder plate, enabling cooling down to –50 °C. Humidity during the experiments is controlled by introducing a flow of inert nitrogen gas into the chamber, thus maintaining a constant 5 ± 3 % relative humidity and preventing unwanted frost formation during testing. For real-time monitoring of both temperature and humidity,

the chamber is also equipped with thermometers and manometers placed over the samples during testing. Furthermore, the test chamber was carefully vacuumed before each experiment to maintain clean, dust-free conditions.

Instead of testing only one sample per cooling cycle, the ice adhesion setup was equipped with a multi-sample platform featuring five sample positions arranged in a horizontal row. This design reduces experiment times, improves reproducibility, and facilitates the collection of statistically meaningful data. An alignment block placed above the sample holders ensures that all ice moulds are positioned consistently into the same locations between experiments. The alignment block also contains dedicated openings that allow the moulds to be filled with deionized water inside the chamber while minimizing disturbance to the temperature and humidity conditions.

During testing, the linear actuator—mounted on a horizontal guide rail in front of the chamber—is aligned with each sample using a manual positioning system. The actuator is equipped with a calibrated load cell and connected to a Picoscope data acquisition system with signal amplification and the Conex controller unit. To push the ice mould off the sample, the actuator is moved using the controller unit while the voltage and time are recorded via the Picoscope software.

To validate the reliability of the ice adhesion test setup, adhesion measurements were performed at −10 °C on several commonly used polymeric reference materials, including polytetrafluoroethylene (PTFE, Teflon), polyethylene (PE), polypropylene (PP), and polycarbonate (PC). A direct and systematic comparison with literature values for such substrates is challenging, as most published ice adhesion studies primarily focus on newly developed icephobic coatings and typically report only limited reference data. In addition, literature values are obtained using a variety of ice adhesion test configurations, including centrifugal, shear, and cone-based tests, which can further contribute to variability in reported adhesion strengths. Despite these limitations, the ice adhesion values obtained in this work (**Figure 5.2**) fall within the ranges reported in the literature[44-48], with Teflon and PC showing the closest agreement with previously published values (~150 kPa and ~350 kPa,

respectively). The measured adhesion strength for PE is slightly higher (~450 kPa vs. ~350 kPa), while that of PP is slightly lower than literature values (~150 kPa vs. ~300 kPa), which may be attributed to differences in surface roughness, substrate thickness, or the specific ice adhesion test configuration employed. As detailed surface and material characteristics are rarely specified alongside ice adhesion results, the exact origin of these deviations cannot be conclusively determined. Overall, the close agreement between our measurements and data available in literature, combined with the low standard deviations found in our tests, confirms the robustness and reliability of the experimental setup. This validation provides a solid and transparent foundation for the quantitative evaluation of the surface modifications presented in the following sections.

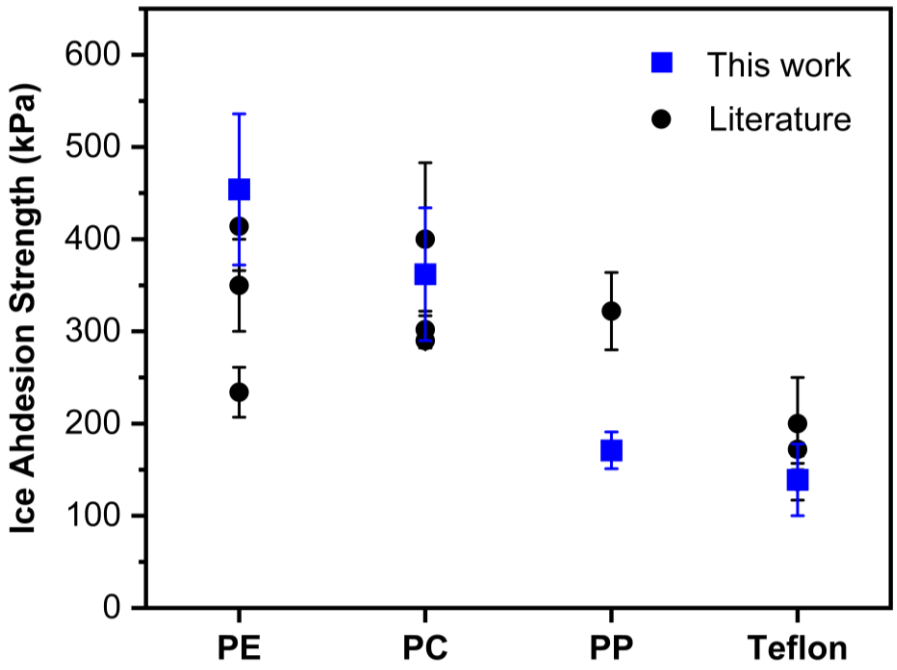

Figure 5.2. Validation of the ice adhesion test setup by comparing ice adhesion strength values of common polymeric substrates measured in this work (blue squares) with literature values[44-48] (black circles) obtained using various ice adhesion test methods at temperatures of −10 ± 2 °C.

Sample Preparation and Surface Characterization

Three substrate materials were selected for this work: a commercial aircraft polyurethane (PU) topcoat, polyvinyl chloride (PVC), and polypropylene (PP). The PU coating provides a direct connection to aviation applications, while PVC and PP serve as model engineering polymers widely used in industrial, medical, and infrastructure applications. These substrates differ substantially in their chemical compositions and surface chemistries, providing a meaningful framework for evaluating various anti-icing strategies.

Each substrate was modified using four different approaches (schematically illustrated in **Figure 5.3**): UV exposure for 5 h and 10 h (**Figure 5.3a**), surface coverage with silicone oil microdroplets (**Figure 5.3b**), micropatterns and uniform coverage covalent grafting with hydrophilic PHEMA-brushes (**Figure 5.3c-i and 5.3c-ii**), and a coating with a hydrophilic spray-coated UV-curable DMC topcoat (**Figure 5.3d**).

Micropatterning was achieved using a surface-initiated atom transfer radical polymerization (SI-ATRP) protocol as described in Chapter 3 and 4.[39,40] First, a multifunctional macroinitiator (PAzBrMA) containing azide and bromide groups was covalently attached to the polymer surface through UV-induced C–N formation. The bromide moiety then served as the ATRP initiator for the polymerization of hydrophilic 2-hydroxyethyl methacrylate (HEMA), forming surface-grafted PHEMA chains. A patterned UV mask was used in the first step to restrict macroinitiator attachment to micrometer-scale striped regions (~150 µm width), resulting in local hydrophilic areas on the hydrophobic polymeric substrates. Without the UV mask, the samples were uniformly covered with the hydrophilic PHEMA brushes.

The methacrylatoethyl trimethyl ammonium chloride (DMC) based hydrophilic coating was prepared by spraying the coating formulation onto the substrate, followed by 15 minutes of UV curing. This process yields a hydrophilic, crosslinked coating with charged groups capable of forming strong hydrogen bonds with water molecules. Compared to micropatterning, this approach is faster, simpler, more scalable, and better suited for coating large, complex geometries such as aircraft surfaces.

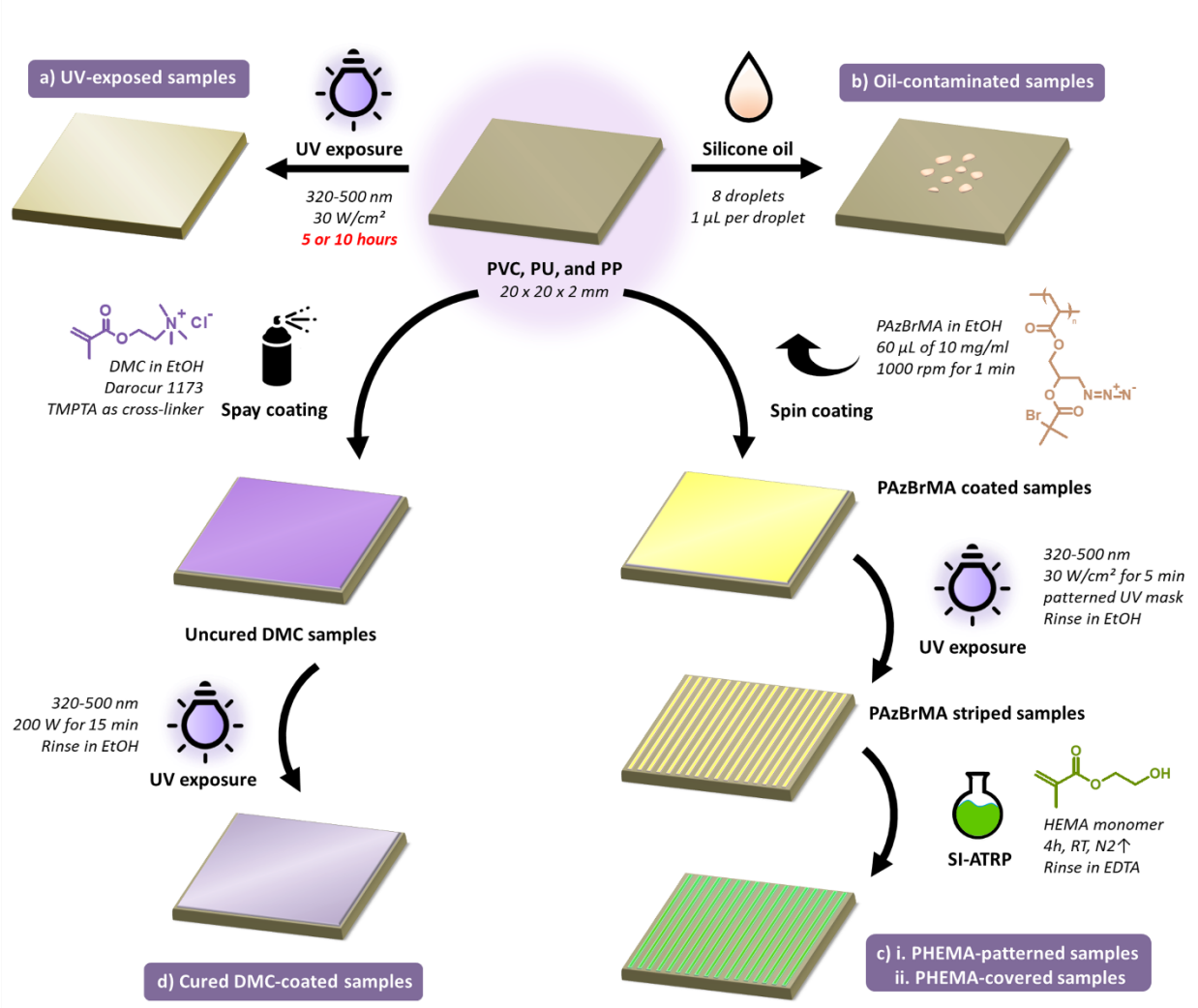

Figure 5.3. Schematic overview of the surface modification strategies applied to the polymeric substrates (PVC, PU, and PP) investigated in this work: (a) UV exposure for 5 or 10 h, (b) contamination with silicone oil microdroplets, (c) hydrophilic grafting via surface-initiated ATRP of HEMA, and (d) spray application of a UV-curable hydrophilic DMC coating.

The static water contact angle and confocal microscopy surface roughness of the studied samples can be seen in **Figure 5.4**. The results show that UV exposure induces distinct, polymer-dependent changes in surface properties. Both PU and PVC exhibited a gradual decrease in water contact angle and surface roughness (Sa) with increasing UV exposure time (i.e., more hydrophilic and smooth surfaces). The static water contact angle of PU

reduced from 87° to 74° after 10h UV exposure, while the surface roughness reduced from 0.25 µm to 0.21 µm. For PVC, the corresponding transitions were from 96° to 92° in water contact angle and from 0.8 µm to 0.5 µm in surface roughness. The enhanced hydrophilicity is attributed to UV-induced chemical modifications[49], including dechlorination in PVC and the formation of polar, oxidized surface functionalities such as carbonyl and hydroxyl groups in PU. The incorporation of these chemical groups on PVC and PU surfaces is evident in the FTIR data (see **Figure 5.5**), showing increasing transmittance peaks for OH stretch at ~3400 cm^{-1} and C=O stretch at ~1700 cm^{-1}. The concurrent reduction in surface roughness is likely associated with a UV-induced planarization effect at the outermost surface layers, resulting from photodegradation as reported elsewhere[50].

A different trend was observed for PP. While a slight planarization effect was also apparent (from 0.16 µm to 0.13 µm), PP showed a measurable increase in wettability after 5 h of UV exposure (from 101° to 87°), followed by a pronounced increase in water contact angle after 10 h (up to 108°). This behaviour suggests the presence of competing processes: initial surface oxidation introduces hydrophilic functional groups, whereas prolonged UV exposure promotes degradation and hydrophobic recovery. This behaviour has been reported for polyethylene (LDPE) and poly(propylene) (PP) exposed to prolonged UV/VUV radiation (100-400 nm).[51] During this recovery process, UV-generated polar groups undergo bond scission and cross-linking, leading to the loss of surface oxidation products and the restoration of hydrophobic surface characteristics. This phenomenon is supported by the FTIR data in **Figure 5.5,** showing subtle emerging C=O stretching peaks at ~1700 cm^{-1} on the PP surface after the initial 5 hours of UV exposure, which later disappear after 10 hours of exposure.

The surfaces modified with a continuous PHEMA grafted hydrophilic layer exhibited the lowest water contact angles among all investigated samples (WCA = 40 ± 3°). Since the reported wettability and roughness values correspond to fully grafted PHEMA regions, these reflect the intrinsic hydrophilicity of the grafted polymer stripes in PHEMA patterned surfaces. The grafting with PHEMA did not lead to a significant increase in surface roughness on any of the polymeric substrates, which is consistent with the relatively short PHEMA

chain lengths obtained after 4 h of polymerization (< 0.3 µm) and our earliest reports on patterned surfaces.[39]

As intended, DMC-coated samples displayed low water contact angles and smooth surface topographies (WCA = 62 ± 1° and Sa = 0.25 ± 0.02 µm), independently of the underlying polymer substrate. This behaviour is consistent with the formation of a continuous, uniform, hydrophilic coating layer that effectively masks the substrate-specific surface properties.

Overall, these results demonstrate that the applied surface modification strategies induce controlled and polymer-specific changes in surface chemistry and morphology. As both wettability and surface roughness play key roles in governing water–surface interactions, these characteristics provide essential context for interpreting the ice adhesion behaviour discussed in the subsequent sections.

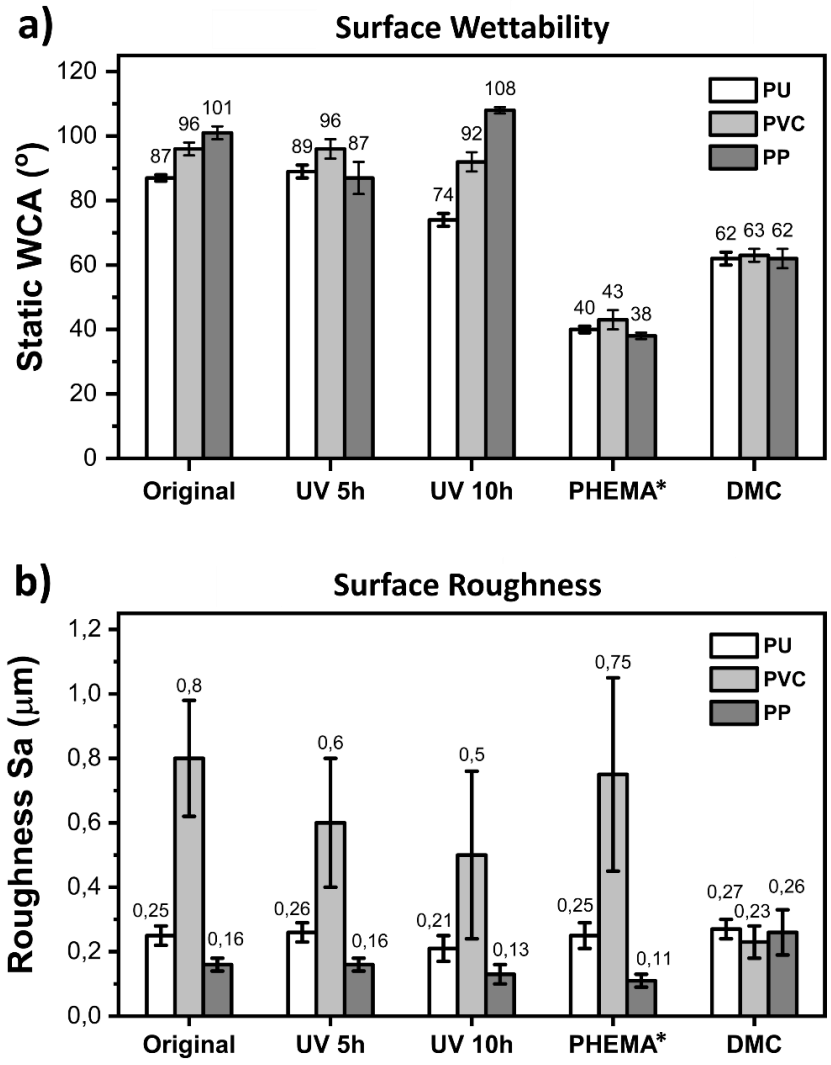

Figure 5.4. Characteristic surface parameters showing: (a) Static water contact angles (WCA) and (b) Surface roughness values (Sa) of PU, PVC, and PP substrates in their original state and after UV exposure (5 h and 10 h), hydrophilic PHEMA grafting, and DMC coating. ***Note 1*:** Silicone-oil-contaminated samples are excluded, as the liquid oil phase exhibits an effectively zero surface roughness and intrinsically high-water repellency. ***Note 2:*** The values reported for PHEMA correspond to surfaces fully grafted with PHEMA and not with PHEMA patterns.

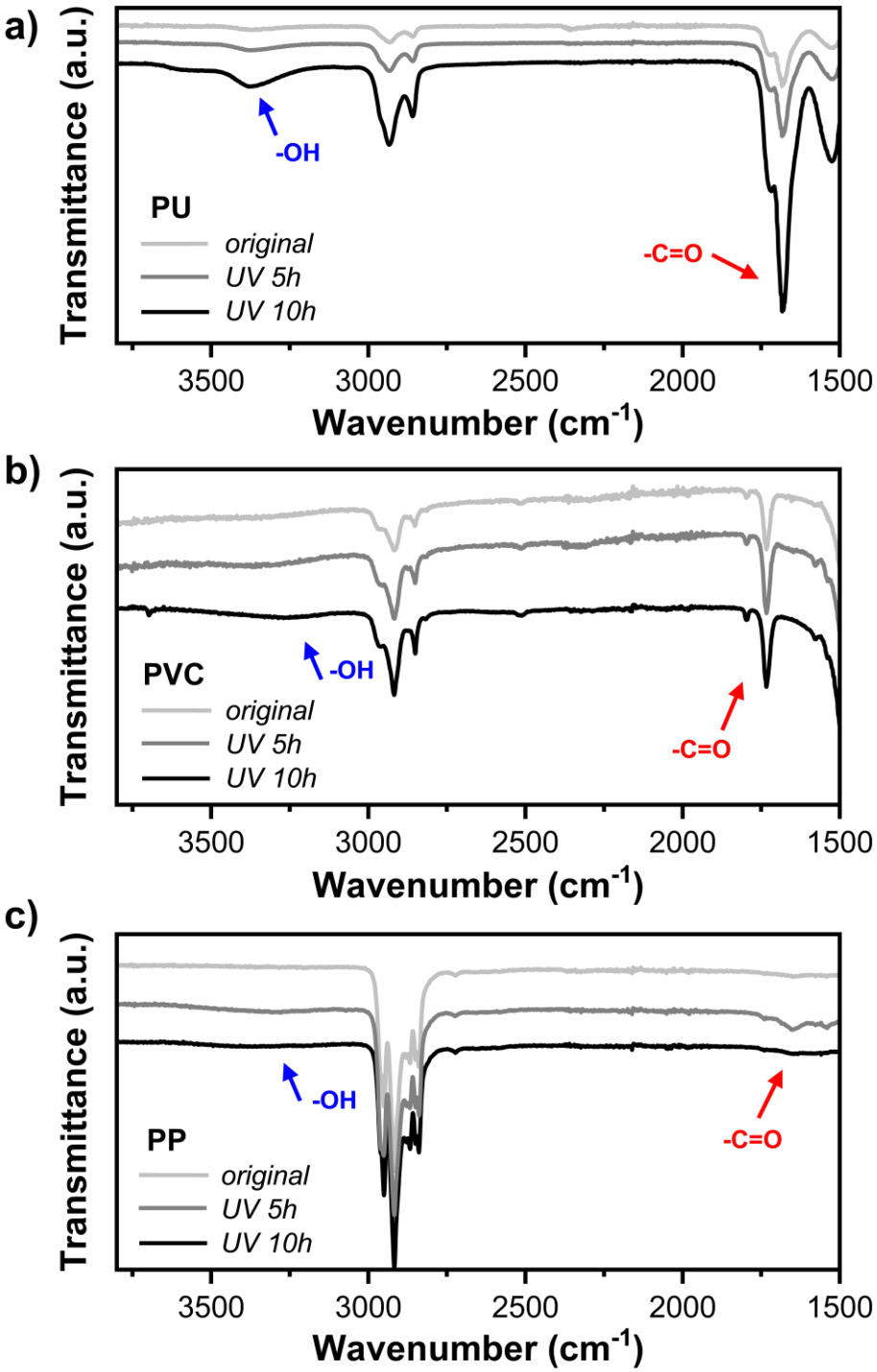

Figure 5.5. FTIR spectra of a) PU, b) PVC, and c) PP substrates before and after UV exposure. For PU and PVC, the progressive increase in the intensity of bands associated with hydroxyl (–OH) stretching and carbonyl (C=O) vibrations with increasing UV exposure time indicates the formation of oxidized, hydrophilic surface functionalities. In contrast, PP exhibits an increase in –OH and C=O-related bands after 5 h of UV exposure, followed by a decrease after 10 h, consistent with UV-induced surface oxidation followed by hydrophobic recovery upon prolonged UV exposure.

Influence of UV Exposure on Ice Adhesion

The ice adhesion results for all investigated surfaces are summarized in **Figure 5.6**. All measurements were conducted at −10 ± 1 °C and 5 ± 3% relative humidity, with at least five independent measurements taken per sample type. A representative force–displacement curve (recorded as voltage–time) is shown in **Figure 5.1**, where the maximum voltage (V_{peak}) corresponds to the moment of ice detachment.

Among the unmodified substrates, the commercial PU topcoat exhibited the highest ice adhesion strength (824 kPa), reaching values comparable to or even exceeding values commonly reported for bare aluminium alloys (~600–1000 kPa). In contrast, PP showed the lowest ice adhesion (171 kPa), while PVC displayed intermediate behaviour (687 kPa). The poor performance of PU is particularly notable given its widespread use in aviation coatings, reinforcing the need for improved passive anti-icing solutions.

UV exposure revealed a clear divergence in ice adhesion behaviour, with PU and PVC responding differently from PP. For both PU and PVC, a slight increase in ice adhesion strength was observed with increasing UV exposure time, reaching 873 kPa and 691 kPa after 10 h. These changes coincide with the increased surface hydrophilicity observed in WCA measurements and the formation of oxidized surface functionalities confirmed by FTIR analysis (**Figure 5.5**). It is hypothesized that the introduction of polar groups on a rigid surface enhances hydrogen bonding at the ice–surface interface, thereby promoting stronger adhesion. At the same time, UV-induced surface planarization[50] led to a reduction in surface roughness for both materials, which may partially counteract the effect of increased wettability. This balance between chemical and topographical changes likely explains why the overall increase in ice adhesion is relatively small, particularly for PVC, where the planarization effect was more pronounced.

In contrast, PP exhibited a distinctly different response to UV exposure. While a small reduction in ice adhesion was observed after 5 h of UV irradiation (from 171 kPa to 164 kPa), prolonged exposure for 10 h resulted in a pronounced decrease in ice adhesion down to 85 kPa. The small decrease in ice adhesion after 5h UV exposure is in contrast with the related

contact angle decrease (**Figure 5.4a**). The further decrease in ice adhesion is nevertheless well in agreement with the contact angle recovery observed after 10h UV exposure with no surface roughness variations (**Figure 5.4a**). This finding is particularly notable, as it suggests that prolonged UV exposure—typically associated with material degradation—may inadvertently decrease ice adhesion to PP substrates.

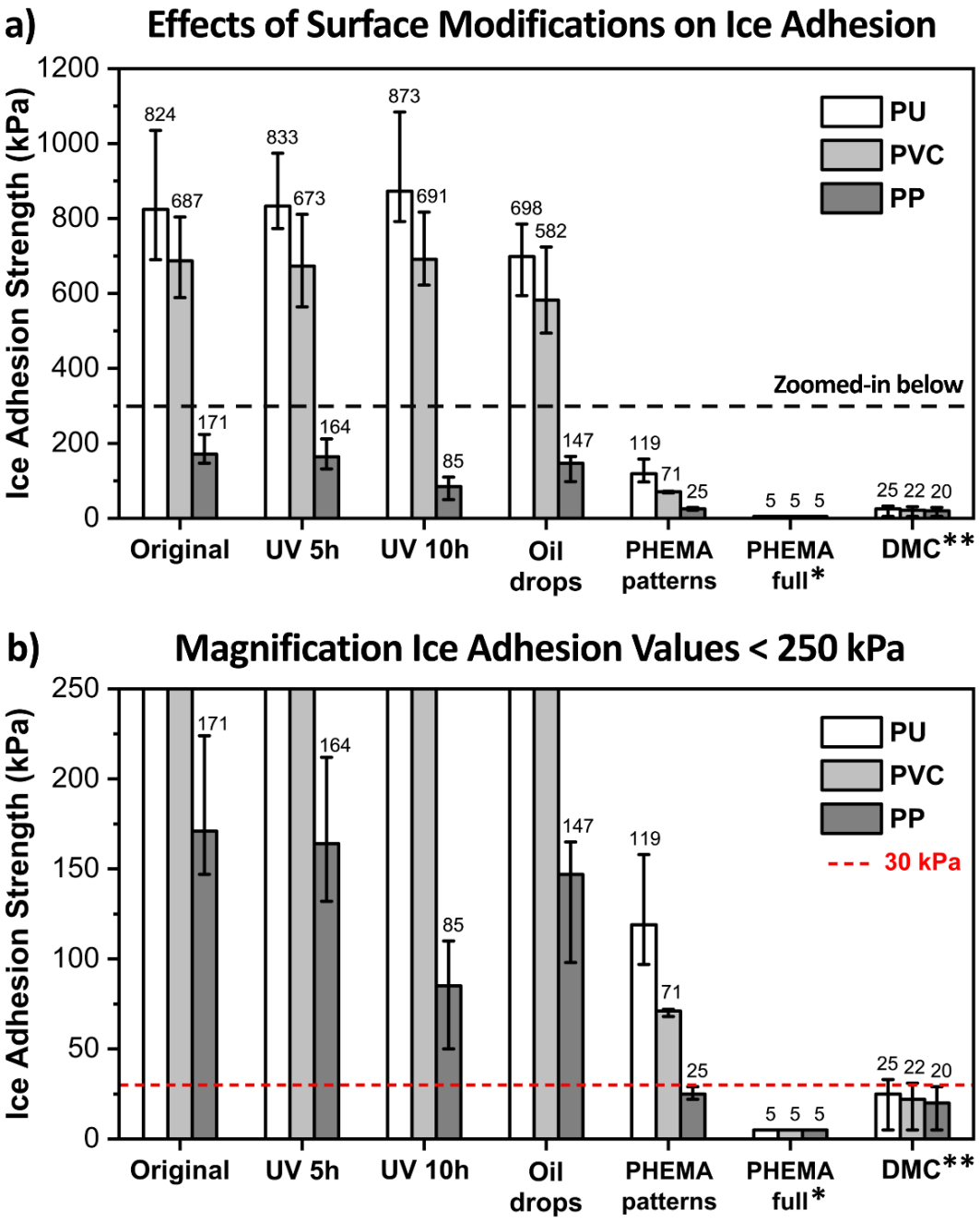

Figure 5.6. Ice adhesion strength of PU, PVC, and PP substrates at −10 ± 1 °C and 5 ± 3 % RH before and after surface modifications. a) Full range of measured ice adhesion values. b) Magnified view highlighting adhesion strengths below 250 kPa. The dashed red line indicates the commonly cited target value of 30 kPa for passive low-ice adhesion surfaces of use in aerospace. ***Note 1*:** For substrates fully grafted with PHEMA (*), the measured ice adhesion strengths were below the detection limit (5 kPa) in all experiments. ***Note 2:*** For DMC-coated samples (**), the measured ice adhesion strengths were below the detection limit (5 kPa) in some experiments, hence marking the lower limit.

Role of Oil and Water Lubrication in Reducing Ice Adhesion

Passive anti-icing strategies based on interfacial lubrication are among the most effective approaches reported for reducing ice adhesion. These strategies generally rely on the presence of a lubricating layer between the ice and the solid surface, either in the form of a thin oil film[25] (LIS or SLIPS) or an unfrozen aqueous layer[34] (hydrated surfaces and hydrogels). In this work, both lubrication mechanisms were investigated: silicone oil microdroplets were used to represent partial oil lubrication, whereas hydrophilic coatings and grafted polymers were employed to promote the formation of interfacial water layers. Rather than studying fully oil-infused surfaces, which are already widely reported in the literature to exhibit ultra-low ice adhesion, this work focused on discrete oil droplets to investigate how localized surface contamination and partial interfacial lubrication influence measured ice adhesion values.

The effect of these localized oil contaminations on ice adhesion is shown in **Figure 5.6**. Contamination with silicone oil droplets reduced ice adhesion to all substrates compared to the unmodified surfaces. Ice adhesion decreased from 824 to 698 kPa on PU, from 687 to 582 kPa on PVC, and from 171 to 147 kPa on PP. This reduction follows the same qualitative trend reported for liquid-infused surfaces (LIS)[25], where the presence of a lubricating oil layer lowers the interfacial shear strength between ice and the substrate. However, in contrast to classical LIS systems, which typically reduce ice adhesion by one to two orders of magnitude, the reductions observed here are comparatively modest. This difference can be attributed to the absence of a continuous lubricant film: the present samples contain only discrete oil droplets. As a result, ice detachment occurred across regions of mixed contact between ice, oil, and the solid substrate, leading to a more limited and substrate-dependent reduction in ice adhesion. Notably, PP exposed to 10 h of UV irradiation exhibited a lower ice adhesion strength (85 kPa) than oil-covered PP (147 kPa), indicating that surface chemistry changes may, in some cases, outperform partial oil lubrication.

In contrast, surfaces with PHEMA (patterned or continuous hydrophilic surface treatment) exhibited a much stronger reduction in ice adhesion across all substrates. Ice adhesion

decreased to 119 kPa on PU, 71 kPa on PVC, and 25 kPa on PP when patterned, and down to under 5 kPa (limit of our load cell) when the surfaces were fully covered with PHEMA. This behaviour is consistent with numerous reports demonstrating that hydrophilic polymer grafts can reduce ice adhesion through the formation of a lubricating aqueous layer at subzero temperatures.[15] Importantly, direct evidence for such a layer in the present system was obtained in Chapter 3, where freezing events on identical PHEMA-patterned surfaces were shown to initiate on the hydrophilic regions and propagate rapidly along the stripes via a liquid-like molecular water layer (MWL).[39] Moreover, freezing on these regions was observed to occur only below approximately −15 °C, indicating that the interfacial water remains unfrozen at the ice adhesion testing temperature of −10 °C. These observations support the presence of a non-frozen interfacial water layer under the present conditions. Given the magnitude of the ice adhesion reduction, the grafted PHEMA patterns appear to generate a more effective lubricating interfacial layer than isolated hydrophobic silicone oil droplets.

To further examine the effect of surface coverage, fully PHEMA-grafted substrates were also prepared using the same procedure without a photomask. For these uniformly grafted samples, the measured ice adhesion strengths were below the detection limit of the experimental setup (~5 kPa) for all three polymer substrates. This observation supports the interpretation that a continuous hydrophilic layer can promote the formation of an interfacial water layer that enhances lubrication at the ice–substrate interface. In contrast, the patterned substrates offer only partial surface coverage, resulting in substrate-dependent adhesion values due to regions where ice remains in direct contact with the underlying polymer.

Surprisingly, no significant difference was observed between stripe orientations parallel and perpendicular to the pushing direction, despite the expectation that anisotropic surface features could influence local stress distributions and promote preferential crack initiation or propagation along specific directions. This indicates that the enhanced reduction in ice adhesion is governed primarily by improved interfacial lubrication associated with the

patterned geometry (stripes vs. dots), rather than by directional crack propagation or fracture mechanics under the tested conditions.

The formation of an unfrozen water layer at hydrophilic polymer interfaces is well documented for PHEMA and other hydrophilic polyacrylate-based materials.[35-37] Water-polymer chain interactions associated with such polymers are typically classified into three categories: freezable free water behaving similarly to bulk water, freezable bound water interacting weakly with the polymer chains, and non-freezing bound water strongly associated with hydrophilic or charged functional groups. While freezable free water freezes near 0 °C, both freezable bound and non-freezing bound water can remain unfrozen well below typical freezing temperatures due to a balance between water–water hydrogen bonding, which promotes ice formation, and water–polymer interactions, which disrupt ice crystallization and stabilize liquid-like states.

Previous studies have shown that non-freezing water associated with PHEMA can remain in a liquid or quasi-liquid state down to approximately −15 °C.[36] At the testing temperature used in this work (−10 °C), both non-freezing and freezable bound water are therefore expected to remain unfrozen. Because the PHEMA grafts form a continuous hydrophilic phase within each patterned region, they can retain and stabilize interfacial water, leading to the formation of a lubricating layer. This liquid water layer reduces the effective ice–substrate contact area and lowers the shear stress required for ice detachment.

Among all strategies investigated in this work, the hydrophilic DMC coating produced the most pronounced reduction in ice adhesion. For all substrates, ice adhesion values fell below 30 kPa, reaching, in the worst, most extreme cases, 25 kPa on PU, 22 kPa on PVC, and 20 kPa on PP, with several samples showing ice adhesion below the detection limit of our device, i.e., below 5 kPa (**Figure 5.6**). In all cases, these values are below the commonly cited threshold required for passive ice removal in aviation applications, where aerodynamic forces alone can promote dynamic ice shedding. As the DMC coating provides complete and continuous surface coverage, ice adhesion is governed by the coating surface chemistry itself rather than by the substrate beneath. We argue that the presence of charged

groups within the DMC-based polymer network strongly promotes bound-water formation, resulting in a replenishable aqueous lubricating layer similar to that formed on PHEMA-grafted surfaces.

Figure 5.7 schematically summarizes the influence of each surface modification on the ice–substrate interface and the resulting ice adhesion behaviour and mechanism behind the ice adhesion. Despite being only slightly hydrophilic compared to PHEMA grafts, the greatest reduction in ice adhesion was achieved with the DMC coating, attributed to the formation of a continuous aqueous lubricating layer. In contrast to oil-based lubrication, which is inherently limited by lubricant depletion and leakage over time, water-based lubricating layers can be continuously replenished from the environment, making them a more robust and sustainable strategy for long-term passive anti-icing applications. Moreover, the DMC coating of 50 micron thick is also expected to maintain icephobicity through the cross-section and possess higher durability than hydrophilic PHEMA brushes due to its crosslinked nature.

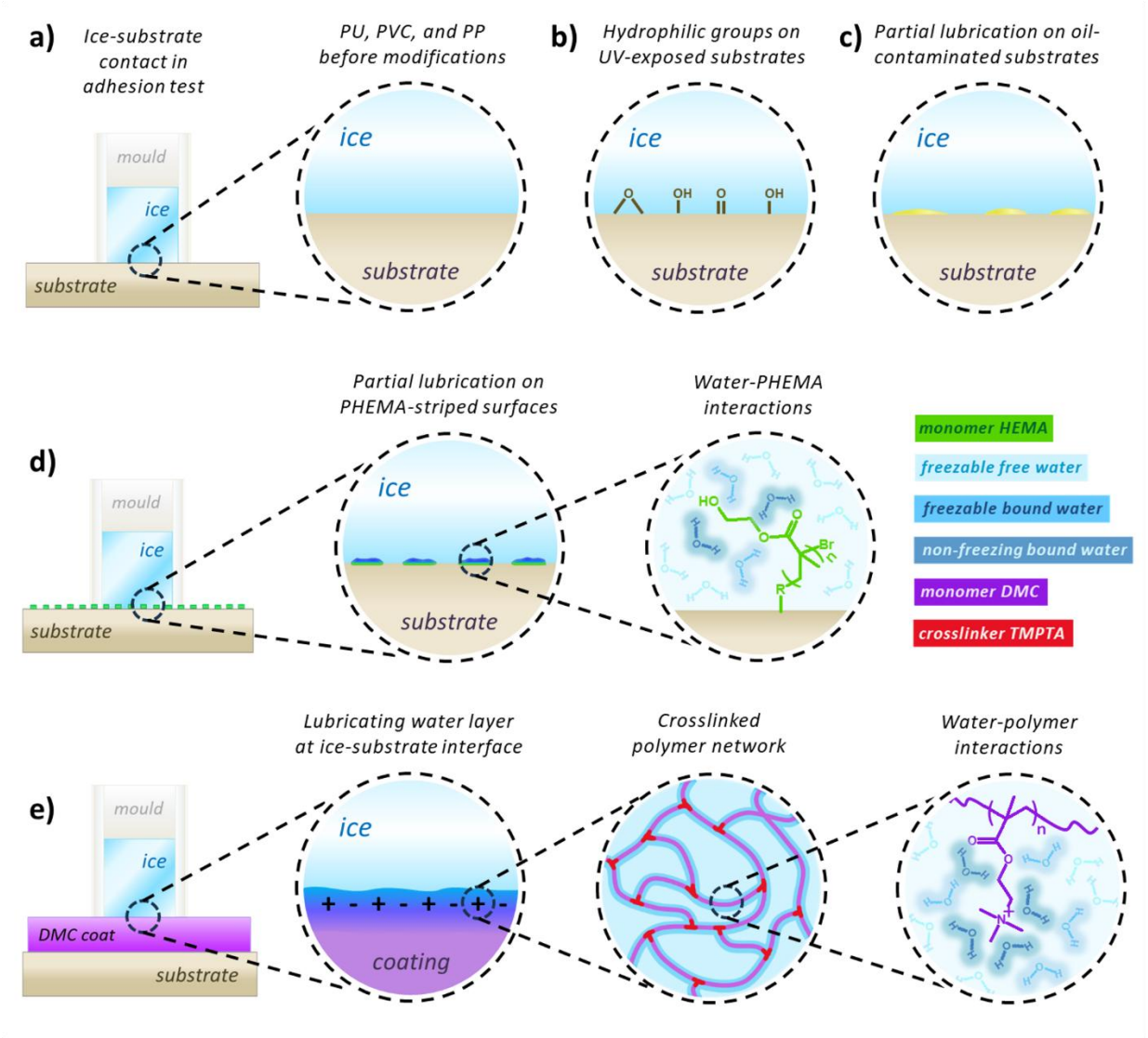

Figure 5.7. Schematic overview of ice adhesion mechanisms for the investigated surface modifications. Ice–substrate interactions are shown for a) unmodified substrates, b) UV-exposed substrates covered with hydrophilic oxidation products, c) oil-contaminated surfaces with partial lubrication, d) PHEMA-patterned surfaces with partial aqueous lubricating layers, and e) DMC-coated surfaces covered with a continuous, replenishable water layer.

Comparison to Existing Anti-Icing Strategies and Literature Benchmarks

To place the results of this study in the context of previously reported low-ice-adhesion surfaces, **Figure 5.8** compares the ice adhesion strengths measured here with values from the literature[16,52-90] obtained under comparable conditions. Only studies employing horizontal shear-based ice adhesion tests at –10 ±2 °C and reporting comparable ice geometries were included to ensure the fairest possible comparison (it should be noted that it was not possible to confirm the used RH in all studies due to a lack of available information).

As shown in **Figure 5.8a**, hydrophobic (HS) and superhydrophobic surfaces (SHS) typically exhibit ice adhesion strengths in the range of ~100–500 kPa at –10 °C. Among these, a Teflon-based SHS[54] reported exceptionally low values below 30 kPa (≈10 kPa). Such performance is generally attributed to nanoscale surface structuring that minimizes effective ice–substrate contact via air entrapment and the hydrophobic nature of fluorocarbons. While this value is comparable to the one achieved by the DMC coating in the present work, nanostructured SHS are known to degrade rapidly under mechanical wear and repetitive icing–deicing cycles.[21-23] In addition, rising environmental concerns around the use of fluorinated materials question their suitability for aviation applications.

Elastic or soft polymer surfaces (ES) constitute another widely studied category for reducing ice adhesion, relying on elastic deformation during ice detachment. PDMS-based coatings, in particular, can achieve extremely low adhesion strengths (~3–10 kPa). However, these materials generally struggle with low mechanical robustness[24], making them unsuitable for demanding aeronautical environments despite their excellent laboratory performance.

Liquid-infused surfaces (LIS) are among the most extensively investigated passive anti-icing strategies and can consistently achieve low ice adhesion values in the range of ~5-100 kPa. As previously described for oil-contaminated samples, the effectiveness of LIS originates from the presence of a lubricating oil layer at the ice–surface interface. However, as with SHS and ES, their durability presents a key limitation.[27] The lubricating liquid is prone to

depletion during repeated icing cycles, and, for that reason, maintaining a stable lubricant reservoir over time remains a significant challenge.

Water-lubricating surfaces (WLS) have recently emerged as an alternative strategy to overcome lubricant depletion by relying on a replenishable aqueous interfacial layer. As presented in **Figure 5.8a**, WLS can achieve ice adhesion values comparable to or even lower than those of LIS. Nevertheless, many reported WLS rely on hydrogel-based materials that exhibit swelling and mechanical degradation under cyclic freezing conditions, limiting their applicability in aviation contexts.

Figures 5.8b and 5.8c focus specifically on WLS and compare the performance of the PHEMA-patterned surfaces and DMC coating developed in this work with corresponding reported water-lubricating systems. Because material selection strongly influences durability and practical applicability, the reported studies were grouped into two categories: **Figure 5.8b** compares the performance of PHEMA-grafted surfaces with other low-durability non-hard coating solutions, including hydrogels and surface grafts[62,63,67] that are generally expected to exhibit limited mechanical durability, and **Figure 5.8c** compares the performance of the DMC coating with other coating systems, such as amphiphilic PEG-grafted coating formulations[61,64-66] that have previously been reported to perform well in durability testing prior to icing experiments but may exhibit swelling or softening after repeated icing cycles.

The PHEMA-grafted surfaces investigated here fall within the lowest range of reported ice adhesion values for hydrophilic non-hard coatings, particularly when included as full homogeneous coverage or patterns on PP. However, despite their strong anti-icing performance, such surface-initiated grafts have poor resistance to abrasion and erosion and therefore belong to the low-durability category.

In contrast, the DMC-based coating ranks among the lowest reported ice adhesion values, achieving adhesion strengths of max 20 kPa without the use of PFAS (with the lowest values below 5kPa). These values are comparable to the best-performing water-lubricating systems reported in the literature, while offering promising potential for durability and

scalability. Notably, the DMC coating showed no visible degradation, delamination, or water absorption after 15 consecutive ice adhesion cycles, suggesting encouraging short-term mechanical stability at this proof-of-concept stage. However, comprehensive long-term durability testing, including UV exposure, abrasion, erosion, and environmental aging studies, remains necessary in future work.

Overall, many previously reported low-ice-adhesion surfaces remain unsuitable for aviation due to fabrication complexity, limited durability, or incompatibility with existing coating systems. While the SI-ATRP-based PHEMA micropatterning employed here performs sufficiently well even on PP, it is impractical for large-scale application due to its multistep preparation methodology, which uses expensive, specialized reagents. By contrast, the DMC coating, which is easily applied via spray coating and UV curing, can be deposited directly onto existing certified PU topcoats, where it exhibits very low ice adhesion and shows no visible deterioration over the repeated icing tests performed in this work. Collectively, these attributes position the DMC coating as a promising candidate for the future development of passive anti-icing coatings for aircraft applications.

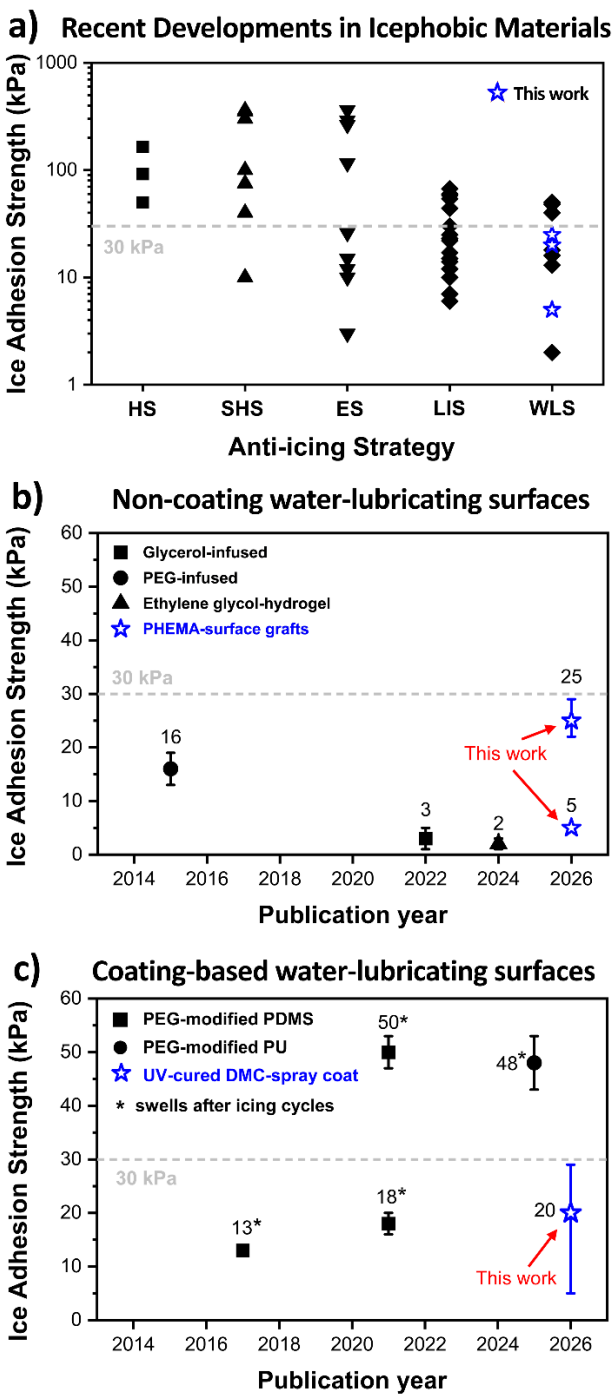

Figure 5.8. Comparison of various passive low-ice adhesion strategies tested under comparable conditions using a horizontal shear test at –10 ± 2 °C. a) Ice adhesion[16,52-90] grouped by anti-icing strategy: hydrophobic (HS), superhydrophobic (SHS), elastic/soft polymers (ES), liquid-infused surfaces (LIS), and water-lubricating surfaces (WLS). b) Comparison of the ice adhesion performance of non-coating WLS as a function of publication year. c) Comparison of the ice adhesion performance of coating-based WLS as a function of publication year. The dashed lines at 30 kPa indicate a commonly cited threshold for sufficiently low ice adhesion.

CONCLUSIONS

This work introduces a horizontal shear ice adhesion testing device with controlled environmental conditions and multiple sample holders, enabling reproducible measurements. Using this framework, the effects of five surface modifications on the ice adhesion behaviour of three polymer substrates (PVC, PP, and PU) were systematically investigated: short and prolonged UV exposure, silicone oil microdroplets, hydrophilic grafting with PHEMA, and a hydrophilic UV-curable DMC coating.

The results show that UV exposure induces a minor ice adhesion increase on PU and PVC due to the formation of hydrophilic oxidation products at the hard surface. In contrast, ice adhesion on PP decreases with UV exposure (10 h) in a process of hydrophobic recovery. Silicone oil hydrophobic microdroplets consistently reduced ice adhesion, in agreement with previous studies on oil-infused passive anti-icing strategies. Notably, prolonged UV exposure proved more effective than oil contamination in reducing ice adhesion on PP.

Both hydrophilic surface modifications (PHEMA surface grafting and the 50 µm thick DMC coating) significantly reduced ice adhesion. This is attributed to the presence of non-freezing surface water later that can act as a lubricating layer at the ice–substrate interface. The more robust PFAS-free cationic DMC coating achieved low ice adhesion strengths of 20 kPa or lower (down to under 5kPa), placing it among the lowest reported values for solid hydrophilic coatings tested under comparable testing conditions. Crucially, this performance is obtained using a simple UV-curable spray-coating process compatible with existing aviation-grade polyurethane coatings, showing no loss of ice adhesion under repeated testing, highlighting its potential for scalability and practical implementation.

Overall, this work provides a comparative framework for evaluating passive anti-icing strategies across different material classes and polymer substrates. It further demonstrates the potential of hydrophilic coatings as a promising foundation for the future development of durable, scalable, and aviation-compatible passive anti-icing treatments. Future work should focus on improving the coating chemistry, durability, and its behaviour in ice wind tunnels and high-speed supercooled droplet impact.

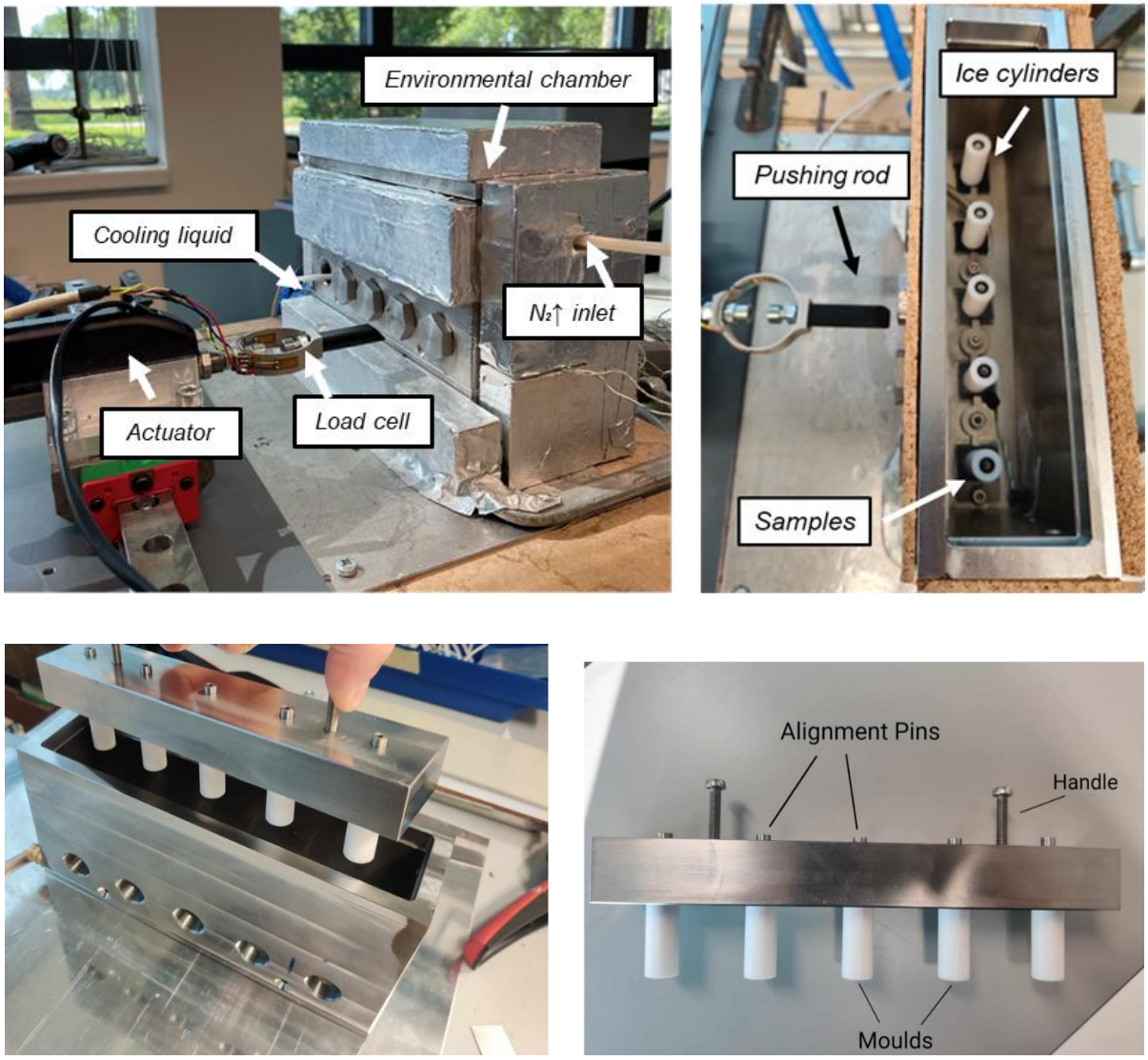

Figure S5.1. Pictures of the horizontal ice adhesion setup used in this study.

Figure S5.2. Detached ice pillar after an ice adhesion test on an aluminium alloy substrate. The lack of frost present inside the environmental chamber validates low humidity conditions throughout the experiment.

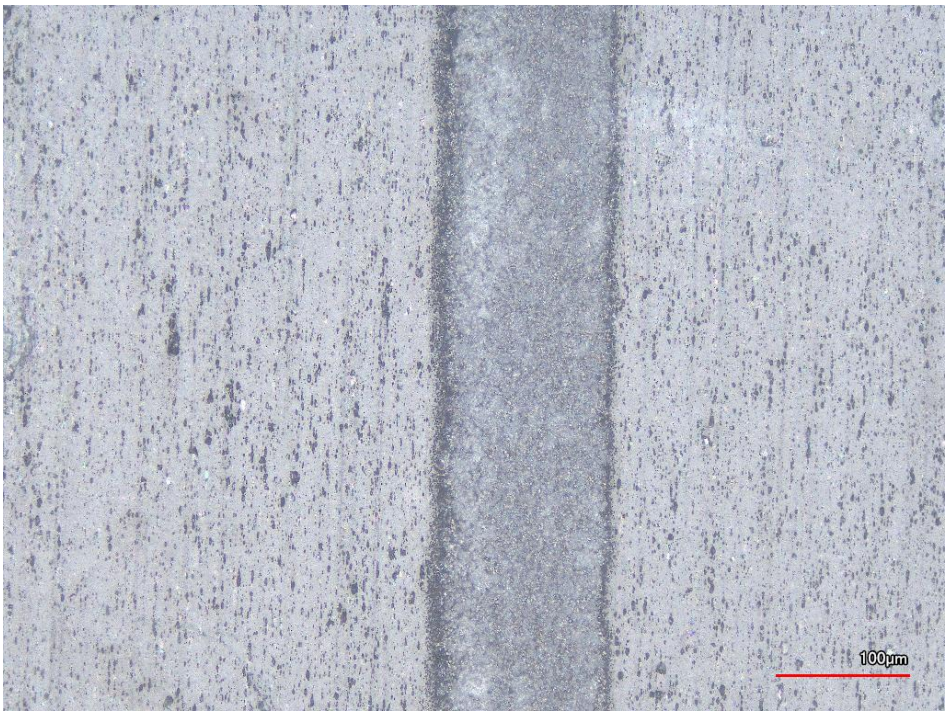

Figure S5.3. LSCM image of a PHEMA stripe on PU substrate. The red scale corresponds to 100 µm.

REFERENCES

(1) Parent, O.; Ilinca, A. Anti-Icing and de-Icing Techniques for Wind Turbines: Critical Review. *Cold Reg. Sci. Technol.* **2011**, *65* (1), 88–96. https://doi.org/https://doi.org/10.1016/j.coldregions.2010.01.005.

(2) Wei, K.; Yang, Y.; Zuo, H.; Zhong, D. A Review on Ice Detection Technology and Ice Elimination Technology for Wind Turbine. *Wind Energy*. John Wiley and Sons Ltd March 1, 2020, pp 433–457. https://doi.org/10.1002/we.2427.

(3) De Koninck, L. H.; Ahmadi, S. F.; Boreyko, J. B. Passive Anti-Frosting Cables. *Int. J. Heat Mass Transf.* **2020**, *146*, 118808. https://doi.org/https://doi.org/10.1016/j.ijheatmasstransfer.2019.118808.

(4) Laforte, J. L.; Allaire, M. A.; Laflamme, J. State-of-the-Art on Power Line de-Icing. *Atmos. Res.* **1998**, *46* (1), 143–158. https://doi.org/https://doi.org/10.1016/S0169-8095(97)00057-4.

(5) DiLorenzo, T.; Yu, X. Use of Ice Detection Sensors for Improving Winter Road Safety. *Accid. Anal. Prev.* **2023**, *191*, 107197. https://doi.org/https://doi.org/10.1016/j.aap.2023.107197.

(6) Sarmiento, A. P.; de Sá Sarmiento, F. I. P.; Shooshtari, A.; Ohadi, M. A Review of Recent Progress in Active Frost Prevention/Control Techniques in Refrigeration and HVAC Systems. *Appl. Therm. Eng.* **2024**, *253*, 123680. https://doi.org/10.1016/J.APPLTHERMALENG.2024.123680.

(7) Cao, Y.; Tan, W.; Wu, Z. Aircraft Icing: An Ongoing Threat to Aviation Safety. *Aerosp. Sci. Technol.* **2018**, *75*, 353–385. https://doi.org/https://doi.org/10.1016/j.ast.2017.12.028.

(8) Yamazaki, M.; Jemcov, A.; Sakaue, H. A Review on the Current Status of Icing Physics and Mitigation in Aviation. *Aerospace*. MDPI AG July 1, 2021. https://doi.org/10.3390/aerospace8070188.

(9) Wang, K.; Xue, Y.; Tian, H.; Wang, M.; Wang, X. The Impact of Icing on the Airfoil on the Lift-Drag Characteristics and Maneuverability Characteristics. *Math. Probl. Eng.* **2021**, *2021* (1), 5568740. https://doi.org/https://doi.org/10.1155/2021/5568740.

(10) Wu, Z. Drop “Impact” on an Airfoil Surface. *Adv. Colloid Interface Sci.* **2018**, *256*, 23–47. https://doi.org/10.1016/J.CIS.2018.05.005.

(11) Lynch, F. T.; Khodadoust, A. Effects of Ice Accretions on Aircraft Aerodynamics. *Progress in Aerospace Sciences* **2001**, *37* (8), 669–767. https://doi.org/10.1016/S0376-0421(01)00018-5.

(12) Caliskan, F.; Hajiyev, C. A Review of In-Flight Detection and Identification of Aircraft Icing and Reconfigurable Control. *Progress in Aerospace Sciences* **2013**, *60*, 12–34. https://doi.org/10.1016/J.PAEROSCI.2012.11.001.

(13) HE, Q.; LI, K.; XU, Z.; WANG, J.; WANG, X.; LI, A. Research Progress on Construction Strategy and Technical Evaluation of Aircraft Icing Accretion Protection System. *Chinese Journal of Aeronautics* **2023**, *36* (10), 1–23. https://doi.org/10.1016/J.CJA.2023.07.003.

(14) Rekuviene, R.; Saeidiharzand, S.; Mažeika, L.; Samaitis, V.; Jankauskas, A.; Sadaghiani, A. K.; Gharib, G.; Muganlı, Z.; Koşar, A. A Review on Passive and Active Anti-Icing and de-Icing Technologies. *Appl. Therm. Eng.* **2024**, *250*, 123474. https://doi.org/10.1016/J.APPLTHERMALENG.2024.123474.

(15) Irajizad, P.; Nazifi, S.; Ghasemi, H. Icephobic Surfaces: Definition and Figures of Merit. *Advances in Colloid and Interface Science*. Elsevier B.V. July 1, 2019, pp 203–218. https://doi.org/10.1016/j.cis.2019.04.005.

(16) Golovin, K.; Kobaku, S. P. R.; Lee, D. H.; DiLoreto, E. T.; Mabry, J. M.; Tuteja, A. Designing Durable Icephobic Surfaces. *Sci. Adv.* **2016**, *2* (3). https://doi.org/10.1126/sciadv.1501496.

(17) Zhan, Y.; Pang, Z.; Tan, G. Advances in Icephobic Coatings: Concepts, Mechanisms, Classifications and Prospects. *Cold Reg. Sci. Technol.* **2025**, *239*, 104596. https://doi.org/10.1016/J.COLDREGIONS.2025.104596.

(18) Chen, J.; Dou, R.; Cui, D.; Zhang, Q.; Zhang, Y.; Xu, F.; Zhou, X.; Wang, J.; Song, Y.; Jiang, L. Robust Prototypical Anti-Icing Coatings with a Self-Lubricating Liquid Water Layer between Ice and Substrate. *ACS Appl. Mater. Interfaces* **2013**, *5* (10), 4026–4030. https://doi.org/10.1021/am401004t.

(19) Dou, R.; Chen, J.; Zhang, Y.; Wang, X.; Cui, D.; Song, Y.; Jiang, L.; Wang, J. Anti-Icing Coating with an Aqueous Lubricating Layer. *ACS Appl. Mater. Interfaces* **2014**, *6* (10), 6998–7003. https://doi.org/10.1021/am501252u.

(20) Ferrari, M.; Cirisano, F. Superhydrophobic Coating Solutions for Deicing Control in Aircraft. *Applied Sciences* **2023**, *13* (21). https://doi.org/10.3390/app132111684.

(21) Kulinich, S. A.; Farhadi, S.; Nose, K.; Du, X. W. Superhydrophobic Surfaces: Are They Really Ice-Repellent? *Langmuir*. January 4, 2011, pp 25–29. https://doi.org/10.1021/la104277q.

(22) Jung, S.; Dorrestijn, M.; Raps, D.; Das, A.; Megaridis, C. M.; Poulikakos, D. Are Superhydrophobic Surfaces Best for Icephobicity? *Langmuir* **2011**, *27* (6), 3059–3066. https://doi.org/10.1021/la104762g.

(23) Chen, J.; Liu, J.; He, M.; Li, K.; Cui, D.; Zhang, Q.; Zeng, X.; Zhang, Y.; Wang, J.; Song, Y. Superhydrophobic Surfaces Cannot Reduce Ice Adhesion. *Appl. Phys. Lett.* **2012**, *101* (11). https://doi.org/10.1063/1.4752436.

(24) Zhuo, Y.; Xiao, S.; Amirfazli, A.; He, J.; Zhang, Z. Polysiloxane as Icephobic Materials – The Past, Present and the Future. *Chemical Engineering Journal* **2021**, *405*, 127088. https://doi.org/10.1016/J.CEJ.2020.127088.

(25) Heydarian, S.; Jafari, R.; Momen, G. Recent Progress in the Anti-Icing Performance of Slippery Liquid-Infused Surfaces. *Prog. Org. Coat.* **2021**, *151*, 106096. https://doi.org/10.1016/J.PORGCOAT.2020.106096.

(26) Villegas, M.; Zhang, Y.; Abu Jarad, N.; Soleymani, L.; Didar, T. F. Liquid-Infused Surfaces: A Review of Theory, Design, and Applications. *ACS Nano* **2019**, *13* (8), 8517–8536. https://doi.org/10.1021/acsnano.9b04129.

(27) Peppou-Chapman, S.; Hong, J. K.; Waterhouse, A.; Neto, C. Life and Death of Liquid-Infused Surfaces: A Review on the Choice, Analysis and Fate of the Infused Liquid Layer. *Chemical Society Reviews*. Royal Society of Chemistry June 7, 2020, pp 3688–3715. https://doi.org/10.1039/d0cs00036a.

(28) Shamshiri, M.; Jafari, R.; Momen, G. A Novel Hybrid Anti-Icing Surface Combining an Aqueous Self-Lubricating Coating and Phase-Change Materials. *Prog. Org. Coat.* **2023**, *177*, 107414. https://doi.org/https://doi.org/10.1016/j.porgcoat.2023.107414.

(29) Shamshiri, M.; Momen, G.; Jafari, R. Icephobic Coatings beyond Boundaries: Layered Integration of Phase Change Materials beneath a PEG-PDMS Copolymer–Containing Coating to Enhance Anti-Icing Performance. *Prog. Org. Coat.* **2024**, *189*, 108324. https://doi.org/10.1016/J.PORGCOAT.2024.108324.

(30) Dou, R.; Chen, J.; Zhang, Y.; Wang, X.; Cui, D.; Song, Y.; Jiang, L.; Wang, J. Anti-Icing Coating with an Aqueous Lubricating Layer. *ACS Appl. Mater. Interfaces* **2014**, *6* (10), 6998–7003. https://doi.org/10.1021/am501252u.

(31) He, Z.; Zhuo, Y.; Wang, F.; He, J.; Zhang, Z. Design and Preparation of Icephobic PDMS-Based Coatings by Introducing an Aqueous Lubricating Layer and Macro-Crack Initiators at the Ice-Substrate Interface. *Prog. Org. Coat.* **2020**, *147*, 105737. https://doi.org/https://doi.org/10.1016/j.porgcoat.2020.105737.

(32) Biro, R. A.; Thormann, E. Ice Adhesion to Cationic, Anionic, Zwitterionic, and Nonionic Polymer Surfaces. *ACS Appl. Polym. Mater.* **2024**, *6* (22), 13744–13752. https://doi.org/10.1021/acsapm.4c02572.

(33) Ozbay, S.; Yuceel, C.; Erbil, H. Y. Improved Icephobic Properties on Surfaces with a Hydrophilic Lubricating Liquid. *ACS Appl. Mater. Interfaces* **2015**, *7* (39), 22067–22077. https://doi.org/10.1021/acsami.5b07265.

(34) Chen, J.; Luo, Z.; Fan, Q.; Lv, J.; Wang, J. Anti-Ice Coating Inspired by Ice Skating. *Small* **2014**, *10* (22), 4693–4699. https://doi.org/https://doi.org/10.1002/smll.201401557.

(35) Abasi, S.; Davis, R.; Podstawczyk, D. A.; Guiseppi-Elie, A. Distribution of Water States within Poly(HEMA-Co-HPMA)-Based Hydrogels. *Polymer (Guildf).* **2019**, *185*, 121978. https://doi.org/10.1016/J.POLYMER.2019.121978.

(36) Gun'ko, V. M.; Savina, I. N.; Mikhalovsky, S. V. Properties of Water Bound in Hydrogels. *Gels* **2017**, *3* (4). https://doi.org/10.3390/GELS3040037.

(37) Guan, L.; Xu, H.; Huang, D. The Investigation on States of Water in Different Hydrophilic Polymers by DSC and FTIR. *Journal of Polymer Research* **2011**, *18* (4), 681–689. https://doi.org/10.1007/S10965-010-9464-7.

(38) Rønneberg, S.; He, J.; Zhang, Z. The Need for Standards in Low Ice Adhesion Surface Research: A Critical Review. *J. Adhes. Sci. Technol.* **2020**, *34* (3), 319–347. https://doi.org/10.1080/01694243.2019.1679523.

(39) Tavaststjerna, M. J.; Picken, S. J.; Garcia, S. J. Controlling Frost Propagation on Polymeric Surfaces Using SI-ATRP Chemical Micropatterning. *Adv. Mater. Interfaces* **2025**, *n/a* (n/a), 2400838. https://doi.org/https://doi.org/10.1002/admi.202400838.

(40) Tavaststjerna, M. J.; Ding, M.; Hussong, J.; Picken, S. J.; Roisman, I. V.; Garcia, S. J. The Influence of Chemical Surface Patterning on the Freezing Behaviour of Impacting Supercooled Water Droplets. *Surfaces and Interfaces* **2025**, *76*, 107918. https://doi.org/10.1016/J.SURFIN.2025.107918.

(41) Hernández Rodríguez, G.; Fratschko, M.; Stendardo, L.; Antonini, C.; Resel, R.; Coclite, A. M. Icephobic Gradient Polymer Coatings Deposited via ICVD: A Novel Approach for Icing Control and Mitigation. *ACS Appl. Mater. Interfaces* **2024**, *16* (9), 11901–11913. https://doi.org/10.1021/acsami.3c18630.

(42) Stendardo, L.; Gastaldo, G.; Budinger, M.; Tagliaro, I.; Pommier-Budinger, V.; Antonini, C. Why the Adhesion Strength Is Not Enough to Assess Ice Adhesion on Surfaces. *Appl. Surf. Sci.* **2024**, *672*, 160740. https://doi.org/10.1016/J.APSUSC.2024.160740.

(43) Stendardo, L.; Gastaldo, G.; Budinger, M.; Pommier-Budinger, V.; Tagliaro, I.; Ibáñez-Ibáñez, P. F.; Antonini, C. Reframing Ice Adhesion Mechanisms on a Solid Surface. *Appl. Surf. Sci.* **2023**, *641*, 158462. https://doi.org/10.1016/J.APSUSC.2023.158462.

(44) Golovin, K.; Dhyani, A.; Thouless, M. D.; Tuteja, A. Low–Interfacial Toughness Materials for Effective Large-Scale Deicing. *Science (1979).* **2019**, *364* (6438), 371–375. https://doi.org/10.1126/science.aav1266.

(45) Qin, C. (Chris); Mulroney, A. T.; Gupta, M. C. Anti-Icing Epoxy Resin Surface Modified by Spray Coating of PTFE Teflon Particles for Wind Turbine Blades. *Mater. Today Commun.* **2020**, *22*, 100770. https://doi.org/10.1016/J.MTCOMM.2019.100770.

(46) Haehnel, R. Evaluation of Coatings for Icing Control at Hydraulic Structures. Ice Engineering. Number 33, January 2002. **2002**, 5.

(47) Landy, M.; Freiberger, A. Studies of Ice Adhesion: I. Adhesion of Ice to Plastics. *J. Colloid Interface Sci.* **1967**, *25* (2), 231–244. https://doi.org/10.1016/0021-9797(67)90026-4.

(48) Meuler, A. J.; Smith, J. D.; Varanasi, K. K.; Mabry, J. M.; McKinley, G. H.; Cohen, R. E. Relationships between Water Wettability and Ice Adhesion. *ACS Appl. Mater. Interfaces* **2010**, *2* (11), 3100–3110. https://doi.org/10.1021/am1006035.

(49) Kuyyakanont, A.; Iwata, M. Study of Different Degradation Effects in UV-Sensitive Polymers Using Xenon Lamp and Deuterium Lamp to Simulate UV Irradiation in Space Environment. *Nucl. Instrum. Methods Phys. Res. B* **2024**, *549*, 165267. https://doi.org/10.1016/J.NIMB.2024.165267.

(50) Lu, T.; Solis-Ramos, E.; Yi, Y.; Kumosa, M. UV Degradation Model for Polymers and Polymer Matrix Composites. *Polym. Degrad. Stab.* **2018**, *154*, 203–210. https://doi.org/10.1016/J.POLYMDEGRADSTAB.2018.06.004.

(51) Primc, G. Hydrophilization of Polypropylene by Gaseous Plasma Treatments and Hydrophobic Recovery. *Polymers (Basel).* **2025**, *17* (19). https://doi.org/10.3390/polym17192644.

(52) Liu, L.; Chen, S.; Hu, Y.; Pan, W.; Dong, T.; Chen, Y.; Lin, L.; Wang, L. Anti-/Deicing Membranes with Damage Detection and Fast Healing. *Adv. Funct. Mater.* **2024**, *34* (40), 2404760. https://doi.org/https://doi.org/10.1002/adfm.202404760.

(53) Yang, Q.; Zhu, Z.; Tan, S.; Luo, Y.; Luo, Z. How Micro-/Nanostructure Evolution Influences Dynamic Wetting and Natural Deicing Abilities of Bionic Lotus Surfaces. *Langmuir* **2020**, *36* (15), 4005–4014. https://doi.org/10.1021/acs.langmuir.0c00145.

(54) Vazirinasab, E.; Maghsoudi, K.; Jafari, R.; Momen, G. A Comparative Study of the Icephobic and Self-Cleaning Properties of Teflon Materials Having Different Surface Morphologies. *J. Mater. Process. Technol.* **2020**, *276*, 116415. https://doi.org/10.1016/J.JMATPROTEC.2019.116415.

(55) Liu, Y.; Zhang, Z.; Hu, H.; Hu, H.; Samanta, A.; Wang, Q.; Ding, H. An Experimental Study to Characterize a Surface Treated with a Novel Laser Surface Texturing Technique: Water Repellency and Reduced Ice Adhesion. *Surf. Coat. Technol.* **2019**, *374*, 634–644. https://doi.org/10.1016/J.SURFCOAT.2019.06.046.

(56) Wang, N.; Tang, L.; Tong, W.; Xiong, D. Fabrication of Robust and Scalable Superhydrophobic Surfaces and Investigation of Their Anti-Icing Properties. *Mater. Des.* **2018**, *156*, 320–328. https://doi.org/10.1016/J.MATDES.2018.06.053.

(57) Fu, Q.; Wu, X.; Kumar, D.; Ho, J. W. C.; Kanhere, P. D.; Srikanth, N.; Liu, E.; Wilson, P.; Chen, Z. Development of Sol–Gel Icephobic Coatings: Effect of Surface Roughness and Surface Energy. *ACS Appl. Mater. Interfaces* **2014**, *6* (23), 20685–20692. https://doi.org/10.1021/am504348x.

(58) Cui, W.; Pakkanen, T. A. Fabrication of Transparent Icephobic Surfaces with Self-Reparability: Effect of Structuring and Thickness of the Lubricant-Elastomer Layer. *Appl. Surf. Sci.* **2020**, *504*, 144061. https://doi.org/10.1016/J.APSUSC.2019.144061.

(59) Vazirinasab, E.; Maghsoudi, K.; Jafari, R.; Momen, G. A Comparative Study of the Icephobic and Self-Cleaning Properties of Teflon Materials Having Different Surface Morphologies. *J. Mater. Process. Technol.* **2020**, *276*, 116415. https://doi.org/10.1016/J.JMATPROTEC.2019.116415.

(60) Meuler, A. J.; Smith, J. D.; Varanasi, K. K.; Mabry, J. M.; McKinley, G. H.; Cohen, R. E. Relationships between Water Wettability and Ice Adhesion. *ACS Appl. Mater. Interfaces* **2010**, *2* (11), 3100–3110. https://doi.org/10.1021/am1006035.

(61) Bakhtiari, M.; Bakhshandeh, E.; Jafari, R.; Momen, G. Enhancing Anti-Icing Efficacy in Hybrid Polyurethane Coatings: Evaluating the Significance of Molecular Weight, Chemical Structure, and Content of PEG/PDMS. *Appl. Surf. Sci.* **2025**, *684*, 161951. https://doi.org/10.1016/J.APSUSC.2024.161951.

(62) Zhang, Y.; Yan, W.; Lin, Y.; Zhu, J.; Zhao, H.; Li, T. Multifunctional Anti-Icing Gel Surface with Enhanced Durability. *ACS Appl. Mater. Interfaces* **2024**, *16* (11), 14198–14207. https://doi.org/10.1021/acsami.4c00617.

(63) Ijaz, A.; Miko, A.; Demirel, A. L. Low Ice Adhesion Anti-Icing Coatings Based on PEG Release from Mesoporous Silica Particle Loaded SBS. *Mater. Adv.* **2022**, *3* (22), 8168–8177. https://doi.org/10.1039/D2MA00661H.

(64) Shamshiri, M.; Jafari, R.; Momen, G. Icephobic Properties of Aqueous Self-Lubricating Coatings Containing PEG-PDMS Copolymers. *Prog. Org. Coat.* **2021**, *161*, 106466. https://doi.org/10.1016/J.PORGCOAT.2021.106466.

(65) Rahimi, A.; Murphy, M.; Upadhyay, V.; Faiyaz, K.; Battocchi, D.; Webster, D. C. Amphiphilically Modified Self-Stratified Siloxane-Glycidyl Carbamate Coatings for Anti-Icing Applications. *J. Coat. Technol. Res.* **2021**, *18* (1), 83–97. https://doi.org/10.1007/s11998-020-00402-8.

(66) Upadhyay, V.; Galhenage, T.; Battocchi, D.; Webster, D. Amphiphilic Icephobic Coatings. *Prog. Org. Coat.* **2017**, *112*, 191–199. https://doi.org/10.1016/J.PORGCOAT.2017.07.019.

(67) Ozbay, S.; Yuceel, C.; Erbil, H. Y. Improved Icephobic Properties on Surfaces with a Hydrophilic Lubricating Liquid. *ACS Appl. Mater. Interfaces* **2015**, *7* (39), 22067–22077. https://doi.org/10.1021/acsami.5b07265.

(68) Moghadam, S. G.; Bakhshandeh, E.; Jafari, R.; Momen, G. In-Depth Analysis of the Effect of Physicochemical Properties of Ionic Liquids on Anti-Icing Behavior of Silicon Based-Coatings. *Cold Reg. Sci. Technol.* **2023**, *216*, 104007. https://doi.org/10.1016/J.COLDREGIONS.2023.104007.

(69) Wang, X.; Lin, Z. A Novel High-Performance Coating with Hybrid Nanofiller Reinforcement for Superior Self-Cleaning, Anti-Icing, and Corrosion Resistance Properties. *Journal of Building Engineering* **2023**, *80*, 107993. https://doi.org/10.1016/J.JOBE.2023.107993.

(70) Buddingh, J. V; Liu, G. Hard Epoxy Coating with Lasting Low Ice Adhesion Strength. *ACS Appl. Polym. Mater.* **2023**, *5* (9), 7485–7496. https://doi.org/10.1021/acsapm.3c01360.

(71) Heydarian, S.; Momen, G.; Jafari, R. Icephobicity and Electrical Assessment of Slippery Coating Impregnated with a Stabilized Hydroxyl-Terminated Lubricant for High Voltage Insulation Application. *J. Mater. Sci.* **2023**, *58* (22), 9264–9281. https://doi.org/10.1007/s10853-023-08600-6.

(72) Liu, Y.; Gao, S.; Liu, J.; Zhang, Q. Biomimetic Slippery Liquid-Infused Porous Surfaces Fabricated by Porous Fluorinated Polyurethane Films for Anti-Icing Property. *Prog. Org. Coat.* **2023**, *179*, 107524. https://doi.org/10.1016/J.PORGCOAT.2023.107524.

(73) Becher-Nienhaus, B.; Liu, G.; Buddingh, J. V; Zheng, H. Robust Polyurethane Coatings with Lightly Cross-Linked Surfaces for Ice Shedding. *ACS Appl. Polym. Mater.* **2023**, *5* (4), 3119–3128. https://doi.org/10.1021/acsapm.3c00259.

(74) Qi, H.; Lei, X.; Gu, J.; Zhang, Y.; Gu, X.; Zhao, G.; Yu, J. Low Modulus of Polydimethylsiloxane Organogel Coatings Induced Low Ice Adhesion. *Prog. Org. Coat.* **2023**, *177*, 107435. https://doi.org/10.1016/J.PORGCOAT.2023.107435.

(75) Lee, S. J.; Park, G. Do. Effective Icephobicity of Silicone Oil-Infused Oleamide–Polydimethylsiloxane with Enhanced Lubrication Lifetime. *ACS Omega* **2022**, *7* (24), 21156–21162. https://doi.org/10.1021/acsomega.2c01956.

(76) Yuan, J.; Huang, Y.; Li, H.; Jiang, L.; Dan, Y. Preparation and Anti-Icing Performance of Cross-Linked Polysiloxane Coatings Containing Silicone Oil. *React. Funct. Polym.* **2022**, *170*, 105124. https://doi.org/10.1016/J.REACTFUNCTPOLYM.2021.105124.

(77) Tian, Y.; Liu, Y.; Su, Z.; Wang, S.; Zhang, B.; Zhang, H.; Zhang, Q. Biomimetic Brushlike Slippery Coatings with Mechanically Robust, Self-Cleaning, and Icephobic Properties. *ACS Appl. Mater. Interfaces* **2020**, *12* (48), 54041–54052. https://doi.org/10.1021/acsami.0c14042.

(78) Liu, Y.; Tian, Y.; Chen, J.; Gu, H.; Liu, J.; Wang, R.; Zhang, B.; Zhang, H.; Zhang, Q. Design and Preparation of Bioinspired Slippery Liquid-Infused Porous Surfaces with Anti-Icing Performance via Delayed Phase Inversion Process. *Colloids Surf. A Physicochem. Eng. Asp.* **2020**, *588*, 124384. https://doi.org/10.1016/J.COLSURFA.2019.124384.

(79) Barthwal, S.; Lee, B.; Lim, S. H. Fabrication of Robust and Durable Slippery Anti-Icing Coating on Textured Superhydrophobic Aluminum Surfaces with Infused Silicone Oil. *Appl. Surf. Sci.* **2019**, *496*, 143677. https://doi.org/10.1016/J.APSUSC.2019.143677.

(80) Yamazaki, T.; Tenjimbayashi, M.; Manabe, K.; Moriya, T.; Nakamura, H.; Nakamura, T.; Matsubayashi, T.; Tsuge, Y.; Shiratori, S. Antifreeze Liquid-Infused Surface with High Transparency, Low Ice Adhesion Strength, and Antifrosting Properties Fabricated through a Spray Layer-by-Layer Method. *Ind. Eng. Chem. Res.* **2019**, *58* (6), 2225–2234. https://doi.org/10.1021/acs.iecr.8b05927.

(81) Sandhu, A.; Walker, O. J.; Nistal, A.; Choy, K. L.; Clancy, A. J. Perfluoroalkane Wax Infused Gels for Effective, Regenerating, Anti-Icing Surfaces. *Chem. Commun.* **2019**, *55* (22), 3215–3218. https://doi.org/10.1039/C8CC09818B.

(82) Golovin, K.; Kobaku, S. P. R.; Lee, D. H.; DiLoreto, E. T.; Mabry, J. M.; Tuteja, A. Designing Durable Icephobic Surfaces. *Sci. Adv.* **2016**, *2* (3), e1501496. https://doi.org/10.1126/sciadv.1501496.

(83) Chen, J.; Dou, R.; Cui, D.; Zhang, Q.; Zhang, Y.; Xu, F.; Zhou, X.; Wang, J.; Song, Y.; Jiang, L. Robust Prototypical Anti-Icing Coatings with a Self-Lubricating Liquid Water Layer between Ice and Substrate. *ACS Appl. Mater. Interfaces* **2013**, *5* (10), 4026–4030. https://doi.org/10.1021/am401004t.

(84) Li, P.; Yuan, J.; Lan, L.; Dan, Y.; Jiang, L.; Huang, Y. Durable and Organic-Solvent-Free Anti-Icing Coating Fabricated from Polyacrylate Grafted with PDMS. *Polymer (Guildf).* **2025**, *317*, 127857. https://doi.org/10.1016/J.POLYMER.2024.127857.

(85) Zhu, T.; Yuan, Y.; Song, L.; Wei, X.; Xiang, H.; Dai, X.; Hua, X.; Liao, R. A PDMS Coating with Excellent Durability for Large-Scale Deicing. *Journal of Materials Research and Technology* **2024**, *29*, 4526–4536. https://doi.org/10.1016/J.JMRT.2024.02.177.

(86) Adja, A. A. S.; Sobhani, S.; Momen, G.; Fofana, I.; Carrière, J. Step by Step Progress to Achieve an Icephobic Silicone-Epoxy Hybrid Coating: Tailoring Matrix Composition and Additives. *J. Appl. Polym. Sci.* **2023**, *140* (32), e54262. https://doi.org/https://doi.org/10.1002/app.54262.

(87) Shamshiri, M.; Jafari, R.; Momen, G. An Intelligent Icephobic Coating Based on Encapsulated Phase Change Materials (PCM). *Colloids Surf. A Physicochem. Eng. Asp.* **2022**, *655*, 130157. https://doi.org/10.1016/J.COLSURFA.2022.130157.

(88) Sarma, J.; Zhang, L.; Guo, Z.; Dai, X. Sustainable Icephobicity on Durable Quasi-Liquid Surface. *Chemical Engineering Journal* **2022**, *431*, 133475. https://doi.org/10.1016/J.CEJ.2021.133475.

(89) Teisala, H.; Baumli, P.; Weber, S. A. L.; Vollmer, D.; Butt, H.-J. Grafting Silicone at Room Temperature—a Transparent, Scratch-Resistant Nonstick Molecular Coating. *Langmuir* **2020**, *36* (16), 4416–4431. https://doi.org/10.1021/acs.langmuir.9b03223.

(90) Bleszynski, M.; Woll, R.; Middleton, J.; Kumosa, M. Effects of Crosslinking, Embedded TiO2 Particles and Extreme Aging on PDMS Icephobic Barriers. *Polym. Degrad. Stab.* **2019**, *166*, 272–282. https://doi.org/10.1016/J.POLYMDEGRADSTAB.2019.06.005.

6

Mobility of Antifreeze Proteins is a Key Factor in Their Use to Control Ice Growth on Surfaces and Polymers

Abstract: The successful use of ice-binding proteins (IBPs) to develop anti-icing coatings requires a comprehensive understanding of their working mechanism when introduced in environments distinct from the protein's natural setting. This study systematically addresses this aspect by investigating how IBPs control ice accretion when grafted onto an aluminium alloy using polyethylene glycol (PEG) linkers of various lengths and on the polymer backbone of a PEG hydrogel matrix. Freezing experiments monitored through thermal imaging reveal that the degrees of freedom of the proteins significantly influence their functionality. Specifically, we demonstrate that when the degrees of freedom of anti-freeze proteins (AFPs) are restricted by their functionalization on surfaces using short linkers or when they are present in restricted volumes in polymers, they behave as ice-nucleating proteins (INPs) promoting ice accretion. In conditions where their degrees of freedom are enhanced (long linkers, water-rich environment), AFPs effectively inhibit ice nucleation and propagation. The work underlines the relevance of protein mobility as a so far unforeseen key design factor needed to fully benefit from the potential use of natural or synthetic AFPs in cryopreservation of biological samples, food preservation, and the creation of the next-generation of low-icing surfaces and coatings for wind turbines and aircraft.

INTRODUCTION

In cold climates, the formation and accumulation of ice on surfaces can instigate safety hazards and damage in a wide range of applications such as building roofs[1], power lines[2,3], wind turbines[3,4], and aircraft[5,6]. For example, ice accumulation on solar panels decreases their efficiency while ice on aircraft wings and tail can disrupt the airflow leading to a decrease in aircraft speed and lift, an increase in fuel consumption, and an overall decrease in safety during flight.[1,6] Moreover, low ice surfaces are of large relevance in the cryopreservation of biological materials and food, where the challenge of manufacturing high-yield cryoprotectants remains.[7,8]

As in many other naturally occurring phenomena, natural evolution has provided solutions for successfully controlling ice formation and growth that can be used as inspiration to develop anti-icing surfaces. To increase the survival potential of species as diverse as plants, algae, fish, or insects, nature mostly relies on the production of a variety of proteins with the ability to interfere with ice crystal growth known as ice-binding proteins (IBPs). IBPs can be grouped in two major classes depending on their principal strategy used to protect the species against freezing: (i) ice-nucleating proteins (INPs) which accelerate ice formation, and (ii) anti-freeze proteins (AFPs) which delay ice formation.[9,10]

Most of the available literature focuses on the role of the natural or synthetic IBP chemistry on ice control in fluids[7,11-13], while only a few groups reported on the use of AFPs on surfaces to induce passive anti-icing behavior.[14-18] One of the major challenges in the use of AFPs on surfaces appears to be the apparently unexplained discrepancy in results regarding the positive or negative effect of AFPs on surfaces. For example, AFPs from *Chaetoceros neogracile* (an Antarctic marine diatom) immobilized on an aluminium surface using an Al-binding peptide delayed ice formation for three hours in an air-cold chamber at −3.5 °C and 84 % relative humidity.[14] Similarly, type III AFP from *Zoarces americanus* (a polar fish), grafted onto a polymer backbone covalently bound to an aldehyde-coated glass slide showed a freezing delay from 20 minutes without AFP to 45 minutes with AFP at -6 ℃ and 40 % RH.[15] Contrary to these results, the same type III AFP on aluminium showed that AFPs

promoted earlier ice nucleation instead of inhibiting it when the surfaces were cooled at -0.5 °C min^{-1} until ice nucleation occurred.[16] Part of the apparently contradicting results in literature can be attributed to the use of very different manufacturing techniques, process conditions, freezing tests, and AFPs. Nevertheless, besides chemistry, other more fundamental AFP architectural factors may also play a relevant role in IBP behaviour used in synthetic materials. For instance, while in nature ice growth inhibition induced by AFPs increases with increasing AFP concentration in solution[19], no systematic studies on the effect of protein concentration on surfaces have been reported. Similarly, a study using AFPs from *Microdera punctipennis dzungarica* (an insect) suggests that the protein orientation relative to the surface may play an important role in ice nucleation.[20] With some reports showcasing the beneficial effects of AFPs and some their negative effects and the myriad of factors affecting behaviour of different proteins, more mechanistic understanding on the factors leading to a positive or a negative effect with the same protein appears as a necessary step to understand discrepancies and boost research and applications of AFP for ice-controlling surfaces.

In this work, we discuss the key role that the degrees of freedom (mobility) of grafted proteins has on surface ice nucleation and growth. To this aim, two model IBPs (an AFP type III from fish and an INP from bacteria) were grafted at varying concentrations and linker chain lengths on (i) aluminium substrates and (ii) as dangling chains in the polymer backbone of a model hydrogel. This strategy allowed us to study the effect of mobility on ice formation using the same protein type in a well-controlled fashion. The work outlines the behavioural similitudes between the studied AFPs and INPs and the relevance of protein mobility and surface water layers for effective anti-freezing. Not disregarding protein chemistry diversity, the work underpins the importance of protein degrees of freedom as a design rule to develop future anti-freezing surfaces and coatings using natural and synthetic proteins and molecules with comparable structures and mechanisms.

MATERIALS AND METHODS

Materials

Two model ice-binding proteins (IBPs) were used in this work selected based on size, functionality, information, and availability: (i) type III AFP from *Marcrozoarces americanus* fish (6.5 kDa, ~2.5 nm coiled diameter), obtained from A/F Protein Inc.; and (ii) INPs derived from *Pseudomonas syringae* bacteria, purchased as the commercial Snomax® powder (Snomax International Corp., USA), containing membrane-associated ice-nucleating protein assemblies reported in literature to be on the order of ~100 kDa and ~10 nm in characteristic dimension. 3-mercaptopropyltrimethoxysilane (MPTS, 96 %) was bought from Gelest Inc. Sodium hydroxide pellets (anhydrous NaOH, ≥ 98 %), phosphate-buffered saline (PBS, pH 7.4) solution, 4arm-PEG-maleimide (average M_n = 10 kDa), PEG dithiol (average M_n = 1 kDa), and three maleimide-PEG-succinimidyl ester linker with three different repeating units of PEG (2, 12, 24) (Mal-$PEG_{2/12/24}$-NHS) were bought from Sigma-Aldrich. All solvents were of technical grade and used as received.

Preparation of IBP-grafted aluminium alloy surfaces

Aluminium alloy surface preparation

AA2024-T3 samples (2 cm x 2 cm x 3 mm) were manually and sequentially ground with 18 µm, 10 µm, and 6 µm grain size grinding paper. Between each grinding step, the samples were placed in an ultrasonic ethanol bath for 2 minutes. After grinding, the samples were sequentially polished with 3 µm and 0.25 µm particle size diamond paste. Finally, to remove any remaining contaminants, the samples were rinsed with acetone prior to subsequent surface treatment steps.

Surface functionalization of aluminium alloy substrates

Surface activation of AA2024-T3 was obtained by submerging the polished samples in a 2 M NaOH solution for 10 seconds, rinsed with deionized (DI) water, and dried in an oven at 100 °C for 30 minutes to remove any excess water. The samples obtained with this process are further named "AA2024-OH". The resulting hydroxyl-rich pseudoboehmite layer was subsequently used for surface modification through silanization to obtain thiol-rich surfaces (samples named "AA2024-SH"). Silanization was obtained by immersing the metal plates in a 2:30 water:methanol mixture (96 ml) with 4 ml of 3-mercaptopropyltrimethoxysilane (MPTS) for 2 hours. Before immersion, the silane solution was stirred for 24 hours to ensure sufficient pre-hydrolysis of the MPTS. After 2 hours immersion in the MPTS solution, the samples were rinsed with methanol, dried in a vacuum for 30 minutes, and cured in an oven for 1 hour at 100 °C.

Modification of the IBPs with PEG linkers of different lengths

An IBP solution (0.1 mM) was prepared by dissolving the dry protein powder in a phosphate-buffered saline solution (PBS, pH 7.4). Next, a stock solution with 250 mM PEG linker was prepared by mixing Mal-$PEG_{2/12/24}$-NHS with DMSO. The linker solution was then added to the IBP solution in tenfold molar excess (4 µl of linker stock solution per 1ml of IBP solution). The mixture was stirred for 1 hour at a pH of 7.4 to ensure a complete and selective reaction between the protein amine end group and the linker succinimidyl ester group. Finally, to obtain Mal-$PEG_{2/12/24}$-NH-IBPs, the excess linker and side products were removed by centrifuging the mixture three times for 5 minutes at 4400 rpm. After each centrifuging step, the heavy Mal-$PEG_{2/12/24}$-NH-IBPs precipitate to the bottom. The supernatant is then pipetted out of the tube while fresh PBS is added to the precipitated Mal-$PEG_{2/12/24}$-NH-IBPs. Finally, Mal-$PEG_{2/12/24}$-NH-IBPs is stored in a PBS solution in a freezer at -20 °C.

Grafting of Mal-PEG$_{2/12/24}$-NH-IBPs on aluminium alloy substrate

The Mal-PEG$_{2/12/24}$-NH-IBPs are extracted from their PBS solution and various weights of Mal-PEG$_{2/12/24}$-NH-IBPs (2.5 mg and 5 mg) are redispersed in 1 ml PBS to obtain different IBP concentrations in solution. The AA2024-SH samples were then immersed in this protein solution for 4 hours. During the process, the maleimide functionality from the modified IBPs reacts with thiol groups at the aluminium surface through thiol-Michael click chemistry hence leading to aluminium surfaces grafted with IBPs with different linker lengths. After immersion, the IBP-modified AA2024 samples were rinsed with DI water and dried in a vacuum at room temperature overnight to remove any excess water.

Preparation of IBP-modified hydrogels on aluminium alloy surfaces

IBP-containing hydrogels of approximately 10 wt% were produced by preparing two separate solutions: (1) solution 1: PEG dithiol dispersed in 0.1 ml PBS at 6.5:100 (w/w) ratio; and (2) solution 2: 4arm-PEG-maleimide (average M_n = 10 000 g mol^{-1}) in 0.1 ml PBS at 15.5:100 (w/w) ratio. To solution 2, 0 mg, 2.5 mg or 5 mg Mal- PEG$_{12}$-NH-IBPs was added to produce hydrogels with varying IBP concentrations. The final protein-hydrogel was produced by spraying with a lab-built Confined Impinging Jet (CIJ) mixer[21]. The PEG dithiol solution (solution 1) was added to one side of the CIJ mixer while the 4-arm PEG maleimide/ Mal- PEG$_{12}$-NH-IBP solution (solution 2) was inserted on the other side. Next, both openings of the mixer are connected to high-pressure inlets, thus spraying the two solutions simultaneously through an outlet point on the AA2024-SH substrate. By Thiol-Michael click chemistry between the thiol functionalities present in solution 1 and the maleimide functionalities from solution 2, a hydrogel with grafted proteins is developed.

Water contact angle (WCA) measurements

Static WCA measurements were performed with a Tensiometer KSV CAM 200 (KSV Instruments Ltd., Finland) as an indirect test to confirm surface modification of the alloys after surface activation and silanization. For each sample condition, three repeats using 5

µl DI water droplets were performed. Droplet shape analysis of the images was done to obtain the WCA of the surfaces. All WCA measurements were carried out at an ambient temperature of 21±2 ℃ and relative humidity of 40±5 %.

Raman spectroscopy

Raman spectroscopy measurements were performed on untreated, activated and silanized AA2024 samples to confirm successful chemical treatments. To this aim, a Renishaw inVia Raman microscope with a laser length of 532 nm was used. For each measurement point, 16 accumulations were made at 10 % laser power with an exposure time of 60 seconds.

Fourier transform infrared spectroscopy (FTIR)

FTIR was first used to monitor the reaction between the protein and PEG linker in solution by measuring the solutions at different points in time. FTIR was further used to confirm surface grafting with proteins. To this aim, a Spectrum 100 FTIR Spectrometer (Perkin Elmer) was used and run from 4000 to 500 cm^{-1} to obtain the FTIR spectra as the average of 32 scans.

Differential scanning calorimetry (DSC)

A DSC 250 (TA Instruments) was used to determine the state of water present in the hydrogel polymer networks (adsorbed and absorbed) following guidelines reported in recent works.[22] Hydrogel samples of 5 mg were placed in the DSC and tested for two cycles with the following cooling-heating protocol: sample equilibration at 20 °C for 5 minutes, cooling from 20 °C to -50 °C at a rate of -10 °C min^{-1}, isotherm at -50 °C for 5 minutes, heating to 20 °C at 10 °C min^{-1}. Three different samples were tested for each hydrogel composition for reproducibility.

Frosting tests monitored by thermal imaging

To monitor and quantify the freezing events of the samples, a home-made freezing set-up was used. Samples are placed on top of a liquid-cooled plate (TECA LHP-300CP) which is powered by a 11.5 DC voltage source within a small isolating chamber to control well humidity (RH was set at 38±3 % for all experiments) and temperature. This allowed cooling the samples at -10 °C min^{-1} until -20 °C. The freezing events and propagation were monitored using a FLIR A655sc thermal camera with a close-up lens (1.5 magnifying factor and 25 µm resolution). The surfaces are monitored with the thermal camera right after cooling starts, hence allowing a good image-freezing time correlation as reposted in Chapter 2.[23] The recorded times and temperatures were directly plot in the FLIR tools program using an emissivity of 0.4 for the protein-modified surfaces (similar to emissivity of oxidized aluminium) and 0.9 for the hydrogels. From the plots the freezing onset time (t_{fo}) was obtained as the time until surface freezing was observed and the freezing onset temperature (T_{fo}), as the temperature on the graph at which the freezing event starts (observed as temperature rise).

RESULTS AND DISCUSSION

Aluminium surface functionalization with IBPs

Figure 6.1a shows the steps used to functionalize the aluminium surfaces with IBPs. This process consists of several steps using click chemistry explained in the experimental section: (i) activation, leading to hydroxyl-rich surfaces (AA2024-OH); (ii) silanization to enrich the surface with thiol groups (AA2024-SH), and; (iii) functionalization with INP or AFP (IBP) using maleimide-PEG oligomers. This step-wise process provided surfaces with different proteins (AFP or INP), chain lengths (2, 12 or 24 PEG chains) and concentration (given by the protein concentration present in solution) as shown in **Table 6.1**. To achieve functionalization with IBPs, the IBPs were modified with a Mal-$PEG_{2/12/24}$-NHS linker where the succinimidyl ester (-NHS) selectively reacts with the IBP amine group at its N-terminus, forming an amide group and leading to the oligomers named as Mal-$PEG_{2/12/24}$-NH-IBP, where IBP can be AFP or INP (**Figure 6.1b** showing the reaction steps). To separate the Mal-$PEG_{2/12/24}$-NH-IBPs from the byproduct, the samples were centrifuged, the surplus liquid with byproduct removed, and the solid product redispersed in PBS forming a Mal-$PEG_{2/12/24}$-NH-IBPs solutions. Finally, the AA2024-SH surfaces were immersed in the Mal-$PEG_{2/12/24}$-NH-IBP solutions to obtain surfaces grafted with different IBPs, PEG chain-length and IBP surface concentration. Since the ice-binding site (IBS) and the end groups of type III AFP are located on the opposite sides of the globular protein, this grafting approach targeting the N-terminus ensures that the IBS of the type III AFP will be exposed after the surface functionalization.

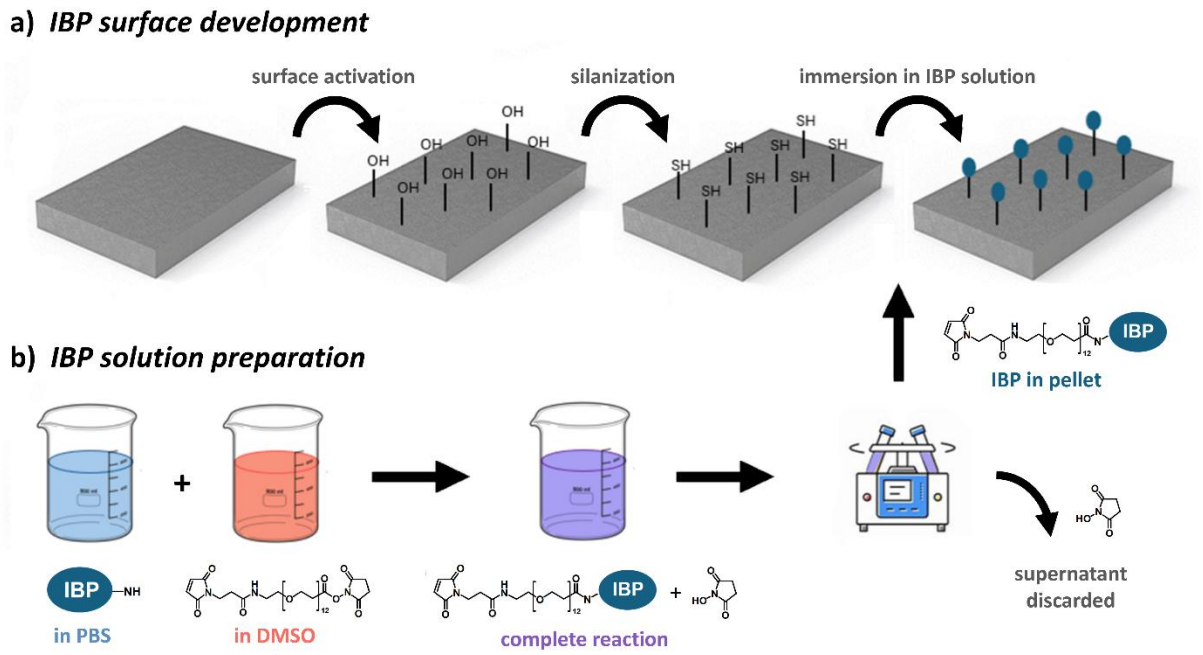

Figure 6.1. a) Step-wise process to functionalize the aluminium surfaces leading to samples rich in -OH, -SH and -IBP; b) Chemical scheme to obtain functionalized IBPs (Mal-PEG$_{2/12/24}$-NH-IBP, in purple) from the reaction between NH2-rich IBP (blue) and Mal-PEG$_{2/12/24}$-NHS oligomer (orange). The maleimide-functionality (Mal) allows grafting the extended IBPs onto the -SH rich aluminium surfaces via click-chemistry.

Table 6.1. Mal-PEG$_{2/12/24}$-NH-IBP solutions with varying protein type (AFP or INP), PEG linker length and protein concentration, used to graft IBPs on the AA2024-SH surfaces.

Characteristic parameters	**Mal-PEG$_{2/12/24}$-NH-IBP solutions in PBS**					
Solution no.	1	2	3	4	5	6
Type of protein	AFP	AFP	AFP	AFP	INP	INP
PEG linker length (number of repeating units)	12	12	2	24	12	12
Protein concentration (mg ml^{-1})	2.5	5.0	2.5	2.5	2.5	5.0

Static WCA measurements and Raman spectroscopy were used to verify the chemical surface changes induced by activation and silanization, as shown in **Figure 6.2a-b**. After immersion in NaOH, the static WCA decreases from 80° to 36° (**Figure 6.2a**) as expected for a surface richer in pseudoboehmite structure containing hydroxyl groups. The surface modification is confirmed by Raman spectroscopy (**Figure 6.2b**) revealing the appearance of peaks related to pseudoboehmite[24]: (i) 3000–3600 cm^{-1} and 1650 cm^{-1} attributed to -OH stretching and deformation vibrations of weakly bound water and (ii) a peak at 1050 cm^{-1} corresponding to Al-O bending vibrations.

After silanization of AA2024-OH with MPTS thiol-terminated silane, the static WCA increases from 36° to 65° (**Figure 6.2a**). This increase in WCA can be explained by the relatively lower hydrophilicity of thiol groups compared to hydroxyl groups. Raman analysis further confirmed the presence of silanes, and consequently thiols, on the surface: two peaks centred around 970 cm^{-1} and 1050 cm^{-1} corresponding to Si-O-Si stretching vibrations, one prominent peak at around 2950 cm^{-1} characteristic for C-H stretching, and a peak around 1450 cm^{-1} associated to the bending vibration of the $-CH_2$ group.[25-27]

To verify the reaction between the IBPs and the Mal-$PEG_{2/12/24}$-NHS linkers in solution, FTIR measurements were taken before, at the start, and at the end of the reaction. As seen in **Figure 6.2c**, most of the peaks in the Mal-PEG_{12}-NHS in DMSO spectrum (circles) can be attributed to the DMSO solvent itself (squares). Nevertheless, one distinct peak at 1741 cm^{-1} is associated with C=O stretching vibration of the succinimidyl ester from Mal-PEG_{12}-NHS and can be used to monitor the reaction with the protein (see the squared region in **Figure 6.2c**). When IBPs are added to the solution, the peaks related to the succinimidyl are still distinguishable right at the start of the reaction (spectrum with triangles up) although relatively smaller than the neighbouring peaks. This suggests a rapid reaction between the succinimidyl ester and the IBP (with amide as a product). Toward the end of the reaction (triangle down), the ester peak further decreases due to the reaction progression. No reaction-related amide peak increase is detected since the incremental addition of amide groups during the reaction in an amide-rich solution (from the protein and the Mal-PEG_{12}-NHS) is not easily detected by FTIR.

To obtain IBP-grafted surfaces, the AA2024-SH samples are immersed in different Mal-$PEG_{2/12/24}$-NH-IBP solutions. The use of solutions with different IBP concentrations and PEG linker lengths led to a range of protein-rich surfaces. Protein enrichment of the surfaces was confirmed by FTIR through the appearance of two protein distinct peaks[28] at 1642 cm^{-1} (amide I) and 1532 cm^{-1} (amide II) as seen in **Figure 6.2d** for the modification of the surface with solution 1 from **Table 6.1** as an example.

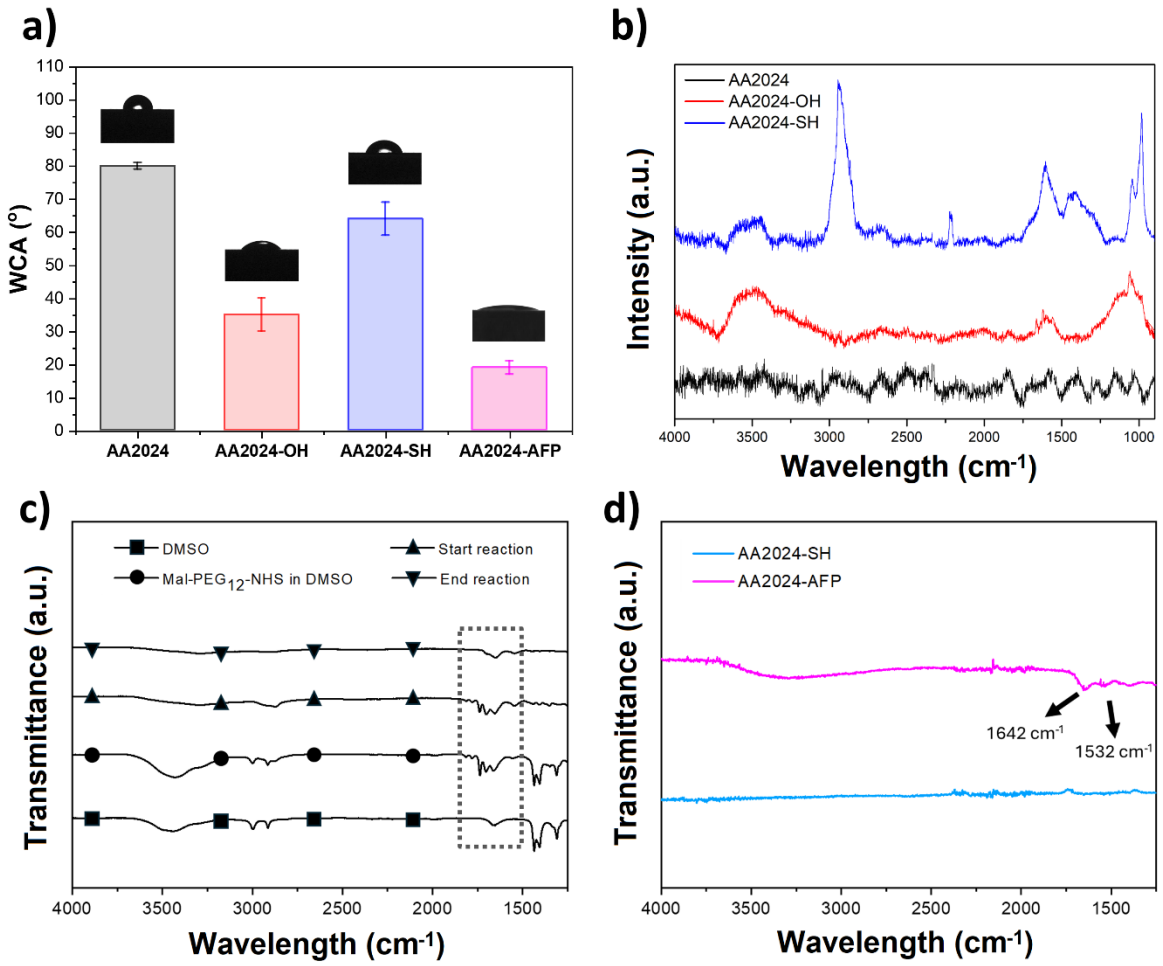

Figure 6.2. a) Static water contact angle (WCA) and b) Raman spectra of polished AA2024 (black colour), AA2024-OH (red colour), and AA2024-SH (blue colour); c) FTIR spectra of DMSO (squares), Mal-PEG_{12}-NHS in DMSO as a solvent (circles), start of the IBP/Mal-PEG_{12}-NHS reaction (triangles up), and end of the reaction (triangles down). d) FTIR spectra of AA2024-SH surface (blue) and AA2024-AFP surface (magenta) after immersion in IBP solution 1. The arrows mark the peaks of interest to confirm the reaction and surface modification.

Influence of protein degrees of freedom on freezing onset and propagation in the presence of molecular water layer

In natural environments, AFPs are typically found in a liquid medium while INPs are integrated in the bacterial membrane.[9,29,30] Previous research on AFPs in liquids, showed that the ice-suppressing behaviour increases initially with the AFP concentration and plateaus when reaching an AFP-dependent specific concentration.[19] To investigate the so far unexplored effect of the AFP concentration on surfaces on frost formation, the AA2024-SH surfaces were immersed in IBP solutions containing Mal-PEG$_{12}$-NH-AFP and Mal-PEG$_{12}$-NH-INP at two concentrations (2.5 and 5 mg ml^{-1}) as shown in solutions 1, 2, 5, and 6 in **Table 6.1**. The freezing process was followed using a high-resolution thermal camera as explained in the experimental section. **Figure 6.3a**, shows a thermal video snapshot of the local temperature increase due to the latent heat release during freezing. The freezing event here can be seen as a yellow-coloured (higher temperature) curved freezing front propagating on the purple-coloured (lower temperature) surface as indicated by the white dashed line and arrows. From these thermal videos (**Movies S6.1-S6.5**), a local temperature at the surface can be obtained and plotted as a function of the time. This allows extracting quantifiable freezing parameters such as freezing onset time (t_{fo}) and temperature (T_{fo}) as shown in **Figure 6.3b**.

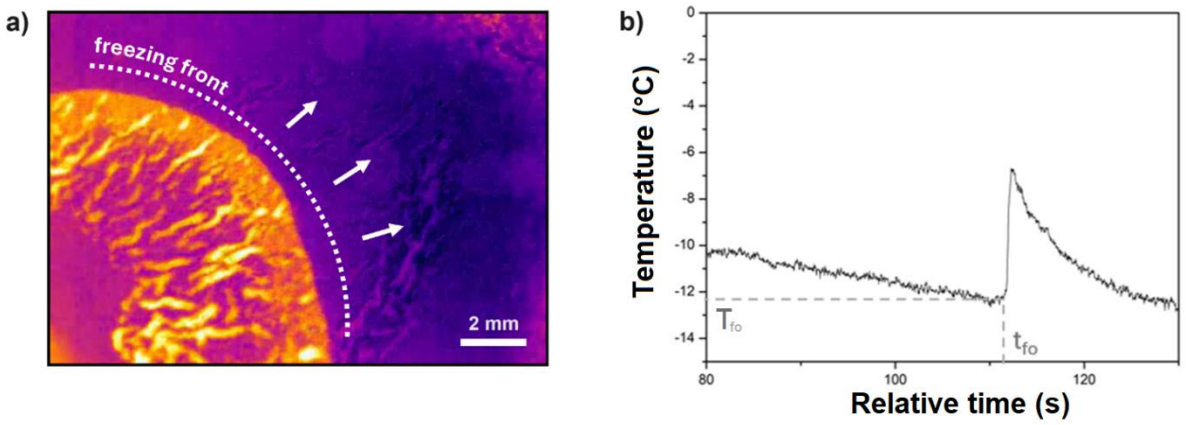

Figure 6.3. a) Snapshot from a thermal video showing the freezing-related high-temperature region (yellow) and the progressing freezing front (marked by a dashed white line and arrows) for an IBP-modified aluminium surface. b) Example of time-temperature graph extracted from the thermal video used to determine freezing onset parameters t_{fo} and T_{fo}.

Figure 6.4 shows the values of t_{fo} and T_{fo} of the different AFP-rich samples varying IBP type, IBP concentration and linker length, and the thiol-terminated surface (AA2024-SH) used as reference. **Figure 6.4a** shows how the surfaces coated with anti-freeze proteins (AFP) and ice nucleating proteins (INP) present shorter times to freeze (lower t_{fo}) and more positive temperatures (higher T_{fo}) than the thiol-terminated reference sample (AA2024-SH). INP samples show the expected behaviour in line with the ice nucleating character of INPs. This ice-promoting effect appears to be independent of the INP concentration for the studied concentration range. More unexpected is the behaviour of the samples with AFPs. For these samples, t_{fo} decreases and T_{fo} increases with increasing AFP concentration (i.e. freezing happens earlier and at more positive temperatures when more AFP is present at the surface). This trend is opposite to the behaviours reported for AFPs in liquid environments, where higher protein concentrations lead to lower freezing temperatures.[19]

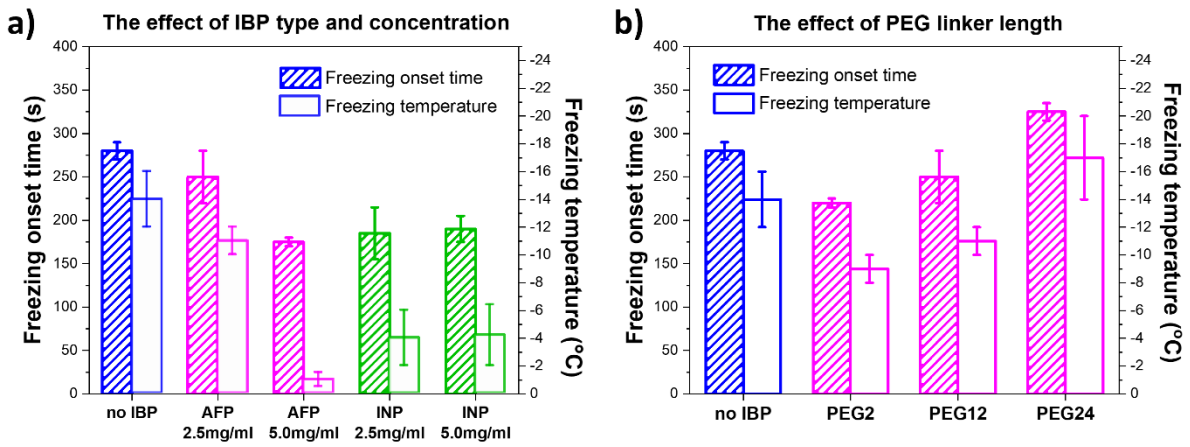

Figure 6.4. Freezing onset time (t_{fo}) and freezing temperature (T_{fo}) for different samples: a) t_{fo} and T_{fo} of AA2024-SH before protein grafting (no IBP, blue colour), grafted with Mal-PEG_{12}-NH-AFP (magenta colour), and grafted with Mal-PEG_{12}-NH-INP (green colour) obtained from solutions at two concentrations (2.5 mg ml^{-1} and 5.0 mg ml^{-1}). b) t_{fo} and T_{fo} of AA2024-SH (no IBP, blue colour) and AFP-modified surfaces (magenta colour) with various linker lengths (PEG2, PEG12, PEG24).

The somewhat unexpected results for the AFPs on the surface behaving like the INPs may be explained by the working principle of these proteins in their natural environments and their physical similarities and differences. While INPs typically have molecular weights ranging between 110-130 kDa, the AFPs are typically smaller with molecular weights in the range 2-50 kDa.[31,32] Both types of IBPs have two distinct structural regions: the ice-binding site (IBS) and the non-ice-binding site (NIBS). These regions lead to different water adsorption and structure: adsorbed ordered water molecules at the IBS lead to organized ice-like (INPs) or semiclathrate-like (AFP type III) configurations while the water layer on top of the NIBS remains disordered liquid-like when freezing.[9,19,33-37] In other words, surface disorder of the adsorbed water molecules leads to limited or no local ice growth.

As shown in **Figure 6.5a**, INPs in their natural environment generally appear attached to the bacterial membrane with their IBS pointing towards the external water phase. The IBS of the INPs orders water molecules into an ice-like arrangement which facilitates the kinetically hindered phase transition from liquid water to ice.[9,36,37] Consequently, INPs promote ice formation around the bacterial membrane. This effect is also reflected in the freezing results in **Figure 6.4a**. Furthermore, since INPs are considerably large proteins with large IBSs, the surface exposed to Mal-PEG_{12}-NH-INP is likely to become rapidly saturated with proteins with IBS at the surface. We therefore hypothesize that the surface saturation was achieved already at 2.5 mg ml^{-1} hence leading to no measurable effect in the freezing time and temperature when solutions at higher concentrations were used (**Figure 6.4a**).

Unlike INPs, AFPs are generally found in natural fluids rather than surfaces and lead to a somewhat more complex mechanism depicted in **Figure 6.5b**. Here, when an ice crystal nucleates in the fluid, the AFPs adsorb onto the ice crystal using their IBS. Further ice lattice growth at these attachment locations is hence inhibited while being surrounded by the NIBS of the proteins to further limit ice growth. The areas of the ice crystal not covered by proteins keep on increasing. This leads to a curvature increase which in turns increases the free energy of the ice phase to make it energetically unfavourable for water to transition from the liquid to the solid phase and hence further delaying ice growth.[19]

The results depicted in **Figure 6.4a** for the AFPs do not show this ice-delaying effect. Instead, they show an ice-promoting effect similar to that of the INPs. We attribute this to two factors: (i) the exposed ice-binding site of the AFPs promoting ordering of water molecules on the surface, and (ii) the lack of degrees of freedom of the proteins attached to the surface. We argue that these two factors should lead to faster freezing at higher protein concentrations due to a steric effect.

In their natural setting, AFPs can move around and adhere to small ice crystals through their IBS hence limiting ice growth. We hypothesize that when the AFPs are attached to the surface (at the concentrations and linker length reported in **Figure 6.4a**), their mobility is hindered significantly (as represented in **Figure 6.5c**) hence changing their natural working mechanism. Mobility decrease makes the formation of a curved ice front at the proteins not possible (i.e. bending of the grafted proteins around ice crystals is not possible). As a consequence, the exposed IBSs each act as individual nucleation templates for ice-like structures, hence exerting the opposite of the intended effect (i.e. AFPs grafted on surfaces behave as INPs in **Figure 6.5a**). By increasing the AFP concentration on the surface, the number of IBSs simultaneously increases, further enhancing their ice-promoting effect (**Figure 6.5c**) as observed in **Figure 6.4a** at higher AFP concentrations.

It is also important to note that the grafting approach chosen in this work targets the N-terminus of each IBP, thus ensuring that the IBSs of the type III AFPs are fully exposed to the surface. On the other hand, the INP is a β-helical protein with its end groups located at both bases of the cylindrical structure.[31-32] Therefore, the IBSs and NIBSs of the INPs are equally exposed after the surface grafting, which likely reduces the efficiency of their ice-nucleating function shown in **Figure 6.4**. The IBSs on samples grafted with AFPs are perfectly exposed for maximum binding to ice, whereas on samples grafted with INPs, the IBSs are less ideally oriented on the surface, thus resulting in less efficient ice growth promotion as expected.

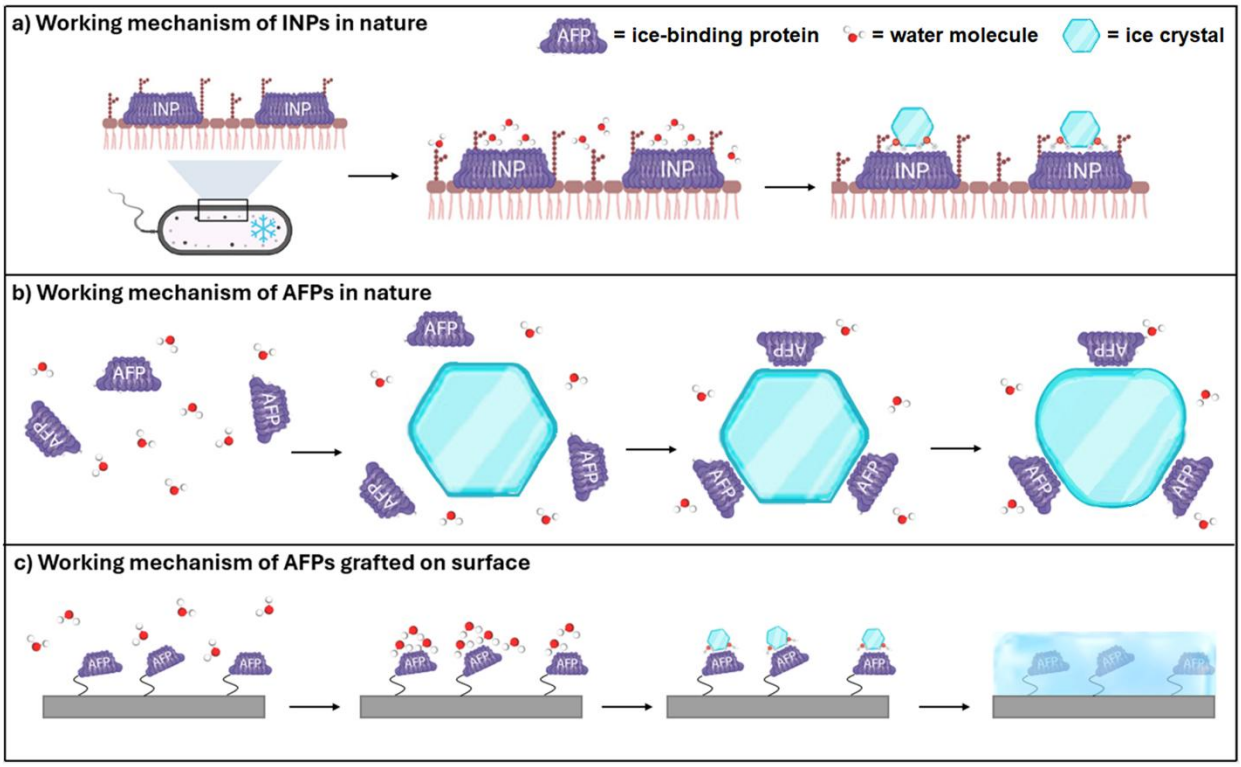

Figure 6.5. Illustrations of the working mechanisms of: a) INPs in their natural environment (e.g. present at the exopolymer substances of bacteria) leading to ice nucleation at the surface; b) AFPs in their natural environment (e.g. dispersed in body fluids of fish) leading to ice nucleation surrounded by proteins from their IBS and protected from further growth through their NIBS facing the fluid and the curvature of the trapped ice crystal; and, c) the AFPs grafted on to surfaces as studied in this work leading to ice nucleation and growth due to reduced mobility at the studied concentration and chain length (12 repeated units).

To further demonstrate our hypothesis that protein mobility and degrees of freedom from an anchored point at a surface is a crucial factor in the (anti)freezing character of (grafted) AFPs, we synthesized the same AFP but with different linker lengths and grafted them on AA2024-SH using solutions 1, 3, 4 shown in **Table 6.1**. **Figure 6.4b** shows the effect of the linker length on T_{fo} and t_{fo}. The results show how increasing the linker length (from PEG2 to PEG24) leads to longer times to freeze (t_{fo}) and more negative freezing temperatures (T_{fo} depletion) outstanding the values for the reference hydrophilic silanized sample (AA2024-SH). If the increasing PEG linker length would lead to lower grafting density due to steric effects reducing reactivity of the grafting, the results would have been opposite, showing a higher ice-promoting effect with the long PEG-24 linker. This result is compatible with our

hypothesis that protein mobility induced by flexible long chain linkers leads to higher anti-freezing character. We further argue that this mobility increase is partly possible due to the presence of a molecular water layer (MWL) formed by the hydrophilic character of AFPs, as supported by the low WCAs<20° of these samples (**Figure 6.2a**).

A close analysis of the freezing front mode and kinetics (**Figure 6.6** and **Movies S6.1**-**S6.2** in the support information) confirms the freezing kinetics of protein-rich surfaces to be in the range of 40-70 mm s^{-1} with no clear PEG-length dependency and with a smooth (non-fractal) frontline compatible with the values and propagation frontline mode reported for frost freezing on hydrophilic surfaces with MWLs.[30] Freezing on the AA2024-SH surfaces shows, on the other hand, a fractal frontline and propagation and much slower propagation rates (around 0.2 mm s^{-1}). This further confirms that the grafted PEG-AFPs increase hydrophilicity of the surface making MWLs more continuous, as illustrated in **Figure 6.6**. The results suggest that the AFP's ability to promote the formation of MWLs accelerates freezing propagation rates and raises the temperature at which freezing onset occurs (**Figure 6.4a**). Nevertheless, freezing at the surface is counteracted when the proteins have sufficient degrees of freedom in the MWL as achieved by longer linker length and experimentally observed by a depression of the freezing temperature below that of the reference sample and longer freezing onset times (**Figure 6.4b**). In other words, the data supports our hypothesis that AFPs recover the ice-depressing function they show in their natural environment when they get sufficient degrees of freedom in a water-rich layer (MWL), a factor that should be considered in future anti-freezing surface developments using IBPs.

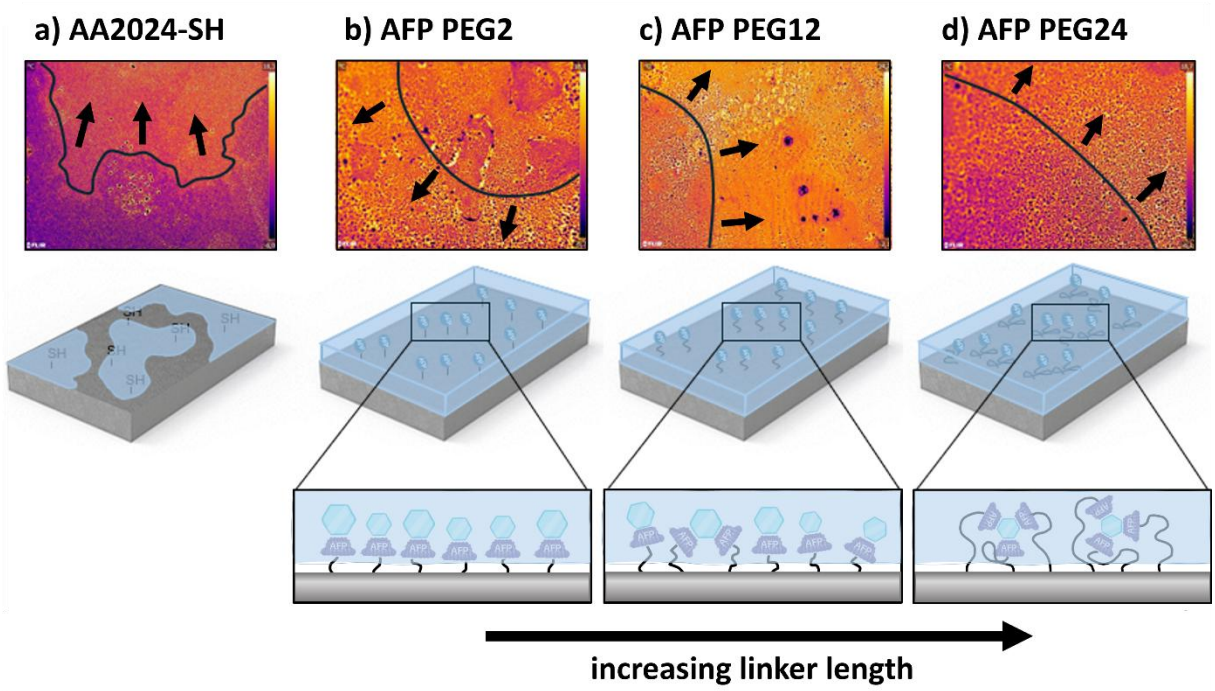

Figure 6.6. Freezing front propagation on AA2024-SH (propagation rate of 0.2 ± 0.08 mm s^{-1}) and on surfaces with AFPs grafted using PEG2, PEG12, and PEG24 linker lengths (propagation rates between 40-70 mm s^{-1}). The high propagation speeds on the AFP surfaces confirm the presence of continuous MWLs on these samples (MWL represented here with a blue box). It is hypothesized that, at sufficiently high linker lengths, the AFPs regain their ice-depressing character due to increased mobility as observed by a drop in T_{fo} and t_{fo}. For the higher linker lengths, this mobility, in combination with the continuous MWL at the IBPs away from the metal surface, makes it possible for the AFPs to gain degrees of freedom and act in a similar way as they would in their natural environment to inhibit ice growth.

AFP-induced freezing delay in confined polymeric environments rich in water

To further investigate the role of the environment, water layers, and degrees of freedom on the anti-freezing character of AFPs and approximate their potential use in organic coatings, hydrogels grafted with IBPs were synthesized as shown in the experimental section. Due to the rapid gelation of the hydrogel used in this work, a co-injection chamber (CIJ)[21], as illustrated in **Figure 6.7**, was used to directly apply the hydrogels on the AA2024-SH surfaces. In this approach, two separate solutions are simultaneously sprayed onto the substrate after a short residence time in a mixing chamber (**Figure 6.7**).

In our work, one solution contains PEG dithiol in PBS, while a second solution contains a four-arm-PEG-maleimide mixed with maleimide-modified AFPs in PBS with the AFPs at two different concentrations. The two solutions are manually positioned with a syringe into separate chambers of the CIJ and simultaneously pushed at high pressure into the mixing chamber and directly onto the metal surface. The thiol-maleimide click chemistry allowed simultaneously a rapid reaction between the hydrogel and the thiol-rich surface and cross-linking of the hydrogel network. A similar strategy was used to incorporate INPs in the hydrogel. However, due to their large size, the INPs are expected to be physically trapped in the hydrogel network instead of covalently bonded to the polymer backbone of the hydrogel as happens for the AFPs.

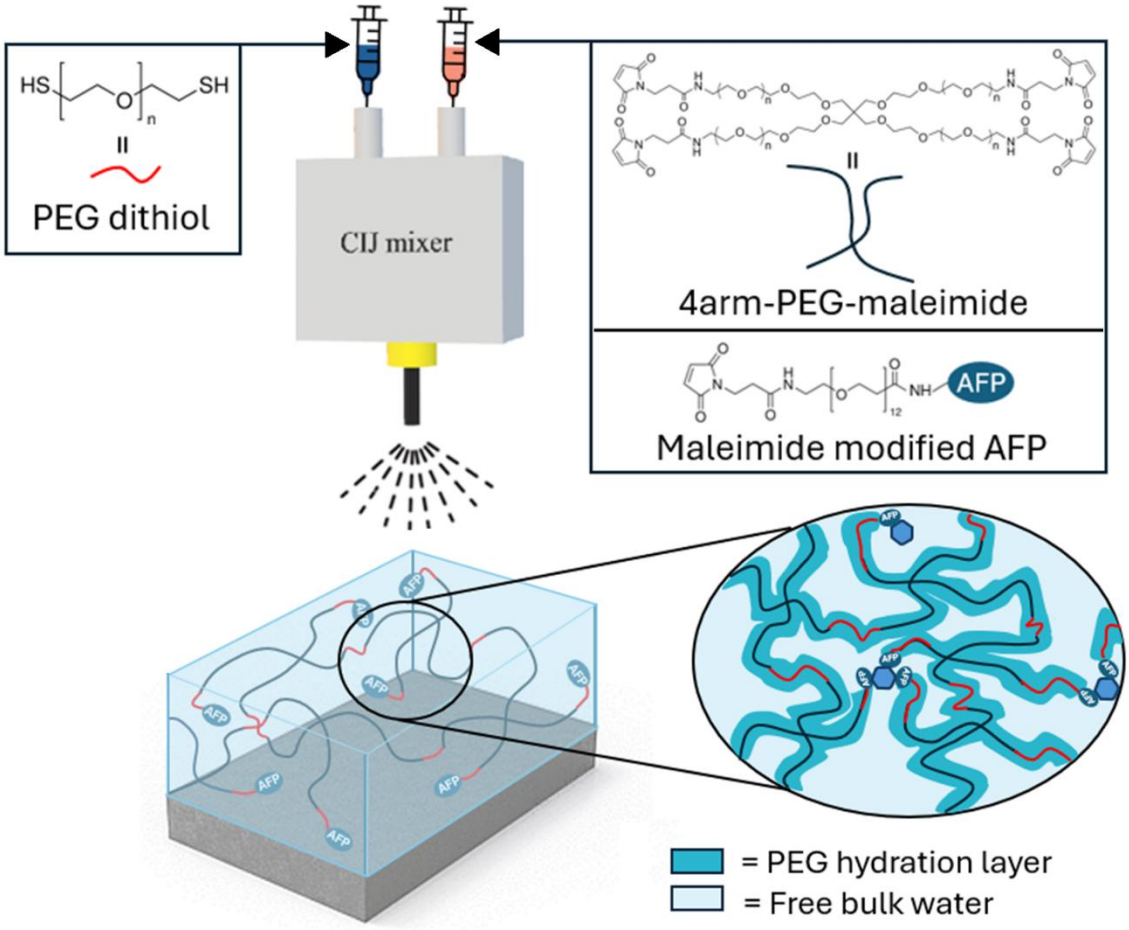

Figure 6.7. Rapid deposition of 500 µm-thick hydrogels onto AA2024-SH substrate using a co-injection mixer (CIJ). The long PEG linker length and hydration layer within the resulting hydrogel ensure high AFP mobility and functioning (bottom right image).

Figure 6.8a shows the freezing onset temperature (T_{fo}) and onset time (t_{fo}) for the different hydrogels. As expected, the presence of INPs in the hydrogels induces freezing at more positive temperatures (T_{fo}) and accelerates freezing (lower t_{fo}) with respect to the reference hydrogel without IBPs. This effect is slightly more pronounced when more INPs are used (2.5 mg ml^{-1} vs 5.0 mg ml^{-1}). Contrary to this effect, hydrogels containing AFPs have longer t_{fo} (freezing happens later) and a more negative T_{fo} when the AFP concentration increases. This confirms that the AFPs grafted inside a hydrated hydrogel network can successfully delay ice growth despite their hydrophilic character.

In agreement with the effects observed when grafted on surfaces using long dangling chains in the presence of a molecular water layer, we attribute the positive effect of AFPs in a hydrated hydrogel with low crosslinking density to the relatively high mobility induced by several factors increasing AFP degrees of freedom in a theoretically constrained media: (i) most AFPs in the hydrogel are attached to one arm of the 4-arm-PEG maleimide (dark blue line) through a PEG dithiol molecule (red line) (i.e. dangling arms) as represented in **Figure 6.7**; (ii) in such an environment, the water acts as a solubilizing medium protecting the AFPs from denaturation and ensuring their optimal function through mobility; and (iii) the hydrophilic character of PEG chains, allows the formation of a hydration layer adsorbed through hydrogen bonding (represented in **Figure 6.7** as dark blue area around the red chains) that prevents protein adsorption on the polymer backbone as observed in protein resistant polymers.[38]

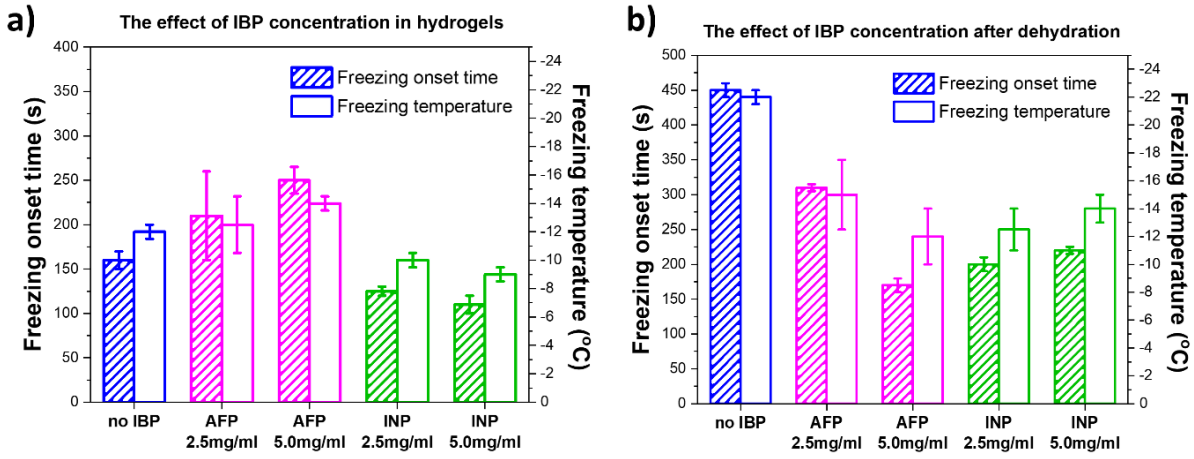

Figure 6.8. a) t_{fo} and T_{fo} of the hydrogels with no IBPs (blue colour), with AFPs (magenta colour), and with INPs (green colour) at two concentrations (2.5 mg ml^{-1} and 5.0 mg ml^{-1}). b) t_{fo} and T_{fo} of the dehydrated hydrogels with no IBPs (blue colour), with AFPs (magenta colour), and with INPs (green colour) at two concentrations (2.5 mg ml^{-1} and 5.0 mg ml^{-1}).

To further confirm our hypothesis proposing that the degrees-of-freedom of physically connected AFPs to polymers and surfaces is a key factor in controlling ice growth and propagation using AFPs, the hydrogels were dehydrated and subjected again to the same freezing tests. **Figure 6.8b** shows the corresponding freezing results. For hydrogels without IBPs, dehydration (**Figure 6.8b**) leads to freezing at much longer times (450 s vs 150 s) and lower temperatures (-21 ℃ vs -11.5 ℃) than the hydrated hydrogels (**Figure 6.8a**). Such an effect might be attributed to the balance between *freezable* and *non-freezable water* content as recently demonstrated in ionic polymers[22,39]. Freezable water is further subdivided into *freezable free water* and *freezable bound water*, depending on the interactions between the water and the polymer network. *Freezable free water* has no interactions with the polymer structure while freezable bound water has limited interactions with the polymer structure (absorbed water). We hypothesize that these interactions slow down the reorientation of water into an ice-like lattice, thus retarding ice growth. On the other hand, non-freezing water is tightly bound to the flexible polymeric structure (adsorbed water), preventing these water molecules from orienting into an ice-like lattice and thereby preventing freezing.[22,39]

The amount of these three different types of water in the hydrogel systems with different AFP concentrations was analysed in this study using differential scanning calorimetry (DSC) following the guidelines reported in a recent study[22]. As seen in **Figure 6.9**, the amount of freezable free water decreases when the AFPs are present in the hydrogel, while simultaneously, the amount of non-freezing water increases. Even though there are no significant changes between the two AFP concentrations, the increase in non-freezing water and decrease of freezable free water in the AFP-hydrogels supports the conclusion that the AFPs grafted inside a hydrated hydrogel network have sufficient mobility and can therefore successfully inhibit ice growth (**Figure 6.8a**). Moreover, recent findings studying hydrogels with various levels of hydration show how drying reduces the amount of freezable free water until only non-freezing water remains.[40]

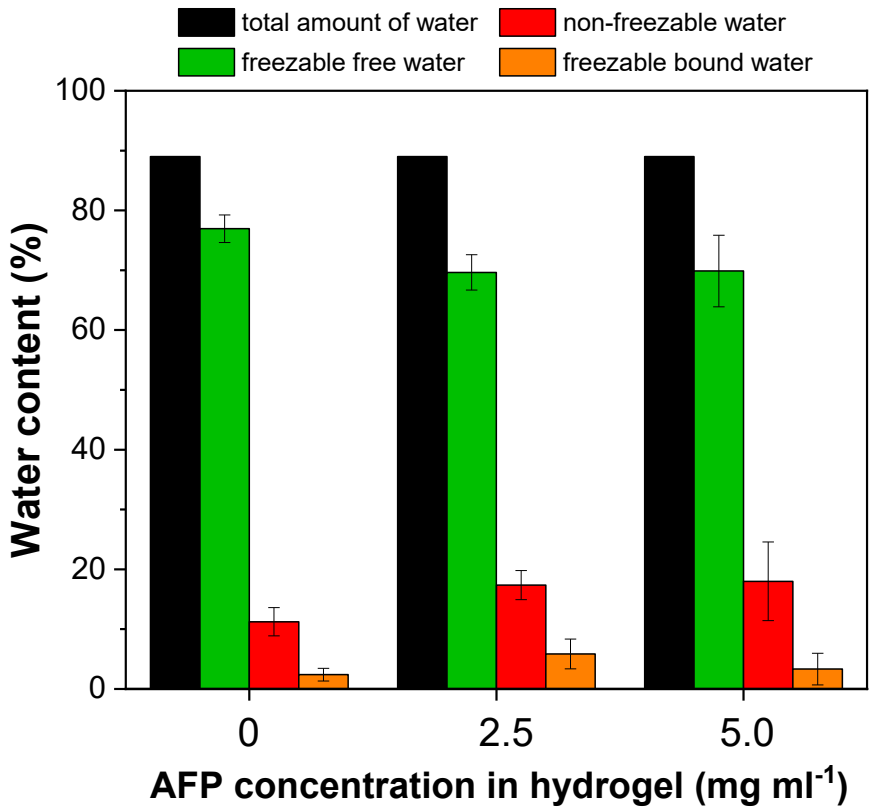

Figure 6.9. The amount of freezable free (green), freezable bound (orange), and non-freezable (red) water in the hydrogel systems with different AFP concentrations. The amount of freezable free water decreases when the AFPs are introduced into the hydrogel, while simultaneously, the amount of non-freezing water increases.

Following this reasoning, the large differences in freezing data between dehydrated and hydrated hydrogels can be explained. The hydrated hydrogels contain freezable free, freezable bound, and non-freezing water. The freezable free water freezes quickly as captured by the thermal camera (**Movies S6.3** and **S6.4**). On the other hand, the dehydrated hydrogels will likely only contain non-freezing and freezable bound water. Since freezable bound water reorients itself at a slower rate compared to freezable free water the dehydrated hydrogels freeze at a slower freezing propagation rate as detected by thermal imaging (**Movie S6.5**).

Conversely, the presence of AFP and INPs in a dry hydrogel accelerates freezing at more positive temperatures (**Figure 6.8b**) with no significant differences between IBP type and

concentration. This result is compatible with the hypothesis of the mobility discussed in this work, as lack of mobility in IBPs (INP and AFP) magnifies the ice acceleration effect of proteins with ice-binding sites (IBS) to further prove that protein mobility is crucial to obtain ice delaying effects when using antifreeze proteins.

Overall, these findings demonstrate that while AFPs can be useful in delaying ice formation, their successful use heavily depends on maintaining an environment that provides sufficient degrees of freedom for the proteins. As summarized in **Figure 6.10**, increasing the PEG linker length of the grafted AFPs or maintaining a hydration layer for AFPs in hydrogel matrices will ensure that the proteins have sufficient mobility to inhibit ice crystal growth on surfaces.

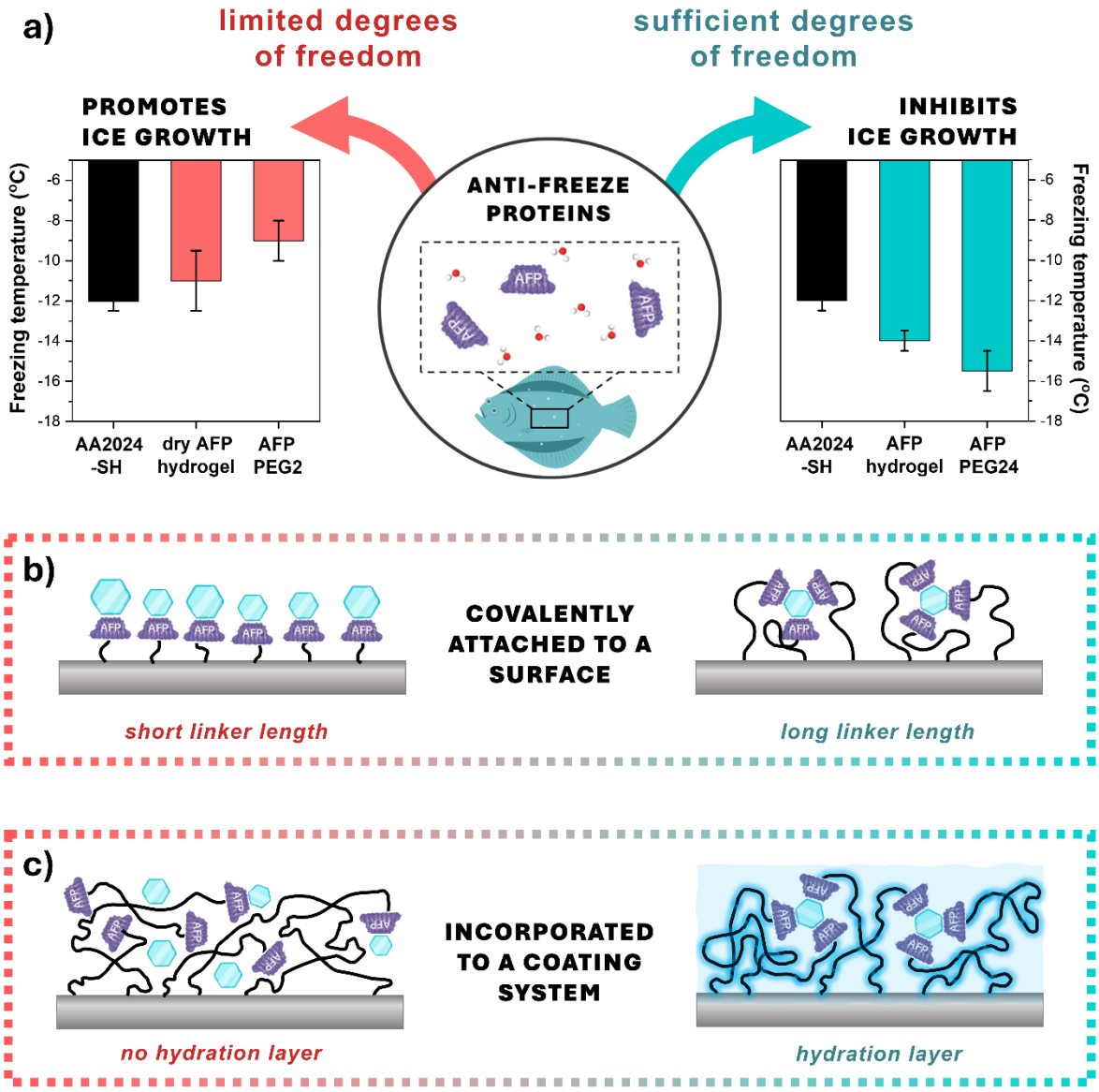

Figure 6.10. a) The AFPs are found to promote ice growth if they are incorporated on surfaces with limited degrees of freedom (left side). With sufficient degrees of freedom, the AFPs can inhibit ice growth on surfaces by lowering the freezing onset temperature and time (right side). b) AFPs covalently linked to surfaces require long chain lengths to provide sufficient degrees of freedom in the presence of molecular water layers, whereas c) inside a polymer network, a hydration layer is needed to ensure AFP mobility.

CONCLUSIONS

Two different types of IBPs (AFP and INP) were covalently attached to aluminium alloy (AA2024) surfaces and to the polymer backbone of a hydrogel using different linker chain lengths and protein concentrations. The results confirm the ice-promoting effect of INPs in all cases independently of the INP concentration used. AFPs, on the other hand, show a large dependency on the dangling chain length and protein concentration when grafted on surfaces or dangled in a PEG polymer backbone. The systematic study demonstrates the relevance of AFP mobility (degrees of freedom) in the reduction of ice accretion. While AFPs lead to the formation of molecular water layers (MWL) due to the overall hydrophilic character of the PEG-AFPs, long dangling chains enhance protein degrees of freedom in the MWL to prevent ice propagation. Conversely, in a constrained environment as a polymer hydrogel, hydration is responsible for the mobility of the dangling proteins and the related drop in freezing temperature and increase in freezing onset time. The findings here reported unveil a new design factor using AFPs and clear the path to the effective use of natural or synthetic AFPs in cutting-edge domains such as surfaces for (long-term) cryopreservation of biological samples, food preservation, electronics and sensors, and the creation of next-generation bioinspired low-icing functional coatings for wind-turbines and aircraft.

Characterization of different states of water in the hydrogel systems

The Differential Scanning Calorimetry (DSC) data shows two overlapping peaks corresponding to freezable free and freezable bound water (**Figure S6.1**). These peaks were deconvoluted and the area under each peak was calculated to obtain the melting enthalpy of the bound and free freezable water.

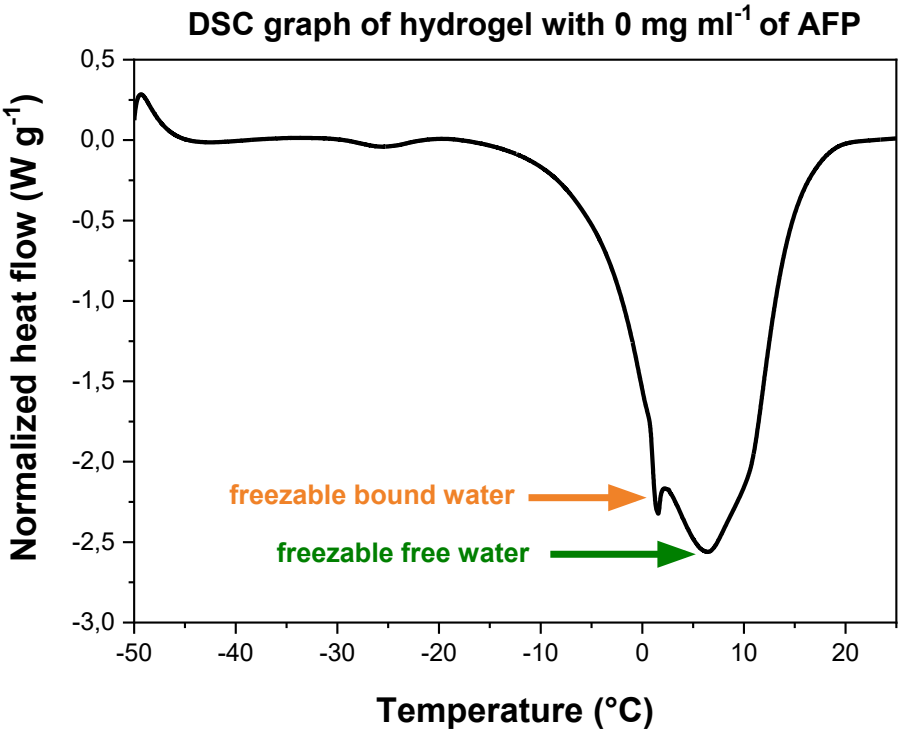

Figure S6.1. An example of a DSC graph showing the distinct peaks connected to freezable free water (green arrow) and freezable bound water (orange arrow) in a hydrogel system with no AFPs.

The fraction of bound freezable water and free freezable water can be found as:

$$W_{fb} = \frac{\Delta H_{fb}}{\Delta H_{PBS}} \tag{6.1}$$

$$W_{ff} = \frac{\Delta H_{ff}}{\Delta H_{PBS}} \tag{6.2}$$

Where ΔH_{fb} and ΔH_{ff} are the melting enthalpy of bound and free freezable water respectively. Both were found with DSC. ΔH_{PBS} is the melting enthalpy of PBS (293,3 J/g which was also found by DSC).

Logically, the total amount of freezable water then equals to: $W_{ftot} = W_{ff} + W_{fb}$

Finally, all hydrogels had a water content of 89%. As such, the total amount of water in the hydrogel (W_{tot}) equals 0,89. From this, the fraction of non-freezable water (W_{nf}) can be found as:

$$W_{nf} = W_{tot} - W_{ftot} \tag{6.3}$$

$$W_{nf} = 0{,}89 - W_{ftot} \tag{6.4}$$

Movie S6.1. QR code to access a thermal video of a slow freezing propagation on the thiol-terminated AA2024-SH surface.

Movie S6.2. QR code to access a thermal video of a rapid MWL-promoted freezing propagation on the AFP-grafted surface (2.5 mg ml^{-1} of AFPs with a PEG24 linker).

Movie S6.3. QR code to access a thermal video showing fast freezing of the freezable free water in a hydrated hydrogel with no AFPs.

Movie S6.4. QR code to access a thermal video showing fast freezing of the freezable free water in a hydrated hydrogel with a concentration of 2.5 mg ml^{-1} of AFPs.

Movie S6.5. QR code to access a thermal video showing slow freezing of freezable bound water in the dehydrated hydrogel with no AFPs.

REFERENCES

(1) He, H.; Guo, Z. Superhydrophobic Materials Used for Anti-Icing Theory, Application, and Development. *iScience* **2021**, *24* (11). https://doi.org/10.1016/j.isci.2021.103357.

(2) Azimi Yancheshme, A.; Allahdini, A.; Maghsoudi, K.; Jafari, R.; Momen, G. Potential Anti-Icing Applications of Encapsulated Phase Change Material–Embedded Coatings; a Review. *Journal of Energy Storage*. Elsevier Ltd October 1, 2020. https://doi.org/10.1016/j.est.2020.101638.

(3) Laforte, J. L.; Allaire, M. A.; Laflamme, J. State-of-the-Art on Power Line de-Icing. *Atmos. Res.* **1998**, *46* (1), 143–158. https://doi.org/https://doi.org/10.1016/S0169-8095(97)00057-4.

(4) Wei, K.; Yang, Y.; Zuo, H.; Zhong, D. A Review on Ice Detection Technology and Ice Elimination Technology for Wind Turbine. *Wind Energy*. John Wiley and Sons Ltd March 1, 2020, pp 433–457. https://doi.org/10.1002/we.2427.

(5) Cao, Y.; Tan, W.; Wu, Z. Aircraft Icing: An Ongoing Threat to Aviation Safety. *Aerosp. Sci. Technol.* **2018**, *75*, 353–385. https://doi.org/https://doi.org/10.1016/j.ast.2017.12.028.

(6) Latthe, S. S.; Sutar, R. S.; Bhosale, A. K.; Nagappan, S.; Ha, C. S.; Sadasivuni, K. K.; Liu, S.; Xing, R. Recent Developments in Air-Trapped Superhydrophobic and Liquid-Infused Slippery Surfaces for Anti-Icing Application. *Progress in Organic Coatings*. Elsevier B.V. December 1, 2019. https://doi.org/10.1016/j.porgcoat.2019.105373.

(7) Surís-Valls, R.; Voets, I. K. Peptidic Antifreeze Materials: Prospects and Challenges. *Int. J. Mol. Sci.* **2019**, *20* (20). https://doi.org/10.3390/ijms20205149.

(8) Ampaw, A.; Charlton, T. A.; Briard, J. G.; Ben, R. N. Designing the next Generation of Cryoprotectants – From Proteins to Small Molecules. *Peptide Science* **2019**, *111* (1), e24086. https://doi.org/https://doi.org/10.1002/pep2.24086.

(9) Eskandari, A.; Leow, T. C.; Rahman, M. B. A.; Oslan, S. N. Antifreeze Proteins and Their Practical Utilization in Industry, Medicine, and Agriculture. *Biomolecules* **2020**, *10* (12). https://doi.org/10.3390/biom10121649.

(10) Lukas, M.; Schwidetzky, R.; Eufemio, R. J.; Bonn, M.; Meister, K. Toward Understanding Bacterial Ice Nucleation. *J. Phys. Chem. B* **2022**, *126* (9), 1861–1867. https://doi.org/10.1021/acs.jpcb.1c09342.

(11) Brotzakis, Z. F.; Gehre, M.; Voets, I. K.; Bolhuis, P. G. Stability and Growth Mechanism of Self-Assembling Putative Antifreeze Cyclic Peptides. *Phys. Chem. Chem. Phys.* **2017**, *19* (29), 19032–19042. https://doi.org/10.1039/C7CP02465G.

(12) Voets, I. K. From Ice-Binding Proteins to Bio-Inspired Antifreeze Materials. *Soft Matter* **2017**, *13* (28), 4808–4823. https://doi.org/10.1039/C6SM02867E.

(13) Tas, R. P.; Sampaio-Pinto, V.; Wennekes, T.; van Laake, L. W.; Voets, I. K. From the Freezer to the Clinic. *The EMBO Reports* **2021**, *22* (3), EMBR202052162. https://doi.org/10.15252/embr.202052162.

(14) Gwak, Y.; Park, J. I.; Kim, M.; Kim, H. S.; Kwon, M. J.; Oh, S. J.; Kim, Y. P.; Jin, E. Creating Anti-Icing Surfaces via the Direct Immobilization of Antifreeze Proteins on Aluminum. *Sci. Rep.* **2015**, *5*. https://doi.org/10.1038/srep12019.

(15) Esser-Kahn, A. P.; Trang, V.; Francis, M. B. Incorporation of Antifreeze Proteins into Polymer Coatings Using Site-Selective Bioconjugation. *J. Am. Chem. Soc.* **2010**, *132* (38), 13264–13269. https://doi.org/10.1021/ja103038p.

(16) Charpentier, T. V. J.; Neville, A.; Millner, P.; Hewson, R.; Morina, A. An Investigation of Freezing of Supercooled Water on Anti-Freeze Protein Modified Surfaces. *J. Bionic Eng.* **2013**, *10* (2), 139–147. https://doi.org/10.1016/S1672-6529(13)60208-5.

(17) Jeong, Y.; Jeong, S.; Nam, Y. K.; Kang, S. M. Development of Freeze-Resistant Aluminum Surfaces by Tannic Acid Coating and Subsequent Immobilization of Antifreeze Proteins. *Bull. Korean Chem. Soc.* **2018**, *39* (4), 559–562. https://doi.org/https://doi.org/10.1002/bkcs.11406.

(18) Gao, Y.; Qi, H.; Fan, D.; Yang, J.; Zhang, L. Beetle and Mussel-Inspired Chimeric Protein for Fabricating Anti-Icing Coating. *Colloids Surf. B Biointerfaces* **2022**, *210* (38), 112252. https://doi.org/10.1016/j.colsurfb.2021.112252.

(19) Kristiansen, E.; Zachariassen, K. E. The Mechanism by Which Fish Antifreeze Proteins Cause Thermal Hysteresis. *Cryobiology* **2005**, *51* (3), 262–280. https://doi.org/10.1016/j.cryobiol.2005.07.007.

(20) Liu, K.; Wang, C.; Ma, J.; Shi, G.; Yao, X.; Fang, H.; Song, Y.; Wang, J. Janus Effect of Antifreeze Proteins on Ice Nucleation. *Proceedings of the National Academy of Sciences* **2016**, *113* (51), 14739–14744. https://doi.org/10.1073/pnas.1614379114.

(21) Han, J.; Zhu, Z.; Qian, H.; Wohl, A. R.; Beaman, C. J.; Hoye, T. R.; Macosko, C. W. A Simple Confined Impingement Jets Mixer for Flash Nanoprecipitation. *J. Pharm. Sci.* **2012**, *101* (10), 4018–4023. https://doi.org/10.1002/jps.23259.

(22) Biro, R. A.; Tyrode, E. C.; Thormann, E. Reducing Ice Adhesion to Polyelectrolyte Surfaces by Counterion-Mediated Nonfrozen Hydration Water. *ACS Appl. Mater. Interfaces* **2024**, *16* (16), 21356–21365. https://doi.org/10.1021/acsami.4c02434.

(23) Tavaststjerna, M. J.; Picken, S. J.; Garcia, S. J. Role of Molecular Water Layer State on Freezing Front Propagation Rate and Mode Studied with Thermal Imaging. *Langmuir* **2024**, *40* (25), 12888–12898. https://doi.org/10.1021/acs.langmuir.4c00323.

(24) Sieber, T.; Ducke, J.; Rietig, A.; Langner, T.; Acker, J. Recovery of Li(Ni0.33Mn0.33Co0.33)O2 from Lithium-Ion Battery Cathodes: Aspects of Degradation. *Nanomaterials* **2019**, *9* (2). https://doi.org/10.3390/nano9020246.

(25) Taghavikish, M.; Subianto, S.; Dutta, N. K.; Roy Choudhury, N. Novel Thiol-Ene Hybrid Coating for Metal Protection. *Coatings* **2016**, *6* (2). https://doi.org/10.3390/coatings6020017.

(26) Tsiourvas, D.; Tsetsekou, A.; Arkas, M.; Diplas, S.; Mastrogianni, E. Covalent Attachment of a Bioactive Hyperbranched Polymeric Layer to Titanium Surface for the Biomimetic Growth of

Calcium Phosphates. *J. Mater. Sci. Mater. Med.* **2011**, *22* (1), 85–96. https://doi.org/10.1007/s10856-010-4181-7.

(27) Oh, T. Comparison Between SiOC Thin Film by Plasma Enhance Chemical Vapor Deposition and SiO2 Thin Film by Fourier Transform Infrared Spectroscopy. *Journal of The Korean Physical Society - J KOREAN PHYS SOC* **2010**, *56*. https://doi.org/10.3938/jkps.56.1150.

(28) Miller, L. M.; Bourassa, M. W.; Smith, R. J. FTIR Spectroscopic Imaging of Protein Aggregation in Living Cells. *Biochimica et Biophysica Acta (BBA) - Biomembranes* **2013**, *1828* (10), 2339–2346. https://doi.org/10.1016/j.bbamem.2013.01.014.

(29) Bar Dolev, M.; Braslavsky, I.; Davies, P. L. Ice-Binding Proteins and Their Function. *Annu. Rev. Biochem.* **2016**, *85* (Volume 85, 2016), 515–542. https://doi.org/https://doi.org/10.1146/annurev-biochem-060815-014546.

(30) Davies, P. L. Ice-Binding Proteins: A Remarkable Diversity of Structures for Stopping and Starting Ice Growth. *Trends in Biochemical Sciences*. Elsevier Ltd 2014, pp 548–555. https://doi.org/10.1016/j.tibs.2014.09.005.

(31) Baskaran, A.; Kaari, M.; Venugopal, G.; Manikkam, R.; Joseph, J.; Bhaskar, P. V. Anti Freeze Proteins (Afp): Properties, Sources and Applications – A Review. *Int. J. Biol. Macromol.* **2021**, *189*, 292–305. https://doi.org/10.1016/j.ijbiomac.2021.08.105.

(32) Hartmann, S.; Ling, M.; Dreyer, L. S. A.; Zipori, A.; Finster, K.; Grawe, S.; Jensen, L. Z.; Borck, S.; Reicher, N.; Drace, T.; Niedermeier, D.; Jones, N. C.; Hoffmann, S. V; Wex, H.; Rudich, Y.; Boesen, T.; Šantl-Temkiv, T. Structure and Protein-Protein Interactions of Ice Nucleation Proteins Drive Their Activity. *Front. Microbiol.* **2022**, *Volume 13-2022*. https://doi.org/10.3389/fmicb.2022.872306.

(33) Mochizuki, K.; Molinero, V. Antifreeze Glycoproteins Bind Reversibly to Ice via Hydrophobic Groups. *J. Am. Chem. Soc.* **2018**, *140* (14), 4803–4811. https://doi.org/10.1021/jacs.7b13630.

(34) Pal, P.; Chakraborty, S.; Jana, B. Deciphering the Role of the Non-Ice-Binding Surface in the Antifreeze Activity of Hyperactive Antifreeze Proteins. *J. Phys. Chem. B* **2020**, *124* (23), 4686–4696. https://doi.org/10.1021/acs.jpcb.0c01206.

(35) Pal, P.; Chakraborty, S.; Jana, B. Differential Hydration of Ice-Binding Surface of Globular and Hyperactive Antifreeze Proteins. *Adv. Theory Simul.* **2021**, *4* (8), 2100090. https://doi.org/https://doi.org/10.1002/adts.202100090.

(36) Aich, R.; Pal, P.; Chakraborty, S.; Jana, B. Preferential Ordering and Organization of Hydration Water Favor Nucleation of Ice by Ice-Nucleating Proteins over Antifreeze Proteins. *J. Phys. Chem. B* **2023**, *127* (27), 6038–6048. https://doi.org/10.1021/acs.jpcb.3c01641.

(37) Pal, P.; Pal, S.; Jana, B. Molecular Insight of the Ice Nucleation by Ice Binding Protein: A Comparative Study With Ice Nucleating Protein, Antifreeze Protein, and Non-Ice-Binding Protein. *The Journal of Physical Chemistry C* **2025**, *129* (1), 600–610. https://doi.org/10.1021/acs.jpcc.4c05443.

(38) Ngo, B. K. D.; Grunlan, M. A. Protein Resistant Polymeric Biomaterials. *ACS Macro Lett.* **2017**, *6* (9), 992–1000. https://doi.org/10.1021/acsmacrolett.7b00448.

(39) Lee, E.; Lee, J.; Kim, D.; Jeong, K.; Seo, J. H. Investigation of Hydration State Effects on Ice and Frost Formation on Hydrogel-Coated Surfaces for Enhanced Anti-Icing/Frosting Properties. *Prog. Org. Coat.* **2024**, *197*, 108857. https://doi.org/10.1016/j.porgcoat.2024.108857.

(40) Ostrowska-Czubenko, J.; Gierszewska-Druzyńska, M. Effect of Ionic Crosslinking on the Water State in Hydrogel Chitosan Membranes. *Carbohydr. Polym.* **2009**, *77* (3), 590–598. https://doi.org/10.1016/j.carbpol.2009.01.036.

Acknowledgements

A PhD dissertation is never the work of one person alone. During the onboarding sessions at the beginning of my PhD at TU Delft, we were told that a PhD is not a typical job. Many candidates, we were warned, would experience burnout, anxiety, depression, or other mental health struggles before reaching the finish line. It was presented as an almost inevitable part of the process. Unsurprisingly, many people speak of their PhD years as something they endured rather than enjoyed. My own experience has been very different.

This does not mean that my PhD journey was without challenges, nor that it was somehow easier than others. If anything, it was unusually eventful. Alongside the research presented in this dissertation, I served in the ASM Management Team as the first Temporary Scientific Staff Representative, supported PhD activities at the Faculty of Aerospace Engineering through the AE PhD Council for three years, supervised several student projects, participated in teaching and laboratory courses, prepared a funding proposal, attended conferences and consortium meetings, moved houses twice, commuted from Amsterdam for two years, learned Dutch, obtained my first driving licence, and navigated the many personal challenges that inevitably accompany a PhD. And yet, despite all of this — or perhaps partly because of it — I genuinely enjoyed my PhD.

That enjoyment exists mostly because of the people around me. First and foremost, I would like to thank my promotors, Santiago and Stephen. **Santiago**, I hope this project has been the kind of delightful, unexpected outlier you are always looking for in the data. Brainstorming ideas with you has always been effortless, and I hope we continue those discussions for many years to come. **Stephen**, every PhD candidate needs a supervisor who can place research into a broader perspective while still supporting independent vision and creativity. Thank you for always encouraging both. I would also like to thank **Sybrand** for his guidance during the first year of my PhD before his retirement. Your support during the early stages of this project is greatly appreciated.

Beyond my supervisors, there are many people who made my PhD years unforgettable. **Tinashe**, if every academic workplace had someone like you, nobody would ever want to graduate. **Jingjing**, having you as my office mate made me one of the luckiest people in the faculty. **Marlon**, karaoke nights and pizza at Bar Sil were never the same without you there. **Lakshmi**, regardless of what you may think yourself, your emotional intelligence surpasses that of half the faculty combined. **Riccardo**, it is rare to meet someone so ambitious and competitive while still appreciating all things unconventional and free-spirited. **Elif**, I will always remember working with you in the chemistry lab and your unmatched hospitality during game nights. **Leith**, you possess both life wisdom and exactly the right attitude for surviving academia, and I have never once worried about your PhD.

I would also like to thank **Farah**, who may have joined our group by accident but quickly became the centre of every social activity. You have a remarkable talent for bringing people together. Many others contributed to the uniquely welcoming atmosphere of the Corridor: **Alejandro, Apurva, Deniz, Mirko, Tingyu, Edward, Orhun, Niklas, Aditya, Nikhil, Anton, Hugo, Vincent, Gawel, Satya, Adrià, Dimos**, and **Théo**. To **Mingyue**, thank you for your hospitality in Darmstadt, and I wish you all the best for the future. I would also like to thank my other SURFICE colleagues (**Theodoros, Navid, Pau, Andrea, Giulia, Luca, Catalina, Simrandeep, Alexandros,** and **Ali**) for the many discussions and collaborations throughout the project.

This dissertation would also not have been possible without the DASML technical staff. **Alexander**, the thermal imaging setup was the first major hurdle of my PhD. As a chemist who had previously assembled little more than glassware inside a fume hood, your help was invaluable — both with the imaging setup and later with the ice adhesion experiments. I would also like to thank **Caitlin, Mohammed, Roy, Dave**, and **Chantal** for their essential technical support throughout the project.

Shanta, thank you for making daily life in the department run so smoothly. More importantly, thank you for encouraging me to step outside my comfort zone and become involved in faculty representation and management activities. That encouragement opened doors that

shaped the rest of my PhD experience. **Ebu**, it is no exaggeration to say that this thesis would not exist without you. Your support came at a moment when I truly needed it, and without it I would likely have returned to Finland. I would also like to thank my fellow members of the PhD Council (**Malte, Jakob, Allard, Sarah, Marina, Ata, Victor, Anton, Flavio**, **Rúben,** and **Stavrow**) as well as **Laurike, Marlon**, and **Piero** at the Graduate School, whose important work often goes unnoticed despite being essential to the AE PhD community.

To the students I had the privilege to supervise: thank you for embracing projects that were perhaps not what one expects at the Faculty of Aerospace Engineering, and for approaching chemistry-driven research with enthusiasm and curiosity. **Laura**, you did not only complete your MSc project, but also truly understood it and developed your own scientific ideas, which is a rare sign of maturity. **Ronan**, your project may have been the most difficult, but I believe its impact will last the longest. **Sara**, your organizational abilities are unmatched, and working with you was always effortless. **Pedro**, your project explored unfamiliar territory, but I am certain it will become the foundation for many future ideas. **Iven**, your motivation and talent exceed that of many students far beyond the BSc level. Supervising you was a pleasure, and I hope our paths cross again someday at a conference.

Finally, I would like to thank my family. **Eve**, there is perhaps no other person who understands me as completely as you do. We shared the same childhood, the same home, the same schools, and many of the same passions. Knowing there is someone who will always understand how I feel is a gift few people have. **Äiti**, thank you for supporting every decision I have made and for believing in my abilities every step of the way. **Iskä**, thank you for always being someone I can speak to honestly and without fear of judgment. Knowing that you will always have my back is more valuable than I can express.

I would also like to thank **Ilias**, for always giving me honest perspective whenever I needed it and for being a constant source of support during the final stages of my PhD. Your rationality, high standards, and refusal to let me approach difficulties emotionally taught me to handle stressful situations with far more clarity and composure than I otherwise would have.

And finally, **Linda**. Towards the end of my PhD, I realized that many of my colleagues saw me as the creative one: the person with artistic vision, strong aesthetics, and a recognizable style. But this was not something that came naturally to me. It is something I learned over time. Whether in designing scientific posters or evaluating Eurovision performances, your influence shaped the way I see creativity and originality in the world. You will never read this, but your impact on my life, and on the work I create, is permanent. Even if my abilities are nowhere near yours, traces of your influence will remain in everything I make.

List of Publications

JOURNAL PUBLICATIONS

1. **Analysing Shear Force-Time Curves to Uncover the Effect of Roughness and Contamination on Ice Adhesion to Aluminium Alloys**

   Miisa J. Tavaststjerna, Iven M. Dolman, Sara Caliari, and Santiago J. Garcia
   Manuscript in preparation **2026**

2. **From Patterned to Continuous Hydrophilic Surface Lubrication as Strategies to Obtain Durable Low Ice Adhesion Coatings**

   Miisa J. Tavaststjerna, Ronan Connolly, Sara Caliari, Stephen J. Picken, and Santiago J. Garcia
   Progress in Organic Coatings **2026**, SSRN 6759921

3. **The Influence of Chemical Surface Patterning on the Freezing Behaviour of Impacting Supercooled Water Droplets**

   Miisa J. Tavaststjerna, Mingyue Ding, Jeanette Hussong, Stephen J. Picken, Ilia V. Roisman, and Santiago J. Garcia
   Surfaces and Interfaces **2025** *76*, 107918

4. **Mobility of Antifreeze Proteins as a Key Factor in their use to Control Ice Growth on Surfaces and Polymers**

   Laura Hoebus, Miisa J. Tavaststjerna, and Santiago J. Garcia
   Applied Surface Science Advances **2025** *28*, 100790

5. **Controlling Frost Propagation on Polymeric Surfaces Using SI-ATRP Chemical Micropatterning**

   Miisa J. Tavaststjerna, Stephen J. Picken, and Santiago J. Garcia
   Advanced Materials Interfaces **2025** *12*, 2400838

6. **Role of Molecular Water Layer State on Freezing Front Propagation Rate and Mode Studied with Thermal Imaging**

   Miisa J. Tavaststjerna, Stephen J. Picken, and Santiago J. Garcia
   Langmuir **2024** *40* (25), 12888-12898

CONFERENCE CONTRIBUTIONS

1. **Do Surface Defects and Impurities Increase Ice Adhesion?**

   Miisa J. Tavaststjerna, Stephen J. Picken, and Santiago J. Garcia
   Oral presentation, Coating Science International (CoSI) Conference, Noordwijk, The Netherlands, June 2025

2. **Polymers for Reducing Ice Accretion and Adhesion on Surfaces**

   Miisa J. Tavaststjerna, Stephen J. Picken, and Santiago J. Garcia
   Oral presentation, Coating Science International (CoSI) Conference, Noordwijk, The Netherlands, June 2024

3. **Effect of Chemical Patterning on Local Frost Propagation**

   Miisa J. Tavaststjerna, Stephen J. Picken, and Santiago J. Garcia
   Oral Presentation, European Materials Research Society (eMRS) Spring Meeting, Strasbourg, France, May 2024

4. **Low-Icing Surfaces – The Effect of Patterning on Surface Freezing Mechanisms**

   Miisa J. Tavaststjerna, Stephen J. Picken, and Santiago J. Garcia
   Poster Presentation, Materialen NL Conference, Arnhem, The Netherlands, December 2023

5. **Controlling Frost Formation on Aircraft Coatings Using Chemical Micro-Patterning**

   Miisa J. Tavaststjerna, Stephen J. Picken, and Santiago J. Garcia
   Oral Presentation, SAE International Conference on Icing of Aircraft, Engines, and Structures, Vienna, Austria, June 2023

6. **Low-Icing Surfaces – The Effect of Patterning on Surface Freezing Mechanisms**

   Miisa J. Tavaststjerna, Stephen J. Picken, and Santiago J. Garcia
   Poster Presentation, Dutch Polymer Days (DPD), Lunteren, The Netherlands, April 2023

7. **The Role of Molecular Water Layer (MWL) on Surface Freezing Mechanisms**

   Miisa J. Tavaststjerna, Stephen J. Picken, and Santiago J. Garcia
   Poster presentation, Coating Science International (CoSI) Conference, Noordwijk, The Netherlands, June 2022

AWARDS

1. **Innovation Award**
   from Coating Science International (CoSI) Conference in 2025 for the presentation "*Do Surface Defects and Impurities Increase Ice Adhesion?"*.

2. **Best Oral Presentation Award**
   from European Materials Research Society (eMRS) Spring Meeting in 2024 for the presentation "*Effect of Chemical Patterning on Local Frost Propagation"*.

3. **Best Poster Presentation Award**
   from Dutch Polymer Days (DPD) in 2023 for the poster presentation *"Low-Icing Surfaces – The Effect of Patterning on Surface Freezing Mechanisms"*.

4. **Best Poster Presentation Award**
   from the PhD Academic Event 2023 of the Faculty of Aerospace Engineering at TU Delft for the poster presentation *"Low-Icing Surfaces – Controlling Aircraft Icing"*.

5. **Creativity Award**
   from Coating Science International (CoSI) Conference in 2022 for the poster presentation *"The Role of Molecular Water Layer (MWL) on Surface Freezing Mechanisms"*.

About the Author

Miisa J. Tavaststjerna was born in Lahti, in the Päijänne-Tavastia region of Southern Finland. She obtained her Bachelor of Science degree in Chemistry from the University of Helsinki in 2018 and completed her Master of Science in Materials Research at the same institution in 2020. Her thesis work at the Laboratory of Polymers and Colloids in the Department of Chemistry focused on the synthesis of aqueous thermoresponsive polymers and the development of self-assembling amphiphilic block copolymers for drug delivery applications.

In 2021, she began her PhD at the Faculty of Aerospace Engineering at Delft University of Technology in the Netherlands under the supervision of Prof. (associate) Dr. Santiago J. Garcia Espallargas and Prof. dr. Stephen J. Picken as part of the SURFICE European Training Network. Funded by the European Union's Horizon 2020 research and innovation programme under the Marie Skłodowska-Curie grant agreement No. 956703, the consortium brought together universities, research institutions, and partner organisations across Europe to train researchers at the intersection of physics, materials science, and surface engineering. During her doctoral research, Miisa delved into the physics and chemistry of ice interaction with surfaces and developed new polymer-based strategies for ice control and removal of interest for aircraft applications. Besides a strong focus on research, Miisa also contributed to teaching and served as the first Temporary Scientific Staff Representative in the Management Team of the Department of Aerospace Structures and Materials and as PhD representative in the Faculty of Aerospace Engineering PhD Council.

In 2026, Miisa joined the Faculty of Applied Sciences at Delft University of Technology as a postdoctoral researcher. Her current work focuses on developing protective coating materials that enable optical hydrogen sensors to operate reliably under challenging environmental conditions, particularly inside alkaline electrolyzers.